ISSN 1811-1165 (Print)
ISSN 2413-2179 (Online)

EURASIAN PHYSICAL TECHNICAL JOURNAL

VOLUME 21, NO. 1(47), 2024

phtj.buketov.edu.kz

EURASIAN PHYSICAL TECHNICAL JOURNAL

p - ISSN 1811-1165
e - ISSN 2413-2179

Volume 21, No. 1(47), 2024

1st issue – June, 2004

Journal Founder and Publisher:

Karagandy University of the name of academician E.A. Buketov

Академик Е.А. Бөкетов атындағы Қарағанды университеті

Карагандинский университет имени академика Е.А. Букетова

https://phtj.buketov.edu.kz

Contact information:
Editorial board of EAPhTJ (Build. 2, room 216)
Karaganda Buketov University
Universitetskaya Str.28, Karaganda,
Kazakhstan, 100024
Subscription index: 75240

Tel: +7(7212) 77-04-03
Fax: +7(7212) 35-63-98
E-mail: ephtj@mail.ru
ephtj2021@gmail.com

Signed to print 27.03.2024
Format 60x84 1/8. Offset paper.
Volume 18.25 p.sh. Circulation 300 copies.
Order No. 29.

Басуға 27.03.2024 ж. қол қойылды.
Пішімі 60×84 1/8. Офсеттік қағазы.
Көлемі 18.25 ес.-б.т. Таралымы 300 дана.
Тапсырыс № 29.

Подписано к печати 27.03.2024 г.
Формат 60×84 1/8. Офсетная бумага.
Объем 18.25 печ.л. Тираж 300 экз.
Заказ № 29.

Printed in the Publishing house of the Karagandy University of the name of acad. E.A. Buketov

First registration Certificate No.4382-Zh, dated November 7, 2003.
Rediscount certificate No.KZ50VPY00027647, dated October 6, 2020 issued by Information Committee of the Ministry of Information and Social Development of the Republic of Kazakhstan

Eurasian Physical Technical Journal, 2024, Vol. 21, No. 1(47)

CONTENTS

PREFACE…… 4

MATERIALS SCIENCE

1 ***Rybina N.V., Rybin N.B., Litvinov V.G.***
STUDY OF CORRELATIONS IN THE RELIEF OF COMPLEX SURFACES USING THE EXAMPLE OF AMORPHOUS HYDROGENATED SILICON…… 6

2 ***Kozlovskiy A.L.***
STUDY OF THE INFLUENCE OF THE ACCUMULATED DOSE OF DAMAGE IN THE NEAR-SURFACE LAYER ON RESISTANCE TO EXTERNAL INFLUENCES ASSOCIATED WITH CORROSION PROCESSES DURING HIGH-TEMPERATURE ANNEALING. …….. 14

3 ***Kurbanov U.T., Zhumabaeva G. K., Dzhumanov S.***
NEW METAL/SUPERCONDUCTOR-INSULATOR TRANSITIONS AND THEIR EFFECTS ON HIGH-T_C SUPERCONDUCTIVITY IN UNDERDOPED AND OPTIMALLY DOPED CUPRATES …… 21

4 ***Ibraev I.K., Ibraeva O.T., Zhakupov T.M.***
MECHANISM OF FORMATION OF INTERNAL AND SURFACE DEFECTS IN CASTING AND THEIR TRANSFORMATION INTO SURFACE DEFECTS OF SHEET. 28

5 ***Baikenov M.I., Seldyugaev O.B., Guchenko S.A., Afanasyev D.A.***
REASON OF PITTING CORROSION OF MARTENSITIC STEEL IN SEA WATER…… 38

6 ***Omarova G.S., Serikov T.M., Seliverstova E.V., Auzhanova A.A., Ibrayev N.Kh.***
INFLUENCE OF PLASMON EFFECT ON THE SENSITIZATION OF TITANIUM DIOXIDE BY DYE MOLECULES……...……. 49

ENERGY

7 ***Skakov M.K., Baklanov V.V., Nurpaissova G.S., Akayev A.S., Bekmuldin M.K., Toleubekov K.O.***
ANALYSIS OF METHODS FOR SIMULATING THE DECAY HEAT IN CORIUM WHEN MODELING A SEVERE ACCIDENTS AT NUCLEAR POWER PLANT…… 57

8 ***Shaimerdenova K.M., Sakipov K.E., Abdirova N.T., Suleimenova S.E.***
IMPROVING THE QUALITY OF EKIBASTUZ COAL USING THE DRY ENRICHMENT METHOD ……...……... 67

ENGINEERING

9 ***Malikov V.N., Ishkov A.V., Voinash S.A., Zagidullin R.R., Sabitov L.S., Vornacheva I.V., Ivanov A.A.***
AUTOMATED CONTROL OF THE THIN FILMS ELECTRICAL CONDUCTIVITY BY THE EDDY CURRENT METHOD. …… 74

10 ***Minkov L.L., Gimayeva N.R.***
EFFECT OF TWO-PHASE FLOW ON THE FUEL GRAIN IGNITION AND ITS DEPARTURE FROM THE CARTRIDGE CASE. …….. 84

11 ***Kostina M.A., Soldatov A.I., Soldatov A.A., Abouellail A.A.***
SIMULATION OF MULTIPOINT CONTACT UNDER THERMOELECTRIC TESTING….. 93

12 ***Madi P.Sh., Al'kina A.D., Mekhtiyev A.D., Yurchenko A.V.***
HARDWARE AND SOFTWARE COMPLEX FOR STABILITY CONTROL OF QUARRY SIDES USING OPTICAL FIBER. ……... 104

13 ***Gadirov R., Borisov A., Trufanova N., Ragimov E., Artischev S.***
NUMERICAL MODELING OF THE PROCESS OF EXTRUSION OF HIGH-VISCOSITY PASTES. ……..……..… 114

PHYSICS AND ASTRONOMY

14 ***Inyang E. P., Ali N., Endut R., Aljunid S.A.***
ENERGY SPECTRA, EXPECTATION VALUES, AND THERMODYNAMIC PROPERTIES OF HCl AND LiH DIATOMIC MOLECULES…… 124

SUMMARIES……... 138

.

Dear authors and readers!
Dear colleagues!

In the preface, we traditionally inform authors and readers about the most important achievements of the Eurasian Physical Technical Journal at the moment. Thanks to our authors and to the qualified work of editorial board members, the Journal indexing in the Scopus database continues.

Since 2022 Eurasian Physical Technical Journal is included in the quartile Q3 on four scientific areas: Energy; Engineering; Materials Science; Physics and Astronomy. As of March 5, 2023, CiteScoreTracker score is 1.1 (max % 25 in Engineering). The value of this indicator directly depends on the number of citations of articles published in our journal.

Statistical data shows that over the past 5 years, 249 articles by authors have been published in the Eurasian Physical Technical Journal, of which 114 articles are by foreign authors from 23 countries. The number of articles by highly cited authors is gradually increasing. In 2023, out of 51 articles published, 17 (32%) articles were co-authored by highly rated authors. And in this first issue of 2024, 10 articles were submitted for publication by co-authors with Hirsh index more than 10, which is 71% of the total number of articles. We hope that this will help increase citations.

In September 2024, a special issue of the Eurasian Physical Technical Journal is planned with the publication of selected papers from the 7th International Conference on Engineering Science and Technology, ICEST2024, which will be held April 16-18, 2024 in Luxor, Egypt - https://ifsdl.org /icest2024/. In accordance with the preliminary agreement, the guest editor from the conference organizers will be professor, Dr. Nouby M. Ghazaly (South Valley University, Qena, Egypt). From the Kazakh side as a guest editor of the special issue, Dr. A.L. Kozlovskiy (Institute of Nuclear Physics, Almaty), was invited.

In this issue, the format of articles has been changed in accordance with the updated rules of the Committee for Quality Assurance in Science and Higher Education of the Ministry of Science and Higher Education of the Republic of Kazakhstan. The new format takes into account recommendations to indicate

- type of publication (Research Article, Review, Essay);
- dates of receipt of materials, examination or approval, acceptance and online publication of articles (Received, Revised, Accepted, Published online) -
- contribution of each author in the preparation of the article according to the application of CRediT (Contributor Roles Taxonomy);
- data of the authors according to the ORCID iD database.

CRediT (Contributor Role Taxonomy) was introduced by Elsevier to recognize the individual authors contributions and to facilitate collaboration by accurately describing each author's diverse contributions to a published work. CRediT applications are provided by authors during the application process. The corresponding author is responsible for the accuracy of the descriptions and their approval by all authors. Information for authors will be updated on the website in the coming days.

As for the actual content of this issue, the section “Materials Science” presents new original results on the study of the properties of various materials. Readers will be interested in the results of the study by Russian authors of “correlations in the surface topography of amorphous hydrogenated silicon using the methods of average mutual information and two-dimensional fluctuation analysis by identifying its structural components using the scale-space technique.” Relevant in terms of practical application are the results of a study of “structural and strength degradation of ceramic fuel cells, which have great potential for the production of hydrogen using electrolysis methods.” Researchers from Uzbekistan have discovered “the possibility of transforming a metal or superconducting system into a dielectric based on the metal/superconductor-dielectric transition mechanism in doped cuprates by studying the formation of polarons and the localization of doped charge carriers (holes) in them.” The “real temperature of the superconducting transition in these materials” has been determined.

Researchers from Temirtau have established the mechanism for the formation of micro- and macrostructural inhomogeneities in the cortical zone of ingots and their transformation into surface defects during the processes of heating, plastic deformation and rolling. In the work of our university employees, it was established that “corrosion of products made of martensitic stainless steel X17 in sea water occurs due to incomplete oxidation of chromium atoms in cells on the surface of the products.” Employees of the Institute

of Molecular Nanophotonics have studied at the nano-level “the influence of the plasmonic effect of metal nanoparticles on electron transfer from the dyes eosin and rhodamine B to TiO2,” which leads “to an increase in the efficiency of sensitization of the semiconductor by the molecules of the dyes under study.”

In the “Energy” section, readers are offered two articles that discuss the environmental aspects of energy. The article by East Kazakhstan researchers the results of a “comparative analysis of existing methods for simulating residual energy release in corium, which are used in various experimental facilities that study the operation of passive protection systems during severe accidents with reactor meltdowns at nuclear power plants" are presented. In second article “the possibilities of improving the quality of Ekibastuz coal through the use of “dry enrichment” technology, which makes it possible to reduce the harmful impact on the environment are discussed.

The “Engineering” section offers ways to solve pressing problems of automation of modern technologies and management and control systems. The article by Altai authors considers the possibility of “using the eddy current non-destructive testing method for measuring the electrical conductivity of thin metal films” using the example of copper films “obtained by vapor deposition in a vacuum.” In the article by authors from Tomsk, “the influence of a two-phase flow on the ignition of a fuel pellet” is considered, a “model of the process of ignition and ejection of a pellet” is proposed, and the ignition time of the end surface of the grain is estimated for various particle sizes.

As a result of joint research by authors from Tomsk and Egypt, “simulation of a multipoint contact in the thermoelectric measurement method” was carried out in the NI LabVIEW package.” The model was verified using three types of thermocouples in various combinations connected in parallel.” The joint work of Kazakh authors with a Tomsk scientist on the implementation of a system for uninterrupted monitoring of quarry operation in order to ensure safety made it possible to develop a “software and hardware complex for monitoring the stability of quarry sides using optical fiber.” The following article by authors from Tomsk presents the results of numerical modeling of the process of extrusion of high-viscosity pastes using a piston dispenser. The resulting solution “for a highly viscous suspension of terpineol and silver particle powder will allow you to control the paste extrusion process.” As a result of joint research by authors from Tomsk and Egypt, “simulation of a multipoint contact in the thermoelectric measurement method” was carried out in the NI LabVIEW package.” The model was verified using three types of thermocouples in various combinations connected in parallel.” The joint work of Kazakh authors with a Tomsk scientist on the implementation of a system for uninterrupted monitoring of quarry operation in order to ensure safety made it possible to develop a “software and hardware complex for monitoring the stability of quarry sides using optical fiber.” The next article of Tomsk authors the results of numerical modeling of the process of extrusion of high-viscosity pastes using a piston dispenser are presented. The resulting solution “for a highly viscous suspension of terpineol and silver particle powder will allow you to control the paste extrusion process.”

In the “Physics and Astronomy” section, an article by authors from Nigeria and Malaysia the solution of the Schrödinger equation using the Nikiforov-Uvarov functional analysis method according to Hultén, taking into account the screened Kratzer potential is shown. The energy equation was derived by the authors to determine the thermodynamic properties of diatomic molecules at various temperatures.

We hope that the presented research results will be of interest to scientists, teachers, researchers, doctoral students and undergraduates. I would especially like to express my deep gratitude to our reviewers for their objective and qualified examination of the materials, which contributed to ensuring the quality of the articles.

We will be glad to see you among our readers and authors of the next issues, in which it is planned to publish articles by leading scientists on the most relevant and priority areas of modern physics and technology.

Best regards,
Editor-in-chief, professor Saule E. Sakipova
March, 2024

EURASIAN PHYSICAL TECHNICAL JOURNAL

2024, Volume 21, No. 1 (47)

https://doi.org/10.31489/2024No1/6-13

Received: 07/11/2023 Revised: 30/01/2024 Accepted: 20/02/2024 Published online: 29/03/2024

Research Article

UDC: 539.213.26

STUDY OF CORRELATIONS IN THE RELIEF OF COMPLEX SURFACES USING THE EXAMPLE OF AMORPHOUS HYDROGENATED SILICON

Rybina N.V.*, Rybin N.B., Litvinov V.G.

Ryazan State Radio Engineering University named after V.F. Utkin, Ryazan, Russia
*Corresponding author: pgnv@mail.ru

Abstract. *The results of a study of correlations in the surface relief of amorphous hydrogenated silicon using the methods of average mutual information and two-dimensional detrended fluctuation analysis by identifying its structural components using the scale-space technique are presented. The experimental samples were model and real surfaces of amorphous hydrogenated silicon. The model surface was formed by superimposing the surfaces "Stochastic fractal", "Particles" and "Gaussian noise". The values of the scaling index were obtained from the dependences of the fluctuation function on the scale, as well as the values of the average mutual information and the maximum mutual information were calculated. A comparative analysis of the correlation dependencies of the model and the real surfaces of amorphous hydrogenated silicon has shown that the model surface "Particles" is closest to the surface structure of the experimental sample in terms of its characteristics. It was found that particles with dimensions of 65±10 nm are present in the surface structure of the experimental sample.*

Keywords: amorphous hydrogenated silicon, surface, relief, information-correlation characteristics, mutual information, fluctuation analysis, scale-space.

1. Introduction

Currently, materials with complex structures (composite, nanocrystalline, disordered, porous, etc.) are becoming increasingly popular in various fields of science and technology. Therefore, there is a need for special methods for studying the structure of such materials. As is known, in disordered materials there is no long-range order in the arrangement of atoms, therefore, to study the features of their structure, methods different from those used for ordered materials (for example, crystalline) are required. Most disordered materials are characterized by short- and medium-range order in the arrangement of atoms. The average order is determined by the interaction of lone pair electrons, van der Waals interaction, and is formed by atoms that are partly included in the second coordination sphere and coordination spheres of higher orders [1]. It is believed that the average order is manifested in the presence of clusters at a distance of about 10 nm. Consequently, average order can characterize the correlations of various structural elements in disordered materials. For example, the average order in amorphous hydrogenated silicon (a-Si:H) determines the order in the arrangement of silicon tetrahedra; in nanocrystalline a-Si:H, the average order determines the ordering of nanosized inclusions in the amorphous matrix. It was shown in [2] that with the formation of nanocrystalline silicon inclusions or $(Si:H_2)n$ chains, structural ordering of the amorphous matrix occurs.

The study of correlations in the surface topography of disordered materials helps to identify structural features at the average order level. Knowledge of the structural features allows connecting the properties of the resulting materials with the technological regimes for their production. To study correlations, it is

necessary to obtain primary information about the material in the form of data on the surface topography. Data on surface relief can be used to study the average order in the structure of disordered materials in cases where the relief is closest to the structure of the material in the bulk. The validity of using data on surface relief is associated with the theorem of F. Takens. According to the embedding method of F. Takens [3], any signal from the system contains information about all processes within it. Consequently, for disordered materials based on the surface topography, it is possible to study correlations [4] in the structure at the level of average order.

To study correlations in the surface topography of disordered materials, methods of average mutual information (AMI) [5] and two-dimensional detrended fluctuation analysis (2D DFA) were developed. The AMI method allows characterizing the structure of the material as a whole, and not individual elements of the structure, as is done by traditional methods based mainly on the calculation of statistical parameters (averaged roughness values, porosity, average grain size, etc.). The 2D DFA method allows identifying the type of correlations in the structure, as well as find correlation vectors, i.e. the scales at which the orderliness of the surface relief is manifested.

Since disordered material has a complex structure, it is also advisable to apply the scale-space technique [6]. The scale-space technique allows decomposing the surface relief into several structural components and study correlation properties for each subsurface. The use of AMI, 2D DFA and scale-space methods in combination makes it possible to study the complex structure of materials, in which both chaotic and harmonic components are present.

The purpose of this work is to study correlations in the surface topography of amorphous hydrogenated silicon using AMI and 2D DFA methods by identifying its structural components using the scale-space technique.

2. Description of the technique

The technique for studying surface relief correlations is as follows.

2.1. Scale-space technique

To study, it is necessary to have a surface height matrix, which is a square image, at each point of which with coordinates (*x*,*y*) the value of its height *f*(*x*,*y*) is stored. For any continuously differentiable and integrable mapping $f: \mathbb{R}^2 \to \mathbb{R}$ there is a set $L: \mathbb{R}^2 \times \mathbb{R}_+ \to \mathbb{R}$, which we will call the scale representation of the image *f*, defined as:

$$L(x, y, \sigma) = f(x, y, \sigma) * g(x, y; \sigma) = \int_{(\xi,\eta)\in\mathbb{R}^2} f(x-\xi, y-\eta) g(\xi, \eta; \sigma) d\xi d\eta, \quad (1)$$

where $g: \mathbb{R}^2 \times \mathbb{R}_+ \to \mathbb{R}$ – Gaussian convolution kernel on the extended plane $g(x, y; \sigma) = \frac{1}{2\pi\sigma} e^{-\frac{x^2+y^2}{2\sigma}}$, $\sigma > 0$.

The result of the convolution L(x,y;σ) is a scale representation of the surface f(x,y) with a scale factor σ. The geometric meaning of convolving a surface f(x,y) with a Gaussian kernel is to smooth the surface with a certain scale parameter σ. In this case, the value σ is related to the result of the operation L(x,y;σ) in such a way that all details are removed from the original image, the linear dimensions of which do not exceed the value √σ, in other words, two local extrema will be mutually destroyed (annihilated) or one will absorb another if the distance between them is less than √σ. This allows, on the one hand, to get rid of the noise of the source material (or significantly weaken it), and on the other hand, to leave the relief elements of the linear dimension that is necessary at the current stage of processing.

Thus, the decomposition of the surface image according to scales σ is the result of differentiation with respect to the second derivative. The most recent image is the most smoothed and should be visually very different from the original. However, it usually contains some features that cannot be seen in images close to the original one. For example, this way can get rid of various noises. In other words, one surface can contain many subsurfaces, the properties of which can be compared with simple models.

When studying complex surfaces that contain both harmonic and chaotic components, it is advisable to isolate their frequency characteristics. Moreover, the presence of a number of surfaces with different levels of detail (smoothing scales) can provide more information about the structure compared to analyzing only the original image. A large number of surface details correspond to the presence of a high-frequency component in the selected structure; a smaller number of details (smoothed surface) correspond to a low-frequency component.

.

2.2 2D DFA method

The 2D DFA method was descripted in [7]. For the height matrix $H(x,y)$ the cumulative surface $Y(x,y)$ is calculated:

$$Y(x,y) = \sum_{n=1}^{x}\sum_{m=1}^{y} H(x,y). \quad (2)$$

The cumulative surface is divided into $M_s \times N_s$ disjoint square segments of size $s \times s$, with $M_s = M/s$ and $N_s = N/s$. In each segment, a surface of the type $Y_{u,w}(x,y) = Y(l1+x, l2+y)$ is formed, for $1 \le x,y \le s$, where $l1 = (u-1)s$ and $l2 = (w-1)s$, where u, w are numbers segments.

In each surface $Y_{u,w}(x,y)$ a first-order polynomial trend function is calculated:

$$\tilde{Y}_{u,w}(x,y) = a \cdot x + b \quad (3)$$

$$\text{or } \tilde{Y}_{u,w}(x,y) = a \cdot y + b. \quad (4)$$

The remainder function is calculated:

$$\varepsilon_{u,w}(x,y) = Y_{u,w}(x,y) - \tilde{Y}_{u,w}(x,y). \quad (5)$$

The local RMS fluctuation function is calculated, bearing in mind that $\langle \varepsilon_{u,w}(x,y) \rangle = 0$:

$$F(s,u,w) = \sqrt{\frac{1}{s^2}\sum_{x=1}^{s}\sum_{y=1}^{s} \varepsilon_{u,w}(x,y)^2}. \quad (6)$$

The full root-mean-square fluctuation function is calculated:

$$F(s) = \frac{1}{M_s N_s}\sum_{u=1}^{M_s}\sum_{w=1}^{N_s} F(s,u,w). \quad (7)$$

For wide ranges of values s, the dependence is valid $F(s) \sim s^{\alpha}$.

In general, by plotting the dependence of F on s on a double logarithmic scale, a scaling index characterizing the type of correlations in the structure can be calculated from the tangent of the slope angle, and a correlation vector showing the scale of manifestation of these correlations can be calculated from the inflection of the fluctuation function.

2.3 AMI method

Mutual information [5] is defined as the amount of information that becomes known about the value of a random function at point A when its value becomes known at point B. If D is the domain of definition, Z is the domain of a random function, P_X is the probability distribution density at point X (as a function on Z), P_{XY} is the joint distribution density at points X and Y (as a function on Z_2), then the mutual information $I_{AB}(z_1,z_2)$ for a pair of known and predicted values is calculated according to the following formula:

$$I_{AB}(z_1,z_2) = log_2\left[\frac{P_{AB}(z_1,z_2)}{P_A(z_1)\cdot P_B(z_2)}\right]. \quad (8)$$

AMI is defined as the average expected value of mutual information for a given pair of points by integrating over Z^2:

$$I(A,B) = \iint_{Z^2} P_{AB}(z_1,z_2)\, log_2\left[\frac{P_{AB}(z_1,z_2)}{P_A(z_1)\cdot P_B(z_2)}\right] dz. \quad (9)$$

For practical tasks, so-called "convolutions" (transformed AMI functions) are calculated:

$$I_s(s) = \oiint_{S(d_1,d_2)=s} \frac{I(d_1,d_2)}{M_{S_D}(s)} d(d_1) d(d_2), \quad (10)$$

where d_1, d_2 are generalized parameters of points in the space D^2 (d_1 corresponds to two coordinates x_1, y_1, and $d_2 - x_2$, y_2). For each value of parameter s integration is carried out over all pairs of points that this convolution maps to a new space S_D, I is the average mutual information between points characterized by parameter s, and M_{S_D} is a measure of the new space S_D displayed by the selected convolution by parameter s in space D^2.

Ultimately, the AMI graph is a surface in a Cartesian coordinate system, the AMI values for any vector are in the range from 0 to 1. The criterion for the presence of correlation between the points of the sample under study is the presence of maxima on the AMI distribution graph.

The AMI method allows calculating directly the AMI value (Ψ_{OR}), which characterizes the degree of ordering of the structure, and the value of maximum mutual information (MMI, Ψ_{IC}), which shows the

spread of data (the number of points of different heights). Knowing the value of the MMI and the number of identical elements in the structure, it is possible to calculate the information capacity of the structure (relief).

The analysis of the results obtained using the scale-space, 2D DFA and AMI methods is carried out taking into account the criteria for determining the structural complexity of the surface of solid-state materials, classification of the values of α, Ψ_{OR} and Ψ_{IC} [8].

At $0.5<\alpha<2$, long-range or non-power correlations may be present in the system. In particular, $\alpha=1$ is characteristic of flicker noise ($1/f$ noise) and regular fractal, $\alpha=1.5$ - for Brownian noise. The value $\alpha=2$ is characteristic of strictly ordered structures.

For the cases of $\Psi_{OR}<0.02$, there is a low orderliness of the structure, $0.02< \Psi_{OR} <0.1$ – average orderliness of the structure, $\Psi_{OR}>0.1$ – high orderliness of the structure.

For the cases of $\Psi_{IC}<0.5$, there is a low information capacity and entropy of the structure, $0.5<\Psi_{IC} <0.7$ – average information capacity and entropy of the structure, $\Psi_{IC}>0.7$ – high information capacity and entropy of the structure.

3. Investigation of correlations in a-Si:H surface relief

To study correlations in the relief of the a-Si:H surface, a model surface was synthesized, and an experimental a-Si:H sample was selected. The model surface was created based on the presence of several components in the a-Si:H structure. Firstly, amorphous silicon has fractal properties [9]. Secondly, there is an average order in amorphous silicon [2, 10], which is manifested in the presence of clusters on the surface. And thirdly, amorphous silicon is a disordered material, so there must be a chaotic component in its structure. Based on these considerations, the model surface a-Si:H was created by superimposing three initial model surfaces on each other: "Stochastic fractal", "Particles", "Gaussian noise" (Fig. 1).

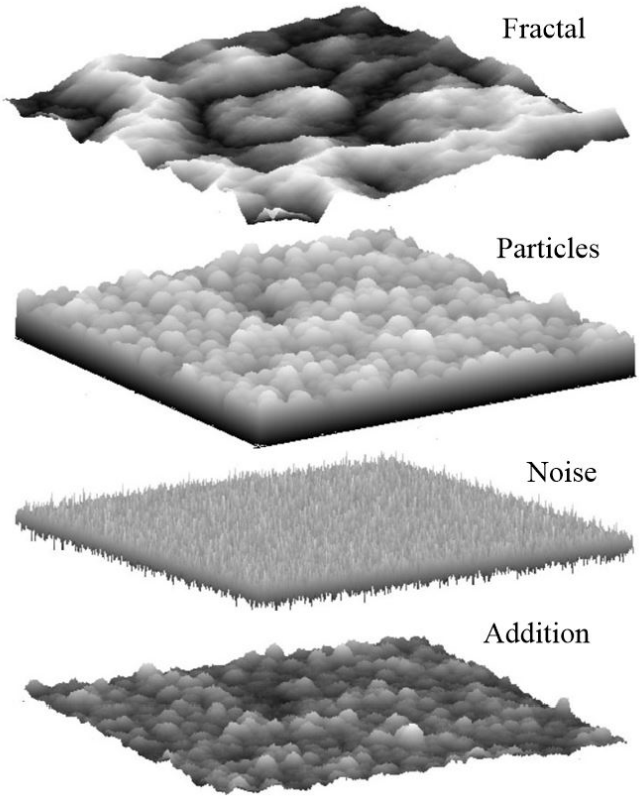

Fig. 1. Obtaining a model surface a-Si:H from the components "Stochastic fractal", "Particles", "Gaussian noise"

The experimental sample a-Si:H obtained by the glow discharge method of silane-containing mixtures was also used in the work. The frequency of the exciting generator was 13.56 MHz, the discharge power was maintained at 200 watts, a mixture of silane and hydrogen (10 % SiH_4+90 % H_2) was used as the supplied

.

gas. The substrate was *n*-type epitaxial silicon doped with antimony. The substrate temperature was 170 °C, the film thickness a-Si:H – 3 microns. The surface images of the experimental sample were obtained using an atomic force microscope (AFM) NTegra Aura in semi-contact mode (the diameter of the cantilever probe was 30 nm, the scan size was 5×5 microns). Enlarged for better visualization, a specific AFM image of the a-Si:H film in in three-dimensional representation is shown in Fig. 2.

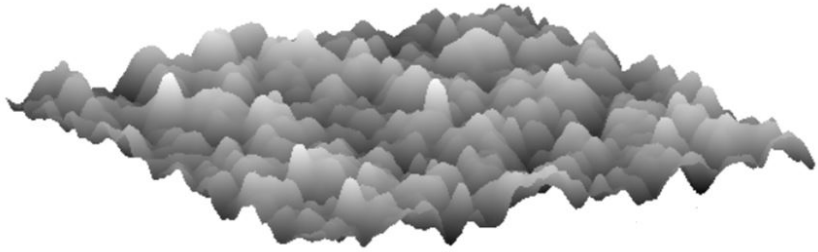

Fig. 2. The surface relief of the experimental sample a-Si:H (the dimensions of the presented area are 2.5×2.5 microns)

The initial model surfaces and the image of the surface of the experimental sample a-Si:H were investigated by 2D DFA and AMI methods. Graphs of the dependence of the fluctuation function *F* on the spatial scale *s* are shown in Fig. 3. It can be seen from the graphs that the model surfaces "Particles" and "Addition", as well as the surface of the sample a-Si:H have similar dependencies. On the one hand, it can be concluded that the structure of the surface of the experimental sample is close to the structure of the model surface of the "Particle", that is, it contains randomly arranged particles of different diameters. On the other hand, on the scales lg*s* = 2.2-2.5, the type of dependence *F*(*s*) of the experimental sample is similar to the addition of the dependencies "Stochastic fractal" and "Gaussian noise".

Table 1 shows the values of the scaling index α calculated from the dependencies *F*(*s*) (Fig. 3) up to the first inflection of the fluctuation function, as well as the values of AMI (Ψ_{OR}) and MMII (Ψ_{IC}) obtained from the distribution of mutual information.

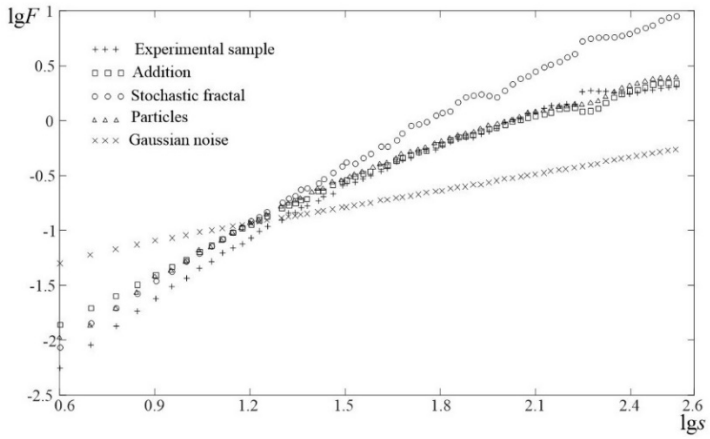

Fig. 3. Dependence of the fluctuation function F on the scale s

According to Table 1, it can be seen that the values of Ψ_{IC} fall into various categories of information capacity [8]: the "Stochastic fractal" surface refers to structures with high information capacity (Ψ_{IC}>0.7), the surface of the experimental sample – with low information capacity (Ψ_{IC}<0.5), and the surfaces "Particles", "Gaussian noise" and "Addition" – with average information capacity (0.5<Ψ_{IC}<0.7). The value of the information capacity of the surface of the experimental sample is closest to the Ψ_{IC} surface "Addition". By the value of Ψ_{OR}, the "Stochastic fractal" surface falls into the category of [8] structures with average ordering (0.02<Ψ_{OR}<0.1), and the rest – with low ordering. In this case, the value of the degree of ordering at the surface of the experimental sample is closest to the value Ψ_{OR} of the surface "Particles" than the surface "Addition". This can be attributed to the peculiarities of obtaining an image of the surface of the experimental sample. Since AFM was used, the surface image is a "convolution" of the probe and therefore the chaotic component is suppressed to some extent.

Therefore, to study correlations in the surface relief of disordered materials, it is advisable to use data obtained not only by AFM, but also by scanning electron microscopy (SEM). This conclusion is also confirmed by the results of calculating the scaling index, since the value of α at the surface of the experimental sample is very close to the value of α for strictly periodic signals (α=2), while for other surfaces the values of α are lower.

Table 1. Information and correlation characteristics of the studied surfaces.

Surface	Ψ_{IC}	Ψ_{OR}	α
Stochastic fractal	0.73	0.034	1.91
Particles	0.60	0.008	1.72
Gaussian noise	0.54	0.002	0.50
Addition	0.51	0.006	1.50
Experimental sample	0.46	0.013	1.98

Fig. 4 shows the results of the study of surface images using the scale-space technique, namely the dependencies of F(s) at different smoothing scales n for the experimental sample (Fig. 4, a) and the "Addition" surface (Fig. 4, b).

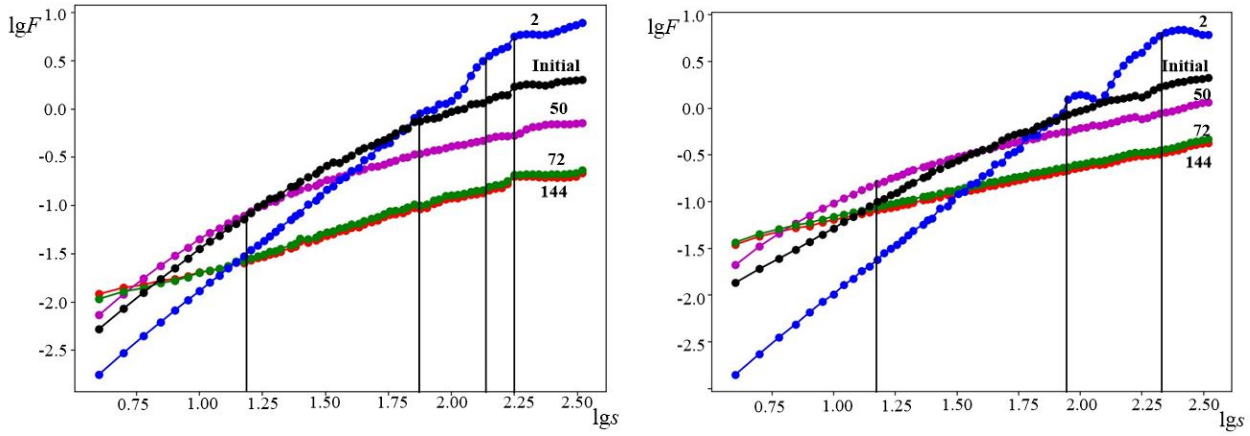

Fig. 4. F(s) dependences at different smoothing scales n for the experimental sample (a) and the "Addition" surface (b)

At large smoothing scales (72, 144 in Fig. 4), where high-frequency components of surfaces are manifested, there are practically no inflections on the dependencies F(s). This means that no harmonic components have been detected in the structure. The scaling index α has values of 0.6 and 0.55 for the experimental sample and the "Addition" surface, respectively. Such a value of α is close to the surface of "Gaussian noise". Thus, at large smoothing scales, the noise component prevails.

On the average smoothing scales (50), areas close to linear were approximated on the dependencies F(s), as a result of which an inflection of the function on a spatial scale of the order lgs = 1.18 was revealed. The presence of an inflection indicates that there is a harmonic component in the surface structure. To determine the period, use the formula, x = (b•10lgs)/a where b is the image size in microns (in this case 1.5 microns), a is the image size in pixels (in this case 350 dots). The period of the harmonic component was 65 ± 10 nm. A similar inflection was found on the dependence F(s) for the surface "Particles" (Fig. 5). Thus, particles with characteristic dimensions of 65± 10 nm are present in the structure of the surface of the experimental sample.

On small smoothing scales (2 in Fig. 4), where low-frequency components of surfaces are manifested, several inflections are observed on the dependencies F(s) in the range of spatial scales lg$s$ = 1,8-2,5. The values of the spatial scales corresponding to these inflections were 320 ±10, 580±10 and 760±10 nm for the experimental sample; for the "Addition" surface – 380±10 and 900± 10 nm.

On the one hand, such scale values can be explained by the frequency of repetition of particles, for example, 380 nm /65 nm ≈ 6, 900 nm / 65 nm ≈ 14, taking into account the error associated with the initial

.

image resolution and the calculation method. On the other hand, the appearance of additional inflections in the dependence of the fluctuation function may be associated with fractal properties.

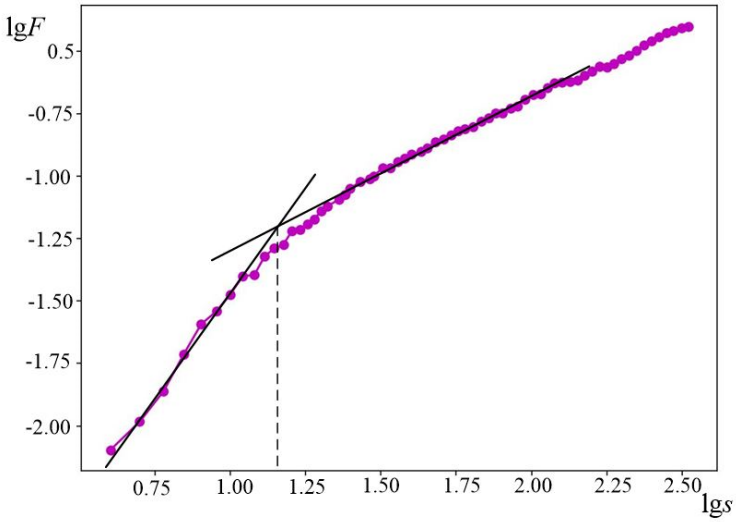

Fig. 5. Example of determining the correlation vector by the inflection of the fluctuation function for the model surface "Particles"

4. Conclusion

In this work, the use of the scale-space technique allowed identifying the structural components of the surface relief of amorphous hydrogenated silicon and investigating information-correlation characteristics at each structural level. The selection of low-frequency components allows studying the features of the harmonic components of the structure. The isolation of high-frequency components allows studying the features of chaotic components of the structure.

A comparative analysis of the information-correlation characteristics of the model surfaces and the experimental sample of amorphous hydrogenated silicon showed that the model surface "Particles" is closest to the structure of the experimental sample surface in its characteristics. This may be due to the peculiarities of obtaining an image of the surface by atomic force microscopy.

The study of the information-correlation characteristics of the a-Si:H film surface showed that the a-Si:H structure at different spatial scales exhibits the properties of all surface components used in the "Addition" model surface. Thus, any complex surface using the methods of AMI, 2D DFA, scale-space can be studied by decomposing into simpler components.

Conflict of interest statement

The authors declare that they have no conflict of interest in relation to this research, whether financial, personal, authorship or otherwise, that could affect the research and its results presented in this paper.

CRediT author statement

Rybina N.V.: Conceptualization, Data Curation, Writing - Original Draft; Rybin N.B.: Methodology, Investigation; Litvinov V.G.: Writing - Review & Editing, Supervision. The final manuscript was read and approved by all authors.

Funding

The work was performed as part of the state assignment of the Ministry of Science and Higher Education of the Russian Federation (FSSN-2020-0003).

Acknowledgements

This work was carried out using facilities of the Regional Center for Probe Microscopy Shared Service Center at Ryazan State Radio Engineering University.

References

1 Popov A.I. *Physics and technology of disordered semiconductors*. Moscow, Publishing house MPEI, 2008, 270 p. https://books.google.ru/books?id=17P2RAAACAAJ&hl=ru&source=gbs_navlinks_s [in Russian].

2 Golikova O.A. Average order and optoelectronic properties of a tetrahedrally coordinated hydrogenated amorphous semiconductor. *Physics and Technology of Semiconductors*, 2001, Vol. 35, No. 11, pp. 1370-1375. https://journals.ioffe.ru/articles/38663 [in Russian].

3 Takens F. Detecting strange attractors in turbulence. *Dynamical Systems and Turbulence*, 1980, Vol. 989, pp. 366-381. https://link.springer.com/chapter/10.1007/BFb0091924

4 Mursalov S.M., Bodyagin N.V., Vikhrov S.P. On the calculation of correlations in the structure of surfaces of solid-state materials. *Letters to the Journal of Technical Physics*, 2000, Vol. 26, No. 15, pp. 53-57. https://journals.ioffe.ru/articles/37864 [in Russian]

5 Avacheva T.G., Bodyagin N.V., Vikhrov S.P., Mursalov S.M. Study of self-organization in disordered materials using information theory. *Semiconductors*, 2008, Vol. 42, No. 5, pp. 499-504. https://doi.org/10.1134/S1063782608050011

6 Witkin A.P. Scale-Space Filtering. *Readings in Computer Vision: Issues, Problem, Principles, and Paradigms*, 1987, pp. 329-332. https://doi.org/10.1016/b978-0-08-051581-6.50036-2

7 Alpatov A.V., Rybina N.V. Application of the scale-space methodology to the study of self-organizing structures. *Surface. X-ray, Synchrotron and Neutron Studies*, 2019, No. 7, pp. 92-98. https://doi.org/10.1134/s0207352819050032 [in Russian]

8 Rybina N.V., Rybin N.B., Vikhrov S.P. Classification of the degree of self-organization of the relief of thin-film structures using 2D DFA and AMI methods. *Bulletin of the Ryazan State Radio Engineering University*, 2017, Vol. 61, No. 3, pp. 143-151. https://doi.org/10.21667/1995-4565-2017-61-3-143-151 [in Russian]

9 Golodenko A.B. Assessment of the adequacy of the fractal model of the atomic structure of amorphous silicon. *Physics and Technology of Semiconductors*, 2010, Vol. 44, No.1, pp. 87-91. https://journals.ioffe.ru/articles/7031 [in Russian]

10 Voyles P.M., Abelson J.R. Medium-range order in amorphous silicon measured by fluctuation electron microscopy. *Solar Energy Materials & Solar Cells*, 2003, Vol. 78, No. 1, pp. 85-114. https://doi.org/10.1016/S0927-0248(02)00434-8

AUTHORS' INFORMATION

Rybina, N.V. — Candidate of phys.-math. sciences, Associate Professor, Ryazan State Radio Engineering University named after V.F. Utkin, Ryazan, Russia; ORCID ID: 0000-0003-0377-5605; pgnv@mail.ru

Rybin, N.B. – Candidate of phys.-math. sciences, Associate Professor, Ryazan State Radio Engineering University named after V.F. Utkin, Ryazan, Russia; ORCID ID: 0000-0003-2000-0158; Nikolay.rybin@yandex.ru

Litvinov, V.G. – Dr. Sci. (Phys. and Math.), Associate Professor, Head of the Department, Ryazan State Radio Engineering University named after V.F. Utkin, Ryazan, Russia; ORCID ID: 0000-0001-6122-8525; vglit@yandex.ru

.

EURASIAN PHYSICAL TECHNICAL JOURNAL

2024, Volume 21, No. 1 (47)

https://doi.org/10.31489/2024No1/14-20

Received: 03/12/2023 Revised: 10/02/2024 Accepted: 23/02/2024 Published online: 29/03/2024

Original Research Article

UDC 538.971

STUDY OF THE INFLUENCE OF THE ACCUMULATED DOSE OF DAMAGE IN THE NEAR-SURFACE LAYER ON RESISTANCE TO EXTERNAL INFLUENCES ASSOCIATED WITH CORROSION PROCESSES DURING HIGH-TEMPERATURE ANNEALING

Kozlovskiy A.L.[1,2*]

[1] Laboratory of Solid State Physics, Institute of Nuclear Physics, Almaty, Kazakhstan

[2] Engineering Profile Laboratory, L.N. Gumilyov Eurasian National University, Astana, Kazakhstan

*Correspondence: kozlovskiy.a@inp.kz

Abstract. Investigating the challenges associated with the structural and strength degradation of ceramic fuel cells, which hold significant potential for hydrogen production through electrolysis methods, is a current focus of research. Understanding the degradation processes and their occurrence rate is crucial in the assessment of the efficacy of these ceramics for applications in alternative energy production, specifically in the realm of hydrogen energy. The aim of this study is to ascertain the impact of doping ceramics with aluminum nitride $NiAl_2O_4$, irradiated with protons with a dose of approximately 50 dpa, on resistance to high-temperature degradation, and associated corrosive processes of oxidation and swelling, as well as migration processes of implanted hydrogen. Three types of ceramics were selected as objects for study: $NiAl_2O_4$ ceramics, $NiAl_2O_4$ ceramics stabilized with 0.05 M AlN, $NiAl_2O_4$ ceramics stabilized with 0.15 M AlN, that are distinguished by the formation of impurity phases in $Al_7O_3N_8$, with an orthorhombic type of crystal lattice. As a result of high-temperature tests, it was observed that $NiAl_2O_4$ ceramics, when stabilized, exhibit reduced susceptibility to destructive alterations in strength characteristics, primarily attributed to the deformation distortion of the crystal structure caused by its swelling. These processes are associated with an augmentation in the thermal expansion of the crystal structure, manifested in the deformation swelling of the crystal lattice volume.

Keywords: ceramic fuel cells, radiation embrittlement, high-temperature aging, degradation, swelling, reduction in strength parameters.

1. Introduction

Addressing challenges in energy production is a crucial criterion for the sustainable development of any country's economy. Exploring alternative energy sources, such as nuclear or hydrogen energy, stands as a cornerstone in the development of the energy sector. The growing interest in alternative energy sources and the diversification of production methods primarily stem from the necessity to diminish the energy sector's reliance on fossil resources, including hydrocarbons [1-3]. The use of new sources of energy, including alternative sources, will in the short term reduce the amount of natural resources consumed for energy production, as well as the pressure on the environment, by reducing harmful emissions from the burning of fossil energy resources for energy production. In this connection, considerable emphasis in research is

directed towards hydrogen energy, particularly focusing on methodologies for hydrogen production through electrolysis or steam reforming [4,5].

The growing interest in ceramic fuel cells within the realm of hydrogen energy primarily stems from the potential to broaden sustainable approaches for hydrogen production and reduce its production costs. This reduction in cost is pivotal for the advancement of green technologies, serving as an alternative means to diminish hydrocarbon dependence within the energy sector [6,7]. Concurrently, study of degradation processes in fuel cells, linked to their operational procedures such as oxidation at elevated temperatures, represents a crucial research area. This exploration not only evaluates the suitability of ceramics in fuel cells but also contributes fundamental insights into the degradation mechanisms. Simulation of operational conditions, especially the elevated temperatures typical of fuel cells, enables an assessment of the degradation mechanisms in ceramic fuel cells. In scenarios involving gas-filled bubbles containing accumulated hydrogen, this simulation aids in understanding the kinetics of their migration and gauging their influence on changes in strength properties [8,9]. It is acknowledged that the high mobility and ability of hydrogen to aggregate within voids and pores can accelerate degradation processes when exposed to external factors, such as high-temperature heating. The high-temperature corrosion processes are instigated not only by the accelerated mobility of accumulated hydrogen in the near-surface layer of ceramic fuel cells, but also the processes of oxygen penetration through pores and microcracks [10-13]. Which results in destruction because of the accumulation of deformation distortions and stresses in cavities filled with hydrogen, as well as the crystalline structure into which oxygen is introduced. Moreover, an elevation in deformation distortions and stresses occurs both due to the expansion of the crystal lattice during the introduction of oxygen into nodes and interstices, and an elevation in gas-filled bubbles due to their merging or a growth in volume during the accelerated migration of hydrogen near these cavities [14,15].

Based on the above, the key aim of this article is to investigate the processes of high-temperature degradation of $NiAl_2O_4$-based ceramics stabilized with aluminum nitride, alongside to determine the influence of accumulated structural damage linked to the accumulation of hydrogen in the surface layer of ceramics on the degradation rate of the strength properties of ceramics.

2. Materials and methods

The objects of investigation were ceramic samples exhibiting a $NiAl_2O_4$ spinel structure, synthesized through mechanochemical solid-phase methods using NiO and Al_2O_3 compounds in a stoichiometric ratio of 1:3 M, followed by annealing at a temperature of 1500°C. Doping of $NiAl_2O_4$ ceramics in order to increase their resistance to external influences was carried out with aluminum nitride (AlN) with different molar ratios of 0.05 and 0.15 M, which were also annealed at a temperature of 1500°C. The specimens underwent grinding using a Pulverisette 6 planetary mill (Fritsch, Berlin, Germany), followed by thermal annealing conducted in a Nabertherm LHT 04/18 muffle furnace. (Nabertherm GnbH, Lilienthal, Germany). The choice of AlN dopant concentrations was determined by the possibility of obtaining ceramics exhibiting a significant structural ordering degree (exceeding 95% at a dopant concentration of 0.05 M) and ceramics containing impurity inclusions in the form of $Al_7O_3N_8$ impurity phases, characterized by an orthorhombic crystal lattice. A detailed study of the structural features of $NiAl_2O_4$ ceramics depending on the AlN stabilizing additive concentration was presented in the work [16]. The samples were irradiated at the UKP-2.1 accelerator (Institute of Nuclear Physics of the Ministry of Energy of the Republic of Kazakhstan, Almaty, Kazakhstan) with protons with an energy of 1.5 MeV and a fluence of 5×10^{15} ion/cm^2 (which, according to SRIM Pro 2013 calculations, corresponds to a displacement value of about 50 dpa).

To determine the degradation mechanisms characteristic of high-temperature corrosion processes of ceramic fuel cells exposed to proton irradiation with accumulated structural distortions caused by high-dose irradiation (about 50 dpa), the following experiments were carried out. The studied ceramic samples after irradiation were subjected to thermal heating in a muffle furnace for 500 hours at temperatures of 500, 600 and 700°C. The choice of the annealing temperature range (500 – 700°C) is due to the possibility of modeling the main operating modes of ceramic fuel cells during hydrogen production under conditions as close as possible to real ones. The choice of research objects subjected to irradiation is based on the ability to ascertain operational conditions and the accompanying structural deformations that manifest in samples with high concentrations of deformation distortions attributed to hydrogen accumulation.

Determination of the resistance of ceramics to high-temperature heating and corrosion processes was assessed by measuring hardness before and after testing. At the same time, measurements were performed

.

both on initial samples that were not exposed to irradiation, and after high-dose irradiation with protons with a dose of about 50 dpa. Determined values of changes in hardness and resistance to single compression made it possible to estimate the rate of degradation of ceramics as a result of high-temperature exposure, as well as to estimate the contribution of accumulated radiation damage to the degree of disorder of the surface layer. The hardness measurement was carried out using the indentation method, which was implemented using a Duroline M1 microhardness tester (Metkon, Bursa, Turkey). A Vickers pyramid was used for indentation; the load on the indenter was about 100 N. At the same time, the measurements were carried out taking into account the possible propagation of cracks at the indentation sites, which could affect the following results, in order to avoid such an influence, each subsequent measurement was performed at a distance of at least 20 μm from the previous indentation. Determination of resistance to single compression was carried out on a testing machine LFM-L 10kH (Walter + Bai AG, Löningen, Switzerland) by compressing samples in special holders at a constant speed of 0.1 mm/min. Determination of crack resistance was carried out by comparing alterations in the maximum pressure that ceramics can withstand during compression before and after external influences (proton irradiation and high-temperature aging).

3. Results and discussion

Figure 1 reveals data on variations in the hardness and cracking resistance of ceramic specimens before and after irradiation. The data were acquired through sequential testing of samples to assess the consistency of the properties of the synthesized ceramics and their resistance to external influences, with the aim of eliminating any artifactual effects stemming from irradiation. As indicated by the presented data, the inclusion of a stabilizing additive like aluminum nitride results in an increase in hardness and resistance to cracking under single compression. Additionally, similar to irradiated samples, it contributes to enhanced resistance to softening linked with the accumulation of structural distortions and deformations in the surface layer. The growth in resistance to radiation-induced softening for stabilized ceramics can be explained by the effects associated with the formation of inclusions in the form of impurity phases (for an additive concentration of 0.15 M), and in the case of lower concentrations of the stabilizing additive by a higher structural ordering degree of the ceramics' crystal structure. Moreover, analysis of variations in hardness and resistance to single compression indicates an almost identical trend of enhancing stability of the ceramics' strength properties as concentration of the stabilizing additive grows. The maximum reduction in strength characteristics is observed for unstabilized $NiAl_2O_4$ ceramics, for which high-dose irradiation results in a decline in strength characteristics by more than 15 – 16 %, while the addition of a stabilizing additive at concentrations of 0.05 and 0.15 M results in a more than twofold and fivefold increase in the stability of the strength characteristics of ceramics. The significant improvement in the resistance to strength property destruction observed in stabilized ceramics with a dopant concentration of 0.15 M is primarily linked to the emergence of inclusions in the shape of an impurity phase, $Al_7O_3N_8$. As demonstrated in work [16], these inclusions fill the intergranular space in the form of a fine fraction, thereby enhancing degradation resistance.

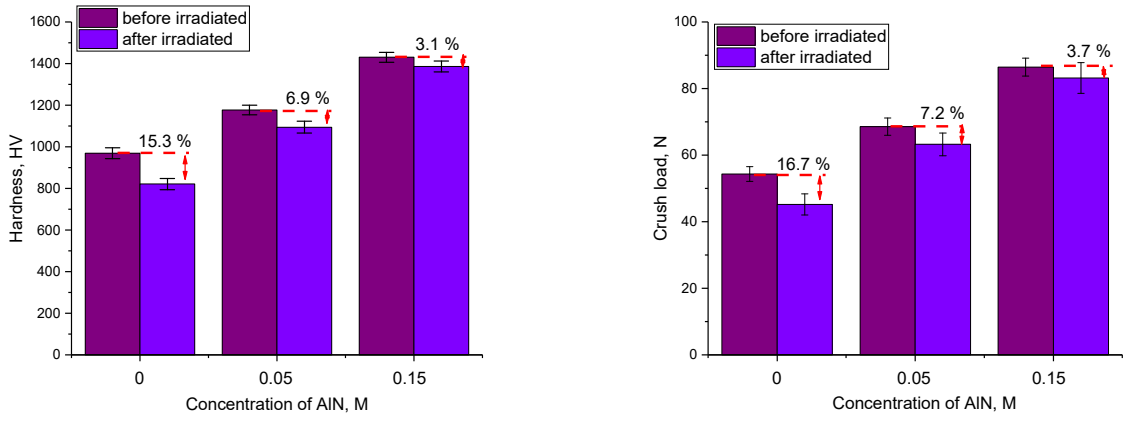

Fig.1. Irradiation effect on variations in strength parameters: a) variation in hardness; b) variation in the compressive force that the ceramic can withstand during a single impact

The observed softening for irradiated samples stems from the accumulation of deformation distortions of the crystal structure, alongside the formation of gas-filled inclusions in the pores, a growth in the concentration of which, alongside their combination into larger agglomerates, results in deformation of the near-surface damaged layer, as a consequence of a rise in internal pressure in the gas-filled cavities. The alteration in the deformation values of the crystal structure as a result of irradiation can be assessed by calculating the volumetric swelling of the crystal lattice, the value of which characterizes the deformation distortion of the damaged layer structure, alongside the effects related to the accumulation of distorting factors and residual tensile stresses. The assessment results are demonstrated in Figure 2 as a diagram reflecting percentage of the crystal lattice' volumetric alteration (swelling) in comparison with the initial values of the crystal lattice volume of ceramic samples.

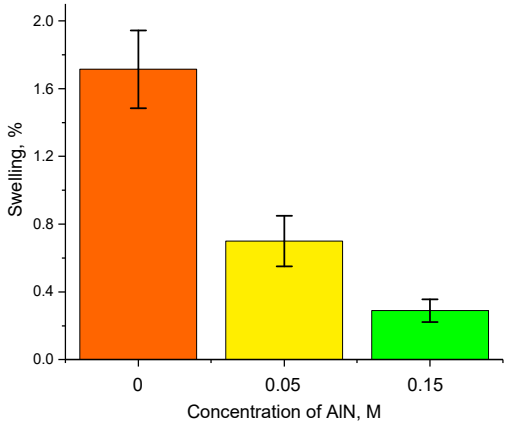

Fig.2. Results of volumetric swelling of the crystal lattice of $NiAl_2O_4$ ceramics subjected to irradiation

In accordance with the data acquired, presented in Figure 2, the incorporation of a stabilizing additive results in an elevation in the swelling resistance of ceramics, which, as a consequence, leads to a rise in resistance to destruction of strength characteristics. Moreover, more pronounced changes in elevated swelling resistance were observed for $NiAl_2O_4$ ceramics stabilized with 0.15 M AlN, for which the emergence of inclusions as $Al_7O_3N_8$ grains was observed. The enhanced swelling resistance is explained by the presence of interphase boundaries, alongside a higher dislocation density, the alteration in which is associated with the appearance of impurity inclusions. Figures 3 and 4 reveals the results of a comparative analysis of changes in strength properties (reduction in hardness and change in resistance to cracking under single compression) of ceramics under varying conditions of high-temperature exposure (temperature change).

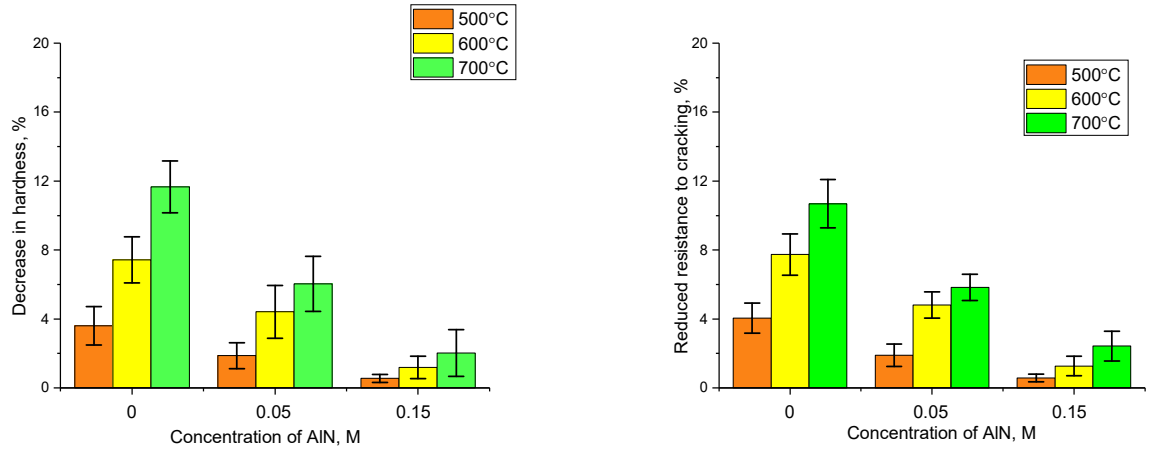

a) b)

Fig.3. Assessment results of variations in strength characteristics of initial ceramics after 500 hours of high temperature exposure: a) change in hardness; b) change in crack resistance

The tests were executed during 500 hours of annealing in a muffle furnace at various temperatures. The samples were subjected to strength properties measurements afterwards. The overall trend in the changes to the strength properties of ceramics suggests the detrimental impact of high-temperature corrosion on the stability of these characteristics, particularly evident at elevated temperatures (600 – 700°C). However, the data obtained indicates that the addition of the stabilizing additive AlN to the ceramic composition leads to an enhanced resistance to high-temperature degradation, manifested in a reduction of more than 2-3 times in the value of changes in strength characteristics. Additionally, it is noteworthy that a comparable pattern is evident not solely in the initial ceramics, where the decline in strength characteristics is primarily attributable to corrosion processes and alterations in the amplitude of thermal vibrations of atoms at the nodes of the crystal lattice, resulting in its destruction. The corrosion processes, in the case of prolonged high-temperature degradation, are prompted by the penetration of oxygen into the ceramics, thereby amplifying the deformation distortion of the structure and generating distorted areas that contribute to the destabilization of strength properties.

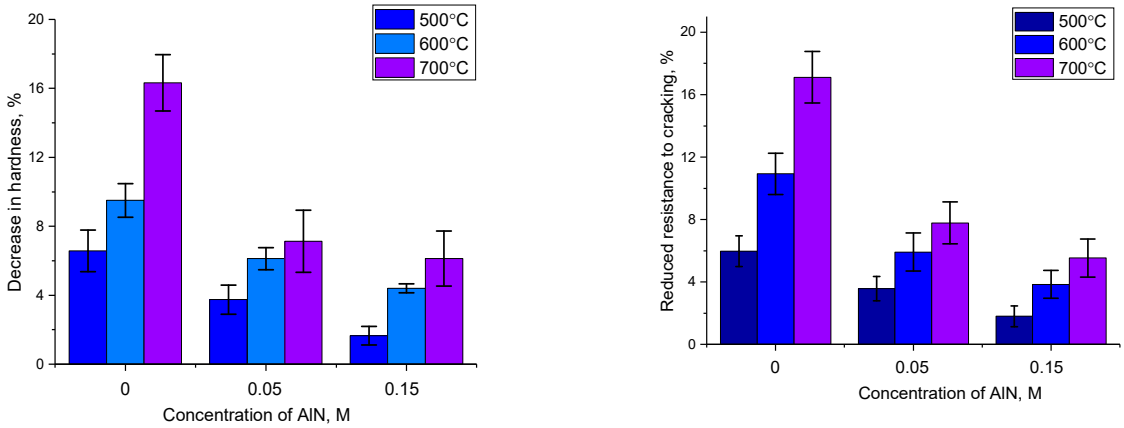

a) b)

Fig.4. Assessment results of variations in strength characteristics of irradiated ceramics after 500 hours of high temperature exposure: a) change in hardness; b) change in crack resistance

More pronounced degradation of the strength characteristics of irradiated ceramics, in addition to deformation distortions associated with corrosion processes, is also due to the presence of gas-filled cavities that distort the crystalline structure (the presence of these inclusions is indirectly explained by the deformation swelling of the crystal lattice, which is caused by high-dose irradiation, as well as the very nature of hydrogen, associated with its poor solubility). Moreover, the addition of stabilizing additives also results in a reduction in destructive alterations in ceramics' strength properties, which in turn indicates the positive effect of incorporation of aluminum nitride to the ceramics' composition, and the very trend of alterations in strength characteristics depending on the stabilizing additive concentration in comparison with similar changes for non-irradiated samples indicates the same mechanisms of destruction of ceramics caused by high temperature exposure. Figure 5 demonstates the alteration results of the structural swelling value of the crystal lattice of ceramics under diverse thermal exposure conditions (variations in annealing temperature).

These variations delineate the processes of structural degradation in ceramics linked to deformation distortions induced by thermal influences (volumetric thermal expansion of the crystal structure). Additionally, they represent degradation processes associated with corrosion and oxygen penetration. In the case of irradiated samples, these processes also involve migration, resulting in the agglomeration of implanted hydrogen due to heightened mobility.

Analyzing the obtained dependences of the crystal lattice swelling value of ceramics in the initial and irradiated states, the subsequent deductions can be made. The exposure temperature growth leads to a rise in the structural deformation of the crystal lattice, which indicates the influence of changes in the amplitude of thermal vibrations and the mobility of vacancy defects in the ceramics' structure (for non-irradiated samples), the combined effects of which lead to deformation swelling of the structure, most pronounced at temperatures of 600 - 700°C.

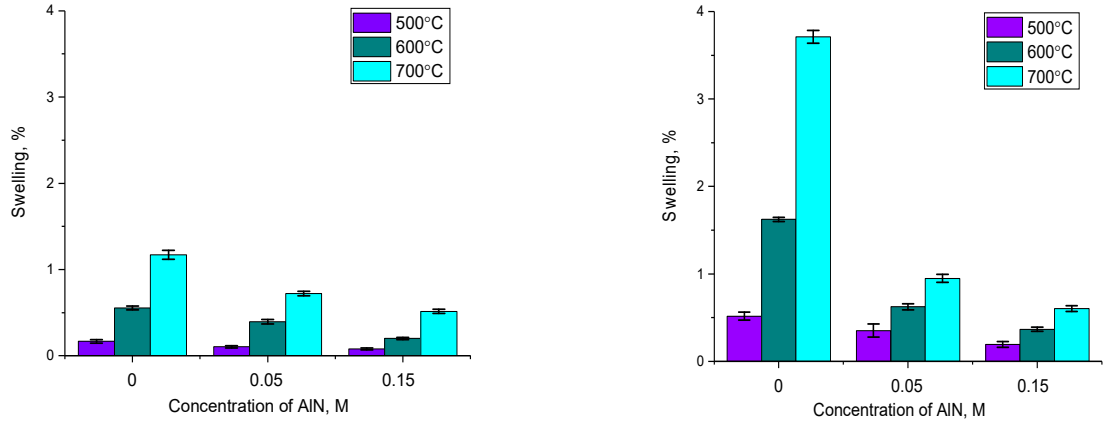

Fig.5. Assessment results of the crystal lattice swelling value of ceramics after 500 hours of high-temperature exposure: a) non-irradiated ceramics; b) irradiated ceramics

In this case, analysis of variations in the crystal lattice swelling value for irradiated unstabilized $NiAl_2O_4$ ceramics implies that irradiation temperature rise from 500 to 700°C leads to a more than a 7-fold crystal lattice volume growth, which indicates the following. For irradiated unstabilized $NiAl_2O_4$ ceramics, in which the concentration of implanted hydrogen can reach the order of several atomic percent (according to estimated calculations of modeling the hydrogen accumulation processes in the damaged layer). Subjected to temperature, implanted hydrogen, given its mobility, can accelerate agglomeration processes, consequently augmenting the volume of gas-filled regions. This phenomenon is widely recognized in metals and alloys during post-irradiation annealing of defects, leading to an elevation in bubbles through their agglomeration. At the same time, for stabilized $NiAl_2O_4$ ceramics, the presence of impurity phases results in the creation of additional barriers to implanted hydrogen in the form of grain boundaries and interphase boundaries, which leads to difficulty in its migration, and as a result, even at high temperatures, little effect on destruction processes.

4. Conclusion

The paper presents the assessment results of the effect of doping $NiAl_2O_4$ ceramics with aluminum nitride on the high-temperature degradation resistance under conditions closely aligned with the actual operating conditions of these ceramics when used as anode materials for solid oxide fuel cells. During determination of the effect of high-dose proton irradiation on variations in the strength properties of $NiAl_2O_4$ ceramics, it was discovered that the stabilizing additive concentration growth results in an enhanced resistance of the near-surface layer of ceramics to softening processes, alongside swelling of the crystal structure due to deformation distortions. During high-temperature tests in the case of varying exposure temperatures, it was found that a rise in the concentration of the stabilizing additive results in a rise in resistance to degradation processes, which are caused by changes in the amplitude of thermal vibrations of atoms, alongside corrosion processes associated with the crystal lattice deformation distortion and swelling. In conclusion, the addition of the stabilizing additive AlN to $NiAl_2O_4$ ceramics is quite effective, which is not only due to a rise in strength characteristics (increased hardness and resistance to single compression) but also enhanced resistance to destructive changes in strength performance as a result of long-term high temperature exposure. Moreover, for irradiated samples, the $NiAl_2O_4$ ceramics without stabilization exhibit the lowest resistance to high-temperature corrosion, with a degradation of strength properties exceeding 15 – 18 %. Testing for resistance to high-temperature corrosion at different exposure temperatures revealed that elevation in the temperature from 500 to 700°C accelerates the degradation processes.

Conflict of interest statement
Author declares that he has no conflict of interest in relation to this research, whether financial, personal, authorship or otherwise, that could affect the research and its results presented in this paper.

.

Funding

The work was performed under financial support of the State Institution "Science Committee of the Ministry of Science and Higher Education of the Republic of Kazakhstan" within the framework of the Scientific-Technical Program BR18574073.

References

1 Dunn S. Hydrogen futures: toward a sustainable energy system. *International journal of hydrogen energy*, 2002, Vol. 27, No. 3, pp. 235 – 264. https://doi.org/10.1016/S0360-3199(01)00131-8

2 Griffiths S. Energy diplomacy in a time of energy transition. *Energy Strategy Reviews,* 2019, Vol. 26, p. 100386. https://doi.org/10.1016/j.esr.2019.100386

3 Zainal B.S., et al. Recent advancement and assessment of green hydrogen production technologies. *Renewable and Sustainable Energy Reviews*, 2024, Vol. 189, p. 113941. https://doi.org/10.1016/j.rser.2023.113941

4 Dash S.K., Chakraborty S., Elangovan D. A brief review of hydrogen production methods and their challenges. *Energies*, 2023, Vol. 16, №. 3, p. 1141 https://doi.org/10.3390/en16031141

5 Chaudhary K., Bhardvaj K., Chaudhary A. A qualitative assessment of hydrogen generation techniques for fuel cell applications. *Fuel*, 2024, Vol. 358, p. 130090. https://doi.org/10.1016/j.fuel.2023.130090

6 Tang D., et al. State-of-the-art hydrogen generation techniques and storage methods: A critical review. *Journal of Energy Storage*, 2023, Vol. 64, p. 107196. https://doi.org/10.1016/j.est.2023.107196

7 Malik F.R., et al. Overview of hydrogen production technologies for fuel cell utilization. *Engineering Science and Technology, an International Journal*, 2023, Vol. 43, p. 101452. https://doi.org/10.1016/j.jestch.2023.101452

8 De Temmerman G., et al. Data on erosion and hydrogen fuel retention in Beryllium plasma-facing materials. *Nuclear Materials and Energy*, 2021, Vol. 27, p. 100994. doi:10.1016/j.nme.2021.100994

9 Hassanpouryouzband A., et al. Gas hydrates in sustainable chemistry. *Chemical society reviews*, 2020, Vol. 49, №. 15, pp. 5225-5309. https://doi.org/10.1039/C8CS00989A

10 Karpov S.A., Tolstolutskaya G.D., Kalchenko A.S. Effect of noble-gas bubbles on deuterium trapping behavior in argon pre-implanted stainless steel. *Journal of Nuclear Materials*, 2022, Vol. 566, p. 153661. https://doi.org/10.1016/j.jnucmat.2022.153661

11 Li Y., et al. In-situ investigation of bubble dynamics and two-phase flow in proton exchange membrane electrolyzer cells. *International Journal of Hydrogen Energy,* 2018, Vol. 43, №. 24, pp. 11223-11233. https://doi.org/10.1016/j.ijhydene.2018.05.006

12 Ito H., et al. Influence of pore structural properties of current collectors on the performance of proton exchange membrane electrolyzer, *Electrochimica Acta*, 2013, Vol. 100, pp. 242-248. https://doi.org/10.1016/j.electacta.2012.05.068

13 Feng Q., et al. A review of proton exchange membrane water electrolysis on degradation mechanisms and mitigation strategies. *Journal of Power Sources*, 2017. Vol. 366, pp. 33-55. https://doi.org/10.1016/j.jpowsour.2017.09.006

14 Arvay A., et al. Characterization techniques for gas diffusion layers for proton exchange membrane fuel cells–A review. *Journal of Power Sources*, 2012, Vol. 213, pp. 317-337. https://doi.org/10.1016/j.jpowsour.2012.04.026

15 Su X., Xu L., Hu B. Simulation of proton exchange membrane electrolyzer: Influence of bubble covering. *International Journal of Hydrogen Energy*, 2022, Vol. 47, No. 46, pp. 20027 – 20039. https://doi.org/10.1016/j.ijhydene. 2022.04.154

16 Kozlovskiy A.L. The Effect of the Addition of Aluminum Nitride to the Composition of $NiAl_2O_4$ Ceramics on Hydrogenation Processes and the Increase in Resistance to Swelling and Degradation. *Ceramics,* 2023,Vol. 6, №4, pp. 2070-2085. https://doi.org/10.3390/ceramics6040127

AUTHOR' INFORMATION

Kozlovskiy, A.L. – PhD (Phys.), Associate Professor, Head of the Laboratory of Solid-State Physics, Astana branch of the Institute of Nuclear Physics; Ministry of Energy of the Republic of Kazakhstan, Astana; ORCID iD: 0000-0001-8832-7443; kozlovskiy.a@inp.kz

EURASIAN PHYSICAL TECHNICAL JOURNAL

2024, Volume 21, No. 1 (47)

https://doi.org/10.31489/2024No1/21-27

Received: 04/01/2024 Revised: 19/02/2024 Accepted: 13/03/2024 Published online: 29/03/2024

Research Article

UDC: 538.91; 538.945

NEW METAL/SUPERCONDUCTOR-INSULATOR TRANSITIONS AND THEIR EFFECTS ON HIGH-T_C SUPERCONDUCTIVITY IN UNDERDOPED AND OPTIMALLY DOPED CUPRATES

Kurbanov U.T.[1,2], Zhumabaeva G.K.[1], Dzhumanov S.[1]

[1] Institute of Nuclear Physics, Uzbek Academy of Sciences, Ulugbek, Uzbekistan

[2] Tashkent State Technical University named after Islam Karimov, Tashkent, Uzbekistan

*Corresponding author: ulughkurbanov@gmail.com

Abstract. *A new approach to the metal/superconductor-insulator transition in doped cuprates by studying the polaron formation and localization of doped charge carriers (holes) in them and the possibility of transforming a metallic or superconducting system into an insulator was developed. A more suitable criterion for such a phase transition by comparing the bandwidth (or Fermi energy) of large polarons with their binding energies in the cuprates was derived. The possibility of the metal/superconductor-insulator transition and phase separation in doped cuprates resulting in the formation of competing metallic/superconducting and insulating phases in underdoped, optimally doped and even in overdoped high-T_c cuprates was predicted. Then the possible detrimental and beneficial effects of the different disorders (e.g. polaron formation and charge-density-wave transition) and the coexisting insulating and superconducting phases on the critical temperature T_c of the superconducting transition of underdoped and optimally doped cuprates was examined. The actual superconducting transition temperature T_c in these materials using the theory of Bose-liquid superconductivity, and not the Bardeen-Cooper-Schrieffer-like theory of Fermi-liquid superconductivity, which is incapable of predicting the relevant value of T_c in high-T_c cuprates was determined. We find that the suppressing of the polaronic and charge-density-wave effects in optimally doped cuprates results in the enhancement of T_c, while some lattice defects (e.g., anion vacancies) in the cuprates may strongly affect, on T_c and enhance high-T_c superconductivity in them.*

Keywords: polaron formation and charge density waves, metal/superconductor-insulator transition, cuprates, Bose-liquid superconductivity, different disorders, suppression and enhancement of high-T_c superconductivity.

1. Introduction

The Mott-Hubbard model is considered appropriate for explaining the metal-insulator transition in undoped cuprates, which are charge-transfer type insulators [1, 2], but not in doped cuprates [2, 3]. Doped cuprates are unique insulators, metals, and superconductors in the intermediate doping regime because they are substantially more complicated systems [1, 2, 4]. The intriguing insulating, metallic, and superconducting properties are particularly seen in underdoped and optimally doped cuprates. These properties cannot be explained by the theories of the Mott and Anderson metal-insulator transitions [1] or the Fermi-liquid superconductivity theory proposed by Bardeen-Cooper-Schrieffer (BCS) [5]. As a result, as the physics of these novel superconducting materials have advanced, so too has interest in the characteristic metal-insulator

and superconductor-insulator transitions in doped cuprates [1-3, 6-8]. It is anticipated that numerous deviations in the superconducting behaviors of high-temperature cuprates noted in underdoped and optimally doped regions are intricately linked to transitions between metal/superconductor and insulator states, phase separation, and the coexistence of competing superconducting and insulating phases [6-11]. The physics of these high-T_c materials has advanced significantly (refer to Refs. [1,4,7,12]), but our knowledge of the strange properties of underdoped and optimally doped cuprates in their superconducting state, as well as the distinctive metal/superconductor-insulator transitions in doped cuprates, remains very incomplete. In particular, yet unanswered concerns include the development of competing metallic/superconducting and insulating phases in underdoped and optimally doped cuprates, as well as the causes of the suppression and amplification of high-T_c superconductivity in these substances.

Here, we investigate the effects of the metal/superconductor-insulator transitions in doped cuprates, which are fueled by strong electron-phonon interactions and polaronic formation at the self-trapping of doped charge carriers on high-T_c superconductivity in both optimally and underdoped cuprates. A more relevant criterion for such transitions in doped cuprates, which occur in the doping range from underdoped to overdoped regime and are accompanied by the phase separation into the competing metallic/superconducting and insulating phases was derived. The critical temperature of the superconducting transition T_c in underdoped and optimally doped cuprates using the theory of Bose-liquid superconductivity and the reasons of the suppression and enhancement of high-T_c superconductivity in them was determined. The competing superconducting and insulating phases strongly affect on T_c especially in underdoped cuprates was found. We investigate the possible detrimental and beneficial effects of different disorders (e.g. the polaron formation or charge-density-wave (CDW)) transition and the radiation defects on the superconducting properties (i.e. critical values of the superconducting transition temperatures T_c) of high-T_c cuprates and show that the suppression of the polaronic and CDW effects are accompanied by increasing of T_c, while radiation-induced defects (e.g. anion vacancies) in these materials may also strongly affect on T_c and enhance high-T_c superconductivity.

2. Materials and research methods

The quasi-free holes carriers introduced to the polar cuprate materials by doping are self-trapped spontaneously at their strong interactions with lattice vibrations and therefore, these doped hole carriers are dressed by the local lattice distortions and become large polarons with effective masses $m_p \simeq (2-3)m_e$ [13,14] (where m_e is the free electron mass). At low doping levels, such polaronic carriers are localized and immobile. When the doping level increases towards underdoped region, the ordering of large polarons results in the formation of their superlattice and a narrow energy band. In doped cuprates the width of the polaronic band increases with increasing the doping level and is sufficiently broadened in underdoped cuprates in which the polaronic transport becomes metallic. The width of such a polaronic band is determined by using the tight-binding method. One can expect that when the doping level increases up to a certain underdoping regime, a doped cuprate material may undergo a phase transition from an insulator to a metallic state. Below T_c, such a metal-insulator transition occurs as a superconductor-insulator transition.

3. Results and discussion

3.1. Localization of doped charge carriers and metal/superconductor-insulator transitions in underdoped and optimally doped cuprates

We now develop a new approach and obtain the relevant criterion for the metal/superconductor-insulator transition in doped cuprates. It is natural to assume that the transition of a hole carrier from the localized (polaronic) state to a delocalized itinerant (metallic) state becomes possible when the kinetic energy (or Fermi energy ε_F) of hole polarons is larger than their binding energy E_p.

Using the relation (1) and Eq. (2) in Ref. [15], we can determine the critical doping level $n = n_c$ (n is the density of large polarons) corresponding to the metal/superconductor-insulator transition in the cuprates from the expression

$$n_c = \frac{1}{3\pi^2}\left[\frac{2m_p E_p}{\hbar^2}\right]^{3/2}. \quad (1)$$

Then the relevant criterion for the metal/superconductor-insulator transition in doped cuprates can be written as

$$x \gtrsim x_c = \frac{n_c}{n_a} = \frac{1}{3\pi^2\hbar^3 n_a}\left[2m_p E_p\right]^{3/2}, \quad (2)$$

where $n_a = 1/V_a$ is the concentration of lattice atoms or CuO_2 molecules, V_a is the volume per CuO_2 formula unit in the cuprate materials.

This newly established criteria for the metal/superconductor-insulator transitions enables us to forecast the likelihood of achieving such phase transitions in underdoped and optimally doped cuprates, driven by the strong electron-phonon interactions and polaronic formation. Firstly, we investigate whether the new metal/superconductor-insulator transitions are possible in these cuprate materials. We consider the effects of both the variation of ε_∞ and the large ionicity of the cuprates $\eta = \varepsilon_\infty/\varepsilon_0 \ll 1$ (where ε_0 and ε_∞ are the static and high frequency dielectric constants, respectively).

Now we calculate the critical doping levels x_c for metal/superconductor-insulator transitions in *La*- and *Y*-based high-T_c cuprates $La_{2-x}Sr_xCuO_4$ (LSCO) and $YBa_2Cu_3O_{7-\delta}$ (YBCO). In so doing, we taking the calculated values of $E_p \simeq 0.078 - 0.2$ eV at $\varepsilon_\infty = 2.5 - 4.0$ and $\eta = 0.04$ [16] and the observed values of $m_p \simeq (2-3)m_e$ [17]. The values of V_a can be determined approximately as $V_a \simeq 190$ Å^3 in LSCO and $V_a \simeq 100$ Å^3 in YBCO, so that the values of n_a are equal roughly to $0.53 \cdot 10^{22} cm^{-3}$ (in LSCO) and $10^{22} cm^{-3}$ (in YBCO). For LSCO using the values of parameters $m_p = 2.2m_e$, $E_p = 0.078 - 0.2\ eV$ and $n_a \approx 0.53 \cdot 10^{22} cm^{-3}$, we find the values of critical doping for metal/superconductor-insulating transitions $x_c = 0.060 - 0.249$ in this system. Then, we use the other values of parameters $m_p = 2.8m_e$, $E_p = 0.078 - 0.2\ eV$ and $n_a \approx 10^{22} cm^{-3}$ for YBCO, we obtain the values of critical doping for metal/superconductor-insulating transitions $x_c = 0.046 - 0.189$ in this cuprate material. Further, the variations of x_c with decreasing ε_∞ in LSCO and YBCO are shown in Figs.1 and 2 for $\eta = 0.04$.

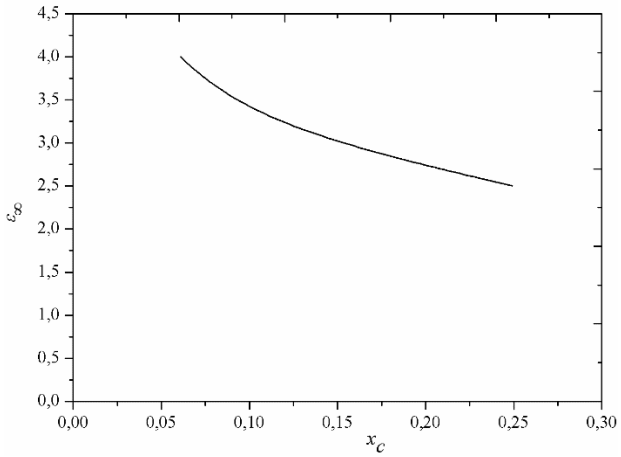

Fig.1. The variation of x_c with decreasing ε_∞ in LSCO for $\eta = 0.04$.

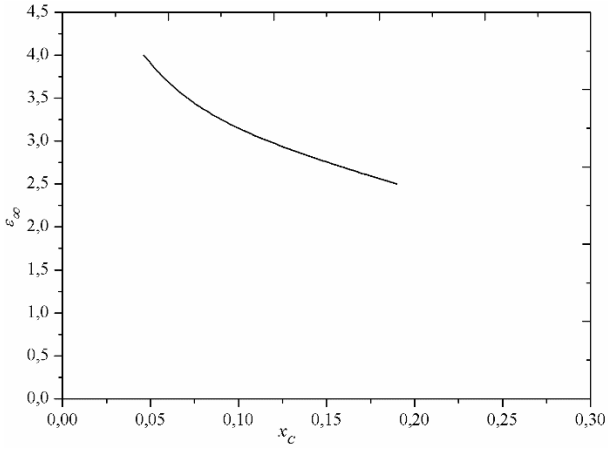

Fig.2. The variation of x_c with decreasing ε_∞ in YBCO for $\eta = 0.04$.

The above presented theoretical results for metal/superconductor-insulator transitions agree well with experimental data on the same transitions in underdoped and optimally doped cuprates [9,11,18-20]. Particularly, our novel and significantly results show that in YBCO the metal/superconductor-insulator transitions and phase separation into competing metallic/superconducting-insulating phases occurs in the doping range $0.05 \lesssim x \lesssim 0.19$ in accordance with experimental observations [9,11]. As a result, the metallic/superconducting and insulating phases will compete with each other in underdoped and optimally doped high-T_c cuprates.

3.2. Possible effects of the competitions between the insulating and superconducting phases on high-T_c superconductivity in underdoped and optimally doped cuprates

Based on the given information, it can be inferred that the insulating and metallic or superconducting phases compete in underdoped and optimally doped cuprates, where the non-superconducting (i.e. immobile)

.

and superconducting hole carriers below T_c reside in carrier-poor (insulating) and carrier-rich (superconducting) domains, respectively. We argue that the hole carriers residing in an adequately broadened polaronic band may become mobile and their Cooper pairing would occur in momentum (k-) space and leads to the formation of polaronic (i.e. tightly-bound) Cooper pairs above T_c, which behave like Bose particles and condense into a superfluid state below T_c. Actually, such preformed Cooper pairs would exist in doped high-T_c cuprates at $\varepsilon_F \sim \varepsilon_A$ (where ε_A is the energy of the attractive interaction among two polaronic carriers). Since the pairing interaction mechanism between large polarons in the energy range $\{-\varepsilon_A, \varepsilon_A\}$ is much stronger than in the usual BCS model [5]. In the present case the pair Hamiltonian of the strongly interacting polaronic Fermi gas can be diagonalized by the Bogoliubov transformation of Fermi operators. Then, we use the model interpolaron interaction potential [21] and get the following BCS-like gap equation for determining the onset temperature T^* of the Cooper pairing of polarons:

$$\frac{1}{\lambda_F} = \int_0^{\varepsilon_A} \frac{d\xi}{\sqrt{\xi^2+\Delta_F^2(T)}} tanh \frac{\sqrt{\xi^2+\Delta_F^2(T)}}{2k_BT}, \tag{5}$$

where $\xi = \varepsilon(k) - \varepsilon_F$ is the energy of large polarons measured from their Fermi energy ε_F $\varepsilon(k)$ is the kinetic energy of these polarons; $\lambda = D(\varepsilon_F)\tilde{V}_F$ is the BCS-like coupling constant, $D(\varepsilon_F)$ is the density of states on the Fermi surface, $\tilde{V}_F = V_A - V_C$, $\tilde{V}_F = V_C/[1 + D(\varepsilon_F)V_C \ln(\varepsilon_C/\varepsilon_A)]]$ is the screened Coulomb interaction between two fermions, V_A and V_C are the interfermion attractive interaction potential and Coulomb interaction potential appropriate to the cutoff energies ε_C and ε_A, respectively, $\Delta_F(T)$ is the BCS-like gap.

At $T \to T^*$energy gap $\Delta_F(T)$ in the excitation spectrum of an interacting Fermi-gas of polarons tends to zero. When $\varepsilon_A \gg k_BT^*$, Eq. (5) gives

$$k_BT^* \simeq 1.134\varepsilon_A \exp[-1/\lambda_F]. \tag{6}$$

The underdoped and optimally doped cuprates have low Fermi energies $\varepsilon_F \simeq (0.1 - 0.3)eV$ [22]. For these materials we can take $\varepsilon_A = E_p + \hbar\omega_0$, where $\hbar\omega_0$ is the energy of optical phonons. By taking $\lambda_F \simeq 0.4$ and $\varepsilon_A \simeq 0.15eV$ (assuming that $E_p \simeq 0.1\,eV$ and $\hbar\omega_0 \simeq 0.05\,eV$) for underdoped cuprates, we find, $T^* \simeq 162K \gg T_c$ (possible values of T_c for underdoped cuprates $YBa_2Cu_3O_{7-\delta}$ and $Bi_2Si_2CaCu_2O_{8+\delta}$ accordingly will be less than 90 K and 100 K) fully consistent with the results of the experiments for T^* in such high-T_c cuprates [23, 24]. If the preformed polaronic Cooper pairs in high-T_c cuprates behave like bosons, then their transition to superconducting state is not described by BCS-like theories of Fermi-liquid superconductivity. For these cuprate materials, the BCS-like theory becomes ineligible for the determination of T_c. Only the alternative Bose-liquid theory for superconductivity [21] might be adequate for describing the high-$T_c$superconductivity in underdoped and optimally doped cuprates. According this theory, T_c in the weak interboson coupling is determinated from the relation

$$T_c \simeq T_{BEC}\left[1 + c\gamma_B\sqrt{k_BT_{BEC}/\xi_B}\right] \tag{7}$$

where γ_B is the interboson coupling constant, $T_{BEC} = 3.31\hbar^2\rho_B^{2/3}/2k_Bm_B$ is the Bose-Einstein condensation temperature of an ideal Bose gas of polaronic Cooper pairs, ρ_B is the density of the attracting bosons, $m_B = 2m_p$ is the mass of bosonic Cooper pairs, k_B is the Boltzmann constant, ξ_B is the characteristic thickness of the condensation layer including the attracting bosonic Cooper pairs, $c = \pi^{3/2}/3.918$, $\gamma_B \ll 1$.

According to the above proposed microscopic picture of the superconductor-insulator transition and evolution of competing superconducting and insulating phases, the insulating regions in underdoped cuprates are gradually narrowed with increasing doping and would persist as small islands in optimally doped cuprates and finally disappear above the doping level $x = 0.19$. This more realistic image shows that only Cooper pairs residing in metallic regions condense in a Bose superfluid below T_c and are involved in high-T_c superconductivity, while the other Cooper pairs progressively become localized in carrier-poor regions due to transition from a superconducting phase to an insulating phase and therefore, they become immobile and non-superconducting. In high-T_c cuprates, T_c determined from the expression (7) reaches the maximum

T_c^{max} at some optimal doping close to overdoped (OD) regime when the insulating regions disappear at this doping level. However, at doping levels $x \lesssim 0.16$ the critical temperature T_c becomes less than T_c^{max} and is ascertained based on the expression

$$T_c = \frac{1}{1+f_I} T_c^{max}, \tag{8}$$

where $f_I = V_I/V_S$ is the fraction of the insulating phase, V_I is the volume of the insulating regions in the cuprates, V_S is the volume of the superconducting regions of these materials.

The variation of the ratio T_c/T_c^{max} in high-T_c cuprates with insulating volume fraction f_I is shown in Fig.3.

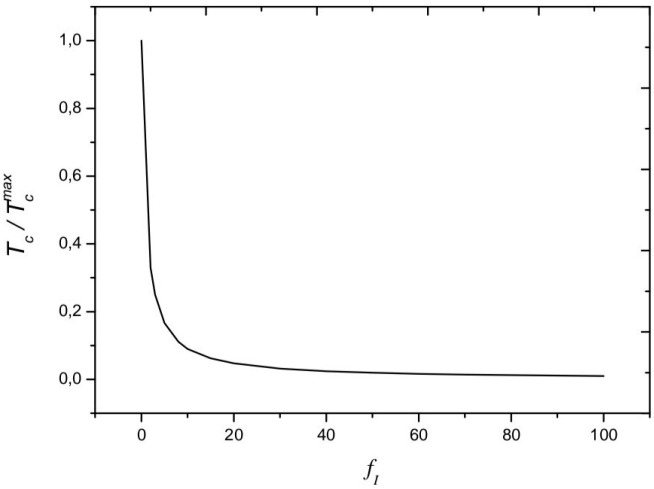

Fig.3. – The variation of T_c/T_c^{max} in high-T_c cuprates with increasing f_I.

Now, we use the expression (7) and can estimate the value of T_c^{max} in optimally doped YBCO. Assuming that $m_B = 4m_e, \gamma_B = 0.25$, $k_B T_{BEC}/\xi_B \simeq 0.15$ and $\rho_B \simeq 6 \cdot 10^{19} cm^{-3}$, we find $T_{BEC} \simeq 112.3\,K$ and $T_c^{max} \simeq 92\,K$ for optimally doped YBCO. For the underdoped (UD) system YBCO ($x \lesssim 0.14$), we can take $f_I = 0.25$. Then we obtain $T_c = T_c^{max}/1.25 \approx 74\,K$, which is in agreement with the experimental information for YBCO [25]. In YBCO the insulating volume fraction f_I is small enough at $x > 0.15$ and T_c changes little between $x_{UD} \simeq 0.15$ and $x_{OD} \simeq 0.16$. The experimental observations in YBCO confirm the predicted behaviour of T_c [25]. If we assume that the ratio V_I/V_s in underdoped LSCO is of order 0.2 at $x \lesssim 0.13$, then we obtain $T_c \simeq 0.83 T_c^{max} \simeq 32K$ which agrees well with experimental results (e.g., at x=0.13 the value of T_c is about $32K$ Ref. [23]). In underdoped and optimally doped cuprates, some part of metallic/superconducting regions goes over to insulating state at the doping level $x < 0.16$.

Therefore, a marked suppression of superconductivity will occur in underdoped cuprates due to more stronger polaronic effect and due to an increase of the insulating volume fraction at the expense of the volume of superconducting regions. The experimental findings depicted in Ref. [17] give evidence that the polaronic effect weakens with increasing doping towards overdoped regime. This means that superconductivity is strongly enhanced in optimally doped regime due to the weakening of the polaronic effect and the decreasing of the mass m_p of polarons entering the expression (7).

The strong electron-phonon coupling in the cuprates also results in the formation of the CDWs which hinder high-T_c superconductivity in underdoped cuprates. Since the formation of CDWs is also accompanied by a lattice distortion [26] and is similar to the polaron formation. Further, the irradiation-induced disorders (i.e. lattice defects) in the cuprates may strongly affect on T_c and enhance superconductivity, since the anion vacancy-enhanced Coulomb repulsion hinders the polaron formation. Actually, it has been found experimentally that disorder created in the cuprate superconductor $La_{1.875}Ba_{0.125}CuO_4$ by proton irradiation increases the superconducting critical temperature T_c by 50 % while suppressing the CDW state [26].

.

4. Conclusions

The possibilities of metal/superconductor-insulator transitions, which are caused by the strong electron-phonon interactions and polaronic formation were studied. This process is accompanied by phase separation into the competing metallic/superconducting and insulating phases in underdoped and optimally doped cuprates. We have argued that the strong hole-lattice interactions in doped cuprates result in the formation of large polarons and the localization of doped hole carriers transforming a metallic or superconducting system into an insulator. We have found that the metal/superconductor-insulator transitions in doped cuprates occur in the doping range from underdoped to overdoped regime ($0.05 < x < 0.19$) and are accompanied by the phase separation and formation of competing superconducting and insulating phases in underdoped, optimally doped and even overdoped high-T_c cupretes. In so doing, we have established that in doped cuprates the metal/superconducting-insulator transitions occur at low doping levels ($x \lesssim 0.05 - 0.06$) for $\varepsilon_\infty \gtrsim 3.5$ and $\eta = 0.04$, but such phase transitions take place at high doping levels ($x \simeq 0.19 - 0.25$) for $\varepsilon_\infty \lesssim 2.5$ and $\eta = 0.04$. We have predicted the possible detrimental and beneficial effects of the different disorders (e.g. polarons and CDWs) and the evolution of the competing insulating and superconducting phases on T_c in underdoped and optimally doped cuprates. We have determined T_c in these unconventional superconductors using the theory of Bose-liquid superconductivity. Unlike the BCS-like theories of Fermi-liquid superconductivity, this alternative theory of unconventional superconductivity is capable of predicting the actual T_c in underdoped and optimally doped cuprates. We conclude that the suppressing of the polaronic and CDW effects is accompanied by enhancement of high-T_c cuprate superconductivity, while some lattice defects (e.g. anion vacancies) in the cuprates may also affect on T_c and strongly enhance high-T_c superconductivity in them.

Conflict of interest statement
The authors declare that they have no conflict of interest in relation to this research, whether financial, personal, authorship or otherwise, that could affect the research and its results presented in this paper.

CRediT author statement:
Kurbanov U.T.: Validation, Formal analysis; Zhumabaeva G.K.: Investigation; Dzhumanov S.: Supervision, Writing - Original Draft. The final manuscript was read and approved by all authors.

Acknowledgments
This work was supported by the Scientific Researches Program
to President Degree 4526 of 21.11.2019.

References

1 Imada M., Fujimori A., Tokura Y. Metal-insulator transitions. *Review of Modern Physics,* 1998, Vol.70, pp.1039. https://doi.org/10.1103/RevModPhys.70.1039

2 Dzhumanov S. *Theory of Conventional and Unconventional Superconductivity in the High-T_c Cuprates and Other Systems.* Nova science publishers, New York, USA, 2013, 356 p. https://novapublishers.com/shop/theory-of-conventional-and-unconventional-superconductivity-in-the-high-tc-cuprates-and-other-systems/

3 Dzhumanov S., Baimatov P.J., Ganiev O.K., Khudayberdiev Z.S., Turimov B.V. Possible mechanisms of carrier localization, metal–insulator transitions and stripe formation in inhomogeneous hole-doped cuprates. *Journal of Physics and Chemistry of Solids,* 2012, Vol.73(3), pp. 484 – 494. https://doi.org/10.1016/j.jpcs.2011.11.029

4 Lee P.A., Nagaosa N., Wen X.-G. Doping a Mott insulator: Physics of high-temperature superconductivity. *Review of Modern Physics,* 2006, Vol.78 (1), pp. 17 – 85. https://doi.org/10.1103/RevModPhys.78.17

5 Bardeen J., Cooper L.N., Schrieffer J.R. Theory of superconductivity. *Physical Review*, 1957, Vol.108 (5), pp.1175. https://doi.org/10.1103/PhysRev.108.1175

6 Lavrov A.N., Gandmakher V.F. Low-temperature resistivity of underdoped cuprates, *Physics-Uspekhi*, 1998, Vol.41(2), pp. 223-226. https://ufn.ru/ufn98/ufn98_2/ufn982ai.pdf

7 Goldman A.M., Markovic N. Superconductor-Insulator Transitions in the Two-Dimensional Limit. *Physics Today*, 1998, Vol.51(11), pp. 39 - 44. https://doi.org/10.1063/1.882069

8 Vedeneev S.I. High-temperature superconductors in high and ultrahigh magnetic fields. *Physics-Uspekhi,* 2012, Vol.55(6), pp. 625 – 632. https://doi.org/10.3367/UFNe.0182.201206h.0669

9 Ino A., Kim C., Nakamura M., Yoshida T., Mizokawa T., Shen Z.-X., Fujimori A., Kakeshita T., Eisaki H.,

Uchida S. Electronic structure of $La_{2-x}Sr_xCuO_4$ in the vicinity of the superconductor-insulator transition. *Physical Review B,* 2000, Vol.62, pp. 4137. https://doi.org/10.1103/PhysRevB.62.4137

10 Ono S., Ando Yoichi, Murayama T., Balakirev F.F., Betts J.B., Boebinger G.S. Metal-to-Insulator Crossover in the Low-Temperature Normal State of $Bi_2Sr_{2-x}La_xCuO_{6+\delta}$. *Physical Review Letters*, 2000, Vol. 85(3), pp. 638 – 641. https://doi.org/10.1103/PhysRevLett.85.638

11 Anshukova A.I., Golovashkin L.I., Ivanova A.P., Rusakov. J. The effect of superstructural ordering on the properties of high-temperature oxide superconductor systems. *Journal of Experimental and Theoretical Physics*, 2003, Vol.96(6), pp. 1045. https://doi.org/10.1134/1.1591216

12 Abrikosov A.A. Resonant tunneling in high-T_c superconductors. *Physics-Uspekhi*, 1998, Vol.41(6), pp. 605 - 616. https://doi.org/10.1070/PU1998v041n06ABEH000411

13 Kastner M.A., Birgeneau R.J., Shirane G., Endoh Y. Magnetic, transport, and optical properties of monolayer copper oxides. *Review of Modern Physics*, 1998, Vol.70(3), pp. 897 – 928. https://doi.org/10.1103/RevModPhys.70.897

14 Basov D.N., Timusk T. Electrodynamics of high-T_c superconductors. *Review of Modern Physics*, 2005, Vol.77(2), pp. 721 – 779. https://doi.org/10.1103/RevModPhys.77.721

15 Dzhumanov, S., Khidirov, I., Kurbanov, U. T., Khudayberdiev, Z. S., Rashidov, J. S. Distinctive Features of Metal-Insulator Transitions, Multiscale Phase Separation, and Related Effects in Hole-Doped Cuprates. *Ukrainian Journal of Physics*, 2019, Vol. 64(4), pp. 322. https://doi.org/10.15407/ujpe64.4.322

16 Dzhumanov S., Sabirov S.S., Karimbaev E.X., Rashidov J.Sh., Djumanov D.S., Kurbanov U.T., Sheraliev M.U. Formation of strong-coupling (bi)polarons and related in-gap states in lightly-doped cuprate superconductors. *Modern Physics Letters B*, 2021, Vol.35, pp. 2150190. https://dx.doi.org/10.1142/s0217984921501906

17 Bi X.X., Eklund P.C. Polaron contribution to the infrared optical response of $La_{2-x}Sr_xCuO_{4+\delta}$ and $La_{2-x}Sr_x$. *Physical Review Letter*, 1993, Vol.70(17), pp. 2625 – 2628. https://doi.org/10.1103/PhysRevLett.70.2625

18 Fink J., Nucker N., Alexander M., Romberg H., Knupeer M., Merkel M., Adelmann P., Claessen R., Mante G., Buslaps T., Harm S., Manzke R., Skibowski M. High-energy spectroscopy studies of high-T_c superconductors. *Physica C: Superconductivity*, 1991, Vol.185–189 (1), pp. 45 – 50. https://doi.org/10.1016/0921-4534(91)91948-4

19 Ono S., Ando Y., Murayama T., Balakirev F.F., Betts J.B., Boebinger G.S. Low-temperature normal state of $Bi_2Sr_{2-x}La_xCuO_{6+\delta}$: comparison with $La_{2-x}Sr_xCuO_4$. *Physica C: Superconductivity,* 2001, Vol. 357–360 (1), pp. 138 – 141. https://doi.org/10.1016/S0921-4534(01)00187-3

20 Ando Y., Ono S., Sun X.F., Takeya J., Balakirev F.F., Betts J.B., and Boebinger G.S. Quantum Phase Transitions in the Cuprate Superconductor $Bi_2Sr_{2-x}La_xCuO_{6+\delta}$. *Physical Review Letters*, 2004, Vol. 92, pp. 247004. https://doi.org/10.1103/PhysRevLett.92.247004

21 Dzhumanov S. Microscopic theory of pseudogap phenomena and unconventional Bose-liquid superconductivity and superfluidity in high-T_c cuprates and other systems. *arXiv:1912:12407*, 2020, pp. 74. https://doi.org/10.48550/arXiv.1912.12407

22 Pietronero L., Strässler S and Grimaldi C., Nonadiabatic superconductivity. I. Vertex corrections for the electron-phonon interactions. *Physical Review B,* 1995, 52, 10516. https://doi.org/10.1103/PhysRevB.52.10516

23 Timusk T., Statt B. The pseudogap in high-temperature superconductors: an experimental survey. *Rep. Prog. Phys*., 1999, Vol.62, pp. 61. doi:0.1088/0034-4885/62/1/002

24 Matsuzaki T., Ido M., Momono N., Dipasupil R.M., Nagata T., Sakai A., Oda M. Superconducting gap and pseudogap behavior in high-T_c cuprates. *J. Phys. Chem. Solids,* 2001, Vol. 62, Is. 1-2, pp. 29-33. https://doi.org/10.1016/S0022-3697(00)00096-2

25 Tallon J.L., Loram J.W., Cooper J.R., Panagopoulos C., Bernhard C. Superfluid density in cuprate high-T_c superconductors: A new paradigm. *Physical Review B*, 2003, Vol. 68, pp. 180501. https://doi.org/10.1103/PhysRevB.68.180501

26 Leroux M., Mishra V., Ruff J.P.C., Claus H., Smylie M. P., Opagiste C., Rodiere P., Kayani A., Gu G. D., Tranquada J.M. Kwok W-K., Islam Z., Welp U. Disorder raises the critical temperature of a cuprate superconductor. Proceedings of the National Academy of Sciences- *PNAS,* 2019, Vol.116, pp. 10691. https://doi.org/10.1073/pnas.1817134116

AUTHORS' INFORMATION

Dzhumanov, S. – Doctor of Phys. and Math. Sciences, Professor, Chief Researcher, Institute of Nuclear Physics of the Academy of Sciences of the Uzbekistan, Tashkent, Uzbekistan; ORCID ID: 0000-0001-6260-8087; dzhumanov@inp.uz

Kurbanov, U.T. – Dr. Sci., Senior Researcher, Head of the laboratory, Institute of Nuclear Physics, Uzbekistan Academy of Sciences, Ulugbek, Uzbekistan; Tashkent State Technical University named after Islam Karimov, Tashkent, Uzbekistan; ORCID ID: 0000-0001-5293-6888; ulughkurbanov@gmail.com

Zhumabaeva, G.K. – 3rd year postgraduate student, Institute of Nuclear Physics, Uzbek Academy of Sciences, Ulugbek, Uzbekistan; ORCID ID: 0009-0008-1137-4450; zhumabaeva@jinr.ru

.

EURASIAN PHYSICAL TECHNICAL JOURNAL

2024, Volume 21, No. 1 (47)

https://doi.org/10.31489/2024No1/28-37

Received: 23/12/2023 Revised: 18/01/2024 Accepted: 23/02/2024 Published online: 29/03/2024

Research Article

UDC: 539.52; 669.112.06

MECHANISM OF FORMATION OF INTERNAL AND SURFACE DEFECTS IN CASTING AND THEIR TRANSFORMATION INTO SURFACE DEFECTS OF SHEET

Ibraev I.K.[1], Ibraeva O.T.[1], Zhakupov T.M.[2]

[1] Karaganda State Industrial University, Temirtau, Kazakhstan
[2] L.N. Gumilyov Eurasian National University, Astana, Kazakhstan
*Corresponding author: ibraevik@yandex.ru

Abstract. *This study aimed to elucidate the formation mechanisms of micro-macrostructural heterogeneities in the ingot's cortical zone and their transformation into surface defects during heating, plastic deformation, and rolling processes. The methodology and results of studying the macro- and microstructural and chemical heterogeneities of ingots and finished rolled sheets are presented. A comparative method of structural-concentration analysis of metal at the end-to-end metallurgical processing stage of ingot - slab - rolled sheets was developed. The technique utilizes metallographic methods to study the structure and perform qualitative analysis of non-metallic inclusions. The research findings indicate that the quality of the rolled sheet surface is predominantly determined by the physical heterogeneity of the ingot's crust zone, while the internal defects in thin rolled sheets are largely influenced by the contamination of the metal with non-metallic inclusions. A novel mechanism is proposed for the transformation of defects in the casting cortical zone into surface and internal defects in rolled sheets. This study contributes to a deeper understanding of the formation and transformation of defects during metal processing, enabling the development of strategies for improving the quality of rolled sheets. Additionally, the study highlights the importance of controlling the physical heterogeneity of the ingot's crust zone and minimizing non-metallic inclusion contamination to achieve high-quality rolled sheets.*

Keywords: ingot, macro - and micro-inhomogeneity, slab, rolled sheet metal, defect, structure

1. Introduction

In the competitiveness of thin-sheet rolled products, a special role is given to the radical improvement and stabilization of the quality of the rolled products produced. Its practical solution largely depends on the quality of the steel ingot. During the formation of an ingot, all types of macro-inheterogeneity greatly develop: physical, structural and chemical. This significantly degrades the quality of cast and rolled metal. This problem is especially acute in the production of sheet metal. The waste-free production of thin sheet metal is inextricably linked with the quality of the metal produced, i.e., the presence of “hidden” internal defects in the structure of castings, which in subsequent processing can lead to both direct losses of metal in the form of trim (head or end) and to losses of metal at the final stage of end-to-end technology.

An analysis of the technical literature [1-10] showed that despite a large number of studies on the quality of thin-sheet rolled products, the results are ambiguous and contradictory. There is no consensus on the source and causes of the formation of surface defects in rolled sheet metal. This is because the

morphological characteristics of the defects in the steelmaking and rolling origins may be similar since all the defects are elongated in the direction of deformation and have similar characteristics and shapes in the transverse direction. In addition, the metallographic method for determining the causes of the formation of surface defects is applicable for metals that have experienced one high-temperature heating, while in practice, the metal undergoes 2-3 high-temperature heating cycles.

However, there is a proven connection between the structural transformation of macro- and micro inhomogeneity in the ingot and surface defects in the rolled sheets.

2. Research methodology

To study the nature and sources of surface defects in rolled sheets, a comparative method of structural-concentration analysis of metals during the end-to-end metallurgical process of ingot slab-sheet metals was developed based on the metallographic method of studying the structure and qualitative analysis of nonmetallic inclusions. To study chemical heterogeneity and contamination with nonmetallic inclusions, characteristic ingots were isolated. Oxygen cutters were used to cut axial plates parallel to the wide edge 120-150 mm above the axial plane. In the machine shop it was planned to an axial plane, sanded, and then sulfur prints were made on photographic paper after etching the surface of the axial template with a sulfuric acid solution.

The contents of the elements [C], [Mn], [Si], [S], [P], [Al], and [N] were determined by chemical methods. Metal contamination with nonmetallic inclusions was determined by electrolytic deposition and the LT metallographic method. To study the macrostructure of the cortical zone of the ingot, a corner template was cut out at 5 levels along the height of the ingot, corresponding to 5, 25, 50, 75 and 95% of the height from the head of the ingot. The cut templates were planned, polished and etched in a sulfuric acid solution to remove sulfur. To study the causes of defects, samples were taken to determine the presence of nonmetallic inclusions and the chemical composition of the metal along the boundaries of the defects. Thin sections were cut from the selected samples to study the microstructure and contamination of the steel with nonmetallic inclusions, as well as from the samples to determine the number of nonmetallic inclusions. The chemical composition of the phases and structural components was determined by the local microprobe method on a Samesa micro analyzer.

In general, the scheme for determining the nature and origin of surface defects included the following steps:

- study of the topography of defects on the surface of rolled sheets;
- metallographic examination of the steel microstructure in the defective areas;

Determination of the composition and nature of nonmetallic inclusions, both in the defect zone and in the volume of “healthy” metal;

- analysis of the technological parameters of smelting out-of-furnace processing, steel casting and metal rolling at the rolling stage;
- Study of the structure of the cortical layer of the ingot and identification of structural heterogeneity using macroanalysis methods.
- Study of the influence of high-temperature heating on the behavior of inclusions and gas bubbles located in the crustal layer of the ingot.

3. Research results

Metallographic analysis of the microstructure of samples of cold-rolled steel sheets in areas where surface defects appear allows us to identify 3 main types of characteristic structures:

1 – coarse films (Fig.1, a), affecting a significant area of metal in the subsurface layers with a specific type of nonmetallic inclusion in the form of globules of iron oxides (wustite) and pinpoint oxide rash (Fig.1, b)

2 – areas of bubbles filled with iron oxides such as wustite (Fig. 1, c), which often form films on the surface of the sheet during rolling (Fig. 1, d);

3 – Group accumulation of oxide nonmetallic inclusions with complex compositions (Fig. 2, a, b).

Figure 1 shows a point chemical analysis of nonmetallic inclusions from the clusters, where it is clear that the inclusions correspond to oxides of the SiO_2–MnO–FeO system. The nonmetallic inclusions

.

identified in places with defects in cold-rolled sheets are brittlely destroyed manganese silicates and have the following chemical composition: 12-18% SiO_2 up to 58% MnO, and up to 10% FeO.

Another type of characteristic steel microstructure in areas with surface defects is revealed by the accumulation of iron oxides of the wustite type (Fig. 3 a, b) between the cavities of pores and discontinuities (gray in the microphotograph: wustite inclusions, dark pores and discontinuities).

Table 1. Chemical composition of the inclusions

Oxides content,% by weight					
SiO_2	MnO	FeO	Al_2O_3	CaO	MgO
11.52	58.20	19.15	0.68	0.32	0.11

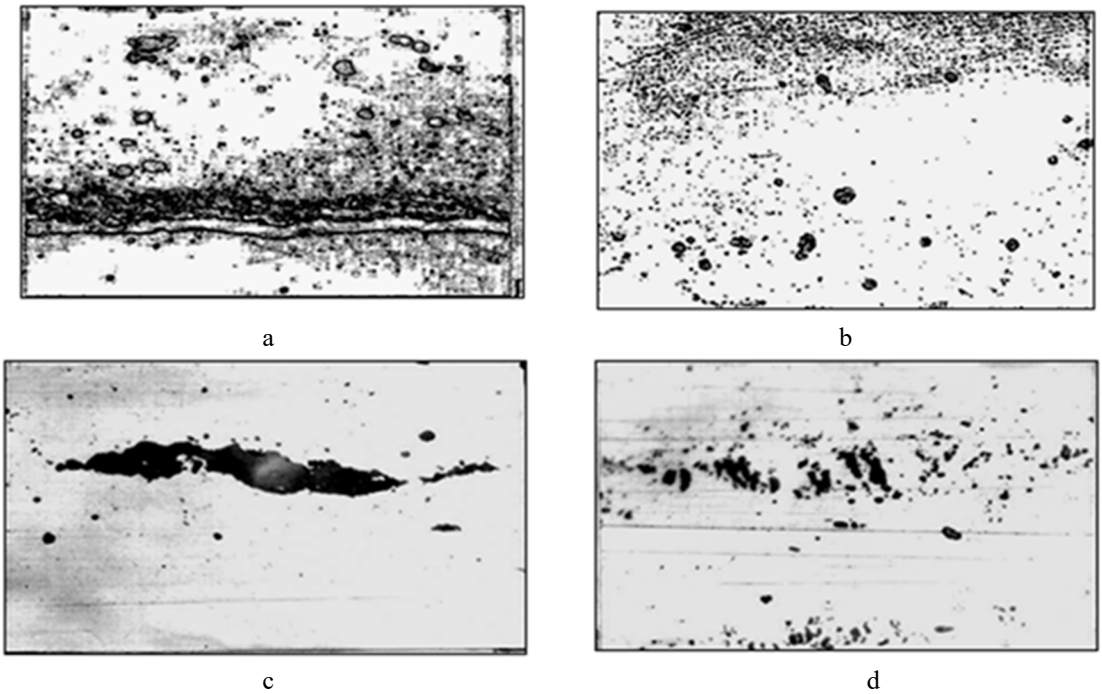

a b c d

Fig.1. Microstructure of cold-rolled steel 08 KPs in place manifestations of the defect:
a), b) inclusions of iron oxides near the film defect **(**x400); c **-** rolled out bubble, sq. section along the thickness of the sheet (x 630); g - the same, grinding along the surface of the sheet (x 500)

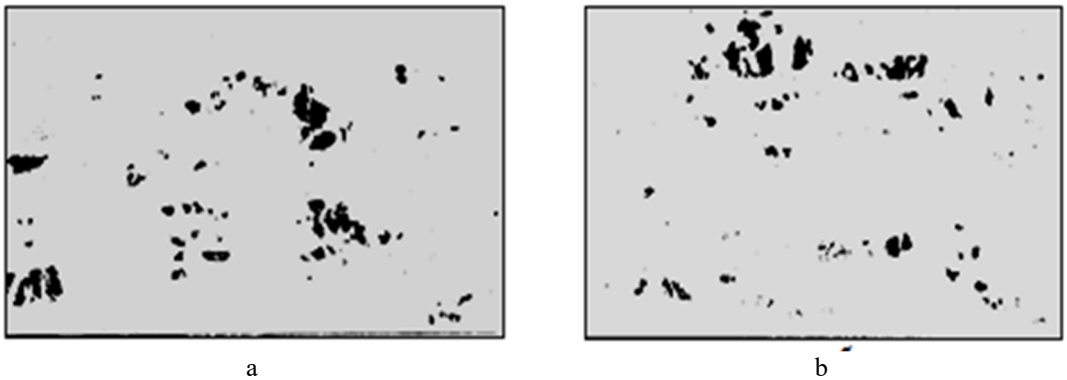

a b

Fig.2. Microstructure of steel at the location of the defect:
a, b - nonmetallic inclusions in a cold-rolled sheet along the surface of the sheet (x 400);

Microprobe point analysis of areas of nonmetallic inclusions confirmed the presence of 91.61% FeO and 2.50% MnO. The analysis revealed that the following types of surface defects formed in the cold-rolled sheets: 1is large films; 2 is a small captivity; 3 are a rolled out oxidized bubbles; and 4 are coarse

nonmetallic inclusions. In almost 1-3 groups of defects, the main nonmetallic phase is iron oxides, the content of which is 90% or more.

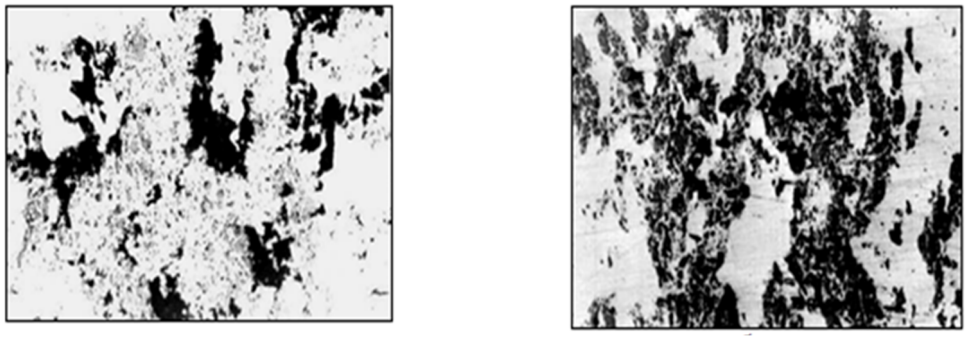

a b

Fig.3. Accumulation of iron oxides at defects on the surface cold-rolled steel sheets grade 08 PS:
a) an increase 125 times; b) an increase of 80 times.

A comparative structural-concentration analysis of metal in cold-rolled steel at the site of a defect in the base metal and the cortical zone of the ingot before and after high-temperature heating revealed the morphological signs of structural heterogeneity (Fig. 4). The differences are only in terms of shape, distribution of inclusions and concentration of FeO in wüstite. An increase in the FeO content from 80-85% to 87-93% indicates the oxidation of subcortical bubbles and micropores during the oxidative heating of ingots in the cells of heating wells.

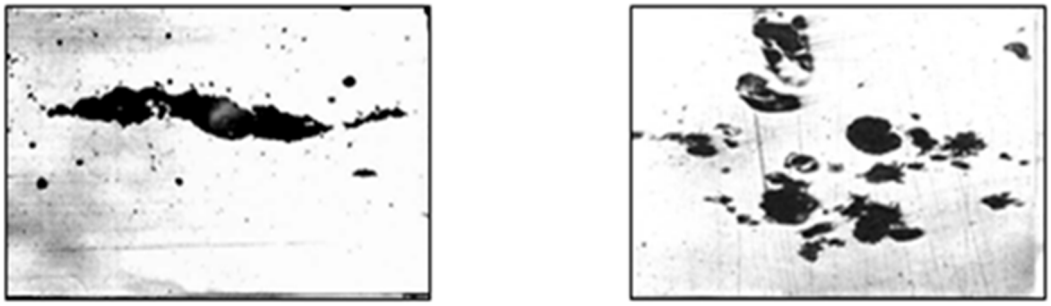

a b

Fig.4. Microstructure of a gas bubble in a cold-rolled product (a) and the cortical zone of the ingot (b)

To determine the moment of formation of these defects, the macro- and microstructure of the near-surface zones of the ingot and slab were studied. A detailed macro- and microstructural analysis of the structure of the surface zones of the ingots indicated unsatisfactory conditions in the crustal layer of the ingot surface. The steel crust zone has an increased content of gas bubbles (subcortical, pores, and shells), which are often oxidized along the inner walls of bubbles or bubbles filled with metal but with an oxide shell composed of ~ 85% FeO and up to 7% MnO (Fig. 5). The surface crust of the metal is loose, porous and contaminated with nonmetallic inclusions in the form of iron oxides such as wüstite, products of secondary oxidation during casting, and slag particles (Fig. 6).

4. Discussion of the research results

Figure 1 shows SEM images of synthesized ceramics depending on the annealing temperature, which reflect the kinetics of changes in the morphological features of the samples under study. during low-temperature annealing indicates the presence of several phases in the structure of ceramics.

A comparative analysis of defects in cold-rolled steel showed that defects originating from steelmaking accounted for 62 to 84% of all surface defects (Table 2). The results of metallographic studies show that 90% of the surface defects in cold-rolled sheets are represented by a nonmetallic oxide phase consisting of iron and manganese oxides.

.

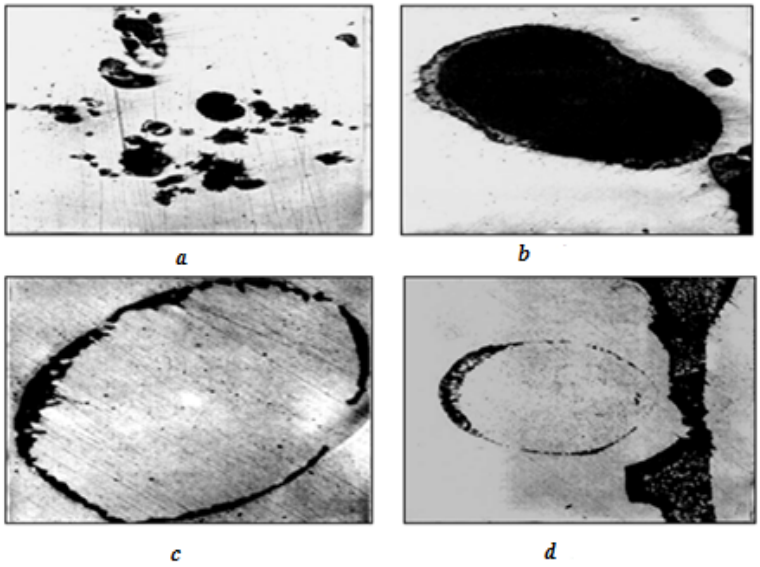

Fig.5. Microstructure of the ingot corner templates: a) x 50; b) x100; c) x 500; g) x200;
a), b) are gas bubbles in the cortical zone of the ingot; c), d) are bubbles filled with metal with an oxide shell.

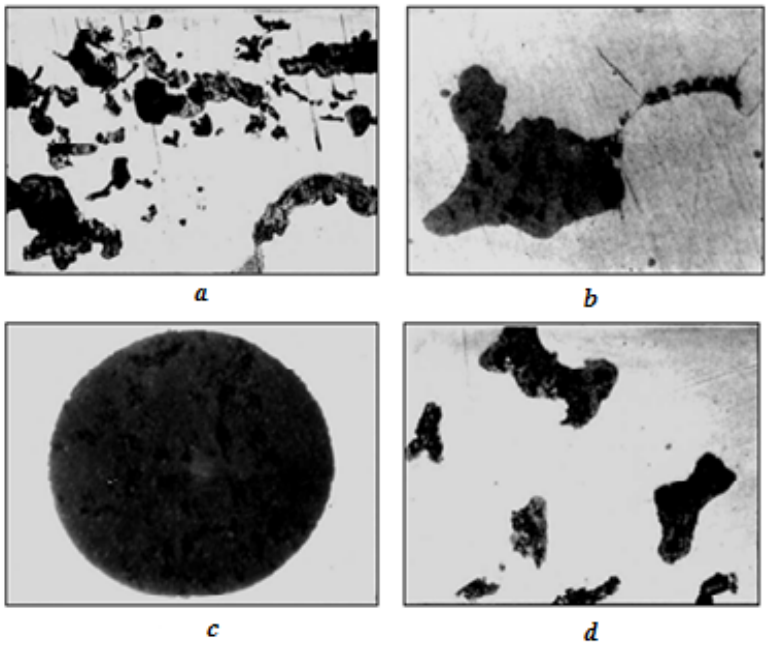

Fig.6. Accumulation of nonmetallic inclusions in a boiling crust: a) x100; b) x630; c), d) x400;
a) oxidized pores; b) slag inclusions in the interaxial sections of the square 3; c) 50% of the top of the ingot, iron oxides in the interaxial areas of the film type; d) slag inclusions.

Table 2. Classification of defects in cold-rolled sheets

Classification defects	pl. No. 380520 08KP	pl. No. 180521 08 KP	pl. No. 0180654 08 PS	Average values
peal bubble, %	48.3	45.8	66.0	56.6
captivity from n/inclusions, %	37. 9	45.8	22.6	32.1
ingot film, %	10.3	-	1.9	3.8
other, %	3.4	8.3	9.4	7.5

A high proportion of surface defects in the film from oxide nonmetallic inclusions (33–38%) and a rolled bubble filled with the oxide phase FeO-MnO indicate their nucleation at the crystallization front in a two-phase zone enriched in manganese, oxygen, carbon, sulfur and phosphorus. Oxidation of manganese occurs at all horizons of the forming ingot, including in the zone of predominant gas release, and the formation of the oxide phase from FeO and MnO occurs both at the crystallization front in the interdendritic sections of the liquid-steel solid surface phase boundary and on the forming outer surface of the bubble CO.

The oxide liquid phase of FeO and MnO, which envelops the CO bubble upon separation, is carried away from the crystallization zone to the head part of the ingot, as evidenced by the appearance of slag foam (ingot slag) on the metal mirror in the mold during boiling. As a result of the movement of bubbles, a specific circulation of the melt occurs at the crystallization front, which promotes the drawing of liquids and their oxidation products after the bubbles and the formation of micro-discontinuous materials and channels filled with an oxide slag phase, mainly FeO and MnO, or metal however, an oxide rim is present along the inner surface of the discontinuity, which was recorded during metallographic analysis. The presence of pores filled with oxides is explained by the much lower values of interfacial tension at the oxide phase-metal boundary than at the gas-metal boundary; therefore, it is easier for an oxide phase nucleus (inclusion of oxides - FeO and MnO) to arise in a liquid metal than a gas nucleus.

The contamination of the cortical zone of the ingot with oxide nonmetallic inclusions formed both on the surface of the CO bubbles and in the interdendritic space was influenced by the intensity of the metal boiling in the mold. With increasing boiling time, first, the thickness of the two-phase zone, which is enriched in liquates and the products of their interaction with oxygen, decreases, and second, intensive leaching of the resulting slag oxide phases into the head part of the ingot occurs.

The intensity of gas formation is determined by the degree of oxidation of the steel by the time it enters the mold, the liquid mobility of the metal, the solidification rate and casting temperature, as well as the chemical composition (oxygen, carbon, manganese content). The main reason for the deterioration of the bottom part of the ingot was boiling (“swelling”) of the metal due to the formation of numerous small CO bubbles covered with a ferromanganese oxide film. The viscous oxide film prevents the free release of CO from the metal, which leads to foaming of the metal. The foamed slag-metal layer rises up wards and, due to the large cooling effect of the cold walls of the mold, settles on its walls to form a frozen “shirt”. The high oxidative potential of the atmosphere in the cavity of the mold, due to the injection of air by a jet of metal, leads to oxidation of the surface of the “splash” frozen on the walls of the mold.

The main share of defects is of steelmaking origin and is determined by three factors:

a - small thickness, porosity and low gas density of the crust layer of the ingot;

b - the formation of internal (hidden) films from splashes (splashes) of metal in the mold during casting;

c - Contamination of the metal in the cortical zone of the ingot with oxide nonmetallic inclusions.

In rolled sheets, this manifests itself in the presence of nonmetallic inclusions of iron and manganese oxides or complex ferromanganese silicates in defective areas of the surface and subsurface layers of the sheets.

The following mechanism is proposed for the transformation of microdefects in the ingot into continuity defects in rolled sheets. When boiling steel ingots with microdefects in the structure of the crustal zone in the cells of heating wells are heated, further oxidation of the “hidden” film, subcrustal bubbles, and microporosity occurs, which leads to a change in the quantitative composition of oxide inclusions, i.e., to increase the FeO content from 34-85% to 91-94%. In addition, diffusion nucleation of oxide satellite inclusions in the form of an oxide rash occurs and the area of the defective metal increases (Fig. 7).

The source of oxygen for the diffusion oxidation of macro- and micro-discontinuities and the nucleation of new satellite oxide phases in the crust zone of the ingot are the oxidizing furnace atmosphere, as well as the oxide phase in the form of a “hidden” film, oxide nonmetallic inclusions, and scale on the surface of the heating ingot. Point quantitative analysis showed that the content of total oxygen in the “hidden” film is 23-31%, which may well serve as an additional oxidizing agent for internal diffusion oxidation of the metal.

When rolling an ingot, the shape changes, and the distribution of microdefects increases. In the surface zones of the steel ingot, accumulations of inclusions are found in the form of films along the interaxial areas of the dendrites (Fig. 8, a).

Coarse defects in the ingot located close to the surface, already at the first rolling stage, roll out onto the surface of the slab and give rise to defects in the form of honeycomb tears and films or after a fire cleaning machine, where a 4-6 mm layer of the metal surface is removed, revealing internal defects in the ingot (Fig. 9 a, b).

.

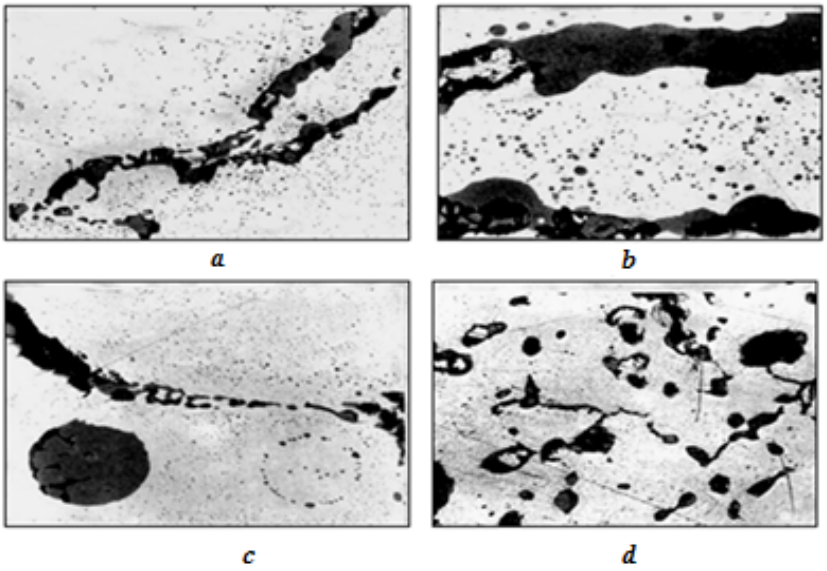

Fig.7. The nature of the distribution of nonmetallic phases after high-temperature heating of steel grade 08 KP: a) general view of the area of the hidden oxide film in the bottom part of the ingot (95% level from the top), heating time 2 hours; b) the same, the nature of the distribution of secondary (diffusion) oxides; c) oxidation around a slag inclusion and a bubble filled with scrap metal at the metal-oxide film interface (holding time during heating for 2 hours); d) oxidation of the cortical zone of the ingot through the tubules and micropores with a holding time of 4 hours (75% of the top).

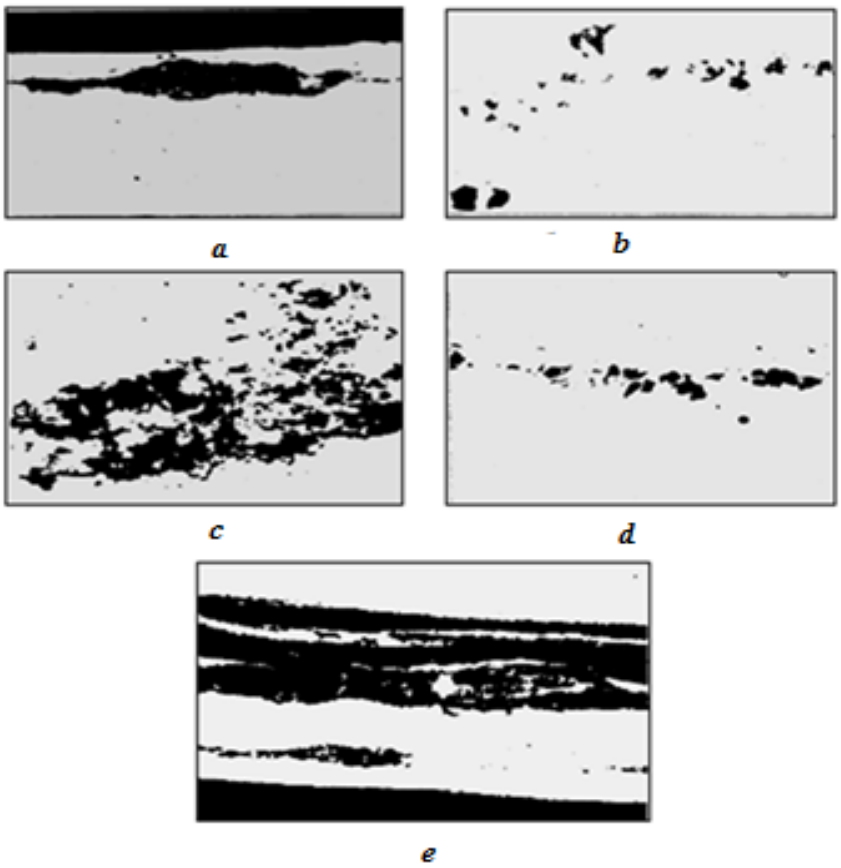

Fig.8. Microstructure of steel at the site of surface defects in cold-rolled sheets: a)rolled out of an oxidized bubble in the surface layer (along the thickness of the sheet) (x 630); b) the same, polished section on the surface of the sheet (x630); c) and d) films in the surface layer of the sheet, 08 KP (x 500); e) coarse inclusions and delamination in the surface layer of the sheet, 08 KP (x125).

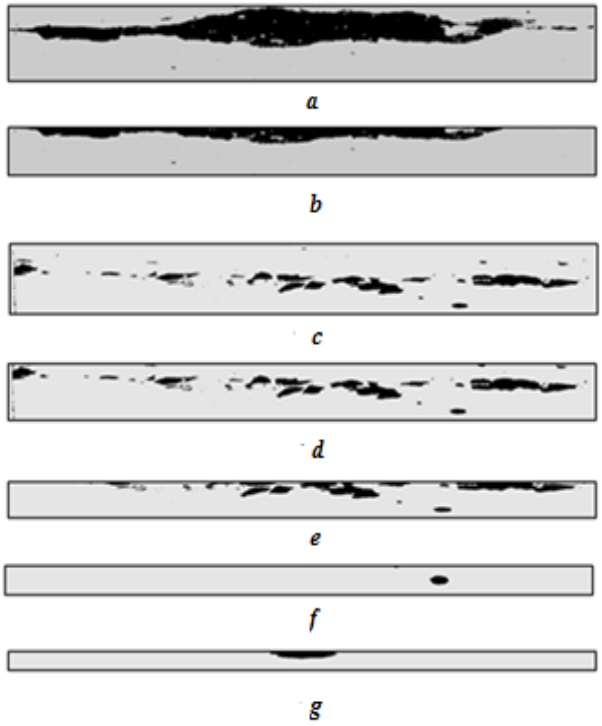

Fig.9. Mechanism of transformation of ingot defects into surface defects in sheet metal:
a), b) formation of captivity and rags in the first stage; c), d), e) formation of a film and a rolled bubble on a hot-rolled product; f), g) formation of a rolled bubble and film on cold-rolled sheet metal

As the layer of healthy metal above the defect thins during subsequent rolling stages, due to the unequal plasticity of the steel matrix and inclusions, the layers reach the surface of the strip and form defects such as rolled bubbles and films; for example, when the slab is heated in methodical furnaces and rolled in a hot mill line (Fig. 9 c, d, e) or during cold-rolled rolling and temper training (Fig. 9 f, g). Large inclusions in the form of oxide films, which are formed mainly in the bottom part of the ingot, form rough defects on the surface of the sheets, usually with peeling or scanlines.

Thus, the results of the experiments make it possible to reveal the nature of nonmetallic inclusions contaminating the surface zones of the ingot to clarify the sources and causes of the formation of the main types of defects in rolled sheets:

1 The main share of surface defects in thin-sheet cold-rolled steel is of steelmaking origin (62-84%) and is determined by three factors:

a – the presence of a thin and loose outer cortical layer on the ingot, damaged by subcortical bubbles, pores, and tubules due to the high oxidation potential of the steel;

b - the presence of an internal (“hidden”) film from boiling of the metal in the mold during casting. In rolled sheets, this manifests itself in the presence of nonmetallic inclusions of iron and manganese oxides or complex ferromanganese silicates at places with defects in the surface and subsurface layers of the sheets;

c – Contamination of the cortical zone of the ingot with oxide nonmetallic inclusions.

2 The identity of the morphological signs of structural heterogeneity in the cortical zone of the ingot and in the location of the defect in cold-rolled steel was established. The differences lie in the shape and distribution of inclusions and the concentration of FeO in wustite.

3 An increase in the concentration of FeO in wustite from 80-85% in the cortical zone of the ingot to 87-93% at the site of the defect indicates that a significant part of the defects are formed during the process of oxidative heating and subsequent hot deformation. During the heating process, oxidation of the internal cavities of microdefects occurs, as does the formation of additional satellite oxide inclusions in the form of dispersed oxide rashes and globules of diffusion wustite oxides near areas of large nonmetallic inclusions, increasing the area affected by defects.

4 The surface defects of cold-rolled sheets are 90% represented by a nonmetallic oxide phase consisting of iron and manganese oxides. A high proportion of surface defects in the film from oxide nonmetallic

.

inclusions (33–38%) and a rolled bubble filled with the oxide phase FeO-MnO indicate their nucleation at the crystallization front in a two-phase zone enriched in manganese, oxygen, carbon, sulfur and phosphorus.

5 The formation of structural heterogeneity in the form of a "hidden" film in the bottom part of the ingot is associated with the boiling of the first portions of steel and its crystallization on the surface of the mold. The boiling of steel is associated with the formation of a large number of small bubbles of CO, which are covered with a thin slag film of viscous ferromanganese oxides, preventing rupture of the film and the release of CO from the metal.

6 Coarse defects in the ingot located close to the surface are rolled out onto the surface of the slab in the form of honeycomb waste and film at the first rolling stage. As the layer of healthy metal above the defect thins during subsequent rolling stages, due to the unequal ductility of the steel matrix and inclusions, the metal particles reach the surface of the sheets and form defects such as rolled bubbles and films. Large inclusions, in the form of oxide films, which are formed mainly in the bottom part of the ingot, form rough films on the surface of the sheets, usually with peeling or scaliness.

5. Conclusion

Structural-concentration analysis of the metal at the end-to-end process of ingot — rolled steel has established the identity of the morphological signs of structural heterogeneity in the crustal zone of the ingot and in the place where the defect of cold-rolled steel appears. The difference lies in the shape, distribution of inclusions and concentration of FeO in wüstite.

The reasons for microstructural heterogeneity and increased contamination of the cortical zone of the ingot have been established. 90% of surface defects in cold-rolled sheets are represented by a non-metallic oxide phase consisting of iron and manganese oxides. A high proportion of surface defects in the film from oxide non-metallic inclusions and a rolled bubble indicates their origin at the crystallization front in a two-phase zone enriched in manganese, oxygen, carbon, sulfur and phosphorus.

The heating mode of the metal before hot rolling has a significant influence on the development of surface defects in rolled sheet metal. During the heating process, oxidation of the internal cavities of microdefects occurs and the formation of additional oxide inclusions in the form of a dispersed oxide rash.

The nature of the relationship between the type of structure of the cortical zone of the ingot and the development of defects on the rolled surface and the mechanism of transformation of structural inhomogeneity of the cortical zone of the ingot into defects on the surface of rolled sheets have been established. The established patterns made it possible to develop methods for controlling structural and chemical heterogeneity in the end-to-end steel-rolled process.

Conflict of interest statement
The authors declare that they have no conflict of interest in relation to this research, whether financial, personal, authorship or otherwise, that could affect the research and its results presented in this paper.

CRediT author statement:
Ibraev I.K.: Conceptualization, Methodology, Software, Investigation; **Ibraeva O.T.**: Data curation, Writing- Original draft preparation, Visualization; **Zhakupov T.M.:** Supervision, Validation, Writing- Reviewing and Editing.
The final manuscript was read and approved by all authors.

References

1 Naumenko E.A., Rozhkova O.V., Kovaleva I.A. Comprehensive study of characteristic signs of defects detected during magnetic powder control at the final stage of production of seamless hot-rolled pipes. *Litiyo i Metallurgiya (Foundry Production and Metallurgy)*, 2023, 1, pp. 69 – 72. [in Russian] https://doi.org/10.21122/1683-6065-2023-1-69-72

2 Guo J.L., Wen G.H., Fu J.J., Tan P. and Gu S.P. Evaluation of carbon equivalent calculation of continuous casting steel based on surface roughness. *Iron and Steel*. 2019, Vol. 54, No. 08, pp. 187. doi:10.13228/j.boyuan.issn0449-749x.

3 Sowa L., Skrzypczak T., Kwiatoń P. Numerical Evaluation of the Impact of Riser Geometry on The Shrinkage Defects Formation in the Solidifying Casting. *Arch. Metall. Mater.*, 2022, Vol. 67, Is. 1, pp. 181-187. https://doi.org/10.24425/amm.2022.137487

4 Ansari M.O., Chattopadhyaya S., Ghose J. Sharma S., Kozak D., Li C., Wojciechowski S., Dwivedi S.P., Kilinc H.C., Królczyk J.B. Productivity Enhancement by Prediction of Liquid Steel Breakout during Continuous Casting Process in Manufacturing of Steel Slabs in Steel Plant Using Artificial Neural Network with Backpropagation Algorithms. *Materials,* 2022, 15(2), pp. 670. https://doi.org/10.3390/ma15020670

5 Chien-Cheng Feng, Ming-Hong Lin, Yi-Cheng Chen, Shih-Fu Ou and Ching-Chien Huang. Optimization of Continuous Casting for Preventing Surface Peeling Defects on Titanium-Containing Ferrite Stainless Steel. *Materials* 2023, 16(4), 1461. https://doi.org/10.3390/ma16041461

6 Zhao F., Hu H., Liu X., Zhang Z., Xie J. Effect of billet microstructure and deformation on austenite grain growth in forging heating of a medium-carbon microalloyed steel. *Journal of Alloys and Compounds*, 2021, Vol.869, pp. 15. https://doi.org/10.1016/j.jallcom.2021.159326

7 Yang Wen', Cao Jing', Wang Xin-hua. Investigation on Non-Metallic Inclusions in LCAK Steel Produced by BOF-LF-FTSC Production Route. *Journal of iron and steel research international*, 2011, Vol.18, No.9, pp. 06 – 12. https://doi.org/10.1016/S1006-706X(12)60027-2

8 Ali N., Zhang L., Zhou H., Zhao A., Zhang C., Fu K., Cheng J. Effect of soft reduction technique on microstructure evaluation and toughness of medium carbon steel. *Mater. Today Commun*., 2021, pp. 102130. https://doi.org/10.1016/j.mtcomm.2021.102130

9 Han Z.J., Liu L., Lind M., Holappa L.E. Mechanism and kinetics of transformation of aluminum inclusions in steel by calcium treatment. *Acta Metallurgica Sinica (English Letters),* 2006, Vol.19, Is. 1, pp. 1 – 8. https://doi.org/10.1016/S1006-7191(06)60017-3

10 Zhang F., Yang S., Li J., Liu W., Wang T., Yang J. Formation mechanism and control of transverse corner cracks in fine blanking steel. *Journal of Materials Research and Technology,* 2022, Vol. 18, pp. 1137 – 1146. https://doi.org/10.1016/j.jmrt.2022.03.042

AUTHORS' INFORMATION

Ibraev, I.K. – Doctor of Techn. sciences, Professor, Department of Metallurgy and Materials Science, Karaganda State Industrial University, Temirtau, Kazakhstan; ORCID ID: 0000-0002-6414-6901: ibraevik@yandex.ru

Ibraeva, O.T. – Candidate of Techn. sciences, Associate Professor, Professor, Karaganda State Industrial University, Temirtau, Kazakhstan; ORCID ID: 0000-0002-8490-1994; ibraevaot@yandex.ru

Zhakupov T.M. – Candidate of Techn. sciences, Senior Lecturer, Department of Thermal Power Engineering, L.N. Gumilyov Eurasian National University, Astana, Kazakhstan; ORCID ID: 0000-0002-9725-0262; sultan_200779@mail.ru

EURASIAN PHYSICAL TECHNICAL JOURNAL

2024, Volume 21, No. 1 (47)

https://doi.org/10.31489/2024No1/38-48

Received: 07/01/2024 Revised: 07/02/2024 Accepted: 11/03/2024 Published online: 29/03/2024

Research Article

UDC: 539.232; 620.193

REASON OF PITTING CORROSION OF MARTENSITIC STEEL IN SEA WATER

Baikenov M.I., Seldyugaev O.B., Guchenko S.A., Afanasyev D.A.*

E.A. Buketov Karaganda University, Karaganda, Kazakhstan
Corresponding author: a.d.afanasyev2@gmail.com

Abstract. *The assumption that corrosion of products from X17 martensitic stainless steel in seawater occurs due to incomplete oxidation of chromium atoms in cells on the surface of the products is made in the presented work. Incomplete oxidation of chromium atoms occurs in the cells of X17 steel. This is due to the fact that oxygen molecules at temperatures up to 350 °C not having enough energy for chemical interaction with trivalent chromium atoms entering the cubic body-centered cells of martensitic stainless steel. There is a significant decrease in the corrosion rate after placing X17 stainless steel products in 5% iodine solution in ethanol after pre- treatment of the product surface with active forms of oxygen. The treatment was carried out during 12 hours with chemically active forms of oxygen (ozone and singlet oxygen) at a temperature of 350 °C. Most of the chromium atoms on the surface of X17 steel samples were completely oxidized as a result of 12 hours exposure to highly active forms of oxygen. The density of the oxide passivation layer on the surface of the products increased significantly as a result of the formation of new bonds CHROMIUM - OXYGEN - CHROMIUM. This resulted in increased corrosion resistance. The rate of interaction with an alcohol solution containing halogen ions was reduced by 71% for the samples with the oxide passivation layer compared to samples of untreated X17 steel.*

Keywords: carbon steel; seawater; localized corrosion, oxidation, halogens, body-centered cubic structure.

1. Introduction

The big problem of intensive corrosion exists in the operation of metal products. It happens when metal products are exposed to seawater or marine climate conditions. For example, products made of ordinary carbon steel are very quickly destroyed even being on the shore under the condition of regular fogs coming from the sea [1, 2]. The construction steel St3 (steel 3), the analogue of which is produced in the USA under the brand name A57036. For this reason, stainless steels are commonly used for seawater applications. These steels are significantly more expensive than conventional carbon steels. In addition, not all stainless steels are equally well preserved in seawater. X18H9T (steel composition: 18% chromium, 9% nickel, 1% titanium), X19H9T (steel composition: 19% chromium, 9% nickel, 1% titanium) and X24H9T (steel composition: 24% chromium, 9% nickel, 1% titanium) steels with chromium content more than 18% and additionally alloyed with nickel have high corrosion resistance in seawater [3, 4], but these steels are quite expensive. For instance, a kilogram of X18H10T steel costs 4.2 US dollars (USD). Cheaper stainless steels with chromium content from 10.5% to 17% chromium (mass percent) [3] are much cheaper than steels with chromium content over 18% and the presence of other alloying elements. A kilogram of 08X17T steel costs 2.55 USD. However, these steels are highly corrosive in seawater. Although the corrosion resistance of X17 type steels is much higher than that of ordinary carbon steels [4]. In this regard, the surface of stainless steels

with mass fraction of chromium less than 18% is often covered with a film of protective coating not sensitive to seawater. However, the creation of such coatings leads to additional increasing of the cost. The steel is coated with a layer of chromium, but this is a complex and expensive operation. 1 kilogram of pure chromium powder costs 130 USD. The development of cheap methods to increase the surface corrosion resistance of stainless steels with a chromium content of less than 18% is very relevant.

Much attention is constantly paid to the study of metal corrosion processes. This is evidenced by a large number of new articles [5-10]. Work is underway both to study the corrosion process of carbon steels [5-7] and martensitic steels [8-10]. The main methods for studying corrosion processes include electrochemical research methods [5, 6, 10] and electron and optical microscopy [5, 6]. A number of works have proposed new research methods [6, 7]. The significant role of the tribological characteristics of steels in the corrosion process was showed in [7]. Despite significant efforts aimed at studying corrosion processes in steels, a large number of issues remain that require consideration. Models of metal corrosion processes are still being discussed.

The article [11] shows that corrosion of aluminium in seawater occurs when the surface of products interacts with negative halogen ions. Seawater is actually a mixture of aqueous solutions of negative halogen ions. The article concluded that corrosion of aluminium in seawater is due to insufficient oxidation of aluminium cells on the surface of aluminium products. It was shown that incomplete oxidation of aluminium cells (42 % of the total number of aluminium atoms in the cells on the surface of the products have no covalent bond with oxygen atoms) is caused by the lack of energy of oxygen molecules under normal conditions (T = 0 °C, P = 10^5 Pa, the concentration of oxygen 19-21% by volume). It was shown that complete oxidation of aluminium cells leads to the creation of a cell structure in which each aluminium atom in the cells is chemically bonded to three oxygen atoms. This eliminates the possibility of chemical interaction of aluminium atoms in such cells with negative halogen ions (i.e. the process of aluminium corrosion in seawater becomes impossible). The introduction of additional oxygen atoms inside the aluminium cells mechanically blocks the possibility of ion penetration inside the structure of aluminium products. In other words, the formed monolithic layer of corundum on the surface of the product is a barrier to the penetration of halogen ions into aluminium cells with not fully oxidized structure.

For conducting experiments to determine the corrosion rate of aluminium, a 5% solution of iodine in ethanol was used in [11]. The use of iodine is due to the fact that alcohol solutions of iodine are industrially produced. They are certified by state standards, they are not expensive, and these iodine solutions are relatively safe when conducting experiments. The opposite of this, fluorine and bromine solutions are highly toxic.

In this work, the possibility of increasing the corrosion resistance of stainless martensitic steel products, on the example of X17 steel, by method of additional surface oxidation is studied.

2. Materials and experimental details

There were 9 atoms in the unit cell model of X17 stainless steel for calculations, which 8 iron atoms and 1 chromium atom were present. Chromium was located in the center of the body-centered cubic lattice. Experiments were carried out with various samples of untreated and treated X17 stainless steel (16 wt% chromium content), with samples of untreated and treated St3 structural steel (US analogue A57036), with samples of treated and untreated chromium with 99.99% purity. All these samples were placed in 5 wt% iodine in ethanol. Experiments with 2.5 wt% iodine in ethanol and with 2.5 wt% iodine in water-ethanol mixture (50 wt% water and 50 wt% ethanol) were also carried out.

The mass of the samples before and after placement in the solution was measured on a RADWAG AS 60/220.R2 with electronic scale. The measurements were carried out to an accuracy of ten thousandths of a gram. There were used samples of X17 stainless steel, stainless steel X19H9T, structural steel St3, pure chromium and chromium with oxidized surface. The samples and the air entering these samples were heated to a temperature of 350 °C with simultaneous irradiation of the incoming hot air by ultraviolet radiation (UVT - ultraviolet treatment) of the DRT-400 lamp. DRT-400 lamp emits ultraviolet radiation in the range from 220 nm to 340 nm.

Elemental analysis of steel was carried out using an energy dispersive detector (EDX, INCAPentaFET-x3, Oxford Instruments, England) included in a scanning electron microscope (MIRA 3LMU, TESCAN).

.

The surface properties of the films were investigated using a HV1000 hardness tester optical microscope. Microphotographs were taken at 160x or 400x magnification over the entire area of the specimen. The average pitting grain size was determined using the ImageJ program.

3. Results of theoretical and experimental research

Under normal conditions, an oxide film consisting of two subsystems is formed on the surface of stainless martensitic steel: iron oxide subsystem and chromium oxide subsystem with a thickness of 4 nm (Figure 1) [12]. Taking into account that the length of the face of a body-centered cubic cell of martensitic steel is 0.3 nm, no more than 13 layers of martensitic steel cells are placed in the passivated layer.

An assumption was made taking for stainless martensitic steels with chromium content from 10.5% to 18% into account the results stated in [11]. It is possible to increase the corrosion resistance of the existing oxidized layer for these types of the steels. The corrosion resistance of the hardened oxidized layer should significantly exceed the chemical resistance of the passivated layer on the surface of untreated martensitic steel. The basis for this assumption is the known fact that the main alloying component of stainless steels chromium atom can have a variable valence from 2 to 6 [13]**.** Chromium atoms have mainly valence 3 in stainless steels with the content of chromium less than 18%, but at the same time some chromium atoms on the surface of these steels have valence 6 [14]. It is still possible to increase the valence of most of the chromium atoms on the surface of stainless-steel samples up to 6 under the appropriate energetic influence on the structure of stainless-steel cells. On each chromium atom two or three additional covalent bonds with oxygen atoms (limiting valence 6) can appear at access of high-energy forms of oxygen. In this case, these oxygen atoms form a second covalent bond either with iron atoms or with other chromium atoms in a given stainless steel cell or in neighboring cells. One possible bonding scheme of trivalent chromium atoms in a stainless-steel cell located on the surface of the product at chromium content from 11% to 17% is shown in Figure 1. All atoms of one stainless martensitic steel cell are shown in full. In addition, the interaction of a chromium atom in a given cell with chromium atoms in neighboring cells is shown schematically. The interaction of chromium atoms occurs through oxygen bridges.

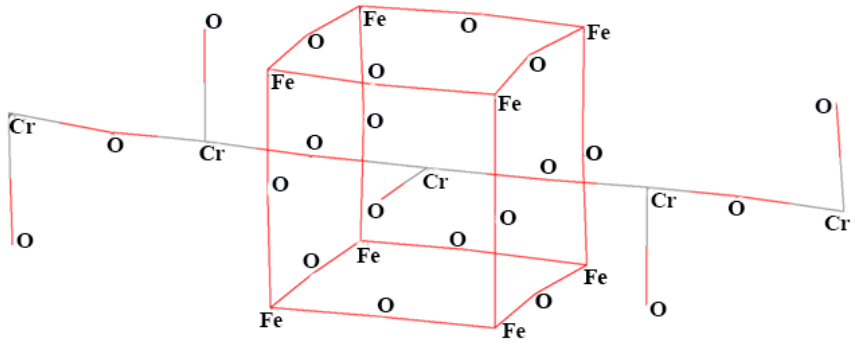

Fig.1. Scheme of possible arrangement of chromium and oxygen atoms in the cell structure on the surface of stainless steel with chromium content from 11 to 18%. Valence of chromium atoms 3.

Theoretical the concentration of 11% chromium at the stainless-steel cell is corresponding to one chromium atom in each stainless-steel cell with uniform distribution of atoms.

The martensitic steel cell is cubic body-centered and has 9 atoms, one of these atoms in the center of the cell [14]. Occurrence of chromium oxide films linking neighboring cells with each other as shown in Figure 1 is possible when the chromium atom is localized in the center of the body-centered cubic lattice. It should be realized that 11% is the average concentration of chromium atoms taking into account all stainless-steel cells. Whereas in a real alloy, the chromium atom may be absent due to the random distribution of chromium atoms in some cells. As a result of iron-chromium alloys are a system with unlimited solubility. These alloys conform to the three Hume-Roseri rules [15, 16]:

1. Close structure of valence shells of atoms of alloy components;
2. The presence of crystal lattices of the same type in the alloy components;
3. The difference in the size of atoms of the alloy components is not more than 8%.

The sizes of chromium and iron atoms differ by less than 8 %. The covalent radius of iron is 1.16 A, chromium is 1.22 A, the metallic radius of chromium is 1.28 A, iron is 1.26 A [17, 18]. In addition, typically,

chromium has valence 3 in alloys, as do iron atoms. Due to the unlimited solubility of chromium in iron with an average chromium content of 11-17 % some cells may have two chromium atoms each. For instance, one chromium atom is located in the center of the cell and the other chromium atom is localized in a node of the crystal lattice and in some cells, chromium atoms will be completely absent. Cells in which chromium atoms are completely absent consist only of iron atoms. These cells will be the centers of corrosion and will be the first to break down when exposed to aggressive media (e.g. seawater). In steel, some cells do not contain a chromium atom, even theoretically if the chromium concentration is less than 10.5 %. These metals do not have a protective oxide film. As a result, the corrosion rate of a product made of this steel will be significant. Theoretically, at least half of the steel cells are missing chromium atoms in X5 steel with 5% chromium content. There are not enough chromium atoms for half of the cells. The appearance of a continuous oxidized chromium film on the surface is impossible. The number of cells that by chance may not contain a chromium atom decreases as the concentration of chromium in stainless steel increases from 11% to 18%. The number of cells unprotected from corrosion in the chromium oxide film on the surface of chromium-doped steel decreases. The significant increase in the corrosion resistance of stainless steel at a chromium content of 18 % is probably due to the fact that, starting from this concentration, at least one chromium atom is guaranteed to be contained in each stainless-steel cell. That is, there are no holes in the outer oxidized chromium film on the surface of the stainless steel product. This is schematically presented in the form of the figures where white squares represent cells not protected from corrosion, black squares represent cells protected from corrosion (Figure 2).

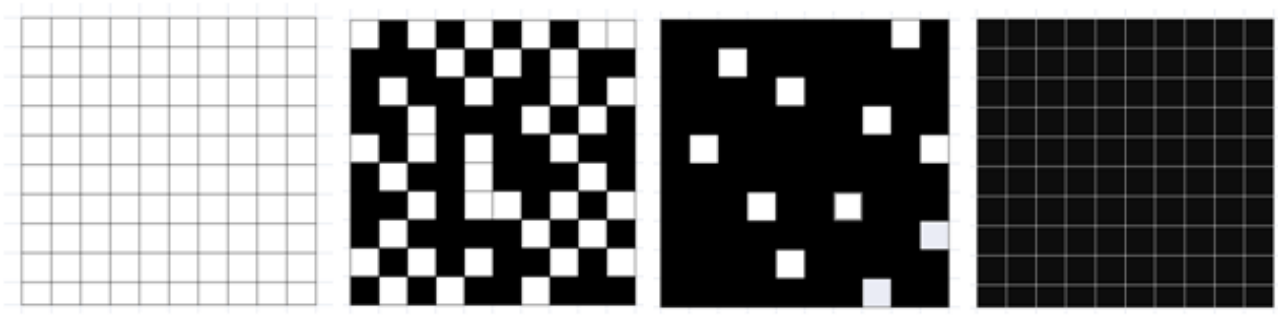

a) b) c) d)

Fig.2. Schematic representation of corrosion resistance of steel surfaces depending on chromium concentration (white squares represent cells not protected from corrosion): a) St3 (chromium 0,3 mass %); b) stainless steel with 11 % chromium content (Large unprotected zones are observed in the structure of the chromium oxide subsystem); c) stainless steel with 17 % chromium content (Pointed unprotected defects are observed in the structure of the chromium oxide subsystem); d) stainless steel with 18 % chromium content (significant corrosion reduction is observed [4]).

Chromium atoms in unit cells of stainless martensitic steel can form additional 2-3 chemical bonds mainly with chromium atoms located in neighboring cells under the influence of high-energy forms of oxygen. The transition of chromium atoms from the trivalent state to the hexavalent state is a consequence of this process. The number of additional bonds of chromium atoms with iron atoms should be insignificant, since iron atoms always exhibit valence 3. Oxidation of iron atoms in the surface layer occurs already during the manufacture of the product, and in the surface layers of stainless steel there are no iron atoms capable of establishing new bonds with chromium atoms.

The establishment of new bonds within the stainless-steel cell will result in the strengthening of the cell itself. The additional CHROMIUM - OXYGEN - CHROMIUM bonds formed within the stainless-steel cells will mechanically block the access of halogen ions and protons to the IRON - OXYGEN - IRON bonds. Protons are the main component causing corrosion in fresh water as opposed to seawater. These protons are formed in any water by dissociation. In pure water and neutral solutions, the concentration of protons $[H+]=10^{-7}$ g-ion/l [19]. The scheme of possible bonds of hexavalent chromium atoms in stainless steel cells located under the first layer of the product surface at a chromium content of 17% is shown in Figure 3.

A significant increase in the density of CHROMIUM-OXYGEN bonds inside stainless steel cells is observed when comparing Figures 1 and 3. The chromium in the hexavalent state is located in the inside

.

stainless-steel cells. That is, the probability of passage of a proton or a halogen ion through a cell having in its structure six bonds of CHROMIUM-OXYGEN is much less than through a cell having only three bonds of CHROMIUM - OXYGEN. The creation of mechanical obstacles occurs for the passage of halogen ions inside the stainless-steel cell structure. Also, the chemical resistance of the cells will increase significantly, since it is known that the CHROMIUM - OXYGEN bond has great chemical resistance. The possibility of breaking the bond of CHROMIUM -OXYGEN bond by protons and negative halogen ions (fluorine) has been calculated by quantum chemical method of PM3 (Parametric Method 3). This method is specifically designed to take into account the parameters of oxygen and halogens [20, 21]. The calculation showed that protons and negative halogen ions cannot break the bond of CHROMIUM-OXYGEN. The calculation showed that protons and halogen ions are trapped by the chromium atom in physical traps, which is consistent with experimental data on the strong saturation of chromium with hydrogen. It is also known that the surface of pure chromium or oxidized chromium at room temperatures does not interact with aqueous solutions of negative halogen ions, nor does metallic chromium interact with pure water, i.e. with the proton [22], which is formed in any water because of dissociation.

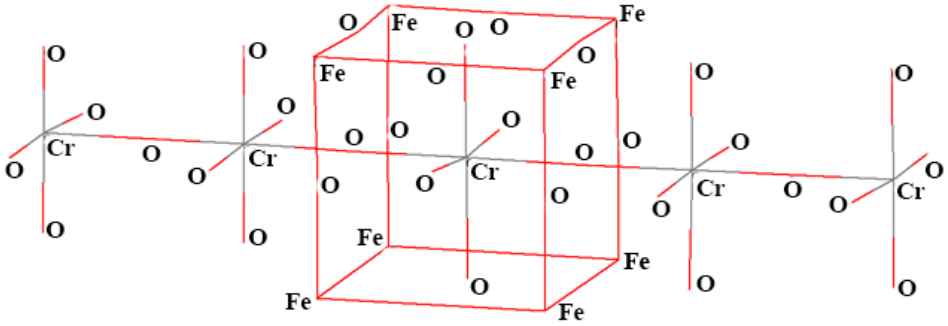

Fig.3. Scheme of possible arrangement of chromium and oxygen atoms in the cell structure.
2 layers of stainless steel surface with chromium content from 12 to 18%. Valence of chromium 6.

Summarizing the above, it can be stated that the transition of most of the chromium atoms on the surface of stainless martensitic steel from the trivalent state to the hexavalent state due to the formation of three new chromium-oxygen bonds should occur in the presence of active oxygen forms. The formation of additional three new chromium-oxygen bonds in each cell should significantly increase the corrosion resistance in seawater of stainless martensitic steels with chromium content less than 18% (having cubic body-centered lattice).

Experiments were conducted to test the hypothesis that increasing the number of OXYGEN-CHROMIUM bonds in the cells on the surface of stainless martensitic steel will result in a significant increase in corrosion resistance. The purpose of the experiments was to determine the corrosion rate on the surface of X17 stainless martensitic steel with 16% chromium content of 5% in iodine solution in ethanol. Two phenomena should be registered simultaneously when increasing the number of OXYGEN - CHROMIUM bonds. An increase in the percentage of oxygen on the surface of stainless steel and a decrease in the corrosion rate. A sample of untreated X17 steel was placed for 96 hours in an alcoholic iodine solution under normal conditions (T= 0 °C, P= 10^5 Pa, oxygen concentration 19-21% by volume). The sample was completely immersed in alcoholic iodine solution, with air above it. The lid of the vessel was hermetically sealed.

The percentage composition of the steels is shown in Figures 4, a-c. Micrographs of the X17 steel specimen were taken before placing it in a container of iodine solution (Figure 5, a). The specimen was polished to a shiny condition. Directional roughness is clearly visible for this specimen.

A similar experiment was performed with a sample of the world's most melted carbon steel St3 (A57036) with a chromium content of 0.3% or less. Also, a sample of X19H9T stainless steel was placed in a 5% alcoholic iodine solution for 96 hours (Figure 4, b). We used X19N9T stainless steel as a benchmark of corrosion resistance to compare the investigated stainless-steel samples with insufficient chromium content. The experiment showed that after 96 hours in 5% iodine solution in ethanol, the reference sample of stainless steel X18H9T with high chromium content lost 0.39% of the initial mass (was 0.39924 g, became 0.39770 g).

At the same time, the sample of X17 stainless steel with insufficiently high chromium content and complete absence of nickel lost 1.96% of the initial mass (was 0.57722 g, became 0.56589 g). That is, the corrosion rate is more than 5 times greater in X17 stainless steel with insufficiently high chromium content than in X19H9T stainless steel with more than 18% chromium content and 9% nickel content. The presence of pitting was detected in a micrograph at 400× magnification in a sample of X17 steel after being in a 5% alcoholic iodine solution for 96 hours (Figure 5, b). The average grain size of pitting is 1.1 μm.

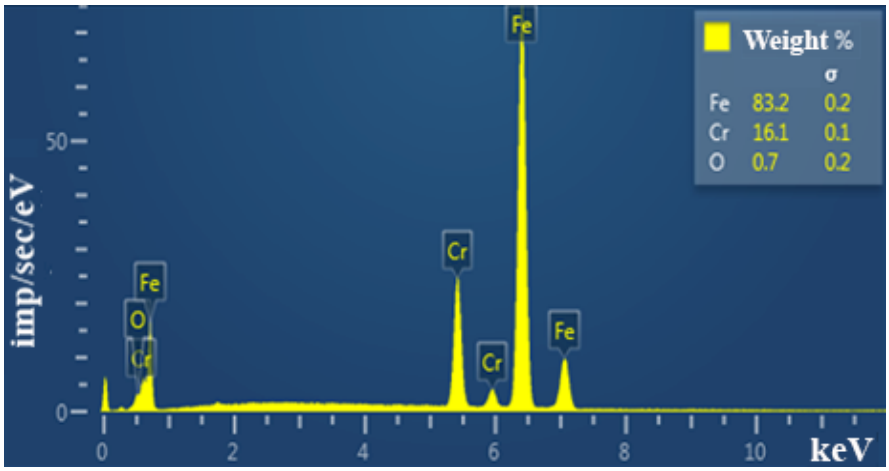

a)

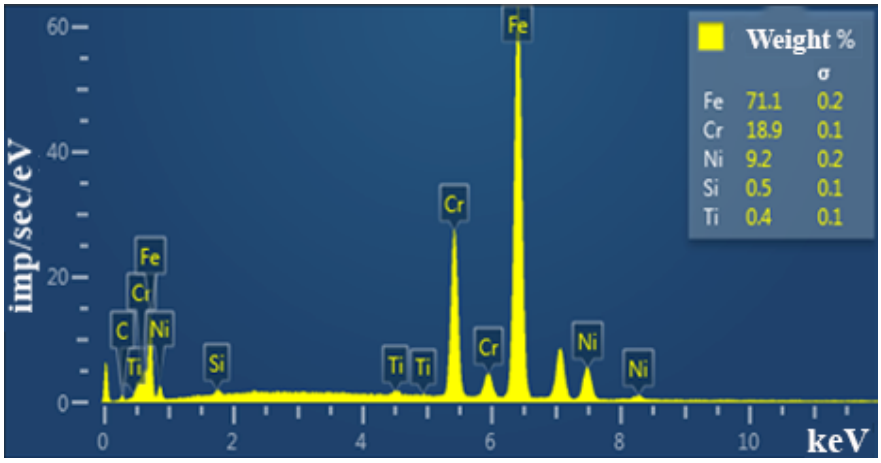

b)

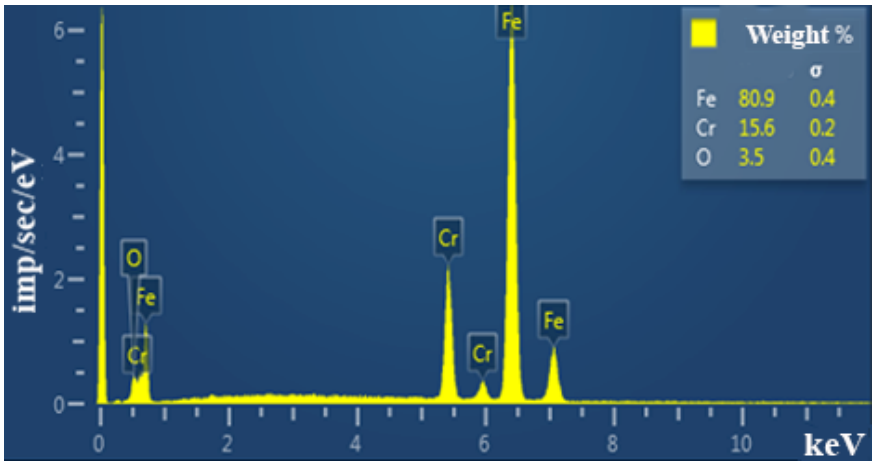

c)

Fig.4. Energy-dispersive X-ray spectra: a) Percentage content of elements in untreated X17 stainless steel; b) Percentage content of elements in X19N9T stainless steel; c) Component composition of X17 steel after complex 6- hours treatment with air heated to 350 °C and UVT.

.

A sample of structural steel St3 (A57036) lost 25% of its weight during 96 hours in a 5% iodine solution in ethanol. St3 contains no less than 98% iron and no more than 0.3% chromium. It was found that even not very high quality X17 stainless steel (which has no nickel and molybdenum in its composition) corrodes in halogen solutions 12 times slower than the most common carbon structural steels. The experiment was conducted to clarify how the interaction of negative halogen ions with the surface of X17 stainless steel leads to corrosion of this steel. The comparative effect of alcoholic iodine solutions on X17 stainless steel samples was studied in the experiment. 5% and 2.5% iodine solutions in ethanol were used. One sample of X17 steel was placed in pure ethyl alcohol. Additionally, one sample was placed in 2.5 % aqueous-alcohol iodine solution. Distilled water and ethyl alcohol were in equal volume doses.

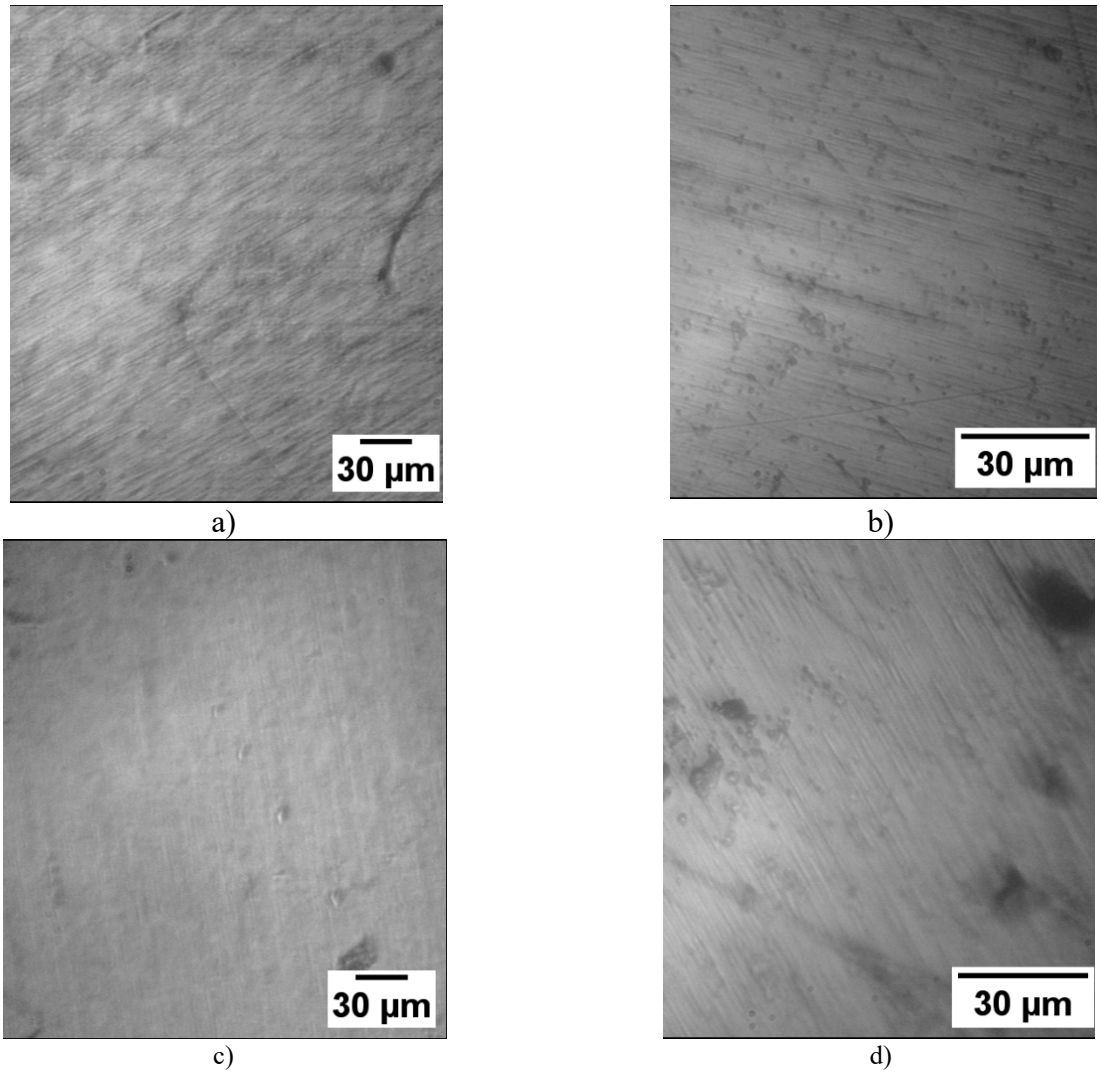

a) b)

c) d)

Fig.5. Surface microphotographs of X17 steel samples on HV1000 optical microscope:
a) untreated steel at 160x magnification (directional roughness is clearly visible); b) 400x magnification of the steel surface after 96 hours in 5% alcoholic iodine solution (pitting is clearly visible); c) sample at 160x magnification after 6 hours UVT treatment at 350 °C; d) at 400x magnification after 96 hours in iodine solution (sample was previously subjected to 24 hours with UVT at 350 °C.

The experiment showed that corrosion of stainless steel is completely absent for the X17 steel sample after placement in pure ethyl alcohol. It was also found that the corrosion rate was 4.7 times higher than that in 2.5% iodine alcohol solution and 8.4 times higher than that in 2.5% iodine water- alcohol solution after being 96 hours in 5% iodine alcohol solution. These results revealed a clear dependence of the corrosion rate of X17 stainless steel on the concentration of halogen ions. The higher the concentration of halogen ions is the higher the corrosion rate. It was also found that protons slow down the corrosion process of stainless martensitic steel. Protons always formed in water by dissociation [19]. It is very likely that protons in seawater reduce the corrosion rate due to electrostatic interaction with negative halogen ions.

Samples of X17 steel were exposed to high-energy forms of oxygen in order to create on the surface of this stainless steel a monolithic oxide layer in which all chromium atoms are in the hexavalent state. Ozone O_3 and singlet oxygen $^1O_2$ are significantly more chemically active than molecular oxygen $^3O_2$ in the ground triplet state [23]. The high-energy molecules of singlet oxygen $^1O_2$ and ozone O_3 were assumed to additionally activate the three valences of chromium atoms. Chromium atoms have six valence orbital's at 3d5 4s1 energy levels. Chromium atoms are normally trivalent in the normal state, but with three more valence orbital's they are capable of making three more chemical bonds.

Thus, an oxide layer of light brown colour was formed on the samples of treated X17 stainless steel as a result of 6 hours exposure. The oxide layer at 12 hours treatment was much darker. At the same time, no increase in the mass of the samples was recorded. It indicated that the oxide layer is very thin. The oxide layer has sufficient mechanical strength. Component composition analysis showed 400% increase in the oxygen content on the surface of the sample subjected to 6 hours treatment (Figure 4, c). The oxygen content on the surface of the X17 stainless steel sample treated for 6 hours increased 5 times from 0.7% to 3.5% (Figure 4, a and c). It was visually determined that as a result of exposure to high-energy forms of oxygen, the surface roughness disappeared (Figure 5, a). The steel surface became almost homogeneous (Figure 5, c).

Further, the treated samples of X17 steel (6 and 12 hours of treatment) were placed for 96 hours in 5% iodine solution in ethanol. This solution simulating the effect of sea water is a very aggressive environment capable of completely dissolving aluminium foil within 24 hours, according to the article [11]. The sample subjected to 6 hours pretreatment with reactive oxygen species lost 1.36 % of mass in 96 hours (was 0.50902 g, became 0.50206 g, mass loss 0.007 g). As a result, the oxide film on the surface of the sample has largely dissolved, discoloured, but still retains some structure and covers 30% of the sample surface. The experiment showed that 6 hours treatment of the surface of X17 steel with reactive oxygen species significantly improved the corrosion resistance of the surface of X17 steel. The mass loss due to corrosion decreased by 30% from 1.96% from the untreated surface of X17 steel to 1.36% from the 6 hours treated surface.

The sample of X17 steel subjected to 12 hours pretreatment for 96 hours of being in 5% iodine solution lost 0.57% of mass. This is comparable to the mass loss of high-alloy steel X19H9T (0.4%). Oxide on the surface of X17 steel covers 80% of the sample after being in 5% iodine solution in ethanol for 96 hours. At the same time, the oxide also discoloured to a light golden shade, as on the sample subjected to a preliminary 6-hours treatment. The oxide is firmly bonded to the surface. The oxygen content on the sample surface at the 12 hours treatment of the samples with reactive oxygen species was 4 %.

X17 stainless steel samples were treated at 350 °C with reactive oxygen species for 24 hours in order to further increase the corrosion resistance. As a result, an even darker colour was formed on the surface of the X17 samples oxide layer (dark brown). These samples practically did not change colour after 96 hours in 5 % alcoholic iodine solution, but deep chips were formed on all samples on the surface covered with oxides during repeated experiments. Holes passing through the oxide layer and partially entering the structure of the stainless steel itself were observed. The occurrence of spalling on the surface is attributed to the high stresses in the oxide layer. Chipping occurs because the volume of fully oxidized stainless steel cells (in which each chromium atom is bonded to 6 oxygen atoms) is much greater than the volume of stainless steel cells in which all chromium atoms are in the trivalent state. The Peeling-Bedworth factor for Cr_2O_3 coatings is 2.02 for trivalent chromium. The Peeling-Bedworth factor will be 2.56 for hexavalent chromium. It is known if the factor is greater than 2.5 cracks are always formed.

Analyses of the surface of X17 steel treated with reactive oxygen species for 24 hours showed that the oxygen content on the surface of the samples increased to 5 %. Microphotograph showed the absence of pitting corrosion on the surface outside the spalling (Figure 5, d). A monolithic oxide layer with increased chromium valence is formed on the surface of X17 stainless steel during prolonged treatment with active forms of oxygen. Local damages (spalling) occur due to internal stresses associated with the increase of the cell volume in this layer. The absence of pitting corrosion outside the chipping shows that the halogen solution does not have a chemical effect on the formed monolithic oxide layer of chromium with increased valence.

Analysis of the experiments showed that due to the formation of spalling it makes no sense to subject the surface of X17 steel to a long treatment, at which the mass fraction of oxygen on the surface reaches 5% (24 hours of treatment with active forms of oxygen). It is better to limit the surface treatment to a treatment in which the oxygen level on the surface does not exceed 4 %. Spalling does not occur with 12 hours treatment and the corrosion rate in seawater is 71% lower.

.

4. Discussion of results

It is revealed that the increase in corrosion resistance of X17 steel occurs with an increase in the oxygen content in the composition of cells on the surface of products from this martensitic steel. The increase in corrosion resistance of X17 steel may be a consequence of the formation on the surface of additional bonds such as CHROMIUM - OXYGENE - CHROMIUM, which do not chemically interact with halogen ions. Additional experiments showed the complete absence of chemical interaction of the fully oxidized surface of pure chromium with 5 % alcoholic iodine solution. An iridescent film of chromium oxide was formed on the surface of pure chromium as a result of 12 hours treatment with reactive oxygen species. The analysis of the composition of the investigated untreated X17 steel showed that there are only two main components in this steel iron atoms and chromium atoms with a small amount of oxygen (0.7% mass fraction of oxygen in X17 steel, with all oxygen in the surface layer 4 nm thick [4]). The mass fraction of oxygen on the surface increased to 4% at 12 hours treatment with active forms of oxygen. There was an increase in the oxygen content of 5.7 times. The corrosion rate of X17 steel at the same time decreased by 71%. All oxygen in this case is in the form of oxygen bridges either between chromium atoms or between iron atoms. Experiments conducted with oxidized surface of St3 steel showed an increase in the corrosion rate of St3 steel samples with oxidized surface compared to samples of unoxidized St3 steel by 2.2% when placed in a 5% alcoholic iodine solution. The whole surface of the steel samples was covered with $Fe(OH)_3$ rust. Therefore, the increase in the number of IRON-OXYGEN-IRON type bonds on the surface comes to increase the corrosion rate of steel St3. Summarizing the above it is possible to allocate two important facts:

1) Increasing the number of IRON-OXYGEN-IRON bonds accelerates the corrosion process of products;

2) Increasing the number of CHROMIUM - OXYGEN - CHROMIUM bonds reduce the corrosion rate of products.

5.7 increases in the number of oxygen bonds with a simultaneous increase in corrosion resistance by 71 % in X17 steel occurred as a result of 12 hours treatment with active forms of oxygen. Considering this, it can be concluded that most of the oxygen introduced into the surface of X17 steel formed CHROMIUM - IRON - CHROMIUM bonds. Table 1 shows the data of the experiments performed.

Table 1. Dependence of mass loss on steel grade and surface treatment of specimens.

	St3, Untreated	St3, UVT, 350 °C, 12 hours	X17 Untreated	X17, UVT, 350 °C, 6 hours	X17, UVT, 350 °C, 12 hours	X19H9T	Chromium (99.99 %)	Chromium (99.99%) coated with chromium oxide
Sample weight loss over 96 hours	25%	27.2%	1.96%	1.36%	0.57%	0.39%	0%	0%

Dependence of mass loss is shown for samples of structural steel St3, steel St3 with strongly oxidized surface, X17 stainless steel without treatment, samples of X17 steel with surface subjected to 6 hours and 12 hours treatment with reactive oxygen species, X19H9T stainless steel, samples of pure chromium, and pure chromium with pre-oxidized surface. These samples were placed in 5% iodine solution in ethanol for 96 hours.

5. Conclusions

The following conclusions were made from the results of the studies conducted:

1) It has been shown experimentally that one of the most probable causes of failure of products from martensitic stainless steels with chromium content below 18% in seawater is the interaction of negative halogen ions with the surface of products from these steels. It was revealed experimentally that with increasing concentration of halogen ions in solutions in which steel samples were placed. The corrosion rate of stainless steel increases significantly. The corrosion rate increases 4.7 times in alcoholic solutions when the concentration of halogen ions increases from 2.5% to 5%. In aqueous-alcoholic solutions, the corrosion

rate increases 8.4 times when the concentration of iodine is increased from 2.5% to 5%.

2) It was shown that in seawater corrosion of martensitic steel products with chromium content less than 18% becomes possible due to incomplete oxidation of chromium atoms on the surface of products. It was shown that the rate of corrosion in seawater X17 stainless steel (chromium content less than 18%, completely absent in the structure of nickel and molybdenum) can be significantly reduced (by 71%), after additional oxidation of chromium atoms included in the structure of stainless steel cells. The total oxygen content on the martensitic steel surface increased from 0.7% to 4%. It is revealed that it is optimal to create an oxide layer on the surface of X17 stainless steel with oxygen concentration not more than 4%.

3) The research method used in this article allows reducing costs associated with increasing the corrosion resistance of martensitic stainless steels. This method can be used to increase the corrosion resistance of non-ferrous metals.

Conflict of interest statement

The authors declare that they have no conflict of interest in relation to this research, whether financial, personal, authorship or otherwise, that could affect the research and its results presented in this paper.

CRediT author statement:

Baikenov M.I.: investigation, formal analysis; Seldyugaev O.B.: conceptualization, writing - review & editing; Guchenko S.A.: investigation, writing - original draft; Afanasyev D.A.: visualization, writing - review & editing.

The final manuscript was read and approved by all authors.

Acknowledgments

The authors are grateful to Zinoviev L.A. for discussion of the research methodology used in this article.

References

1 Sun M., Du C., Liu Zh., Liu, Ch., Li X., Wu Y. Fundamental understanding on the effect of Cr on corrosion resistance of weathering steel in simulated tropical marine atmosphere. *Corrosion science,* 2021, Vol.186, N.109427. https://doi.org/10.1016/j.corsci.2021.109427

2 Refait P., Grolleau A.-M., Jeannin M., Rémazeilles C., Sabot R. Corrosion of Carbon Steel in Marine Environments: Role of the Corrosion Product Layer. *Corrosion and Materials Degradation,* 2020, Vol.1(1), pp.198–218. https://doi.org/10.3390/cmd1010010

3 Interstate standard GOST 5632-2014. Alloy stainless steels and alloys are corrosion-resistant, heat-resistant and heat-resistant. Stamps. Moscow, 2015. [in Russian] https://mkm-metal.ru/upload/iblock/11c/5632_2014.pdf

4 Berezovskaya V.V., Berezovsky A.V. *Corrosion-resistant steels and alloys.* Ekaterinburg. 2019, 244 p. [in Russian] https://elar.urfu.ru/bitstream/10995/75926/1/978-5-7996-2684-6_2019.pdf

5 Zhou, X., Wang X., Wang Q., Wu T., Li C., Luo J., Yin F. Study on Corrosion Behavior of Q235 Steel in a Simulated Marine Tidal Environment. *J. Mat. Eng. and Perf.,* 2022, Vol.31(6), pp. 4459-4471. https://doi.org/10.1007/s11665-021-06551-0

6 Quan B., Xie Zh. Study on corrosion behavior of Q235 Steel and 16MN steel by electrochemical and weight loss method. *Archives of Met. And Mat*., 2023, Vol.68(2), pp. 531-540. https://doi.org/10.24425/amm.2023.142432

7 Xue S., Shen R., Xue H., Zhu X., Wu Q., Zhang Sh. Failure analysis of high-strength steel wire under random corrosion. *Structures,* 2021, Vol.33, pp. 720-727. https://doi.org/10.1016/j.istruc.2021.04.082

8 Lu X.-H., Zhang F.-X., Yang X.-T., Xie J.-F., Zhao G.-X., Xue Y. Corrosion Performance of High Strength 15Cr Martensitic Stainless Steel in Severe Environments. *J. Iron and Steel Research. Int.,* 2014, Vol.21(8), pp. 774-780. https://doi.org/10.3390/cmd1010010

9 Dalmau A., Richard C., Igual-Munoz A. Degradation mechanisms in martensitic stainless steels: Wear, corrosion and tribocorrosion appraisal. *Tribology Intern*., 2018, Vol.121, pp. 167-179. https://doi.org/10.1016/j.triboint.2018.01.036

10 Kazum O., Kannan M.B., Beladi H., Timokhina I.B., Hodgson P.D., Khoddam S. Aqueous corrosion performance of nanostructured bainitic steel. *Mat. & Des.,* 2014, Vol.54, pp.67–71. https://doi.org/10.1016/j.matdes.2013.08.015

11 Berdibekov A.T., Khalenov O.S., Zinoviev L.A., Laurynas V.Ch., Gruzin, V.V., Dolya, A.V. Reason of corrosion of aluminium products in sea water. *Eurasian phys. tech. j.,* 2023. Vol.20, No.3(45), pp. 20 – 26. https://doi.org/10.31489/2023No3/20-26

.

12 Ershov N.S. *Resistance of stainless steels to pitting and crevice corrosion in seawater at elevated temperatures*. Candidate Diss. of the Techn. Science degree, Moscow, 1986, 167 p. [in Russian] https://www.dissercat.com/content/ustoichivost-nerzhaveyushchikh-stalei-k-pittingovoi-i-shchelevoi-korrozii-v-morskoi-vode-pri

13 Tretyakov Yu.D., Martynenko L.I., Grigoriev A.N., Tsivadze A.Yu. *Inorganic chemistry. Chemistry of elements.* Moscow, 2007, 537 p. [in Russian]. https://www.chem.msu.su/rus/books/2001-2010/tretyakov-inorg-2/welcome.html, https://vk.com/wall-155764560_7693

14 Koval, Yu.N., Lobodyuk, V.A. The Deformation Phenomena at Martensitic Transformations. *Usp. Fiz. Met.,* 2006, Vol.7, N.2. pp. 53-116. https://doi.org/10.15407/ufm.07.02.053

15 Mizutani U., Sato H. The Physics of the Hume-Rothery Electron Concentration Rule. *Crystals,* 2017. Vol.7, I.1, pp.9(1-112). https://doi.org/10.3390/cryst7010009

16 Mizutani U. *Hume-Rothery Rules for Structurally Complex Alloy Phases*. *CRC Press*. 2010, 356 p. https://doi.org/10.1201/b10324

17 Huheey J.E., Keiter E.A., Keiter R.L. *Inorganic Chemistry: Principles of Structure and Reactivity. 4th.* ed. *HarperCollins, New York, USA.* 1993, 964 p.

18 Greenwood N.N., Earnshaw A. *Chemistry of the Elements.* 2nd. ed. *Butterworth-Heinemann.* 1997, 1600 p.

19 Zabolotskii V.I., Shel'deshov N.V., Gnusin N.P. Dissociation of water molecules in systems with ion-exchange membranes. *Russian Chem. Rev*., 1988, Vol.57, I.8, pp. 801–808. https://doi.org/10.1070/rc1988v057n08abeh003389

20 Tubert-Brohman I., Guimaraes C.R.W., Repasky M.P., et al. Extension of the PDDG/PM3 and PDDG/MNDO semiempirical molecularorbital methods to the halogens. *J. Comp. Chem*., 2004, Vol.25. No.1, pp.138-150. https://doi.org/10.1002/jcc.10356

21 Stewaet J.P. Optimization of parameters for semiempirical methods 2. Applications. *J. Comp. Chem.,* 1989, Vol.10, No.2, pp.221-264. https://doi.org/10.1002/jcc.540100209

22 Tomashov N.D., Chernova G.P. *Theory of corrosion and corrosion-resistant structural alloys*. Moscow, Metallurgy, 1993, 358 p. [in Russian] https://masters.donntu.ru/2006/feht/marienkov/library/index.html

23 Pyzhyanova E.A., Zamyslovsky V.A., Remennikova M.V. Study of singlet oxygen formation in distilled water under the influence of laser radiation with a wavelength of 1.24 μ. *J. Comp. Chem.*, 2018, Vol.5, No.4, pp.297-309. [in Russian]. http://www.applied.photonics.pstu.ru/_res/fs/4424file.pdf

AUTHORS' INFORMATION

Baikenov, M.I. – Doctor of Chem. sciences, Professor, E.A. Buketov Karaganda University, Karaganda, Kazakhstan; ORCID ID: 0000-0002-8703-0397; Murzabek_b@mail.ru

Seldyugaev, O.B. – Candidate of Chem. sciences, junior researcher, E.A. Buketov Karaganda University, Karaganda, Kazakhstan; ORCID ID: 0009-0004-9729-1015; oleg.seldyugaev@gmail.com

Guchenko, S.A. – Master (Sci.), Junior researcher, E.A. Buketov Karaganda University, Karaganda, ORCID ID: 0000-0002-9954-5478; guchen@mail.ru

Afanasyev, D.A. – PhD, Professor, E.A. Buketov Karaganda University, Karaganda, Kazakhstan; ORCID ID: 0000-0002-0437-5315; a.d.afanasyev2@gmail.com

EURASIAN PHYSICAL TECHNICAL JOURNAL

2024, Volume 21, No. 1 (47)

https://doi.org/10.31489/2024No1/49-56

Received: 31/01/2024 Revised: 27/02/2024 Accepted: 14/03/2024 Published online: 29/03/2024

Research Article

UDC535.37

INFLUENCE OF PLASMON EFFECT ON THE SENSITIZATION OF TITANIUM DIOXIDE BY DYE MOLECULES

Omarova G.S., Serikov T.M., Seliverstova E.V.*, Auzhanova A.A., Ibrayev N.Kh.

Institute of Molecular Nanophotonics, Karaganda Buketov University, Karaganda, Kazakhstan
*Corresponding author: genia_sv@mail.ru

Abstract. *The influence of the plasmon effect of metal nanoparticles on electron transfer from Eosin and Rhodamine B dyes to TiO_2 was studied. Spectral-kinetic measurements showed that, compared to SiO_2, not only the intensity but also the fluorescence lifetime of both dyes decreases on the TiO_2 surface, which indicates the charge transfer from the dye to the semiconductor. In the presence of core@shell ($Ag@TiO_2$) plasmon nanostructures, an intensification of the fluorescence of both dyes is observed, as well as a decrease in the duration of the dyes emission. The optimal concentration for which the maximum plasmon effect was recorded is 3 wt% of $Ag@TiO_2$. The plasmon effect also leads to an increase in the efficiency of sensitization of the semiconductor by molecules of the dyes under study, which is expressed as an increase in the photovoltaic and charge-transport characteristics of the semiconductor films. The results obtained on the plasmon effect on the charge transfer process in the dye/semiconductor system can be used in the development of devices for photovoltaics, photocatalytic, and optoelectronic elements.*

Keywords: semiconductor, dye, core@shell nanostructure, plasmon effect, charge transfer, sensitization.

1. Introduction

Solar energy is one of the most widespread energy resources on our planet, which far exceeds the total needs of Earth [1]. Solar energy can be converted into electrical energy [2,3], obtain an environmentally friendly and economically profitable fuel – hydrogen, and effectively purify water resources from various pollutants [4,5]. In photovoltaic elements based on semiconductors and their sensitizers, the main processes are the absorption of light and its further transformation through photoinduced charge separation at the semiconductor/dye interface [6-9].

The process of generation and transfer of photoinduced charge carriers between dye molecules and a semiconductor plays a key role in the efficiency of photovoltaic systems [10-13]. One of the ways to increase their efficiency is to improve the absorption of light by both a semiconductor and its sensitizer, as well as creating of conditions for the effective separation of electron-hole pairs in such a system. A promising strategy for enhanced performance of photovoltaic systems is the integration of plasmon nanoparticles of metal (NPs) into the working electrode of device. This makes it possible to significantly increase the light-harvesting characteristics of the sensitizing layers [14-18] without affecting their functionality.

Metal NPs are characterized by strong interaction with incident photons through the excitation of localized surface plasmon resonance (LSPR), which can facilitate the transfer of energy and/or electrons from the NPs to both the sensitizer and the semiconductor. After the LSPR excitation, an enhanced electromagnetic field is formed around the NPs, which affects on the rate of intramolecular transitions of

sensitizer molecules [19,20]. Currently, a limited number of works are devoted to a comprehensive analysis of the interaction in the "dye/semiconductor/plasmonic NPs" systems. For example, the method of the model Hamiltonian was used in Ref. [21], which includes the processes of plasmon-induced energy transfer (PIRET) and charge-transfer (PICT) processes from the Au NPs to the dye molecules. It was found that PIRET deforms the dynamics of the wave packets of the excited state of the molecule. It led to the increased absorption and growth of the electron density in the LUMO orbitals of the dye molecule, which leads to a 10-fold improvement in the separation of charge carriers. A PIRET from plasmonic NPs to dye molecules was also studied in [22]. It has been shown that PIRET leads to the delayed photoluminescence in metal-conjugated fluorophores. The observed increase in the fluorescence lifetime in metal-conjugated fluorophores was confirmed by theoretical calculations. The delayed luminescence of the dye indicates a longer stay of the molecule in the excited state, which will increase the probability of electron and/or energy transfer to the semiconductor.

By the authors of [18] the electron injection kinetics from a dye into mesoporous TiO_2 layers has been studied. Multistage ultrafast electron injection in the time range of 300-400 fs was shown. The introduction of Ag NPs led to ultrafast and enhanced electron injection and a decrease in charge recombination dynamics. In this paper, the concentration dependence of the plasmon effect of Ag NPs on the sensitization process of TiO_2 semiconductor films was investigated. The influence of the core@shell ($Ag@TiO_2$) nanostructures (NSs) on various ways of the enhancement of the efficiency of charge carriers transfer and transport in the "dye/semiconductor" system is considered.

The choice of the core@shell NSs is due to the fact that often organic dyes and electrolyte is used in photovoltaic systems to regenerate dye molecules. In the electrolyte plasmonic NPs can degrade or form an oxide layer on the surface, which reduces the LSPR effect. Core@shell NSs will protect the metal NPs from oxidation by electrolyte. Also, the presence of a semiconductor shell will avoid the occurrence of recombination processes between the metal NPs and the dye.

2. Experimental part

To study the dynamics of charge transfer at the "semiconductor/dye" interface, two types of semiconductors as SiO_2 (Silufol) and TiO_2 (Sigma Aldrich) were selected, and Rhodamine B (RB) and Eosin as dyes. Semiconductor films with an area of 2 cm^2 were obtained. Next, a 1 mL of dye solution with a concentration of 10^{-4} mol/L was dropped on the surface of SiO_2 and TiO_2 films. After that, the samples were dried at room temperature for 2 hours.

To study charge transfer at the "semiconductor/dye" interface in the plasmon field $Ag@TiO_2$ NSs were synthesized, where the core is the Ag NPs and shell is TiO_2. NSs were obtained according to the method of [23]. In detail, the synthesis of $Ag@TiO_2$ NSs was carried out according to the following method. First, cores were synthesized – Ag NPs. To do this, 0.1 mmol of $AgNO_3$ (99.8%, Sigma Aldrich) is added to a solution of polyvinylpyrolidone (PVP, Sigma Aldrich) in ethylene glycol (0.5 g per 25 mL). Next, the mixture is heated with intensive stirring at 50°C for 10 minutes, after which the temperature is increased to 120°C and heated for another 30 minutes. During the reaction, the solution turned yellowish-brown, which indicates the formation of silver NPs. The obtained Ag NPs are separated from ethylene glycol by centrifugation (8000 rpm, 30 min) and washed several times sequentially with acetone and ethanol. In this way, the Ag NPs are converted to absolute ethanol, and then a TiO_2 shell is synthesized around the obtained Ag NPs. To do this, a solution of titanium tetraisopropoxide ($Ti(OCH(CH_3)_2)_4$, TIPT, Sigma Aldrich) is added to the solution of plasmonic NPs with intensive stirring. The volume ratio of TIPT and Ag NPs was equal to 1:10, respectively. The formation of titanium dioxide occurs as a result of the following chemical reaction [22]:

$$Ti(OCH(CH_3)_2)_4 + C_2H_5OH \rightarrow TiO_2 + 4(CH_3)_2CHOH$$

The resulting mixture was shaken for 24 hours on a multifunctional rotator at room temperature in the dark. The formation of a TiO_2 shell around the Ag NPs was checked both by changing the size of the metal NPs before and after the addition of TIPT using dynamic light scattering (Zetasizer Nano ZS analyzer, Malvern). Measurements showed that the average diameter of the Ag NPs were 26±7 nm (Figure 1a), and the $Ag@TiO_2$ NSs were 44±18 nm (Figure 1b). That is, the average thickness of the shell is ~9 nm. The uniformity of the coating of silver NPs with a semiconductor shell was studied using scanning electron

microscopy (SEM, Mira 3LMU, Tescan). As the SEM studies have shown, the TiO_2 shell evenly covers the synthesized silver NPs. The obtained Ag@TiO_2 NSs have a spherical shape.

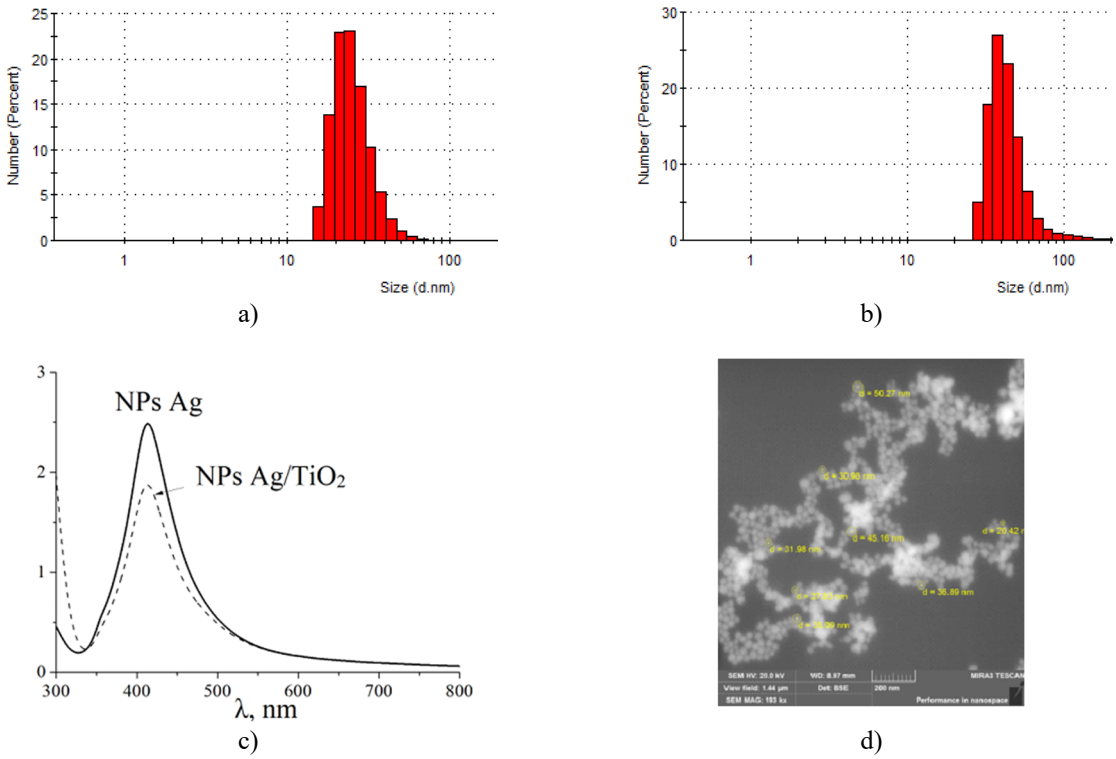

Fig.1. Size distribution (a, b) and absorption (c) spectrum of Ag NPs before shell synthesis (a) and NSs Ag@TiO_2 (b), as well as SEM image (d) of Ag@TiO_2 NSs

The resulting NSs were doped into the semiconductor layers. The concentration of Ag@TiO_2 NSs in TiO_2 paste was equal to 1, 2, 3 or 5 wt%. The samples obtained are designated as TCS-1 (TiO_2+core@shell, 1wt%), TCS-2, TCS-3 and TCS-5. The registration of the fluorescence lifetime of dyes in the time-correlated photon counting mode was performed with the Becker&Hickl TCSPC system. The samples were excited by a femtosecond FX200 laser (SolarLS) with λ= 515 nm and pulse duration of τ = 150 fs. The fluorescence lifetime was estimated using the SPC Image software [24] according to the procedure described in [24-26].

Dye-sensitized solar cells (DSSC) were assembled to study the effectiveness of sensitization of titanium dioxide by excited states of dyes. For this purpose, a working electrode of TiO_2 or TSC was formed on the surface of FTO-coated glasses (8 Ohms/cm^2, Sigma-Aldrich). Electrochemically deposited Pt was used as the counter electrode [27]. An iodide/triiodide electrolyte (Iodolyte Z-150, Solaronix) was used as the electrolyte. The sorption of Eosin or RB was carried out within 24 hours from an ethanol dye solution with a concentration of 10^{-4} mol/L. The DSSC was assembled according to the works of [10, 27–29]. The photovoltaic parameters of the cells were obtained from the curent-voltage characteristics recorded with solar radiation simulator CT150AAA (PET Photo Emission Tech.) at AM 1.5. The source power is 100 mW/cm^2. The charge-transport properties of the prepared films were estimated from impedance spectroscopy data in the frequency range from 1 to 100 MHz using a potentiostat/galvanostat with an integrated EIS analyzer (CS350, Corrtest Instr.). Based on the data obtained with the using of the equivalent scheme (Figure 2), the following parameters were evaluated [16, 30]: effective lifetime of charge carriers $\tau_{eff.}$, resistance to the electron transport in the material R_s(R_1) and R_k is the resistance of charge carriers' transport.

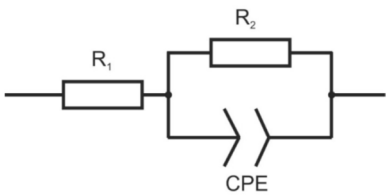

Fig.2.Equivalent electrical circuit for DSSC analysis.

3. Results and discussion

The main condition for effective sensitization of a semiconductor by dye molecules is the location of its LUMO orbital above the bottom of the TiO_2 conduction band (CB) on the energy scale. As can be seen from Figure 3, both RB and Eosin satisfy this condition. The values of HOMO/LUMO levels from the Refs. [31,32] were used to plot the diagram. The CB of SiO_2 is located higher than the LUMO level of RB or Eosin. Therefore, when the dyes are photoexcited, the charge transfer from the dyes to SiO_2 will not occur.

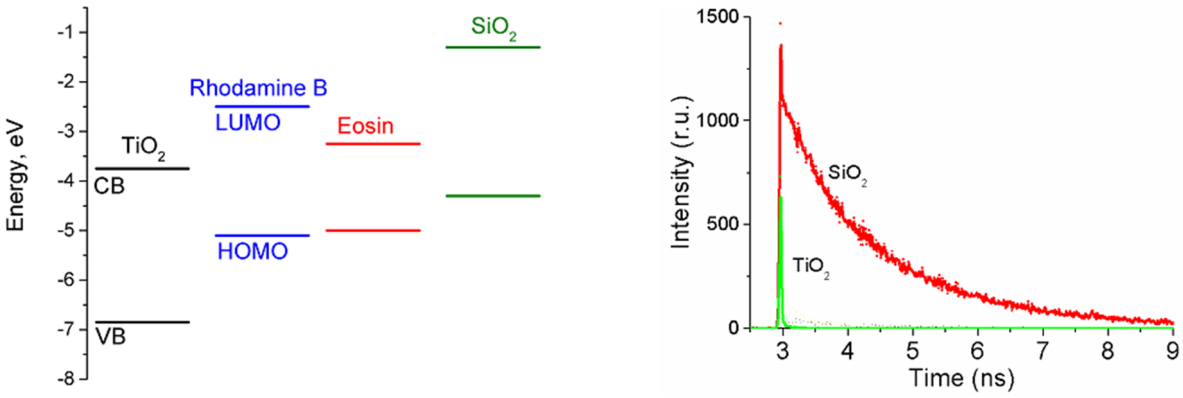

a) b)

Fig.3. (a) Energy diagram for the TiO_2 and dyes; (b) fluorescence decay kinetics of Eosin on the surface of porous SiO_2 or TiO_2 films.

In ethanol solution, the maximum of absorption band of RB exhibits at 545 nm, and the maximum of fluorescence band is at 565 nm. For Eosin, these parameters are at 525 and 545 nm.

Measurements of the spectral luminescent properties of dyes have shown that in the adsorbed state, the absorption and fluorescence spectra of RB are bathochromically shifted on the surface of SiO_2 (~20 nm compared with the dye solution in ethanol). On the surface of TiO_2, the absorption and fluorescence bands of both dyes undergo to hypsochromic shift (~5 nm compared with the dye solution in ethanol). At the same time, the fluorescence spectra of the dye are broadened.

The efficiency of charge transfer from dyes to a semiconductor was estimated from the fluorescence decay kinetics (Figure 3, Table 1). The fluorescence decay kinetics is bi-exponential. It can be seen from the data that not only the intensity, but also the lifetime of the luminescence of both dyes decreases on the surface of TiO_2. At the same time, the luminescence intensity was decreased by 1.95 times for RB, and by almost 52 times for Eosin. The average fluorescence lifetime $<\tau_{fl}>$ of RB in the presence of TiO_2 was decreased by 4.2 times. Whereas for Eosin, this ratio is equal to 7.1 times.

Table 1. Integral intensity (I) and lifetime (τ)* of fluorescence of dyes on the surface of porous SiO_2 or TiO_2 films

Sample	I (r.u.)	$<\tau_{fl}>$ (ns)	τ_1 (ns)	A_1 (%)	τ_2 (ns)	A_2 (%)
RhB						
SiO_2	128.12	1.55±0.01	0.950±0.01	59.0	2.30±0.01	41
TiO_2	65.65	0.37±0.01	0.156±0.01	79.0	0.99±0.01	21
Eosin						
SiO_2	1705.04	1.49±0.01	0.995±0.01	54.3	2.09±0.01	45.7
TiO_2	32.88	0.21±0.01	0.130±0.01	81.0	0.556±0.01	19.0

*$<\tau_{fl}>$ – average lifetime of fluorescence estimated form the equation $\langle \tau_{fl} \rangle = \sum_{i=1}^{n} A_i \tau_i$, where τ_i is the lifetime of the i-th component of fluorescence decay, A_i is the magnitude (the part of contribution) of i-th component of fluorescence decay ($\sum_i A_i$ =1,0).

The observed quenching of the fluorescence lifetime indicates the electron transfer from an excited dye molecule to a semiconductor [31]. In the case of Eosin, charge transfer from the dye to the semiconductor is carried out more efficiently.

A pure TiO_2 film, which was not sensitized with a dye, demonstrates a low-intensity signal associated with scattered radiation. The lifetime of such signal is ~10 ps, which is associated with the instrumental response function (IRF) of the measuring system. Since the wavelength of the exciting laser does not coincide in position with the absorption of TiO_2, the recorded signal can be considered as a background signal. When the Eosin and Rhodamine were adsorbed into TiO_2 films without plasmon NSs, the duration of the recorded signal from the dye was on an order of magnitude longer.

Measurements showed that in the presence of plasmon NSs, an intensification of fast fluorescence of both RB and Eosin is observed (Table 2). Changes in the fluorescence intensity of the dye registered at various concentration of core@shell NSs have a nonlinear character with a maximum at 3 wt% for RB and Eosin. At the same concentrations, the maximum reduction in the fluorescence lifetime of the dye is observed. A further increase in the content of plasmonic NSs in the film leads to a decrease in the intensity enhancement of the dyes and the restoration of the luminescence lifetimes to its original value.

Table 2. Effect of Ag@TiO_2NSs concentration in TiO_2 film on the intensity (I) and average fluorescence lifetime ($<\tau_{fl}>$) of dyes.

Core@shell concentration(wt%)	I (r.u.)	I_{TCS}/I_0	$<\tau_{fl}>$ (ns)	$<\tau_{fl\ TCS}>/<\tau_{fl}>$
RB				
TiO_2 neat	12.2	–	0.01	–
TiO_2	65.7	–	0.370±0.01	–
TCS-1	250.3	3.8	0.367±0.01	0.99
TCS-2	281.6	4.3	0.323±0.01	0.87
TCS-3	329.3	5.0	0.299±0.01	0.80
TCS-5	321.1	4.9	0.327±0.01	0.88
Eosin				
TiO_2 neat	12.2	–	0.01	–
TiO_2	32.89	–	0.210±0.01	–
TCS-1	86.7	2.6	0.205±0.01	0.98
TCS-2	124.7	3.8	0.200±0.01	0.95
TCS-3	136.7	4.2	0.190±0.01	0.90
TCS-5	131.2	4.0	0.207±0.01	0.99

The observed increase in the fluorescence intensity of dyes is associated with a plasmon enhancement of the radiative rate of fluorophore molecules in the near field of plasmon NPs, as shown in Ref. [25,33]. The decrease in fluorescence enhancement may be result of two factors. The first of them relates to the quenching of the fluorophore by plasmon NPs through the Förster energy transfer [25,33]. The second channel can be associated with a plasmon enhancement of the quenching of dye molecules by electron transfer to the CB of a semiconductor.

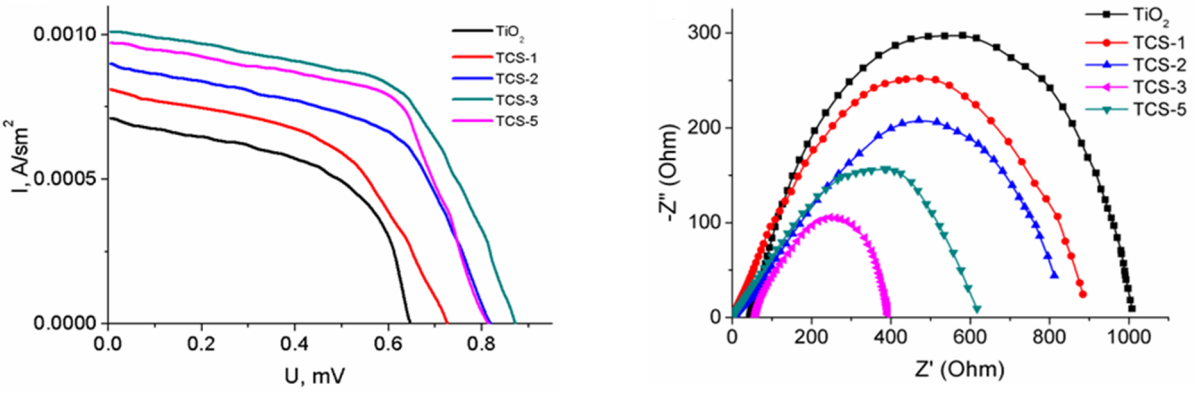

a) b)

Fig.4.The effect of the concentration of the core@shell NSs on the CVC (a) and impedance spectra (b) of DSSCs sensitized by Eosin.

To detail these channels, the photovoltaic and charge-transport properties of DSSCs with the addition of plasmon NSs sensitized by RB or Eosin were estimated. In the absence of plasmon NSs in the TiO_2 film, the current density, which is directly related to the number of photogenerated charge carriers in the working electrode, is equal to 0.0007 A/cm^2 and 0.00088 A/cm^2 for Eosin and Rhodamine B, respectively (Figure4, Table 3).

Table 3. Effect of the concentration of Ag@TiO_2 NSs in the TiO_2 film on the photovoltaic and charge-transport parameters of DSSCs sensitized by RB or Eosin.

Sample	U_{oc} (mV)	J_{sc} (A/cm^2)	Efficiency (%)	R_s(Ohm)	R_p(Ohm)	τ_{eff}(s)
RB						
TiO_2	64.00	0.00088	0.0047	15.00	1000	0.36
TCS-1	71.00	0.00089	0.0068	18.00	820	0.27
TCS-2	72.00	0.00100	0.0072	21.00	580	0.24
TCS-3	77.00	0.00110	0.014	23.00	190	0.22
TCS-5	80.00	0.00109	0.0074	26.00	250	0.26
Eosin						
TiO_2	65.00	0.00070	0.0010	25.00	1008	0.32
TCS-1	72.00	0.00080	0.0018	13.00	900	0.24
TCS-2+ Eosin	81.00	0.00090	0.0027	12.00	810	0.22
TCS-3+ Eosin	87.00	0.00098	0.025	35.00	400	0.18
TCS-5+ Eosin	82.00	0.00110	0.021	8.00	600	0.22

The addition of Ag@TiO_2 NSs leads to an increase in the values of the short-circuit current density. This is reflected in the increased efficiency of DSSCs. The maximum increase in the efficiency of solar cells was recorded at an Ag/TiO_2 concentration equal to 3 wt% for both dyes. Impedance measurements and estimation of electrophysical parameters have shown that the resistance and effective lifetime of charge carriers τ_{eff} in the TiO_2 film decreases under the influence of the plasmon effect of Ag NSs. Thus, the R_s resistance of TCS-3+dye films are almost in 2.5 times and 5 times less for Eosin and RB, respectively, than in TiO_2+dye samples. The resistance to electronic transport of films decreased from 1008 to 400 Ohms for Eosin and from 1000 to 190 Ohms for Rhodamine.

Thus, it can be seen that the addition of core@shell NSs to the volume of the semiconductor leads to a reduction in the lifetime of charge carriers in the semiconductor, preventing their recombination. This is reflected in an increase in the efficiency of electron migration and counting from the semiconductor surface, leading to an increase in the photocurrent density and an increase in efficiency of DSSCs.

4. Conclusions

The plasmon effect of metal nanoparticles on electron transfer to TiO_2 from Eosin and RB dyes has been studied. Spectral-kinetic measurements have shown that, compared with SiO_2, not only the intensity but also the duration of fluorescence of both dyes decreases on the surface of TiO_2. At the same time, in the case of Eosin, charge transfer from the dye to the semiconductor is carried out more efficiently. In the presence of plasmonic NSs, an intensification of fast fluorescence of both dyes is observed, as well as a decreasing in the luminescence lifetimes. The optimal concentration for which the maximum plasmon effect was recorded is equal to 3 wt% of Ag/TiO_2 NSs. The observed increase in the intensity and decrease in the fluorescence lifetimes of dyes is associated with a plasmonic enhancement in the radiative rate in dyes molecules in the near field of plasmonic NSs. Measurements of electrophysical parameters have shown that the plasmon effect also leads to an increase in the efficiency of semiconductor sensitization by molecules of the studied dyes, which is expressed in an increase in the photovoltaic and charge-transport characteristics of the studied semiconductor films. Detailed establishment of the ways of exposure of plasmonic NPs on various ways of sensitization enhancement of the TiO_2 by dye molecules will be studied in our further research.

Conflict of interest statement
The authors declare that they have no conflict of interest in relation to this research, whether financial, personal, authorship or otherwise, that could affect the research and its results presented in this paper.

CRediT author statement:
Omarova G.S.: investigation, data curation; Serikov T.M.: methodology, investigation, formal analysis, writing - original draft; Seliverstova E.V.: validation, formal analysis, writing - original draft, writing - review & editing; Auzhanova A.A.: investigation; Ibrayev N.Kh.: conceptualization, writing - original draft, writing - review & editing.
The final manuscript was read and approved by all authors.

Funding
This research is funded by the Science Committee of the Ministry of Science and Higher Education of the Republic of Kazakhstan (Grant No. AP19680241).

References

1 Pourasl H.H., Barenji R.V., Khojastehnezhad V.M. Solar energy status in the world: A comprehensive review. *Energy Reports*, 2023, Vol. 10, pp. 3474 – 3493. https://doi.org/10.1016/j.egyr.2023.10.022

2 Chiarello G.L., Dozzi M.V., Selli E. TiO_2–based materials for photocatalytic hydrogen production. *Journal of Energy Chemistry*. 2017, Vol. 26(2), pp. 250–258. https://doi.org/10.1016/j.jechem.2017.02.005

3 Ibrayev N., Seliverstova E., Aimukhanov A., Serikov T. Role of energy transfer in conversion of light to electric energy. *Molecular Crystals and Liquid Crystals.* 2014, Vol. 589, pp. 202 – 208. https://doi.org/10.1080/15421406.2013.872827

4 Sun X.Y., Wang C.Y., Su D.W., Wang G., Yunhao Z. Application of photocatalytic materials in sensors. *Advanced Materials Technologies,* 2020, Vol. 5, pp.1900993. https://doi.org/10.1002/admt.201900993

5 Tong H, Ouyang S.X., Bi Y.P., Umezawa N., Oshikiri M., Ye J. Nano-photocatalytic materials: possibilities and challenges. *Advanced Materials.* 2012, Vol. 24, pp. 229 – 251. https://doi.org/10.1002/adma.201102752

6 Clifford J.N., Martínez–Ferrero E., Viterisi A., Palomares E. Sensitizer molecular structure–device efficiency relationship in dye sensitized solar cells. *Chemical Society Reviews.* 2011, Vol. 40(3), pp. 1635 – 1646. https://doi.org/10.1039/B920664G

7 Ardo S., Meyer G.J. Photo-driven heterogeneous charge transfer with transition–metal compounds anchored to TiO_2 semiconductor surfaces. *Chemical Society Reviews.* 2009, Vol. 38(1), pp. 115-164. https://doi.org/10.1039/B804321N

8 Haque S.A., Palomares E., Cho B.M., Green A. N. M., Hirata N., Klug D. R., Durrant, J. R. Charge separation versus recombination in dye–sensitized nanocrystalline solar cells: the minimization of kinetic redundancy. *Journal of the American Chemical Society.* 2005, Vol. 127(10), pp. 3456 – 3462. https://doi.org/10.1021/ja0460357

9 Anderson N.A., Lian T.Q. Ultrafast electron transfer at the molecule–semiconductor nanoparticle interface. *Annual Review of Physical Chemistry.* 2005, Vol. 56(1), pp. 491–519. https://doi.org/10.1146/annurev.physchem.55.091602.094347

10 Regan B.O., Grätzel M. A low-cost, high-efficiency solar cell based on dye sensitized colloidal TiO_2 films. *Nature*. 1991, Vol. 353(6346), pp. 737 – 740. https://doi.org/10.1038/353737a0

11 Hagfeldt A., Boschloo G., Sun L., Kloo L., Pettersson H. Dye-sensitized solar cells. *Chemical Reviews,* 2010, Vol. 110(11), pp.6595 – 6663. https://doi.org/10.1021/cr900356p

12 Listorti A., O'Regan B., Durrant J. R. Electron transfer dynamics in dye sensitized solar cells. *Chemistry of Materials.* 2011, Vol. 23, pp. 3381. https://doi.org/10.1021/cm200651e

13 Wang J., Liu K., Ma L., Zhan X. Triarylamine: Versatile platform for organic, dye-sensitized, and perovskite solar cells. *Chemical Reviews.* 2016, Vol. 116(23), pp. 14675 – 14725. https://doi.org/10.1021/acs.chemrev.6b00432

14 Zhou N., López-Puente V., Wang Q., Polavarapu L., Pastoriza-Santos I., Xu Q.-H. Plasmon-enhanced light harvesting: applications in enhanced photocatalysis, photodynamic therapy and photovoltaics. *RSC Advances.* 2015, Vol. 5, pp. 29076-29097. https://doi.org/10.1039/C5RA01819F

15 Adnan A., Fedwa E., Anirban M., Brahim A. Research progress of plasmonic nanostructure-enhanced photovoltaic solar cells. *Nanomaterials.* 2022, Vol. 12(5), pp. 788. https://doi.org/10.3390/nano12050788

16 Ibrayev N., Omarova G., Seliverstova E., Ishchenko A., Nuraje N. Plasmonic effect of Ag nanoparticles on polymethine dyes sensitized titanium dioxide. *Engineered Science.* 2021, Vol. 14, pp. 69 – 77. https://doi.org/10.30919/es8d1168

17 Jiang N., Zhuo X., Wang J. Active plasmonics: principles, structures and applications. *Chemical Reviews,* 2018, Vol. 118(6), pp. 3054 – 3099. https://doi.org/10.1021/acs.chemrev.7b00252

18 Biswas C, Ahmed S., Santosh S., Kumar R.S.S. Ultrafast electron injection kinetics and effect of plasmonic silver nanoparticle at organic dye-TiO_2 interface. *Asian Journal of Physics.* 2021, Vol. 30(6), pp. 933 – 945. https://doi.org/10.54955/AJP.30.6.2021.933-945

19 Geddes C.D., Lakowicz J.R. Metal–enhanced fluorescence. *Journal of Fluorescence,* 2002, Vol. 12, pp. 121 – 129. https://doi.org/10.1023/A:1016875709579

.

20 Maier S.A. *Plasmonics fundamentals and applications*. NY, Springer, 2007, 209p. https://doi.org/10.1007/0-387-37825-1

21 Zhang B., Zhao Y., Liang W. Collaborative effect of plasmon-induced resonance energy and electron transfer on the interfacial electron injection dynamics of dye-sensitized solar cell. *The Journal of Chemical Physics.*2019, Vol.151(4), pp. 044702. https://doi.org/10.1063/1.5111601

22 Yang M., Moroz P., Jin Z., Budkina D. S., Sundrani N., Porotnikov D., Zamkov M. Delayed photoluminescence in metal-conjugated fluorophores. *Journal of the American Chemical Society,* 2019, Vol. 141(28), pp. 11286 – 11297. https://doi.org/10.1021/jacs.9b04697

23 Afanasyev D.A., Ibrayev N.Kh., Serikov T.M., Zeinidenov A.K. Effect of the titanium dioxide shell on the plasmon properties of silver nanoparticles. *Russian Journal of Physical Chemistry A.* 2016, Vol. 90(4), pp. 833 – 837. https://doi.org/10.1134/S0036024416040026

24 Becker W. *The BH TCSPC e-Handbook*, 2023. https://www.becker-hickl.com/literature/documents/flim/the-bh-tcspc-handbook

25 Ibrayev N.Kh., Seliverstova E. V., Valiev R. R., Kanapina A. E., Ishchenko A. A., Kulinich A. V., Kurten T., Sundholm D. Influence of plasmons on the luminescence properties of solvatochromicmerocyanine dyes with different solvatochromism. *Physical Chemistry Chemical Physics.* 2023, Vol. 25, pp. 22851 – 22861. https://doi.org/10.1039/D3CP03029F

26 Kanapina A.E., Seliverstova E.V., Ibrayev N.K., Derevyanko N.A., Ishchenko A.A. Features of the decay of excited states of ionic dyes in the near field of metal nanoparticles. *Eurasian Physical Technical Journal.* 2023, Vol. 20, No. 2(44), pp. 106 – 111. https://doi.org/10.31489/2023NO2/106-111

27 Ibrayev N.Kh., Seliverstova E.V., Omarova G.S., Derevyanko N.A., Khamza T., Photovoltaic properties of functionalized indodicarbocyanine dye. *Eurasian Physical Technical Journal,* 2022, Vol. 19(3), pp. 55–59. https://doi.org/10.31489/2022No3/55-59

28 Ito S., Murakami T.N., Comte P., Liska P., Grätzel C., Nazeeruddin M.K., Grätzel M. Fabrication of thin film dye sensitized solar cells with solar to electric power conversion efficiency over 10%. *Thin Solid Films,* 2008, Vol.516(14), pp. 4613 – 4619. https://doi.org/10.1016/j.tsf.2007.05.090

29 Yang C.C., Zhang H., Zheng Y. DSSC with a novel Pt counter electrodes using pulsed electroplating techniques. *Current Applied Physic.* 2011, Vol. 11, pp. S147-S153. https://doi.org/10.1016/j.cap.2010.11.012

30 Bisquert J., Garcia-Belmonte G., Fabregat-Santiago F., Bueno P.R. Theoretical models for ac impedance of finite diffusion layers exhibiting low frequency dispersion. *Journal of Electroanalytical Chemistry.* 1999, Vol. 475, pp.152 – 63. https://doi.org/10.1016/S0022-0728(99)00346-0

31 Zhang F., Shi F., Ma W., Gao F., Jiao Ya. Controlling adsorption structure of Eosin Y dye on nanocrystalline TiO_2 films for improved photovoltaic performances. *The Journal of Physical Chemistry C,* 2013, Vol. 117. pp. 14659 – 14666. https://doi.org/10.1021/jp404439p

32 Kim H., Do–Hyun L., Son Y. Electrochemical study on Rhodamine 6G–indole, based dye for HOMO and LUMO energy levels. *Textile Coloration and Finishing*. 2013, Vol.25(1), pp. 83 – 88. https://doi.org/10.5764/TCF.2013.25.1.7

33 Seliverstova E., Ibrayev N., Omarova G., Ishchenko A., Kucherenko M. Competitive influence of the plasmon effect and energy transfer between chromophores and Ag nanoparticles on the fluorescent properties of indopolycarbocyanine dyes. *Journal of Luminescence.* 2021, Vol. 235, p. 118000. https://doi.org/10.1016/j.jlumin.2021.118000

AUTHORS' INFORMATION

Ibrayev, N.Kh. – Doctor of Phys. and Math. Sciences, Professor, Director of the Institute of Molecular Nanophotonics, E.A. Buketov Karaganda University, Karaganda, Kazakhstan; ORCID iD: 0000-0002-5156-5015; niazibrayev@mail.ru

Omarova, G.S.– PhD, Associate Professor, E.A. Buketov Karaganda University, Karaganda, Kazakhstan; ORCID iD: 0000-0003-2900-2168; guldenserikovna@mail.ru

Serikov, T.M. – PhD, Associate Professor, E.A. Buketov Karaganda University, Karaganda, Kazakhstan; ORCID iD: 0000-0003-4302-96744; serikov-timur@mail.ru

Seliverstova, E.V. – PhD (Phys.), Senior Research Fellow, Institute of Molecular Nanophotonics, E.A. Buketov Karaganda University, Karaganda, Kazakhstan; ORCID iD: 0000-0002-9507-8825; genia_sv@mail.ru

Auzhanova, A.A.– Master student, E.A. Buketov Karaganda University, Karaganda, Kazakhstan; ORCID iD: 0009-0002-3963-6367; aliya26122001@gmail.com

EURASIAN PHYSICAL TECHNICAL JOURNAL

2024, Volume 21, No. 1 (47)

https://doi.org/10.31489/2024No1/57-66

Received: 11/10/2023 Revised: 08/02/2024 Accepted: 27/02/2024 Published online: 29/03/2024

Research Article

UDC: 538.953; 621.039.587

ANALYSIS OF METHODS FOR SIMULATING THE DECAY HEAT IN CORIUM WHEN MODELING A SEVERE ACCIDENTS AT NUCLEAR POWER PLANT

Skakov M.K.[1], Baklanov V.V.[2], Nurpaissova G.S.[2,3]*, Akaev A.S.[2], Bekmuldin M.K.[2], Toleubekov K.O.[2]

[1] National Nuclear Center of the Republic of Kazakhstan, Kurchatov, Kazakhstan
[2] Institute of Atomic Energy of the National Nuclear Center of the Republic of Kazakhstan, Kurchatov, Kazakhstan
[3]Shakarim University, Semey, Kazakhstan
*Corresponding author: nurpaissova@nnc.kz

Abstract. *It is known that during development of a severe accident at a nuclear power plant, the melting of core materials and the formation of corium occurs. A feature of corium is the presence of a decay heat, which contributes a lot to the nature of its interaction with the structural materials of the reactor facility. In this regard, quite serious requirements are imposed on methods for simulating decay heat in the corium prototype, which relate to both the uniformity of the volume distribution and its intensity. This paper presents a comparative analysis of existing methods for decay heat simulation in corium, which are used at various experimental facilities investigating the operation of passive protection systems in severe accidents with reactor meltdown at nuclear power plants. By comparing the advantages and disadvantages, a more practical method of decay heat simulation is determined and ways are proposed to further improve the chosen method to fully simulate the thermal field of a real corium.*

Keywords: nuclear power plant, severe accident, corium, decay heat, simulation

1. Introduction

One of the main directions of the development of nuclear energy safety is the research of the final stage of a severe accident at a nuclear power plant (NPP) with core meltdown. During the melting of the reactor core, the so-called corium is formed - a melt of a radioactive mixture of uranium oxide, zirconium, zirconium oxides and steel components (products of high-temperature interaction of metals with an oxidizing medium) and other structural elements [1]. A special feature of corium is a large amount of stored energy and the presence of residual energy release due to the fact that the nuclear fuel contained in the corium continues to be a source of heat released due to the decay reactions of fission fragments of ^{235}U nuclei accumulated during the operation of the reactor, which allows the melt to remain in a liquid state for a long time and melt the reactor structure with its subsequent release down to the ground and groundwater [2-3].

The contribution of residual energy release to the thermal state of the corium was noted in [4]. This work examines the influence of the accuracy of determining the residual energy release during neutronics calculations on the results of thermal calculations. Analysis of the results shows that the amount of power of the residual energy release affects the value of the maximum temperature. Thus, it was found that a change in the power of the residual energy release by 5% leads to a significant change in the temperature field,

which in turn affects the nature of the interaction of the corium with various structural elements. In this regard, it is obvious that in order to ensure physical modeling conditions that are as close as possible to full-scale ones, it is necessary to take into account not only the correspondence of the composition of the corium prototype to the real one, but also the amount of energy release in the melt at a given level. Currently, two methods of obtaining corium during experiments exists: in-pile and out-of-pile.

In the first case, for research aimed at studying the physical and mechanical properties of corium, the so-called "model corium" is obtained under in-pile test conditions. The peculiarity of the model corium is that it is obtained due to the decay heat of nuclear fuel contained in the composition of corium [5].

In the second case, in experiments on physical modeling of processes occurring in severe accidents, the so-called "prototype corium" is used, a substitute whose characteristics are close to real corium in most parameters, but do not create a dose load on personnel (hereinafter corium is understood as prototype corium) [6]. Since in experiments with prototype corium it is not possible to maintain the temperature of corium within the specified limits due to radioactive decay, this process is carried out by external energy supply to the corium melt using various devices. In this regard, the device providing energy input into the simulator melt should simulate the fission reaction both in magnitude and in the nature of its distribution through the volume of corium.

The purpose of this work is to conduct a comparative analysis of all existing methods of a decay heat simulation to determine the optimal way to fully simulate the thermal field of a real corium.

2. Practical methods of a decay heat simulation during various tests with corium

Experiments to study the interaction between corium and various structural elements of a nuclear power plant began after the accident at the Three Mile Island NPP. At the same time, over the entire period of this type of research, a number of different experimental installations of different designs and devices have been created to simulate residual energy release. As an example, we can cite such methods of decay heat simulation used in experimental installations as methods of direct transmission of electric current through the melt (DEH) [7], induction heating [8], heating using thermite mixtures [9], indirect electric arc heating [10], etc.

2.1 Direct electric heating (DEH)

Simulation of a decay heat in corium by direct transmission of electric current (DEH) was used in the first experiments to study the interaction of the corium with various structural elements. Some examples in this regard are the series of ACE/MC, MAKE and NEAM SI experiments [11]. These experiments allowed specialists to obtain a lot of information about the interaction between corium and various types of concrete used at power plants operating at that time. Figure 1 shows a schematic diagram of the experimental device when conducting experiments of the NEA-MCCI series.

The method of passing an electric current through the melt is implemented using two opposite walls of MgO lined with tungsten electrodes. During the experiment, an electric current was conducted through a central transverse span of electrodes that were in direct contact with the corium melt. The decay heat compensation system is built in such a way that, as the tungsten electrodes in direct contact with corium fail and the side walls erode, additional electrodes were exposed to the surface of the corium melt, to which an electric current is applied, thereby maintaining a homogeneous picture of heating the melt during the experiment. Thus, such a solution allows maintaining a constant rate of melt heating despite the failure of the tungsten electrodes and erosion of the side walls of the experimental section in an aggressive corium environment [12]. The electrical conductivity of the melt is very uncertain and unstable for each experiment due to changes in composition due to chemical interactions between corium and structural elements. This is the disadvantage of using this method. After all, during experimental studies the amount of energy injected into the melt strongly depends on the electrical conductivity of the melt. In this regard, the power distribution in the melt is unknown with a high degree of accuracy, which significantly affects the accuracy of the results obtained.

2.2. Induction heating method

A similar issue associated with the uncertainty of the electrical conductivity of corium also exists when using an alternative method of decay heat simulation - an induction heater. Induction method is the heating of materials by electric currents that are induced by the alternating magnetic field of the inductor.

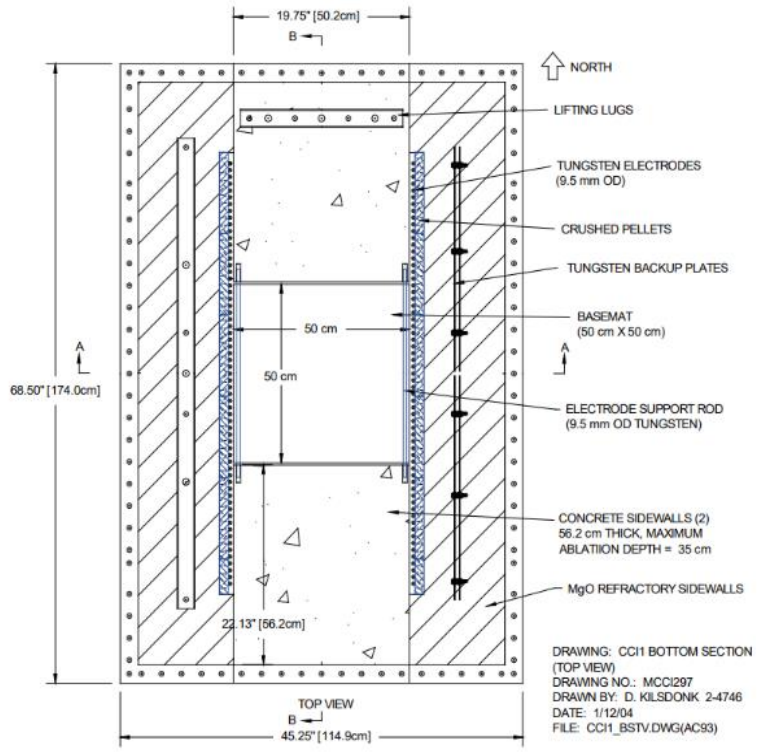

Fig. 1. Schematic diagram of the device used in the NEO-MCCI series experiments

Induction heating, as a method for simulating decay heat, is today the most widely used method when conducting experimental studies with corium melts, which is implemented in many large-scale and small-scale experimental installations, among which are such installations as: VULCANO, LAVA-B, VESTA, VESTA – S, BETA, COMET, COMETA, SICOPS, etc. [13-16]. Figure 2 shows schematic diagrams of some experimental installations.

In general, the principle of using an induction heater as a simulation method in various installations is identical. For example, at the LAVA-B and VESTA installations, corium is obtained in an electric melting induction furnace, which, after reaching the required temperature, is poured into a special experimental section surrounded by an induction heater, thereby simulating the decay heat in the melt, while the VULCANO installation differs from previously described installations only in the method of obtaining corium. The main advantage of induction heating is the non-contact method of transferring energy into the melt, which:

1) Eliminates the problem of contamination of the melt by foreign substances. For example, in the case of using electrodes with direct electric heating or thermite mixtures, which will be mentioned below;

2) Provides the possibility of long-term heating of corium in comparison with other methods of simulating decay heat in the experimental section, since the heating element is not in direct contact with the aggressive environment of the corium melt.

At the same time, despite the above advantages, installations for induction heating of corium have relatively low efficiency values. In addition, the efficiency of induction heating depends on many electrical and geometric parameters of both the inductor and the experimental section, which leads to the need to use more powerful sources of electricity to achieve the energy release in the melt required by the experimental conditions [17-18]. Another disadvantage of using an inductor is the pronounced surface skin effect. This means that most of the energy is released in some surface layer, which, in fact, is a disadvantage of induction heating as a method of simulating the residual energy release in the corium during experiments. For example, a situation may arise when, during induction heating, overheating of the surface layer of the melt will be observed, while the internal layers will not be heated sufficiently or even cooled, given the low thermal conductivity properties of corium.

.

2.3 Heating method using thermite mixtures

Decay heat is a feature of nuclear fuel, which means that under prototype conditions, heat generation is mainly concentrated in the oxide phase of corium.

This causes difficulties in reproducing such conditions during experimental studies, taking into account the currently available melt heating technologies. To some point this issue was managed in MOCKA experiments, where the heat of an aluminothermic exothermic chemical reaction was used to compensate the decay heat (Fig. 3). Such a chemical reaction releases a fairly large amount of heat, and the temperature of the mixture can reach 3000 °C.

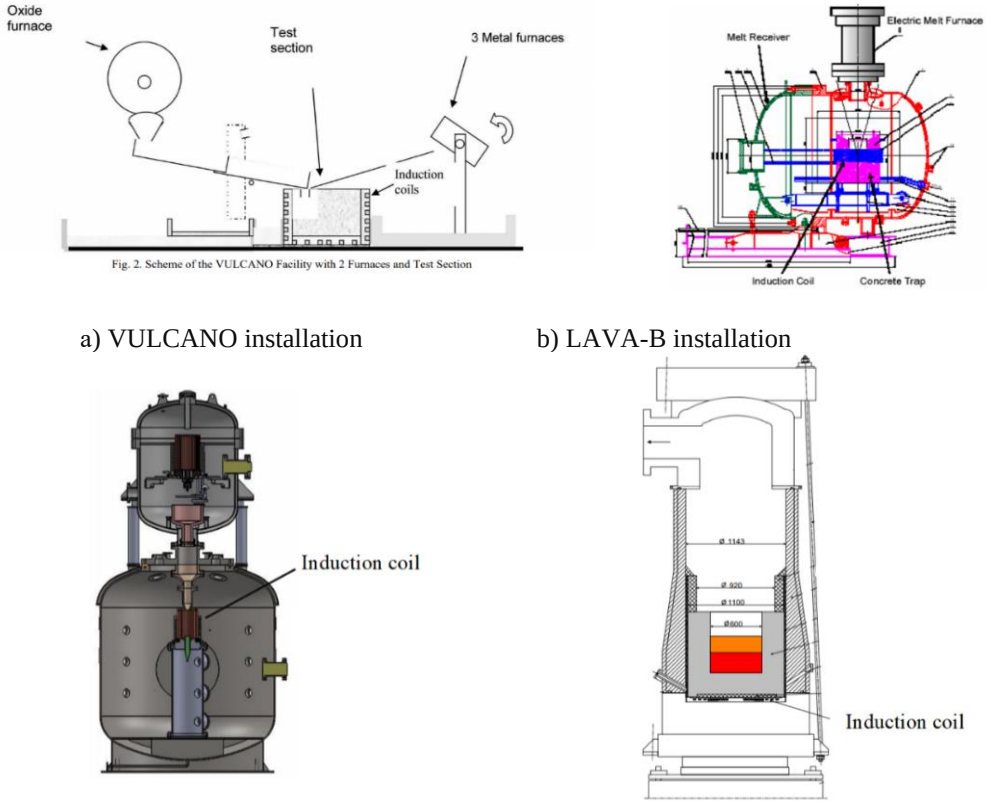

Fig. 2. Schematic diagrams of test devices

Fig. 3. MOCKA experimental installation

The advantage of this method, the authors point out, is the fact that during experiments, the heat released by the thermite reaction and the exothermic reaction of Zr oxidation is mainly deposited in the oxide phase (approximately 80% of the heating power was invested in the oxide phase and 20% in the metallic phase), which is not possible achieved using other methods for simulating decay heat. Unfortunately, this method is not a priority when choosing the most optimal simulation method due to the need to constantly add large volumes of new portions of thermite mixtures to maintain the simulation of decay heat. These actions lead to a significant change in the mass and chemical composition of the corium, which affects the nature of the interaction of the corium with various structural elements and can distort a reliable picture of the interaction occurring in a real situation.

2.4 Indirect electric arc heating method

Another way to simulate decay heat release, which gives opportunity to the heat release in the required area of the melt, is the plasmatron method. This method was implemented on the basis of the branch of the Institute of Atomic Energy of the RSE NNC RK. During a series of INVECOR experiments to study the interaction of corium with the vessel of a light water reactor at the Lava-B installation, the indirect electric arc heating method was used, which uses the idea of the electroslag process and was implemented using closed-type coaxial plasmatrons immersed in the melt. To protect the heating device from corium, the plasmatrons were placed in special graphite tips. Figure 4 shows a schematic diagram of the experimental installation “Lava-B” with plasmatron heaters.

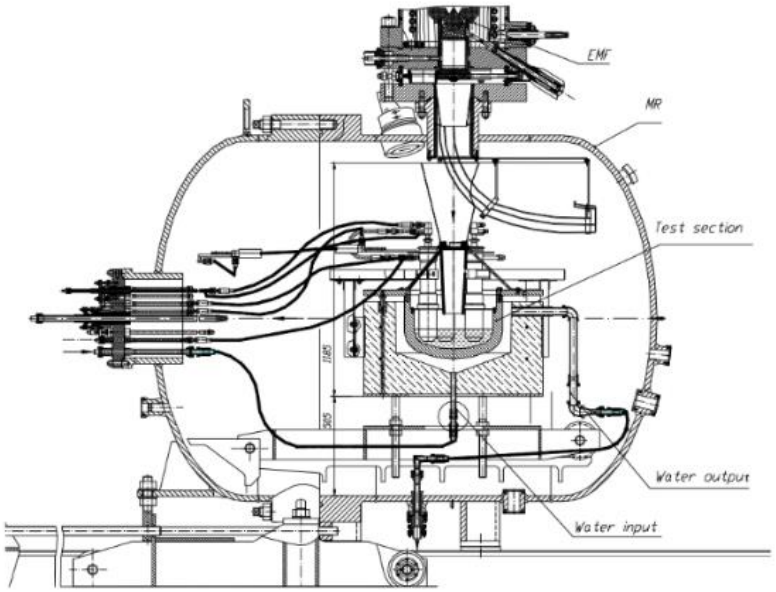

Fig. 4. Schematic diagram of the LAVA-B installation with plasmatron heaters

The advantage of indirect electric arc heating, for example, over induction heating or direct electric heating, is the absence of dependence on the electrically conductive properties of corium, since the transfer of energy to the melt is not associated with the flow of electric current in the melt. In this regard, the energy transferred to the melt can be determined with great accuracy.

The disadvantage of this method is the low unit power of plasma torches. In this regard, in order to achieve the required energy release in the melt, it is necessary to use a sufficient number of plasma torches, since a large amount of energy is required to maintain the corium simulator in the molten state when it interacts with various materials. As noted above, to protect plasmatronic heaters, they are placed in a special graphite tip. However, such graphite tips have a low durability in the aggressive environment of corium. This means that graphite plasma torch tips can significantly limit the possibilities of conducting an experiment, in particular regarding the duration of heating of the melt. To increase the service life of graphite tips, additional measures must be taken. For example, the use of a special zirconium carbide coating on the outer surface of graphite tips can extend the life of the tips to 2 hours at temperatures above 2500 °C, which fully satisfies the requirements of many experiments.

.

2.5 Ohmic heating method

Another method of decay heat release simulating, which was used in experiments with corium melts, is the method of electric heating by resistance. This method was used as part of the LIVE experiment on the installation of the same name (Fig. 5). The use of spiral heaters as in the LIVE installation, at first glance, is a more optimal way to simulate decay heat. Each heating plane consists of a spiral-shaped heating element, located in a special cage to ensure proper placement. To ensure uniform volumetric energy release, the heating system has six heating planes at different heights with fixed distances between them. This arrangement of the heaters allows one to regulate the uniformity of heating throughout the volume of the corium melt.

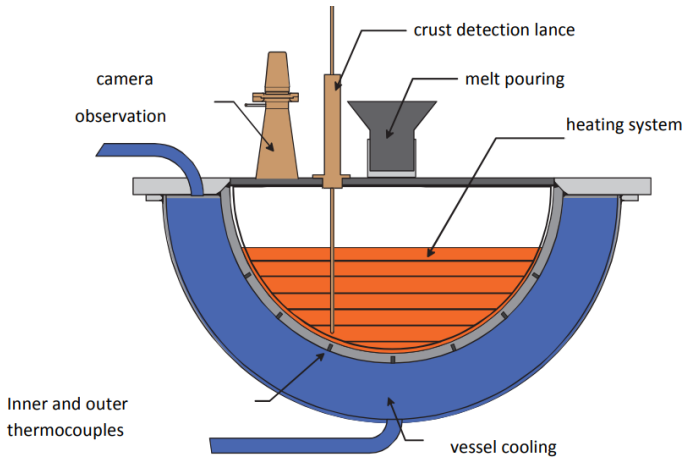

Fig. 5. Schematic diagram of the test section of the LIVE installation

However, the maximum permissible temperatures for indirect electric heating by the melt resistance in the LIVE installation were limited by the thermophysical properties of the spiral heater material, which was 1100 °C. This indicator is significantly lower than the required temperature values when conducting many experiments using a corium melt [19].

3. Comparative analysis, discussion

To select the optimal method for simulating decay heat in corium when conducting various studies on experimental installations by comparing the advantages and disadvantages, as well as suggesting possibilities for their improvement and assessing possible threats when conducting experiments, a SWOT analysis of the above methods was conducted, which is presented in Table 1. The review of practical methods for decay heat simulating in corium leads to the conclusion that all existing methods, although used at different experimental facilities to study the interaction of corium with structural materials, cannot fully simulate the thermal qualities of real corium.

At the same time, according to the table, induction, electric arc and ohmic heating are considered the most optimal. It is worth noting that various studies are currently being conducted on the interaction of corium with structural materials such as steel, concrete, sacrificial and heat-resistant materials, etc. This means that the choice of method for simulating residual energy release should be determined by the specifics of experimental research. For example, when studying the interaction of corium with steel, induction heating cannot be used as a method for simulating decay heat. This is due to the fact that, once exposed to the electromagnetic field of the inductor, the steel will heat up, thereby distorting the picture of the real interaction. In this regard, it is recommended to use methods of indirect water energy into the melt such as ohmic and electric arc heating.

Induction and plasmatron methods for simulating decay heat in the corium in relation to the LAVA-B installation are discussed in detail in paper [20]. Based on the fulfilled work, the parameters of heating the melt by each of the methods under consideration were determined, they were compared, the limits of their applicability for simulating residual energy release were determined, as well as the possibilities for further use.

The use of spiral heaters in the LAVA-B installation as in the LIVE installation, at first glance, is a more optimal method to simulate decay heat. The system for simulating decay heat is a device (Fig. 6), where each heating plane consists of a spiral-shaped heating element located in a special cage to ensure correct placement. This arrangement of the heaters allows one to regulate the uniformity of heating throughout the volume of the corium melt. To ensure uniform volumetric energy release, the heating system has six heating planes at different heights with fixed distances between them.

Table 1. SWOT analysis of methods for decay heat simulating.

Methods of decay heat release simulation:	**Strength**	**Weakness**	**Opportunities**	**Threats**
Induction heating	Non-contact heating of corium, heating duration	Low efficiency factor, skin effect	Increasing efficiency by optimizing the parameters of the induction system	All conductive materials are subject to heating
Indirect electric arc heating method	No dependence on the conductive properties of corium	Low unit power of the plasma torch	The possibility of increasing the heating efficiency by using several plasma torches	Limited heat transfer area
Direct electric heating	High heating temperature	The time limit of the experiment due to the failure of tungsten electrodes	Missing	Dependence of the amount of energy injected into corium on its electrical conductivity
Heating method using thermite mixtures	High heating temperature (up to 3000℃)	Short-term heating	Missing	Changes in the physical and chemical properties of corium
Ohmic heating (resistive heating)	Provides sufficient uniformity of heating of the melt throughout the volume	Low heating temperature	Increasing the maximum heating temperature due to the use of refractory materials	The threat of melting of the heater in the active medium of corium

Fig. 6. Ohmic heater in LIVE experiment

At the same time, the problem of temperature limitation of the use of a spiral heater can be solved by using more refractory metals as a material for its manufacture. One of the most optimal metals is tungsten, which has a melting point of over 3000 ° C, which is significantly higher than the operating temperatures when conducting experiments with corium. In the ANSYS program, an ohmic heater model was built based

.

on the parameters of the experimental installation of the LAVA-B melt subreactor trap. The appearance of the heater, height is 240 mm, diameter is 190 mm, and the wire diameter is 1 mm, is shown in Figures 7 and 8.

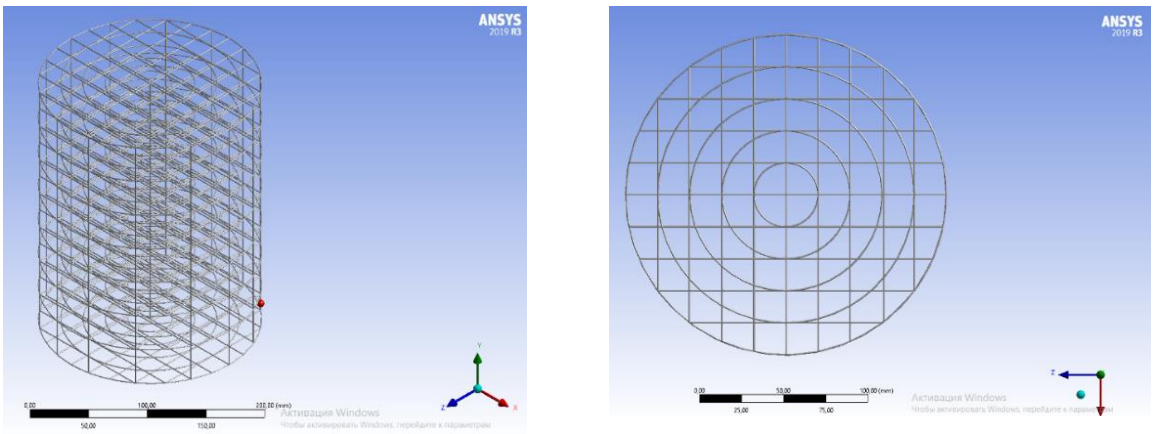

a) b)

Fig. 7. Type of heater a) in an isometric system, b) in the XZ plane

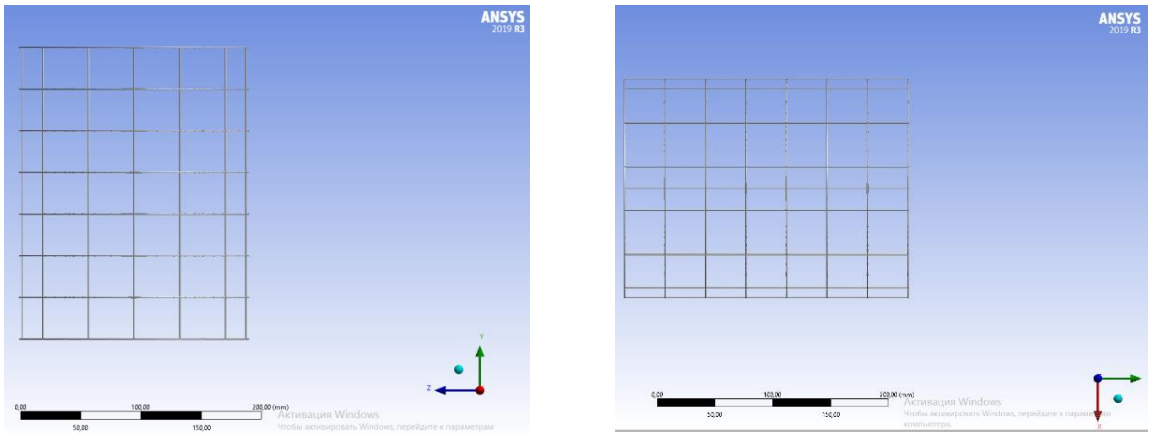

a) b)

Fig. 8. Type of heater a) in an isometric system, b) in the XZ plane

In further studies, electrical calculations of heaters with different parameters will be carried out, as well as thermal calculations of corium during the use of this heater in a melt trap at the LAVA-B installation.

4. Conclusion

Five methods of decay heat simulating in corium were considered in this paper. According to the results of the comparative analysis, it turned out that each of the methods has the following strengths and weaknesses. The induction method, although it provides long-term heating and is a non-contact heating method, but due to the low efficiency and skin effect, it cannot provide sufficient compliance with the picture of the thermal field of real corium. In addition to the listed disadvantages, all conductive materials of the experimental installation will be heated during the application of this method. The plasmatron method does not depend on the electrical conductivity of corium, but due to the low unit power of the plasmatron this method requires the use of several plasmatrons. However, even with the installation of several plasmatrons, the corium heat transfer area will be limited. During the application of the method of direct transmission of electric current through the melt, it becomes possible to achieve high temperatures, but the duration of heating will depend on the duration of operation of the electrodes. The method of heating with thermite mixtures is described with the same short heating duration. The only advantage of this method is the achievement of high temperatures, and the main disadvantage is the change in the physical and chemical properties of corium during the application of this method. Of all the methods considered, ohmic heating is

the only method that provides a uniform thermal field throughout the entire volume. Moreover, it is possible to change the nature and intensity of melt heating by using heaters of different shapes and parameters. There are also prospects for improving the effectiveness of this method through the use of refractory metals.

Taking into account these data and the possibilities of using each of the methods of simulating residual energy release in experiments with different specifics, it can be concluded that the most optimal of all existing methods is ohmic heating. The study of the possibility and practicality of using the ohmic heating method opens up the possibility for further experiments at the LAVA-B installation, which in turn will allow us to investigate the processes occurring during a severe accident at a nuclear power plant.

Conflict of interest statement
The authors declare that they have no conflict of interest in relation to this research, whether financial, personal, authorship or otherwise, that could affect the research and its results presented in this paper.

CRediT author statement
Skakov M.K., Baklanov V.V.: Conceptualization, Methodology; Nurpaissova G.S., Toleubekov K.O.: Data curation, Writing- Original draft preparation; Akaev A.S., Bekmuldin M.K.: Writing- Reviewing and Editing;
The final manuscript was read and approved by all authors.

References

1 Molchanov I.A., Shumilin M.P. Retention of the core melt inside the containment during severe accidents of nuclear power units. *Eastern-European journal of enterprise technologies*, 2011, Vol. 2, No. 8(50), pp. 65-67. https://doi.org/10.15587/1729-4061.2011.1843 [in Russian].

2 Dolganov K.S. Possibility of misleading readings of water level in VVER steam generator during severe accidents with account for the Fukushima lessons. *Nucl. Eng. Des.*, 2023, Vol. 413, https://doi.org/10.1016/j.nucengdes.2023.112519

3 Skakov M.K., Toleubekov K.O., Baklanov V.V., Gradoboev A.V., Akayev A.S., Bekmuldin M.K. The method of corium cooling in a core catcher of a light-water nuclear reactor. *Eurasian phys. tech. j.*, 2022, Vol. 41, pp. 69–77. https://doi.org/10.31489/2022No3/69-77

4 Bondar F.D., Artamonov M.V., Sidorov A.S. The influence of the accuracy of the calculation of residual energy release on corium catcher justification during BDBA. *Journal of Physics: Conf. Series, 2018,*, pp. 1-10. DOI:10.1088/1742-6596/1133/1/012014

5 Mukhamedov N.Ye., Kozhakhmetov Ye.A., Tskhe V.K. Microstructure and mechanical properties of the solidified melt obtained by the in-pile test. *Annals of Nuclear Energy*, 2022, pp. 179. https://doi.org/10.1016/j.anucene.2022.109404

6 Andrushechko S.A., Afrov A.M., Vasiliev B.Yu. *WWER-1000 reactor NPP. From physical basis of operation up to project evolution*, Logos. 2010. pp. 604. [In Russian] https://elib.biblioatom.ru/text/andrushechko_aes-s-reaktorom-vver-1000_2010/p0/

7 Fink J.K., Thompson D.H., Spencer B.W. Aerosol and melt chemistry in the ACE molten core-concrete interaction experiments. *High Temperature and Materials Science*. 1995. Vol. 33(1), pp. 51-76. https://inis.iaea.org/search/search.aspx?orig_q=RN:27019724

8 Journeau C., Piluso P., Haquet J.F. Two-dimensional interaction of oxidic corium with concretes: The VULCANO VB test. *Annals of Nuclear Energy* series, 2009, Vol. 36, pp. 1597– 1613. https://doi.org/10.1016/j.anucene. 2009.07.006

9 Foit J.J. MCCI of a Metal and Oxide Melt with Reinforced Siliceous Concrete in MOCKA Experiments. *Proc. of the 22nd Intern. Conf. on Nuclear Engineering*, Prague, Czech Republic, 2014. https://doi.org/10.1115/ICONE22-30200

10 Baklanov V.V., Zhdanov V.S., Malysheva Ye.V. Experimental study of processes during retention of corium melt in the reactor vessel (INVECOR). *Bulletin of NNC RK*, 2009, Vol. 37, pp. 55-65. [In Russian] https://www.nnc.kz/media/bulletin/files/AIVJZeUkpq.pdf

11 Foit J.J. Experiments on MCCI with oxide and steel. *Annals of Nuclear Energy*, 2014, Vol.74, pp.100 – 109. https://doi.org/10.1016/j.anucene.2014.06.025

12 Farmer, M.T., Lomperski, S., Kilsdonk, D.J. *OECD MCCI-2 Project Final Report. OECD/MCCI*. 2010. Vol. 07, pp. 91. https://doi.org/10.13140/RG.2.2.27550.79687

13 Journeau C. Contributions of the VULCANO Experimental Programme to the Understanding of MCCI Phenomena. *Nuclear engineering and technology*, 2012, Vol. 44 (3), pp. 261-272. https://doi.org/10.5516/NET.03.2012.703

.

14 Maruyama Yu., Tahara M., Nagasaka H. Recent results of MCCI studies in COTELS project. *Proceeding of the 3rd Korea-Japan Symposium on Nuclear Thermal Hydraulics and Safety Kyeongju*, Korea, 2002. https://doi.org/10.13140/2.1.3997.1206

15 Song, J., Kim, H., Hong, S. A use of prototypic material for the investigation of severe accident progression. *Progress in Nuclear Energy*, 2016, Vol. 93, pp. 297–305. https://doi.org/10.1016/j.pnucene.2016.09.003

16 Spindler B., Atkhen, K., Cranga M. Simulation of Molten Corium Concrete Interaction in a Stratified configuration: the COMET L2-L3 Benchmark. *Proceeding of the 2nd European Review Meeting on Severe Accident Research (ERMSAR-2007)* Karlsruhe, Germany, 2007. https://www.researchgate.net/publication/239556995 Simulation of_Molten_Corium_Concrete_Interaction_in_a_Stratified_Configuration_the_COMET-L2-L3_Benchmark

17 Bekmuldin M.K., Skakov M.K., Baklanov V.V. Experimental Simulation of Decay Heat of Corium at the Lava-B Test-Bench. *Nuclear Technology*, 2023, Vol.210, pp. 46-54. https://doi.org/10.1080/00295450.2023.2226539

18 Toleubekov K.O., Akaev A.S., Bekmuldin M.K. Improving the efficiency of the induction heating system to simulate decay heat in corium when interacting with heat-resistant materials. *Bulletin of the NNC RK*, 2020, Vol. 4, pp. 47-52. [In Russian] https://www.nnc.kz/media/bulletin/files/wus8l5EKb2.pdf

19 Miassoedov A., Cron T., Gaus-Liu X. LIVE experiments on melt behavior in the reactor pressure vessel lower head. *Proceeding of the 8th Intern. Conf. on Heat Transfer, Fluid Mechanics and Thermodynamics*, 2011. Vol. 34(14), pp. 793 – 801. https://doi.org/10.1080/01457632.2013.777247

20 Toleubekov K.O. Modeling the process of decay heat imitation in the corium at the Lava-B facility. *Recent Contributions to Physics*, 2022, Vol. 81, No 2, pp. 97-106. https://doi.org/10.26577/RCPh.2022.v81.i2.012

AUTHORS' INFORMATION

Skakov M.K. - Doctor of phys.-math. sciences, Professor, Chief Researcher, National Nuclear Center of the Republic of Kazakhstan, Kurchatov, Kazakhstan; ORCID ID: 0000-0003-3716-8846; skakov@nnc.kz

Baklanov V.V. - PhD, First Deputy Director, Institute of Atomic Energy of the National Nuclear Center of the Republic of Kazakhstan, Kurchatov, Kazakhstan; ORCID ID: 0000-0001-7627-8752; baklanov@nnc.kz

Nurpaissova G.S. - PhD student, Shakarim University, Semey, Kazakhstan; Engineer, Laboratory of Experimental Thermophysics, Institute of Atomic Energy of the National Nuclear Center of the Republic of Kazakhstan, Kurchatov, Kazakhstan; Kazakhstan; ORCID ID**:** 0009-0004-5573-1510; nurpaissova@nnc.kz

Akaev A.S. – Head of the Department of non-reactor tests, Institute of Atomic Energy of the National Nuclear Center of the Republic of Kazakhstan, Kurchatov, Kazakhstan; ORCID ID: 0000-0003-4792-6161; akaev@nnc.kz

Bekmuldin M.K. - PhD student, Shakarim University, Semey, Kazakhstan; Head of the group of the Laboratory of Experimental Thermophysics, Institute of Atomic Energy of the National Nuclear Center of the Republic of Kazakhstan, Kurchatov, Kazakhstan; ORCID ID: 0000-0002-6895-536X; bekmuldin@nnc.kz

Toleubekov K.O. - PhD student, Shakarim University, Semey, Kazakhstan; Junior Researcher, Laboratory of Experimental Thermophysics, Institute of Atomic Energy of the National Nuclear Center of the Republic of Kazakhstan, Kurchatov, Kazakhstan; ORCID ID: 0000-0001-8731-363X; toleubekov@nnc.kz

EURASIAN PHYSICAL TECHNICAL JOURNAL

2024, Volume 21, No. 1 (47)

https://doi.org/10.31489/2024No1/67-73

Received: 18/12/2023 Revised: 04/02/2024 Accepted: 07/03/2024 Published online: 29/03/2024

Research Article

UDC 53.09; 662.612.3; 62.663.2

IMPROVING THE QUALITY OF EKIBASTUZ COAL USING THE DRY ENRICHMENT METHOD

Shaimerdenova K.M.[1], Sakipov K.E.[2], Abdirova N.T.[1], Suleimenova S.E.[1]

[1] Karaganda Buketov University, Karaganda, Kazakhstan

[2] L.N. Gumilyov Eurasian National University, Astana, Kazakhstan

*Corresponding author: gulzhan.0106@mail.ru

Abstract. *This paper discusses the possibility of improving the ekibastuz coal quality through the use of "dry enrichment" technology. The experiments and calculations carried out made it possible to determine the optimal scheme for enrichment of samples of thermal coals from the Ekibastuzsky open-pit mine of "Angrensor-Energo" LLP. Testing of technical characteristics, such as moisture content, ash content, volatile matter yield and calculation of energy characteristics of enriched samples of thermal coal was carried out in 3 stages in a coal chemistry laboratory. As a result, it was found that the energy content of the enriched fuel samples increased to 28.5% of the original. This significantly improved consumer properties by obtaining the maximum yield of high quality coal concentrate. Consequently, the developed scheme of enrichment allows to significantly reduce the consumption of electricity, reduce emissions into the atmosphere, reduce the harmful impact on the environment, and expand the markets for coal.*

Keywords: ekibastuz coal, thermal coals, harmful emissions, humidity, ash content, volatile substance, “dry enrichment" technology

1. Introduction

Global climate change, caused by increasing harmful emissions into the atmosphere, necessitates a widespread transition from hydrogen energy to the development of technologies for converting renewable energy sources (RES). According to the Sixth Assessment Report of the International Panel on Climate Change (IPCC), anthropogenic greenhouse gas (GHG) emissions have reached the highest levels in human history, which is already having a negative impact on the Earth's climate [1-7]. In the production of electricity and heat, coal generation retains a dominant position. According to data at the end of 2022 in Kazakhstan, 68.2% of electricity is generated from coal, 20% from gas, about 8.8% from water energy conversion, and about 3.0% comes from renewable energy sources [2, 3]. These statistics are due to the fact that Kazakhstan has huge coal reserves, approximately 34 billion tons. Therefore, to achieve carbon neutrality by 2060 and reduce GHGs in general, along with strategic plans to increase the share of renewable energy projects, the development and implementation of “clean coal” technologies is important.

At the state level, voluntary commitments have been made to reduce harmful carbon emissions into the atmosphere. Kazakhstan has developed a national low-carbon development strategy until 2060, aimed at reducing the energy intensity of gross domestic product (GDP). “The medium-term goal of the Strategy of the Republic of Kazakhstan is to reduce GHG emissions by 15% by 2030 relative to the 1990 emissions level

(unconditional goal) and achieve a reduction of 25%, subject to receiving international support for decarbonization of the economy (conditional goal)" [3].

The priority in the modern thermal power engineering development is the problem of energy saving due to the economical use of fuel and energy reserves. Increasing energy consumption with a simultaneous increase in energy prices and widespread environmental degradation necessitates the development and implementation of energy efficient technologies to save fuel, materials and labor costs [5-8]. Energy conservation includes a wide range of interrelated activities and techniques to ensure efficient use of energy. One of the methods is to clean the walls of pipelines of heat exchange devices from scale, which forms during long-term operation and worsens the hydrodynamics of the flow and the intensity of heat transfer processes [5]. To ensure higher combustion efficiency of ekibastuz coal and, accordingly, less harmful emissions into the atmosphere, it is proposed to use laser ignition of the coal mixture [6]. The "three-stage" combustion method makes it possible to increase the reactivity of low-grade Ekibastuz coal and to reduce the content of harmful oxides in combustion products [7]. Energy conservation includes a wide range of interrelated activities and methods that ensure efficient use of energy.

One of the ways to reduce the volume of harmful emissions into the atmosphere, including greenhouse gases, from coal combustion is its enrichment [9-12]. The beneficiation process involves refining coal, where "clean" coal is separated from unnecessary impurities to produce a higher quality fuel. The study of methods and technologies for the enrichment of thermal coals, a technical analysis of the characteristics of coal from the Ekibastuz open-pit mine of Angrensor-Energo LLP, made it possible to develop a technology for their enrichment. The fundamental novelty lies in the use of the dry enrichment method instead of the traditional averaging of low-grade thermal coals from the ekibastuz coal basin by mixing with high-grade coals.

2. Materials and research method

The developed method of dry enrichment using a combined dry enrichment machine type FGX-12 was applied at the Ekibastuz open-pit mine for processing KSN grade coals. To develop a scheme for enriching ekibastuz coal and obtaining the maximum yield of coal concentrate of the required quality, the technical (working) characteristics of ekibastuz coal were previously determined, such as humidity, ash content, volatile matter yield, etc. Studying the characteristics of thermal coal from the Ekibastuz open-pit mine of Angrensor-Energo LLP in the coal chemical laboratory of Gamma LLP in Ekibastuz. The preparation of thermal coal before the enrichment process was carried out in three stages.

Stage 1: sampling of coal from the surface of the massif (on a stack) of the Ekibastuz open-pit mine. A coal sample was selected manually from the massif prepared for transportation from each coal unit composing it. Spot samples taken evenly throughout the entire volume of the batch of raw coal, in the amount of 32 samples of 5 kg each. each, according to GOST 10742-71, were combined into a common sample [13-15].

The pooled sample was then thoroughly mixed by hand and divided in half. Thorough mixing of one part followed by its division into 2 parts was repeated until the final result was obtained in the form of a sample weighing 10 kg.

Stage 2: processing of the coal sample for laboratory testing.

The coal sample was placed on a baking sheet to dry for 8 hours. The laboratory sample, dried in this way and cooled in air, is crushed in a crushing machine to a particle size of 0.2 mm to 0.8 mm.

Stage 3: determination of the technical (working) characteristics of coal in the laboratory.

Technology of enrichment of Ekibastuz coal based on the use of a combined dry enrichment machine type FGX-12. The dry enrichment scheme for Ekibastuz coal is shown in Figure 1.

A detailed description of the structure and parts of the dry enrichment machine type FGX-12 and a general view are given in [12]. The developed method for processing ekibastuz coal using the dry enrichment method consists of 3 stages too. At the first stage, coal extracted from the face is cleaned of large pieces of rock, then transported to a coal receiving funnel with a feeder, where coarse coal is crushed to a fraction of 0 - 80 mm. This fraction size is determined by the size of the sieve with holes with a diameter of no more than 80 mm, located under the funnel corner of the receiving area with the feeder. At the second stage, crushed coal is loaded into the receiving hopper of a combined dry preparation machine.

Then, along a conveyor belt, it enters a gravity sieve, where the process of coal enrichment directly occurs by separating rock and mineral impurities from the coal with strong air flows and vibration of the sieve. Strong air currents lift small dust particles upward, which are then sent to the dust collector, and the

broken rock and middling product, under the influence of vibration and air currents, are directed upward through the vibrating sieve and fall onto different conveyor belts designed for their output (two separate outlets).

Coal purified from fine dust, rock and clay with fractions up to 80 mm in size is enriched, as its energy characteristics are significantly improved. In order to verify this, we will calculate the technical parameters before and after processing.

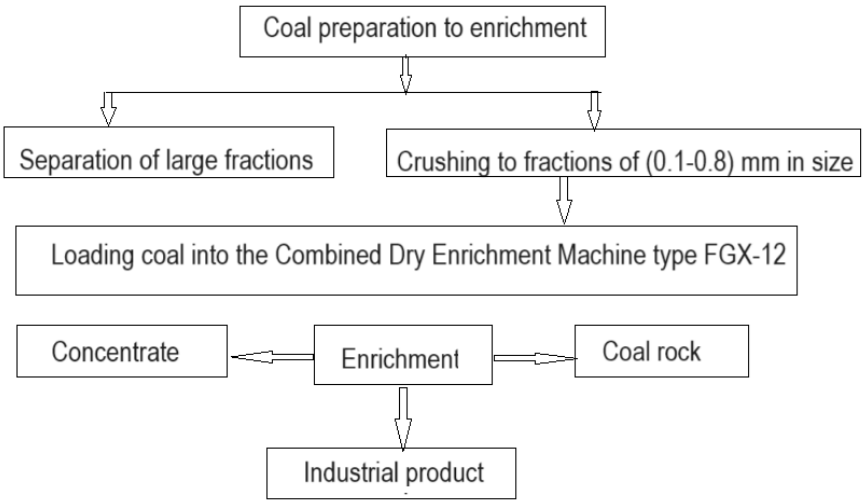

Fig.1. Scheme of enrichment of ekibastuz coal using the dry enrichment method using FGX-12

Coal of the 0-80 mm fraction, cleared of fine dust, rock and clay, is enriched, as its quality characteristics are significantly improved. The dry enrichment method using a combined dry enrichment machine type FGX-12 was used at the Ekibastuz open-pit mine for processing KSN grade coals.

3. Calculation of coal technical characteristics

The crushed sample was thoroughly mixed and laboratory tests were carried out on its basis and the following results were obtained. The moisture content of coal of this sample from the Ekibastuz open-pit mine of Angrensor-Energo LLP was determined. To determine the moisture content of coal from the Ekibastuz open-pit mine of Angrensor-Energo LLP, the crushed sample was thoroughly mixed and prepared.

$$W_t = W_{ex} + W_h \frac{100 - W_{ex}}{100}, \quad (1)$$

where W_t is the total amount of moisture; W_{ex} is external moisture per mass fraction of coal; W_h is the moisture of air-dry fuel

External moisture W_{ex} per mass fraction of coal was calculated using equation:

$$W_{ex} = \frac{G_3}{G_t} 100,$$

where G_t is the mass of the baking sheet with a portion before drying, g; G_3 is the weight loss of the sample during drying, g.

The weight of the baking sheet with the attachment is the sum of the mass of the baking sheet (1.6 kg) plus the weight of the attachment (10 kg), a total of 11.6 kg, or 11600 g. The weight loss of the sample during drying was 348 g.

Thus, the mass fraction of external moisture is determined as

$$W_{ex} = \frac{348}{11600} \cdot 100 = 3\%.$$

.

1) To determine the moisture of air-dry fuel (A^d) per mass fraction of coal, we need to determine the analytical moisture of coal W_t, since if a coal sample is dried to a constant mass at room temperature, external moisture is released, and the sample is brought to an air-dry state (analytical mass), i.e. the formula [13]:

$$W^a = W_h$$

Let us calculate the analytical mass of coal moisture as follows:

$$W^a = \frac{m_1}{m} \cdot 100 .$$

Here the loss of mass of a sample of fuel during drying, measured in grams, is already known to us and amounts to 348 g; the mass of the fuel sample, also measured in grams, is also known and amounts to 10,000 grams. Therefore, the analytical mass of coal moisture W_t and the moisture fraction of air-dry fuel W_h equals to 3.48%. The total moisture of coal can determine using (1):

$$W^a = \frac{348}{10000} \cdot 100 = 3.48\%$$

Having received all the necessary data, the total moisture of coal is determined:

$$W_t = W_{ex} + W_h \frac{100 - W_{ex}}{100} .$$

$$W_t = 3 + 3.48 \cdot \frac{100 - 3}{100} = 6.38\%$$

Thus, the total moisture per mass fraction of coal is 6.37%.

$$W^r = W_{ex} + W^a \frac{100 - W_{ex}}{100},$$

where, an analytical moisture W_a is calculated within the total concentration of the visible fraction of coal and moisture 3.48%.

The results obtained showed the same values of total moisture per mass fraction of coal W_t and the working moisture indicator W_r.

2) To determine the ash content of coal (A^d), we burned a fuel sample under laboratory conditions in a muffle furnace heated to a temperature of 820°C. As a result, a mass of ash (A) was obtained, amounting to 40.5% of the burned sample. The indicator of analytical moisture of coal (Wa) was calculated by us above and amounted to 3.48%. Thus, the ash content of the coal sample from the Ekibastuz open-pit mine was 41.9%

$$A^d = 40.5 \cdot \frac{100}{100-3.48} = 41.9\%.$$

This indicator is generally similar to the ash content of coals from other open-pit mines of the ekibastuz coal basin, which, on average, is 40–45%.

3) The volume of volatile substances released from the sample from the Ekibastuz open-pit mine of Angrensor-Energo LLP was calculated for the combustible mass of fuel (V^{daf}) based on the results of determination in the analytical sample (V^a). The volume of volatile substances released in the analytical fuel sample (V^a) was calculated using the formula [13]

$$V^a = \frac{M_{vol}}{M_m} 100 - W^a,$$

where M_{vol} is the mass of released volatile substances, g; M_m is the fuel weight, g; Wa is moisture content in the analytical fuel sample, %.

To determine the yield of volatile substances in practice, we used a high-shaped porcelain crucible No.5 with a lid, weighing 110 g and volume 85 ml. We placed a 1gramm sample of air-dry fuel into the crucible,

placed the lidded crucible with the fuel sample into the stable temperature zone of a muffle furnace, preheated to (900 ± 5°C), and held it for 7 minutes.

Then the crucible was removed from the furnace, cooled first in air for 5 minutes, and then in a desiccator to room temperature. After the non-volatile residue cooled down to room temperature, we weighed it and calculated it using the formula given above. As a result, a yield of volatile substances was obtained

$$V^a = \frac{0.28}{1} \cdot 100 - 3.48 = 24.5\%$$

Next, the ash content in the analytical fuel sample (A^a) is calculated

$$A^a = \frac{M_{ash}}{M_m} \cdot 100 ,$$

where M_{ash} is the mass of ash after calcination, g; M_m is fuel weight, g.

To do this, the crucible is placed in a sample of air-dry fuel weighing 1 g, where it is installed at the leading edge of a muffle furnace, preheated to 820°C. The crucible is kept in this position for 30 minutes, which helps prevent the active release of volatile substances. The crucible is then gradually moved to a constant temperature zone to avoid fuel flare-ups. The duration of ashing process is 30 minutes. After the set time has elapsed, the crucible is removed from the furnace and cooled to room temperature. At the end of the procedure, the crucible with the ash residue is weighed. Thus, the initial data were obtained for calculating the ash content in the fuel sample M_m, which, as a result of a laboratory study, amounted to 41.9%, which was almost identical to the ash content of coal on a dry weight basis

$$A^a = \frac{0.41}{1} \cdot 100 = 41\%$$

Calculation using the standard formula for the volume of volatile substances released per combustible mass of fuel V^{daf} showed 24.1%, it's a slight decrease. The value of this indicator generally corresponds to similar values of the volume of volatile substances obtained in other quarries of the Ekibastuz coal basin, and varies from 24 to 26%.

4. Discussion of results

The practical implementation of the dry enrichment scheme for thermal coal using the FGH-12 combined dry enrichment machine at the Ekibastuz open-pit mine was carried out in March 2020. Before the implementation of this scheme, it was not clear exactly the possibility of dry enrichment of coal from the KSN arch of the ekibastuz coal mine. Enrichment of KSN grade coal was carried out according to our proposed model of the ekibastuz coal enrichment scheme using the dry enrichment method using a combined dry enrichment machine of the FGH-12 type.

The results of the study using this method showed the feasibility of using the installation of a combined dry enrichment machine FGX-12 at the Ekibastuz open-pit mine of Angrensor-Energo LLP. The results are presented in Table 1. An improvement in the technical characteristics of coal according to the main indicators (humidity, ash content, calorific value) of the finished product (concentrate) after processing is shown.

Table1. Characteristics of coal and of the finished product before and after enrichment

Basic characteristics	before enrichment	after enrichment
Moisture, W_t	6.37%	4.2%
Ash content, A^d	41.9%	37.0%
Specific calorific value, Q_i	13179.6 kJ/kg	16945.2 kJ/kg
Release of volatile substances V_{daf}	24.5%	24.1%

.

Thus, the new technology made it possible to increase the energy content of enriched fuels to 28.5% of the original, which indicates the effectiveness of the proposed enrichment scheme for ekibastuz coal, which includes the dry enrichment method using the FGX-12 combined machine.

The obtained indicators confirm the effectiveness of dry enrichment of coals from the Ekibastuz mine. The proposed enrichment scheme will significantly reduce energy consumption, reduce the harmful impact on the environment and, as a result, expand coal sales markets. The developed coal enrichment scheme was tested experimentally on thermal coals of the KSN grade from the Ekibastuz open-pit mine of Angrensor-Energo LLP. The enrichment results confirmed its effectiveness, as well as the feasibility of installing a combined dry enrichment machine FGX-12 at the Ekibastuz open-pit mine of Angrensor-Energo LLP to obtain an enriched product of the required quality (concentrate).

5. Conclusions

An analysis of the quality of ekibastuz coal was carried out. Technical characteristics of ekibastuz coal (moisture content, ash content, release of volatile substances and calorific value) were determined using the example of coal from the Ekibastuz open-pit mine of Angrensor-Energo LLP. Thermal coals of the Ekibastuz basin are characterized as low-caking, high-ash, low-calorie. A technical analysis of a coal sample from the Ekibastuz open-pit mine was carried out in the coal chemical laboratory of Gamma LLP.

It should be noted that in the experiments, 100 tons of KSN grade coal were taken as the test sample. At the output after dry enrichment using the FGX-12 combined machine, the concentrate of the required quality was 35%, middling product is 35%, and coal rock is 30%. The obtained indicators are quite high for this type of coal, which confirms the possibility of processing difficult-to-enrich coal using the dry enrichment method. Such results were obtained due to the fact that the pneumatic separation process in the FGX-12 installation occurs in an air flow of constant speed, in which coal particles are suspended and stratified by density.

Thus, as a result of the enrichment of thermal coal using the dry enrichment method at the FGX-12 installation, the moisture content Wt decreased by 2.17% and amounted to 4.2%. The ash content of Ad also decreased by 41.9% and amounted to 37.0%; and the heat of combustion (Q_i), on the contrary, increased by 3765.6 kJ/kg and amounted to 16945.2 kJ/kg.

This, in turn, helps to improve the consumer properties of coal by obtaining the maximum yield of coal concentrate of the required quality. This enrichment scheme can significantly reduce energy consumption, reduce the harmful impact on the environment, and, as a result, expand coal sales markets.

Conflict of interest statement

The authors declare that they have no conflict of interest in relation to this research, whether financial, personal, authorship or otherwise, that could affect the research and its results presented in this paper.

CRediT author statement

Shaimerdenova K.M.: Supervision; Conceptualization, Methodology; Sakipov K.E.: Formal analysis, Review & Editing; Abdirova N.T.: Data Curation, Writing - Original Draft; Suleimenova S.: Investigation, Visualization.
The final manuscript was read and approved by all authors.

Acknowledgements

The authors express their gratitude to Shunkeev T.3., Head of the Coal Chemical Laboratory "Gamma" (Ekibastuz), for the opportunity to take part in test experiments on processing of KSN grade coal by the “dry enrichment” method using the combined installation FGH-12.

References

1 State and prospects of the coal industry in Kazakhstan: Mining and metallurgical industry. 2017. https://eabr.org/press/news/sostoyanie-i-perspektivy-ugolnoy-promyshlennosti-kazakhstana/

2 BP Statistical Review of World Energy 2022. https://www.bp.com/content/dam/bp/business-sites/en/global/corporate/xlsx/energyeconomics/statistical-review/bp-stats-review-2022-all-data.xlsx

3 On approval of the Strategy for achieving carbon neutrality of the Republic of Kazakhstan until 2060. Decree of the President of the Republic of Kazakhstan dated February 2, 2023 No. 121. https://adilet.zan.kz/rus/docs/U2300000121

4 Kalmykov D.E., Malikova A.D. Driven into coal. Review. Coal mining and coal power generation in Kazakhstan Status and prospects. Karaganda, Center for the Introduction of New Environmentally Friendly Technologies, *CINES*T, 2017, 70 p. https://usea.org/sites/default/files/122011_Prospects%20for%20coal%20%20clean

5 Sakipova S.E., Nussupbekov B.R., Ospanova D.A., Shaimerdenova K.M., Kutum B.B. Analysis of the Heat Exchanger Energy Efficiency of Variable Cross Section with an Inhomogeneous Coolant. *Latvian Journal of Physics and Technical Sciences*, 2023, Vol.60, No. s6, 2023, pp.142 - 150. https://doi.org/10.2478/lpts-2023-0051

6 Askarova A.S., Messerle V.E., Ustimenko A.B., Bolegenova S.A., Maksimov V.Yu. Numerical modeling of the coal combustion process initiated by a plasma source. *Thermophysics and Aeromechanics*, 2014, Vol.21 (6), pp.779–786. https://doi.org/10.1134/S0869864314060092

7 Kussaiynov K., Korabeinikova V.K., Sakipova S.E. *Method of burning ekibastuz coal in a steam boiler BKZ-420-140-5*. National Patent of the RK for invention. No. 13930. Publ. 10/15/2007. Bull.10, 8p. [in Russian]. https://kzpatents.com/4-13930-sposob-szhiganiya-ekibastuzskogo-uglya-v-parovom-kotle-bkz-420-140-5.html

8 Kijo-Kleczkowska A. Combustion of coal-water suspensions. *Fuel*, 2011, Vol.90, Is.2, pp. 865 – 877. https://doi.org/10.1016/j.fuel.2010.10.034

9 Murko V.I., Khyamyalyainen V.A., Volkov M.A., Baranova M.P. Potential and prospects of coal processing waste management. *Mining informational and analytical bulletin*, 2019, Is. 6, pp. 165 – 172. https://doi.org/10.25018/0236-1493-2019-06-0-165-172 [in Russian].

10 Safonov A.A., Parafilov V.I., Mausymbayeva A.D., Ganeeva L.M., Portnov V.S. Microcomponent composition of coals of Central Kazakhstan. *Coal*, 2018, No. 9 (1110), pp. 70 – 75. http://dx.doi.org/10.18796/0041-5790-2018-9-70-75. [in Russian].

11 Klein M.S., Vakhonina T.E. Coal enrichment technology. Kemerovo, 2011. [in Russian] http://www.geokniga.org/bookfiles/geokniga-kleintehnologiyaobogasheniyauglei.pdf.

12 Shaimerdenova, K., Ospanova, D., Shunkeyev T. Improving fuel properties using the FGX-12 crushing and screening complex. *Eurasian phys. tech. j.*, 2019, Vol. *16*, *No.* 2(32), pp. 68 – 73. https://doi.org/10.31489/2019No2/68-73

13 ST RK ISO 1171-2010. *Solid mineral fuel. Determination of ash content* (ISO 1171: 2010, 12, 30. Astana: Committee for Technical Regulation and Metrology of the Ministry of Industry and New Technologies of the Republic of Kazakhstan, 2010, 24 p. https://www.iso.org/obp/ui/#iso:std:iso:1171:ed-4:v1:en

14 *Interstate standard GOST 147-2013 (ISO 1928:2009). Solid mineral fuel. Determination of the higher calorific value and calculation of the lower calorific value (Solid mineral fuel. Determination of gross calorific value and calculation of net calorific value*). Instead of GOST 147 - 95 (ISO 1928 – 76; Moscow, 2014, 38 p. https://www.iso.org/standard/41592.html

15 *Interstate standard GOSTISO 5071-1-2013. Brown coals and lignite. Determination of the yield of volatile substances in an analytical sample*. Part 1. *Method using two furnaces*. Instead of GOST 6382–2001; Minsk, Eurasian Council for Standardization, Metrology and Certification, 2013, 15 p. https://www.iso.org/standard/63045.html

AUTHORS' INFORMATION

Shaimerdenova K.M. — Candidate of Techn. Sciences, Professor, Head of Department of Engineering Thermophysics named after professor Akylbayev Zh.S., Karaganda Buketov University, Kazakhstan; ORCID ID: 0000-0002-9588-4886; gulzhan.0106@mail.ru

Sakipov K.E. — Candidate of Techn. Sciences, Associate Professor, Power Engineering Department, L.N. Gumilyov Eurasian National University, Astana, Kazakhstan; ORCID ID: 0000-0003-2477-3879; sakamer2100@gmail.com

Abdirova N.T. — Master (Sci.), Lecture, Department of Engineering Thermophysics named after professor Akylbayev Zh.S., Karaganda Buketov University, Kazakhstan; ORCID ID: 0009-0005-1985-6081; abdirova_nurgul@mail.ru

Suleimenova S.E. — Master (Sci.), Lecture, Department of Engineering Thermophysics named after professor Akylbayev Zh.S., Karaganda Buketov University, Kazakhstan; ORCID ID: 0009-0000-2673-6938; Saniy_93 @mail.ru

.

EURASIAN PHYSICAL TECHNICAL JOURNAL

2024, Volume 21, No. 1 (47)

https://doi.org/10.31489/2024No1/74-83

Received: 10/11/2023 Revised: 22/01/2024 Accepted: 26/02/2024 Published online: 29/03/2024

Original Research Article

UDC 53.082

AUTOMATED CONTROL OF THE THIN FILMS ELECTRICAL CONDUCTIVITY BY THE EDDY CURRENT METHOD

Malikov V.N.[1]*, Ishkov A.V.[2], Voinash S.A.[3], Zagidullin R.R.[3], Sabitov L.S.[3,4], Vornacheva I.V.[5], Ivanov A.A.[6]

[1] Altai State University, Barnaul, Russia,
[2] Altay State Agricultural University, Barnaul, Russia
[3] Kazan Federal University, Kazan, Russia
[4] Kazan State Power Engineering University, Kazan, Russia
[5] South-West State University, Kursk, Russia
[6] Tver State Agricultural Academy, Tver, Russia
*Corresponding author: osys11@gmail.com

Abstract. *The article considers the possibility of using the eddy current method of non-destructive testing for the problems of measuring the electrical conductivity of thin metal films. As the object of measurement, we used copper films of various thicknesses obtained by vacuum vapor deposition. A review of current trends in the use of copper films in modern industry and science is presented, and an analysis is made of current methods of non-destructive testing suitable for studying thin copper films. A brief description of the deposition method and the hardware-software complex for measuring the electrical conductivity of the film is presented. A calibration curve is presented, which makes it possible to restore the values of the electrical conductivity of the film from the value of the signal of the eddy current transducer. GaAs samples were selected to construct a calibration curve. The decision is explained by the proximity of the values of the electrical conductivity of this chemical compound to the calculated indicators of the obtained thin films. The results of testing films with different characteristics are presented and the distribution of the electrical conductivity of the films depending on the batch is shown. A series of practical measurements of thin films demonstrated the existence of a relationship between the mass of the initial substance that was subjected to deposition and the characteristics of the resulting films. According to different values of electrical conductivity within the same batch, it was concluded that there is a difference in the quality of deposition of different films.*

Keywords: eddy current transducer, electrical conductivity, thin films, copper, non-destructive testing.

1. Introduction

Currently, in the research environment, there is a rapid development of a direction that studies the production and application of thin layers of material, the thickness of which is in the range from fractions of a nanometer (monoatomic layer) to several microns. Many branches of modern production have turned their eyes towards thin metal films, in view of the prospects that such innovative materials open up. At the moment, thin films are already being used in a wide range of industries, including microelectronics, optics, microwave technology, metalworking, high vacuum technology, etc. These circumstances allow us to talk not only about the improvement of technical characteristics, but also about new technological directions.

Thin films are characterized by an extreme breadth of the spectrum of possible structures and properties, the presence of which is determined by the thickness of such materials. In this regard, the physical properties of thin films can differ significantly from the characteristics of a substance in a bulk state. These circumstances increase the interest in these materials on the part of scientific research, since they can be used to discover properties and regularities previously unknown to physics. In practical terms, the study of thin films is essential in the development of innovative technologies and devices based on them.

At present, the electrical resistance determined by the film thickness is considered to be the key parameter possessed by thin films. Practical developments allow us to make a conclusion that the regulation of the electrical conductivity of thin films makes it possible to control their structure. According to the results of the analysis of modern publications on this topic, the eddy current testing (ECT) is the most optimal direction for continuous non-destructive testing in terms of ecology, ease of use, as well as efficiency and productivity. This method is based on the phenomenon of eddy currents, the excitation of which in the object under study (in this case, in thin metal films capable of conducting electric current) makes it possible to reveal hidden inconsistencies (Figure 3).

As follows from the provisions that have been developed in modern publications, systems with overhead and screen transducers demonstrate a stable efficiency of non-destructive testing using ECT. Researchers focus on such parameters of thin films as specific electrical conductivity, thickness, as well as the detection of violations of the structure of the substance and damage. The development of special transducers and the optimization of existing ones will serve as the basis for creating general principles for the implementation of the necessary control tools.

The use of non-destructive testing methods based on eddy current effects in relation to violations of the structure of the substance of thin films has some specificity compared to typical test objects, which is expressed in the breadth of the spectrum of manifestations. The thickness of thin films varies from fractions of a nanometer to several microns; at the same time, the possible nature of violations of the structure of a substance is diverse. In modern publications devoted to the problems of eddy current testing, some conceptual directions can be traced, which can be recognized as common to the entire field of non-destructive testing, including both the theoretical part and the measuring technique itself. In particular, the emphasis is on improving measurement accuracy and expanding functionality.

Eddy current non-destructive testing systems have their own specificity, which consists in the need for constant changes in the design of sensors in accordance with the conditions of a specific task. These circumstances are due to the fact that the key informative indicator of this approach is the voltage directed to the measuring winding of the converter. It correlates with the consolidated characteristic of the β_0 sensor, which is a function of the nature of the substance, the type and parameters of internal disturbances in the structure, parameters and structure of the converter, as well as the frequency of the exciting alternating electromagnetic field. Also, when calculating the electrical characteristics of the sensor, it is necessary to take into account the defect-sensitive material parameter, the location and parameters of possible violations of the internal structure of materials, and the locality of the eddy current converter.

Electromagnetic non-destructive testing (NDT) is widely used for the evaluation of conductive materials [1–3]. One common approach, ECT, employs a system of coils that induces eddy currents in a conductive sample and subsequently monitors changes in the secondary magnetic field generated by the eddy currents [2, 4]. Defects in the sample distort the eddy currents, resulting in a change in the magnetic field detected by the coils. ECT has limitations, including shallow penetration depth, an inability to detect defects with interfaces parallel to the surface, and the requirement that the probe maintain minimal lift-off from the test material. Despite these limitations, ECT is widely used for NDT and inspection because of the advantages offered in terms of cost, portability and ease of interpretation of results. Currently, the practical utility of ECT is restricted to conductive materials. However, with the growing use of nonconductive materials in industrial applications that require non-destructive evaluation, there is a need for an approach for these materials with comparable advantages to ECT.

During ECT testing, the conductive or semiconductive material is excited by a coil with high frequency alternating currents. Defects including cracks, voids or delamination alter the eddy current distribution around the defect. ECT have been recently used for the inspection of composision materials [5-7]. For example, Liang Cheng et al. [8] compared ECPT with ultrasound and flash thermography for the detection of delamination in composites. However, to date, a quantitative comparison of the damage detection performance of eddy-current method for composite and metallic materials is still missing [9]

Copper (Cu) has become widely used as a connection material in very large integrated circuits due to its low electrical resistance and high resistance to electromigration [10-12]. However, copper can diffuse into silicon dioxide (SiO2) [13–15] and silicon (Si) at temperatures up to 200°C [16], which has a negative effect on the stability of electronic devices. Recently, many materials have been studied that can be used to create a thin metal film [17–19], but copper remains the most interesting of them, since it is difficult to form an intermetallic compound with Cu/Si, which ensures a relatively stable interface between them. When the thickness of the copper film is reduced to about 600-1000 nm, the measurement of the electrical conductivity of the copper film becomes relevant, both to control the deposition process and to control the thickness. Currently, there are several methods for monitoring electrical conductivity, including the four-probe method (4PP) [20-–22], the optical method [23], and the eddy current method [24]. The 4PP method is a common method for determining the thickness of a copper film in the semiconductor industry, but it requires contact of the probes with the sample surface [25]. The optical method uses the principle of interference of a light beam reflected from the surface and bottom of the film [26]. This method is well suited for transparent film, but cannot be applied to metal. The eddy current method [27-29] is a non-destructive and non-contact method with high sensitivity [30-31] that satisfies the requirements for measuring the electrical conductivity of a copper film.

The current range of scanning devices using the principles of eddy currents has limited application to the problems of measuring thin films. The thickness of such materials (100 - 500 nm) causes difficulties in flaw detection and imposes increased requirements on eddy current transducers and other elements of the scanning system. For example, the operating frequency required for efficient investigation of thin films is in the range of 1 – 10 MHz [32].

Summing up the intermediate results, we have reason to speak with confidence about the relevance of this area of research. This publication aims to describe the practice of using the eddy current method of non-destructive testing in the study of the electrical conductivity of thin metal films. Measurements will be carried out using the developed setup based on an ultra-compact transducer that uses the principles of eddy currents and is capable of effectively localizing the electromagnetic field in small areas. According to the scanning plan, the received signal from the eddy current probe will be subjected to hardware and software processing aimed at data analysis using special algorithms.

The successful achievement of this goal necessitates addressing a comprehensive set of tasks:

1. Transducer Design: Develop an eddy current transducer optimized for the specific flaw detection application. This requires selection of the core size and shape, alongside the number and turns of coils within the core, to effectively focus the electromagnetic field onto the object under investigation.

2. Software-hardware system development: Create a dedicated software and hardware system based on the designed transducer. This system should perform precise control of the eddy current testing (ECT) process, encompassing:

- Generation of alternating current with variable frequencies
- Coordinated current within the ECT windings
- Acquisition and clear visualization of the resulting signal

3. Rigorous experimental validation through controlled experiments investigated the electrical conductivity of representative thin film samples, emphasizing accurate determination of their final values.

2. Materials and methods of research

In scientific research, the method of resistive heating of a substance with subsequent deposition from the gas phase in vacuum on a glass substrate has proven itself well as a method for obtaining thin films. This method is characterized by high efficiency, low cost of equipment, safety in operation and small overall dimensions. Copper, which is widely used in science and technology due to the parameters of its electrical conductivity, was chosen as the source of the film material. The evaporation of the substance was carried out in the VUP-5 installation.

The scheme of operation of the vacuum universal post VUP-5 is shown in Figure 1 [33].

On Figure 1 under the symbols are: D1, D2 and D4 is low vacuum pumps, used to remove the main part of the gas from the chamber, D3 is high vacuum pump - to maintain vacuum by removing gas flowing from the surfaces, K is valves, K4 is high vacuum valve. WL is working volume, FP is foreline pump, FC is foreline cylinder, DP is diffusion pump.

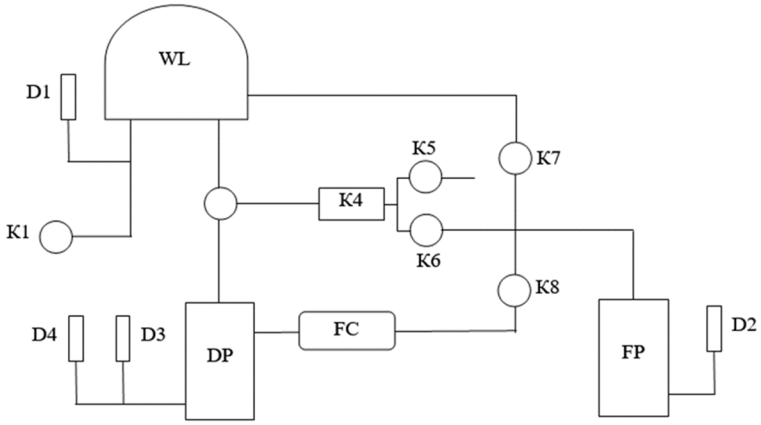

Fig.1. Scheme of work of VUP-5.

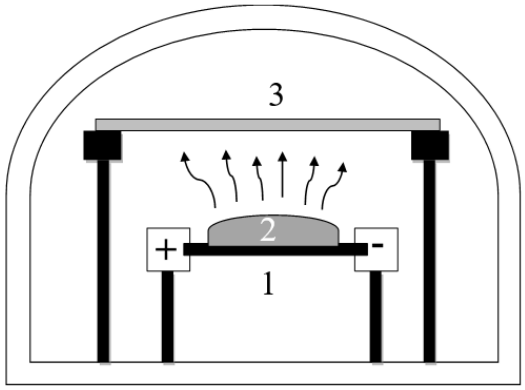

Fig.2. Scheme of evaporation and deposition in a vacuum chamber.
1) evaporator, 2) evaporated substance, 3) substrate

The scheme of evaporation of the source of the film material, as well as subsequent deposition, is shown in Figure 2. The calculated volume of copper is located on a thin tungsten plate, which acts as an evaporator. An electric current is applied to the plate, as a result of which it is heated to high temperatures and leads to the evaporation of the source of the film substance. Breaking away from the surface, the particles of the substance propagate in a vacuum, forming a vapor, which subsequently settles on a glass substrate. The glass plates used for the substrate had different areas.

Differences in the thickness of the final film is due to the different volume of the substance of the film source subjected to evaporation. According to the study plan, the amount of copper increased as the lot number increased. Within the same batch, the film samples also differ in thickness, since they were located in the chamber at different distances from the center of the evaporator.

The transducer is positioned perpendicular to the plane of the film under study, so that the measuring winding is at a minimum distance from the surface of the film, but the ECP is not in contact with it.

To control the operation of the developed converter, automate the measurement process and convenient visualize the results obtained, a hardware and software complex is required.

The developed diagram of the software and hardware complex is presented in Fig. 2.

The control unit, executed on the basis of a personal computer (PC), generates and sends commands to the generator (GEN) and the VTP positioning system. The generator, having received a control signal, generates an alternating electric current of a given frequency, which, passing through the Amplifier, acquires a given amplitude and is supplied to the exciting coil of the VTP.

The voltage on the measuring coil, passing through the Amplifier and Filter, is supplied to an analog-to-digital converter and then, in the form of a digital signal, enters the processing and visualization unit (PC). To move the ECP over the object of study, a positioning system based on Cartesian kinematics, based on a Cartesian coordinate system, was developed; this technology operates on the basis of three axes is X, Y, Z.

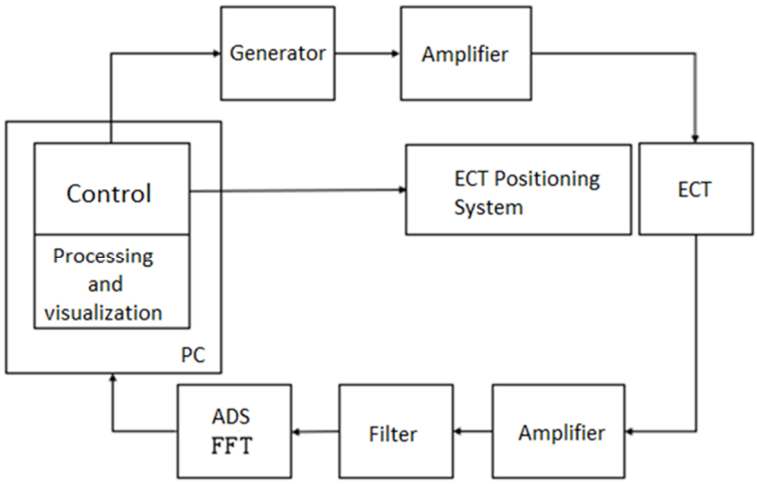

Fig.3. Scheme of the eddy current complex

The platform for securing the research object moves along the Y axis, and the sensor holder moves along the X and Z axis. Each direction has its own motor, the Y and X axes have a belt drive, the Z axis is driven by a screw system consisting of a stepper motor, a flexible coupling and a screw, the pitch of which determines the step size along this axis. The maximum size of the probing area is 22 × 22 cm, the maximum movement speed is 180 mm/s, the movement accuracy is 100 μm.

3. Results and discussion

To conduct direct measurements of electrical conductivity with the involvement of an eddy current transducer, a scale was compiled in units of the measured value and equipped with a calibration curve (Figure 4.). Approximation was carried out using the least squares method. Gallium arsenide GaAs samples were selected to construct a calibration curve. GaAs samples were cylinders of various sizes, with different types of conductivity (p, n), mobility (200-2400 cm^2/s), carrier concentration ($3{,}75\cdot10^{17}$-$3{,}3\cdot10^{18}$ $1/cm^3$) and dislocation density (10^4-3 10^4). The solution is explained by the closeness of the values of the electrical conductivity of this chemical compound to the calculated values of the obtained thin films. The operating frequency during direct measurement was 7 MHz, the signal amplitude was 1.45 V. The results obtained are shown in Table 1.

Table 1. Response amplitude from GaAs.

Electrical conductivity of the standard, MSm	0.00138	0.001792	0.071808	0.09984	0.09216	0.11616	0.12144
Amplitude, V	0.02125	0.02247	0.08553	0.09716	0.09847	0.10520	0.10828

To compile a holistic picture of the studied parameters, the results of the responses of the scanning eddy current system were collected and analyzed when measuring samples of thin films from different batches. Several batches of films with different materials and thicknesses were obtained using the resistive evaporation method. The thickness of the films in different batches varied from 100 to 800 nm, which was achieved by using different amounts of the evaporated material. The substrate dimensions were 23 x 23 mm. The films had a polycrystalline structure. Figure 5 shows the results of the measurement of the obtained samples from the first batch. It can be observed how the distribution of the incoming signal from the eddy current transducer shown in the image is uniform. Thus, we get grounds to speak about the uniformity of the deposition of the film substance and, accordingly, the quality of the material obtained.

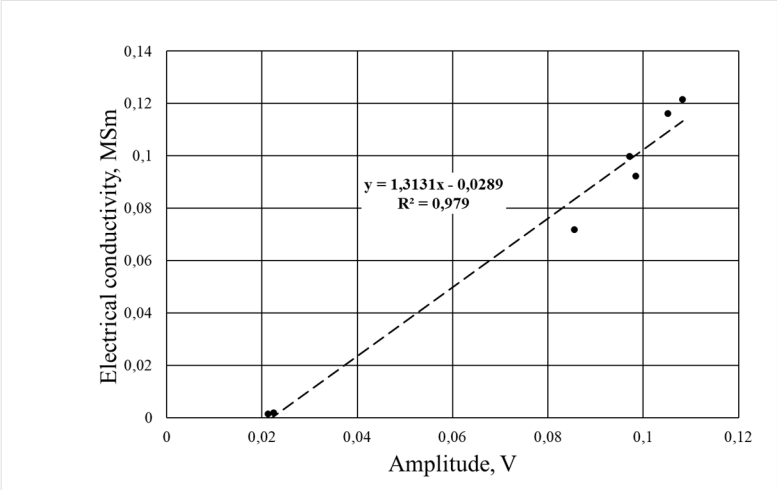

Fig.4. Calibration curve based on GaAs.

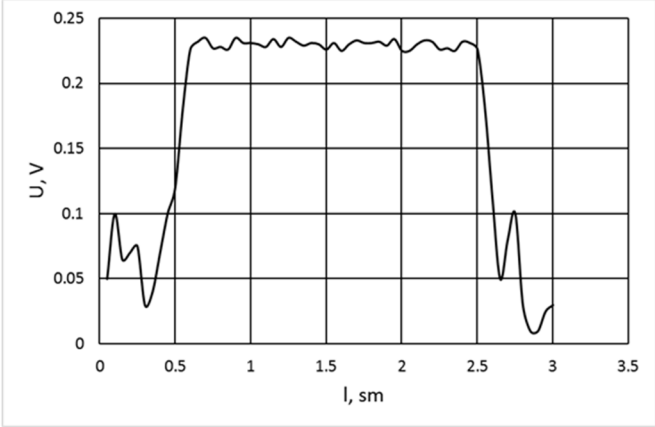

Fig.5. Results of measurements of films from batch No. 1.

Figure 6 shows the results of measuring films from the second batch. The nature of the incoming signal from the ECP has changed significantly: we can confidently speak of the presence of two regions with different signal amplitudes. This indicates the existence of some differences in the electrical conductivity of different regions of the same sample. It is important to note that within the boundaries of these areas, the signal is largely stable.

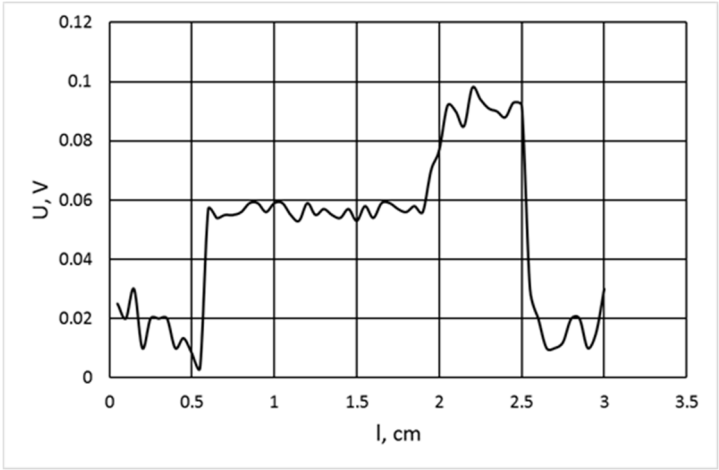

Fig.6. Results of measurements of films from batch No. 2.

Figure 7 shows the results of measuring films from the third batch of films. Judging by the nature of the distribution of the signal coming from the transducer, the samples also contain regions with different electrical conductivity (similar to the picture in the second batch). However, unlike the second batch, even within the same region, the signal is not stable either, the limits of signal change are quite wide. Thus, the electrical conductivity varies both in individual areas and throughout the sample.

Figure 8 shows the results of measuring films from the fourth batch of films. The picture demonstrates the unsystematic nature of the distribution of the signal level from the eddy current transducer. This is explained by the fact that the electrical conductivity of the samples varies significantly over their entire area without the possibility of isolating relatively stable regions. This can be explained by a change in the structure of conductive films and, accordingly, the mechanisms of movement of electric charges that create an electric current.

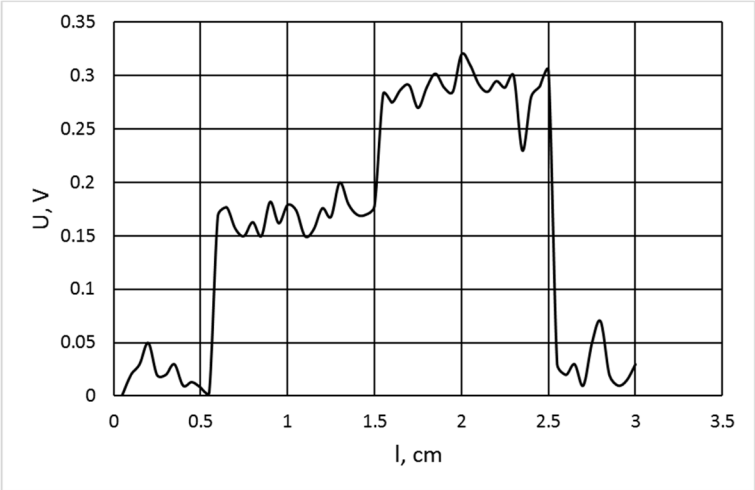

Fig. 7. Results of measurements of films from batch No. 3.

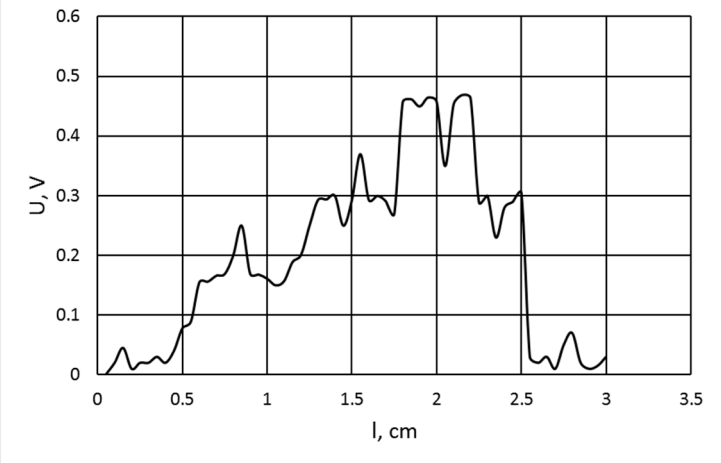

Fig. 8. Results of measurements of films from batch No. 4.

The results of film measurements are shown in Table 2.

Table 2. Average conductivity by batch.

Sample No.	Party 1 (1)	Party 1 (2)	Party 2 (1)	Party 2 (2)	Party 3 (1)	Party 3 (2)	Party 4 (1)	Party 4 (2)
Electrical conductivity MSm	0,28	0,23	0,084	0,087	0,138	0,22	0,80736	0,22469

4. Conclusion

Summing up the results of the study, it is necessary to note some key provisions.

1. In particular, it was possible to work out the practical aspects of obtaining thin metal films with various parameters, including thickness, electrical conductivity, and oxidation resistance. As part of the study, a VUP-5 vacuum unit was used to create several batches of thin films by resistive deposition.

2. To measure individual parameters of thin metal films, which are of the greatest interest, a special scanning setup was developed on the basis of an ultra-compact transducer using the principles of eddy currents.

3. The measuring setup was successfully tested on thin copper films and proved to be effective in establishing the values of the parameters of interest. The response from the measuring winding, which is part of the ECT, which is the result of the interaction of the transducer field with the film, has sufficient information content for subsequent analysis.

4. The method of calibration of the scanning setup using samples with known electrical conductivity was used in the work. Both high and low electrical conductivity values were included in the system. This made it possible to build a calibration curve, which can be used as a guide when obtaining the calculated values of the conductivity of the current film.

5. Analysis of the amplitude values of the input signal, which by their nature are derivatives of the interaction of the magnetic field of the transducer with the film, carried out taking into account the calibration curve, makes it possible to draw conclusions regarding the electrical conductivity values of thin films from different batches.

6. A series of practical measurements of thin films demonstrated the existence of a relationship between the mass of the initial substance that was subjected to deposition and the characteristics of the resulting films. This circumstance indicates that the stability of the values of the parameters of the final materials can be achieved by increasing the accuracy of taking into account the mass of the initial substance.

The scientific and practical significance of the results obtained in the work are as follows:

1. For the first time, a design of an eddy current transducer with characteristics that enables thin metal film analysis, including detecting and characterizing defects and inhomogeneities with an area of 10,000 μm2 and more, as well as determining the coordinates of film boundaries.

2. A dedicated software-hardware system based on the eddy current method was developed to enable experimental investigation of inhomogeneities and defects in thin metal films with a thickness of 100 nm or more and a specific conductivity of 14 MS/m.

3. The determined frequency range of the excitation signal of the eddy current transducer is 10-30 MHz, which allows for research of defects in the structure of films with a thickness of 100 nm and more.

Conflict of interest statement

The authors declare that they have no conflict of interest in relation to this research, whether financial, personal, authorship or otherwise, that could affect the research and its results presented in this paper.

CRediT author statement

Malikov V.N.: Conceptualization, Methodology; Ishkov A.V.: Software; Voinash S.A.: Validation; Zagidullin R.R. and Sabitov L.S.: Writing - Review & Editing; Vornacheva I.V. and Ivanov A.A.: Supervision.
The final manuscript was read and approved by all authors.

Funding

This project was funded by the Russian Science Foundation, project No. 21-79-00026 «Development of hardware and software complexes for the study of conductive materials based on subminiature eddy-current transducers».

Acknowledgments

The work is carried out in accordance with the Strategic Academic Leadership Program "Priority 2030" of the Kazan Federal University of the Government of the Russian Federation.

References

1 Sophian A., Tian G.Y. Electromagnetic and eddy current NDT: A review. *Insight*, 2001, Vol. 43, pp. 302–306. https://www.researchgate.net/publication/282684852_Electromagnetic_and_eddy_current_NDT_A_review

2 Auld B.A., Moulder J.C. Review of Advances in Quantitative Eddy Current Nondestructive Evaluation. *J. Nondestruct. Eval.,* 1999, Vol. 18, pp. 3–36. https://doi.org/10.1023/A:1021898520626

3 Garcia-Martin J., Gomez-Gil J., Vazquez-Sanchez E. Non-Destructive Techniques Based on Eddy Current Testing. *Sens.,* 2011, Vol. 11, pp. 2525–2565. https://doi.org/10.3390/s110302525

4 Lee H., Jane E., Kevin M. Low Frequency Eddy Current Testing of Insulators and Composites. *J. of Nondestr. Eval.,* 2018, Vol. 37, pp. 58-70. https://doi.org/10.1007/s10921-018-0513-1

5 Mizukami K., Mizutani Y., Kimura K., Sato A. Visualization and size estimation of fiber waviness in multidirectional CFRP laminates using eddy current imaging. *Compos. Part A.,* 2016, Vol. 90, pp. 261–70. https://doi.org/10.1016/j.compositesa.2016.07.008

6 Gao B., Lu P., Woo W. L., Tian G. Y., Zhu Y., Johnston M. Variational Bayesian subgroup adaptive sparse component extraction for diagnostic imaging system. *IEEE Trans. Ind. Electron,* 2018, Vol. 65, No 10, pp. 8142–8152. https://doi.org/10.1109/TIE.2018.2801809

7 Abidin I. Z., Tian G. Y., Wilson J., Yang S., Almond D. Quantitative evaluation of angular defects by pulsed eddy current thermography. *NDT E Int.,* 2010, Vol. 43, No 7., pp. 537–546. http://dx.doi.org/10.1016/j.ndteint.2010.05.010

8 Cheng L., Tian G. Y. Surface crack detection for carbon fiber reinforced plastic (CFRP) materials using pulsed eddy current thermography. *IEEE Sensors J.,* 2011, Vol. 11, No 12, pp. 3261-3268. https://doi.org/10.1109/JSEN.2011.2157492

9 Zijun W., Junzhen Z., Gui Yun T., Francesco C. Comparative analysis of eddy current pulsed thermography and long pulse thermography for damage detection in metals and composites. *NDT E Int.,* 2019, Vol. 107, pp. 102–155. https://doi.org/10.1016/j.ndteint.2019.102155

10 Zhu Q., Zhang X., Li S., Liu C. Communication-electrodeposition of nano-twinned Cu in void-free filling for blind microvia of high density interconnect. *Journal of The Electrochemical Society,* 2019, Vol. 166, No 1, pp. 3097-3099. https://doi.org/10.1149/2.0131901jes

11 Liang C.L., Lin K.L. Non-equilibrium supersaturation behavior in a Cu/Sn/Cu interconnect induced by room temperature electromigration. *Journal of Alloys and Compounds,* 2019, Vol. 789, No 15, pp.336-344. https://doi.org/10.1016/j.jallcom.2019.03.055

12 Baklanov M.R., Adelmann C., Zhao L., Gendt S.D. Advanced interconnects: materials, processing, and reliability. *ECS Journal of Solid State Science and Technology,* 2015, Vol. 4, No 1, Y1-Y4. https://doi.org/10.1149/2.0271501jss

13 Shang J., Hao J.X., Hang T., Li M. Diffusion barrier effect of Ta/Ti bilayer in organic dielectric/Cu interconnects. *Thin Solid Films,* 2018, Vol. 653, No 1, pp.113-118. https://doi.org/10.1016/j.tsf.2018.03.025

14 Mardani S., Norström H., Smith U. Electromigration behavior of Cu metallization interfacing with Ta versus TaN at high temperatures. *Journal of Vacuum Science & Technology,* 2016, Vol. B, 34. http://dx.doi.org/10.1116/1.4967372

15 Laurila T., Zeng K., Kivilahti J.K. Failure mechanism of Ta diffusion barrier between Cu and Si. *Journal of Applied Physics,* 2000, Vol. 88, pp. 3377-3384. https://doi.org/10.1063/1.1288692

16 Ono H., Nakano T., Ohta T. Diffusion barrier effects of transition metals for Cu/M/Si multilayers (M=Cr, Ti, Nb, Mo, Ta, W). *Applied Physics Letters,* 1994, Vol. 64, No. 12, pp.1511-1513. https://doi.org/10.1063/1.111875

17 Fang J.S., Chen J.H., Chen G.S., Cheng Y.L., Chin T.S. Sequential growth of copper film on TaN/Ta barrier substrates by alternation of Pb-UPD and Cu-SLRR. *Electrochimica Acta,* 2016, Vol. 206, No.10, pp. 45-51. https://doi.org/10.1016/j.electacta.2016.04.129

18 Lane M., Dauskardt R.H. Adhesion and reliability of copper interconnects with Ta and TaN barrier layers. *Journal of Materials Research,* 2000, Vol. 15, No 1. pp. 203-211. https://doi.org/10.1557/JMR.2000.0033

19 Zantye P.B., Kumar A., Sikder A.K. Chemical mechanical planarization for microelectronics applications. *Materials Science and Engineering: R: Reports,* 2004, Vol. 45, No 3-6, pp. 89-220. https://doi.org/10.1016/j.mser.2004.06.002

20 Wrschka P., Hernandez J., Oehrlein G.S. Chemical mechanical planarization of copper damascene structures. *Journal of The Electrochemical Society,* 2000, Vol. 147, No. 2, pp. 706-712. https://doi.org/10.1149/1.1393256

21 Xu Q., Fang J., Chen L. A chip-scale chemical mechanical planarization model for copper interconnect structures. *Microelectronic Engineering,* 2016, Vol. 149, No 5, pp.14-24. https://doi.org/10.1016/j.mee.2015.08.012

22 Bowler N., Huang Y.Q. Electrical conductivity measurement of metal plates using broadband eddy-current and four-point methods. *Measurement Science and Technology,* 2006, Vol. 16, No 11, pp. 2193-2200. https://doi.org/10.1088/0957-0233/16/11/009

23 Fujita T., Kitade K. Development of endpoint detection using optical transmittance and magnetic permeability based on skin effect in chemical mechanical planarization. *Precision Engineering,* 2019, Vol. 57, pp. 95-103. https://doi.org/10.1016/j.precisioneng.2019.03.004

24 Wang Z., Yu Y. Thickness and Conductivity Measurement of Multilayered Electricity-Conducting Coating by Pulsed Eddy Current Technique: Experimental Investigation. *IEEE Transactions on Instrumentation and Measurement,* 2019, Vol. 68, No 9, pp.3166-3172. https://doi.org/10.1109/TIM.2018.2872386

25 Kjeldby S.B., Evenstad O.M., Cooil S.P., Wells J.W. Probing dimensionality using a simplified 4-probe method. *Journal of Physics: Condensed Matter,* 2017, Vol. 29, No 39, pp.1-6. https://doi.org/10.1088/1361-648X/aa8296

26 Kim M.G., Pahk H.J. Fast and reliable measurement of thin film thickness profile based on wavelet transform in spectrally resolved whitelight interferometry. *International Journal of Precision Engineering and Manufacturing,* 2018, Vol. 19, No 2, pp. 213-219. https://doi.org/10.1007/s12541-018-0024-0

27 Dmitriev S.F., Malikov V.N., Ishkov A.V. Application of an eddy-current method to measure electrical conductivity of thin films. *IOP Conf. Series: Materials Science and Engineering,* 2018, Vol. 441, 012029. https://doi.org/10.1088/1757-899X/441/1/012029

28 Li W., Wang H., Feng Z. Non-contact online thickness measurement system for metal films based on eddy current sensing with distance tracking technique. *Review of Scientific Instruments,* 2016, Vol. 87, No 4, pp. 1-9. https://doi.org/10.1063/1.4947234

29 Wang H., Li W., Feng Z. Noncontact thickness measurement of metal films using eddy-current sensors immune to distance variation. *IEEE Transactions on Instrumentation and Measurement,* 2015, Vol. 64, No 9, pp. 2557-2564. https://doi.org/10.1109/TIM.2015.2406053

30 Li W., Ye Y., Zhang K. A thickness measurement system for metal films based on eddy current method with phase detection. *IEEE Transactions on Industrial Electronics,* 2017, Vol. 64, No. 5, pp. 3940-3949. https://doi.org/10.1109/TIE.2017.2650861

31 Sakran F., Golosovsky M., Goldberger H. High frequency eddy-current technique for thickness measurement of micronthick conducting layers. *Applied Physics Letters,* 2001, Vol. 78, No 11, pp. 1634-1636. https://doi.org/10.1063/1.1355298

32 Yin W.L., Xu K. A novel triple-coil electromagnetic sensor for thickness measurement immune to lift-off variations. *IEEE Transactions on Instrumentation and Measurement,* 2016, Vol. 65, No 1, pp. 164-169. https://doi.org/10.1109/TIM.2015.2479106

33 Porada O.K., Ivashchenko V.I. Plasma-Enhanced CVD Equipment for Deposition of Nanocomposite Nanolayered Films. *Journal of Superhard Materials,* 2019, Vol. 41, pp. 32-37. https://doi.org/10.3103/S1063457619010040

AUTHORS' INFORMATION

Malikov, V.N. – Candidate of Techn. Sciences, Associate Professor, Department of General and Experimental physics, Altai State University, Barnaul, Altai Territory, Russia; ORCID iD: 0000-0003-0351-4843; osys11@gmail.com

Ishkov, A.V. – Doctor of Techn. Sciences, Candidate of Chem. Sciences, Professor, Department of Technology structural materials and repairs machines, Altai State Agricultural University, Barnaul, Russia; ORCID iD: 0000-0003-1637-2258; svaritrffi@gmail.com

Voinash, S.A. – Junior researcher, Research laboratory "Intelligent Mobility", Institute of Design and Spatial Arts, Kazan Federal University, Kazan, Russia; Scopus Author ID: 57194339935; ORCID iD:0000-0001-5239-9883; sergey_voi@mail.ru

Zagidullin R.R. – Candidate of Techn. Sciences, Associate Professor, Kazan Federal University, Kazan, Russia; ORCID iD: 0000-0001-5185-2690; r.r.zagidullin@mail.ru

Sabitov L.S. – Doctor of Techn. Sciences, Professor, Kazan Federal University, Kazan, Russia; ORCID iD: 0000-0001-7381-9752; l.sabitov@bk.ru

Vornacheva, I.V. – Candidate of Techn. Sciences, Associate Professor, Southwestern State University, Kursk, Russia; ORCID iD: 0009-0003-5511-235X; vornairina2008@yandex.ru

Ivanov, A.A. – Candidate of Techn. Sciences, Associate Professor, Tver State Agricultural Academy, Tver, Russia; ORCID iD: 0000-0001-8190-0577; aivanov@tvgsha.ru

EURASIAN PHYSICAL TECHNICAL JOURNAL

2024, Volume 21, No. 1 (47)

https://doi.org/10.31489/2024No1/84-92

Received: 29/12/2023 Revised: 26/01/2024 Accepted: 24/02/2024 Published online: 29/03/2024
Research Article

UDC: 533.6.011, 621.453, 519.63

EFFECT OF TWO-PHASE FLOW ON THE FUEL GRAIN IGNITION AND ITS DEPARTURE FROM THE CARTRIDGE CASE

Minkov L.L., Gimayeva N.R.

National Research Tomsk State University, Tomsk, Russia
*Corresponding author: lminkov@ftf.tsu.ru

Abstract. *False heat targets play an important role in the safety of aircraft and helicopters. The main task is to ensure stable ignition of the fuel grain before leaving the cartridge case. In order to optimize this process, it is important to study the influence of various parameters, such as the size of the gap between the cartridge case and the cylindrical surface of fuel grain, as well as the size of the particles coming from the initiator and fuel grain. This article offers a physical and mathematical model of the ignition and departure process of the grain, and studies the influence of the specified parameters on the ignition time. The ignition times of the grain end surface for different particle sizes equals r = 1 μm and r = 25 μm have been estimated, the gap between the cartridge case and the cylindrical surface of grain ranged from 0.5 mm to 2 mm. The output velocities of the grain from the cartridge case are obtained for particles equal to 1 μm and 25 μm and different gap between the cartridge case and the cylindrical surface of fuel grain.*

Keywords: false heat targets, combustion, combustion products, mathematical modeling, muzzle velocity, internal ballistics

1. Introduction

Systems known as false heat targets play an important role in ensuring promotion of safety of fixed wing aircraft and helicopters flights on various missions [1]. False heat targets are devices capable of emitting a large amount of heat during propellant mixture combustion, which prevents detection of the exact location of the aircraft whose engine temperature is high [2].

False heat targets are similar to the ammunition of signal or illuminating launchers [3] and consist of a cartridge case filled with solid fuel composition. The successful use of false heat targets requires the stable ignition of the pyrotechnic composition of the fuel grain before it leaves the cartridge case [4].

In order to achieve full ignition of the end part of the fuel grain while it is in the cartridge case, it is necessary to identify the influence of various parameters on the ignition process and the grain discharge from the cartridge case. Within the framework of this task, it is necessary to determine the optimal design parameters, such as the size of the gap between the cylindrical surfaces of the cartridge case and grain, as well as the size of the particles coming from the initiating device and the pyrotechnic composition of the fuel grain. Information about the impact of these parameters on the ignition process is important to minimize the possibility of false start-ups.

The purpose of this article is to develop a physic-mathematical model of the process of ignition and departure of the fuel grain from the cartridge, to study the influence of the particle size coming from the initiating device and the pyrotechnic composition of the grain, the gap between the cartridge case and the cylindrical surface of fuel grain on the ignition time of the end grain surface.

2. Physical statement of the problem

The fuel grain 3 in cartridge case 2 is shown in Figure 1. The cartridge case at one end is closed by a membrane 4, which opens when the shot-start pressure is reached. At the initial time, combustion products consisting of the initiator gas and inert particles are received from the initiator's surface 1. Between the grain surface and the combustion products there is heat exchange due to radiation, particle conduction and convection of combustion products. When the grain surface reaches the ignition temperature, combustion products consisting of fuel grain gas and particles enter the cartridge case free volume. At the moment when boosting pressure is reached on the membrane, the membrane opens. In this case, under the influence of the dynamic pressure of combustion products flowing from the free volume, the grain begins to move along the *x* axis and leaves the cartridge case.

This article considers the research of process within the following assumptions. The combustion products flow is two-dimensional axisymmetric, the combustion products are a viscous compressible multi-temperature and multispeed medium [5] consisting of a multi-component gas (air, initiator gas and grain gas) and particles of the initiator and particles of the grain.

To estimate the time of the grain ignition, the problem of involving the fuel grain surface to the burning is solved. It is assumed, that the ignition of the surface, i.e. its inclusion in the combustion process, occurs gradually after the temperature at a given point has reached some critical value. The surface temperature is usually found either by numerically solving the non-stationary thermal conductivity equation [6, 7] or by solving the ordinary differential equation [8] obtained by one of the integral methods [9, 10]. This work uses the second method as less resource-intensive.

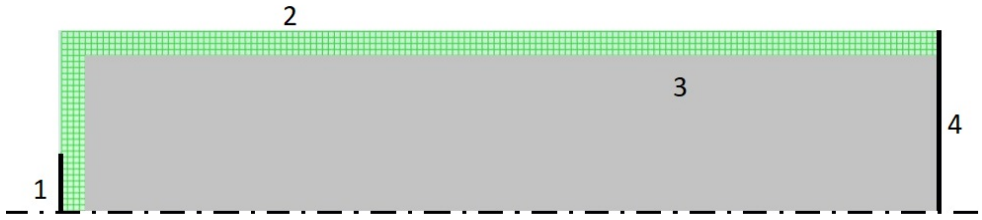

Fig.1. Product appearance: 1 – initiator, 2 – cartridge case, 3 – fuel grain, 4 – membrane

The process of fuel grain movement in the cartridge case is modeled using the equation of motion and dynamic mesh technique.

3. Governing equations

The movement of the fuel grain is modelling with the next system of equations:

$$\frac{dV_t}{dt} = \frac{1}{m_t}\left(2\pi \int_0^{y_1} y p_t dy - \pi y_1^2 p_н\right), \frac{dX_t}{dt} = V_t, \quad (1)$$

With initial conditions: $t = 0$, $V_t = 0$, $X_t = x_1$; где m_t - the mass of grain, p_t - the pressure on the left end of the grain, p_{out} - the pressure outside the cartridge case.

The system of equations describing the gas-dynamic processes occurring inside the free volume of the cartridge case can be written as:

$$\frac{\partial \mathbf{U}}{\partial t} + \nabla \cdot \mathbf{F} = \mathbf{S} \quad (2)$$

The components of the column-vectors U, F, S are presented in Table 1.

Table 1. Components of column-vectors of the system of equations (2)

	U	F	S
Continuity equation for gas	ρ_g	$\rho_g \mathbf{V}_g$	$(1-z_2)\cdot \dot{m}_T$
Equation for the i^{th} gas component	$\rho_g Y_i$	$\rho_g \left(\mathbf{V}_g Y_i - D_{i,eff}\nabla Y_i\right)$	$\begin{cases} 0, & i=1 \\ (1-z_2)\cdot \dot{m}_T, & i=2 \end{cases}$
Momentum equation for gas	$\rho_g \mathbf{V}_g$	$\rho_g \mathbf{V}_g \mathbf{V}_g - \bar{\boldsymbol{\tau}}_{eff,g}$	$\sum_{s=1}^{2} \mathbf{R}_{sg} - \alpha_g \nabla p$
Energy conservation equation for gas	$\rho_g E_g$	$\rho_g \mathbf{V}_g H_g - \bar{\boldsymbol{\tau}}_{eff,g}\cdot \mathbf{V}_g - \alpha_g \lambda_{eff,g}\nabla T$	$-p\frac{\partial \alpha_g}{\partial t} + \sum_{i=1}^{3} h_{i,g}\rho_g D_{i,eff}\nabla Y_i + \sum_{s=1}^{2}\left(Q_{sg} + \mathbf{R}_{sg}\mathbf{V}_g\right) + c_{p,g}T_{P2}(1-z_2)\cdot \dot{m}_T$
Continuity equation for the particles s^{th} fraction	ρ_s	$\rho_s \mathbf{V}_s$	$\begin{cases} 0, & s=1 \\ z_2 \dot{m}_T, & s=2 \end{cases}$
Momentum equation for the particles s^{th} fraction	$\rho_s \mathbf{V}_s$	$\rho_s \mathbf{V}_s \mathbf{V}_s - \bar{\boldsymbol{\tau}}_{eff,s}$	$-\mathbf{R}_{sg} - \alpha_s \nabla p$
Energy conservation equation for the particles s^{th} fraction	$\rho_s H_s$	$\rho_s \mathbf{V}_s H_s - \bar{\boldsymbol{\tau}}_{eff,s}\cdot \mathbf{V}_s - \alpha_s \lambda_{eff,s}\nabla T_s$	$-p\frac{\partial \alpha_s}{\partial t} - Q_{sg} - \mathbf{R}_{sg}\mathbf{V}_s + \begin{cases} 0, & s=1 \\ c_2 T_{P2} z_2 \dot{m}_T, & s=2 \end{cases}$

Here $\dot{m}_T = \rho_{T2} u_{02} p^{\nu_2}\cdot \delta(\mathbf{x}-\mathbf{x}_p)\cdot \eta(T-T_*)$ is the mass burning rate of the fuel grain per volume unit, ρ is the density, $\mathbf{V} = U\cdot\mathbf{i} + V\cdot\mathbf{j}$ is the velocity vector, p is the pressure, α is the volume fraction, Y_i is the mass fraction of the i^{th} gas component, i = 1 is the gas coming from the initiator, i = 2 is the gas coming from the surface of the burning grain, s = 1 is particles coming from the initiator, s = 2 is particles coming from the surface of the burning grain, z_2 is the mass fraction of particles in the grain, ρ_{T2} is the density of the grain composition, u_{02} is the coefficient in the burning law of grain composition, ν_2 is the exponent in the burning law of grain composition, $\delta(\mathbf{x}-\mathbf{x}_p)$ is Dirac delta function, $\mathbf{x}_p$ is the vector of burning grain surface position, $\eta(T-T_*)$ is the unit function, T_* is the grain surface ignition temperature.

Ideal gas equation:

$p = \rho_g R T_g$,

$R = \sum_{i=1}^{2} R_i Y_i + \left(1 - \sum_{i=1}^{2} Y_i\right) R_3$ is the gas constant, R_3 is the gas constant of air.

The volume fraction of particles and gas is determined from the relations:

$$\alpha_1 = \frac{\rho_1}{\rho_{10}},\ \alpha_2 = \frac{\rho_2}{\rho_{20}},\ \alpha_g + \alpha_1 + \alpha_2 = 1,$$

where ρ_{s0} is the density of particle material.

Stress tensor is written as:

$$\bar{\boldsymbol{\tau}}_{eff,j} = \alpha_j \mu_{eff,j}\left[\left(\nabla \mathbf{V}_j + \nabla \mathbf{V}_j^T\right) - \frac{2}{3}\nabla\cdot\mathbf{V}_j\cdot\bar{\mathbf{I}}\right],$$

where $j = g$ is gas, $j = s$ are particles, $\bar{\mathbf{I}}$ is unit tensor.

Gas enthalpy $E_g = H_g - \frac{\alpha_g p}{\rho_g}$.

Particle enthalpy $H_s = h_s + \frac{\mathbf{V}_s^2}{2}$, $h_s = h_s^0(T_{ref}) + \int_{T_{ref}}^{T_s} c_s dT$.

Phase interaction $\mathbf{R}_{sg} = K_{sg}\left(\mathbf{V}_s - \mathbf{V}_g\right)$, where $K_{sg} = \frac{18\alpha_s\mu_g}{d_s^2}\left(1 + 0.15\,Re_{sg}^{0.687}\right)$.

Heat-exchange rate between phases $Q_{sg} = \frac{6\alpha_p\lambda_g}{d_s^2}\mathrm{Nu}_{sg}\left(T_s - T_g\right)$,

where $\mathrm{Nu}_{sg} = 2 + 0.6\mathrm{Re}_{sg}^{1/2}\mathrm{Pr}_g^{1/3}$, $\mathrm{Pr}_g = \frac{c_{p,g}\mu_g}{\lambda_g}$

To close the governing equations (2), the SST mixture turbulence model is used.
The system of transport equations for the turbulence model has the form [11]:

$$\begin{aligned}&\frac{\partial}{\partial t}\left(\rho_m k\right) + \nabla\cdot\left(\rho_m \mathbf{V}_m k\right) = \nabla\cdot\left(\Gamma_k \nabla k\right) + G_k - Y_k + S_k\\ &\frac{\partial}{\partial t}\left(\rho_m \omega\right) + \nabla\cdot\left(\rho_m \mathbf{V}_m \omega\right) = \nabla\cdot\left(\Gamma_\omega \nabla\omega\right) + G_\omega - Y_\omega + S_\omega\end{aligned}, \tag{3}$$

where Γ_k and Γ_ω are the effective diffusivity of k and ω, respectively, Y_k and Y_ω are the dissipation of k and ω due to turbulence, G_k is the production of turbulence kinetic energy, G_ω is the generation of ω,

$\mu_{eff,j} = \mu_j + \mu_{t,j}$, $\mu_{t,j} = \frac{\rho_j}{\rho_m}\mu_{t,m}$, $\mu_{t,m} = \rho_m \frac{k}{\omega}a$, $\lambda_{eff,j} = \lambda_j + \frac{c_{p,m}\mu_{t,j}}{Pr_t}$, $D_{eff,i} = D_i + \frac{\mu_{t,i}}{\rho_m Sc_t}$, $\rho_m = \sum_{i=1}^{3}\alpha_i\rho_{i0}$,

$\mathbf{V}_m = \frac{1}{\rho_m}\sum_{i=1}^{3}\alpha_i\rho_{i0}\mathbf{V}_i$, $\mu_m = \sum_{i=1}^{3}\alpha_i\mu_i$, $S_k = k_p\dot{m}_T$, $S_\omega = \omega_p\dot{m}_T$, $k_p = \frac{3}{2}\left(I\frac{\dot{m}_T}{\rho_{m,p}}\right)^2$, $\omega_p = \frac{k_p}{10\nu_{m,p}}$, $\nu_m = \mu_m/\rho_m$.

D_i is the diffusion coefficient of the i^{th} gas component. Index p is related to near wall cell.

The source terms are: $S_{1,g} = 0$, $S_{2,g} = S_{m,g}$, $S_{m,1} = 0$, $S_{m,2} = \frac{z_2}{1-z_2}\cdot S_{m,g}$, $S_{h,g} = S_{m,g}T_{P2}c_{p,g}$, $S_{h,1} = 0$, $S_{h,2} = S_{m,2}T_{P2}c_2$, $\mathbf{V} = U\cdot\mathbf{i} + V\cdot\mathbf{j}$.

Initial condition: $\mathbf{V}_g = \mathbf{V}_s = \mathbf{0}$, $p = p_{in}$, $\rho_g = \rho_{g,н}$, $\rho_s = 0$, $Y_1 = Y_2 = 0$.

Boundary condition:

- wall boundary condition $\nabla Y_i = 0$, $\nabla T = 0$, $\frac{\partial k}{\partial n} = 0$, $\omega = \frac{80\mu_m}{y_p^2\rho_m}$;

  for cartridge case: $\mathbf{V}_g = \mathbf{V}_s = 0$;

  for fuel grain: $\mathbf{V}_g = \mathbf{V}_s = \mathbf{V}_t$, where $\mathbf{V}_t = V_t\cdot\mathbf{i} + 0\cdot\mathbf{j}$;

- outflow boundary condition: $p = p_{out}$, $\frac{\partial\varphi}{\partial n} = 0$, where $\varphi = \{\rho_s, \mathbf{V}_s, H_s\}$, $\frac{\partial^2 k}{\partial n^2} = 0$, $\frac{\partial^2\omega}{\partial n^2} = 0$;

- condition on the axis of symmetry: $V_s = V_g = 0$, $\frac{\partial\varphi}{\partial y} = 0$, where $\varphi = \{\rho, U, H, \rho_s, U_s, H_s, p, Y_i, k, \omega\}$;

- boundary between the initiator and the free volume of the cartridge case: $\rho_g U_g = \left(1 - z_1\right)\cdot\rho_{T1}u_{01}p^{\nu_1}$,

$V_g = 0$, $\rho_1 = \frac{z_1}{1-z_1}\cdot\rho_g$, $V_1 = 0$, $U_1 = U_g$, $T_g = T_1 = T_{init}$, $Y_1 = 1$, $Y_2 = 0$, $k = \frac{3}{2}I^2U_g^2$, $\omega = \frac{k}{10\nu_m}$, where: $I = 0.05$.

The temperature of the fuel surface is determined from the solution of the ordinary differential equation obtained by the method of integral ratios by approximating the temperature profile inside the fuel with an exponential function [12]

$$\frac{dT_w}{dt} = \frac{q_w^2}{\lambda_T \rho_T c_T \left(T_w - T_{wn}\right)}, \tag{4}$$

with initial condition:

$T_w\big|_{t=0} = T_{wn}$,

where $q_w = q_{conv} + q_{rad} + q_{cond}$, $q_{conv} = \alpha_{conv}\left(T - T_w\right)$, $q_{rad} = \varepsilon\sigma_0\left(T^4 - T_w^4\right)$, $q_{cond} = \rho_{s0} V_s c_s \left(T_1 - T_w\right)$, ε is the gas emissivity, σ_0 is Stefan-Boltzmann constant, c_s is the heat capacity of the particle substance, $\alpha_{conv} = 0.021\mathrm{Re}^{0.8}\mathrm{Pr}_g^{\,0.43}\lambda_g / D_{ef}$, $\mathrm{Re} = \rho_g V_{m,g} D_{ef} / \mu_g$, $D_{ef} = 4S/\Pi$ is the effective channel diameter, S is the channel cross section area, Π is the gas-touched channel cross section perimeter.

4. Numerical technique

Layering method (layer generation) was used to simulate the forward movement of the fuel grain in the cartridge case, which completes the calculation grid layers according to the movement of the grain. The result is a computational grid consisting of rectangular cells layers of a given size with a constantly changing number of cells [13]. This type of dynamic mesh is quite simple to implement through user functions in ANSYS Fluent, the application of which allows one to remesh the grid based on the geometry of the model (as a result of solving the equation of motion for the grain) in the calculation process [14].

To solve the system of governing equations, a SIMPLE-like method was used, based on a separate solution of momentum equation for each phase (Phase Coupled SIMPLE) [15]. To approximate the convective parts of the equation, an implicit upwind difference scheme of first order accuracy was used. The PRESTO (PREssure STaggering Option) scheme was used to find pressure on cell faces. Numerical methods for studying viscous gas flows with particles in channels of complex shapes show their effectiveness [16, 17].

5. The discussion of the results

The length of the grain was taken to be 72 mm, the diameter of the initiator was 10 mm, the size of the gap between the end of the grain and the cartridge case was 2 mm, and the diameter of the cartridge case was 30 mm. The size of the gap between the cylindrical surfaces of the grain and the cartridge case varied from 0.5 mm to 2 mm, the particle sizes equal r = 1 μm and r = 25 μm. The membrane boosting pressure was assumed to be 8 atm.

Calculations were carried out using the following data for the initiator igniter composition: $\rho_{T1} = 3220\ kg/\mathrm{m}^3$, $\nu_1 = 0.408$, $u_{01} = 3.74\cdot10^{-4}\ m/(\mathrm{s}\cdot Pa^{\nu_1})$, $z_1 = 0.499$, $T_{P1} = 3430\ K$; for the gas phase: $k = 1.25$, $R_1 = 156.3\ J/(\mathrm{kg}\cdot K)$; for fuel grain pyrotechnic composition: $\rho_{т2} = 1800\ kg/\mathrm{m}^3$, $\nu_2 = 0.4$, $u_{02} = 5\cdot10^{-5}\ \mathrm{m}/(\mathrm{s}\cdot Pa^{\nu_2})$, $z_2 = 0.681$, $T_{P2} = 2035\ K$, $T_* = 1100\,K$, $\lambda_т = 1.77\ W/(\mathrm{m}\cdot K)$, $c_\mathrm{T} = 1030\ J/(\mathrm{kg}\cdot K)$, for the gas phase: $k = 1.48$, $R_2 = 343\ J/(\mathrm{kg}\cdot K)$.

For analysis the numerical solution for mesh independence, the ignition time t_{ig} of the grain surface end part, which opposite the initiator was chosen as the criterion. Calculations were carried out on a sequence of grids with a step of 1 mm (mesh 1), 0.5 mm (mesh 2) and 0.25 mm (mesh 3). The time step was 10^{-5} s. The height of the gap between the cylindrical surfaces of the grain and the cartridge case was 2 mm, the particle size was chosen r = 1 μm. On grid 1, the ignition time of t_{ig} was 1.3ms, on grid 2 - 1.5ms, on grid 3 - 1.6ms. Finite-difference mesh 2 was chosen for further calculations.

Figure 2 shows gas flux line for various positions of the grain, obtained for a particle radius of 1 μm and a cylindrical gap size of 2 mm. It can be noted, that starting from the moment of time t = 5 ms, a vortex zone is formed between the ends of the cartridge case and the grain, pushed away from the grain end by the combustion products of the grain. As the fuel grain moves towards the exit from the cartridge case, the

vortex zone moves in the same direction, to the left of which a stagnation zone is formed. In the central axial zone of the free volume, a jet flow is formed due to combustion products coming from the initiator.

It will be seen from figure 3, that particles with a radius of 1 μm are carried away by the gas flow and do not accumulate on the fuel grain end surface, which complicates the process of grain heating. Particles with a radius of 25 μm are characterized by sedimentation and accumulation of particles from the initiator at the end of the grain, as well as a more intense heating process of the grain end surface compared to smallest particles.

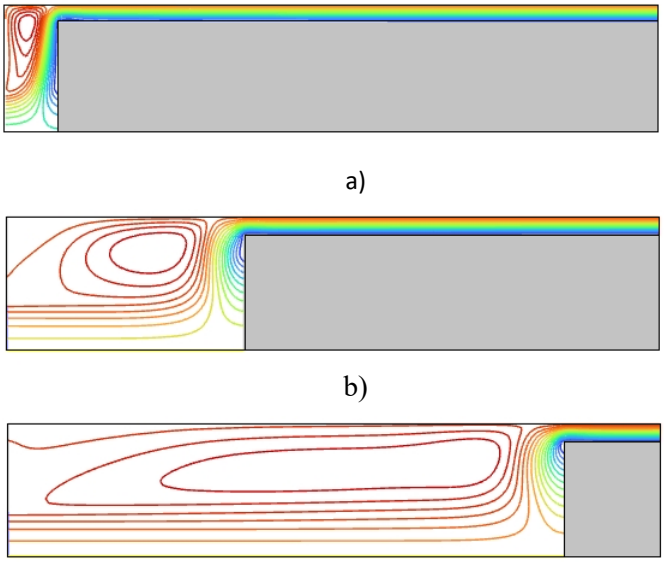

a)

b)

c)

Fig.2. Streamline d=2mm. a) t = 6 ms, b) t = 20 ms, c) t = 40 ms.

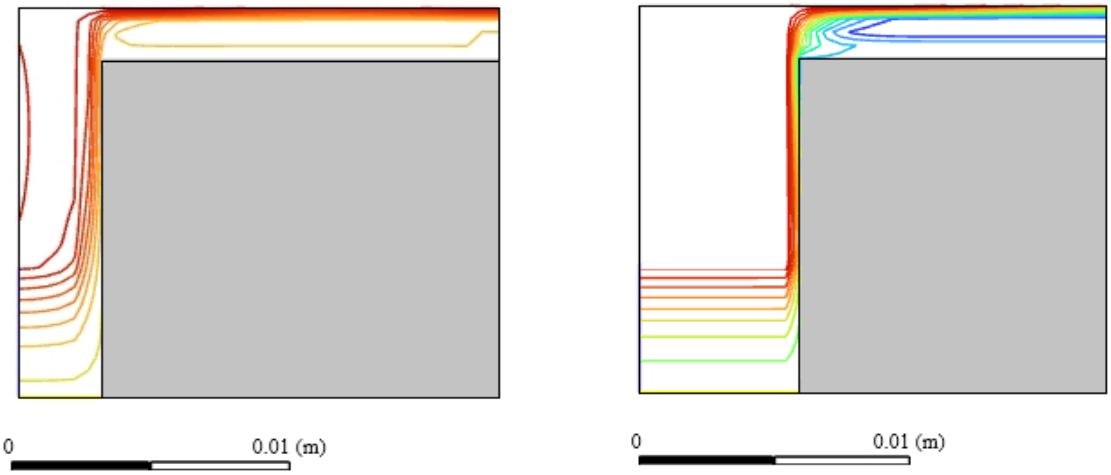

a) b)

Fig.3. Particles trajectory emitted from the initiator at time 5 ms: a) r = 1 μm, b) r = 25 μm

Figure 4 a shows the effect of the size gap between the cylindrical surface of fuel grain and cartridge case on the time ignition of the grain end part for the radius of particles r = 1 μm. The ignition time of the surface part grain, which is located opposite the initiator, is practically independent of the size gap. For the remaining surface part of the grain face, the reducing size gap increases the ignition time. When the radius of the particles is increased to r = 25 μm, (figure 4 b) the effect of the size gap has a slight effect on the ignition time of the grain end face, while the ignition time with a narrower gap is minimal.

Calculations show that increasing of the size gap between the cartridge case and the grain cylindrical part as well as an increasing particle size leads to a decrease in the ignition time of the grain end surface, which is associated with more favorable heat exchange conditions between the combustion products and the grain.

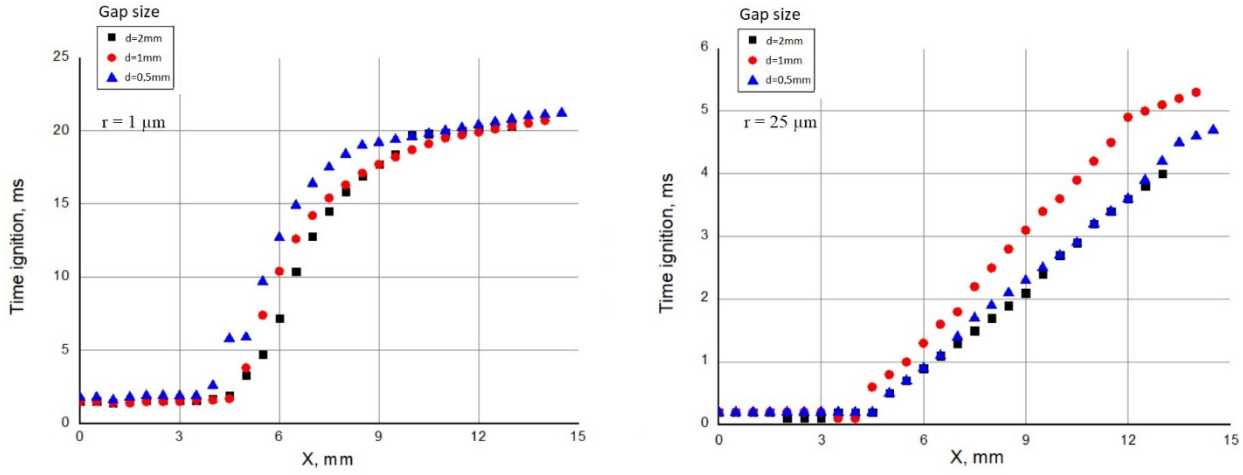

a) b)

Fig.4. Influence of the gap size between the cylindrical surfaces of the cartridge case and the fuel grain on the ignition time of the end part of the fuel grain: ■ – *d*=2mm, ● – *d*=1mm, ▲ –=0.5mm, a) *r* = 1 μm, b) *r* = 25

The speed at which the end surface of the fuel grain is connected to the combustion process, as well as the free volume in the cartridge case, affect the pressure rise rate in the cartridge case. Figure 5 shows the dependence of the average pressure in the cartridge case from time for different values of the cylindrical gap and different particle sizes. After reaching the boosting pressure of the membrane (8 atm), the pressure drops and is set equal to the quasi-static pressure.

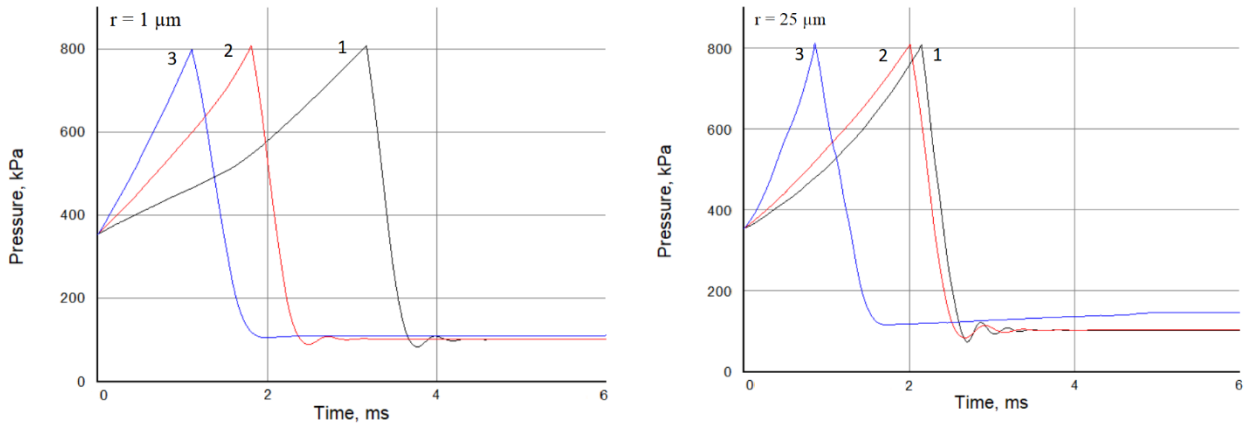

a) b)

Fig.5. Dependence of average volume pressure in the cartridge case on time:
1 - *d*=2mm, 2 - *d*=1mm, 3 - *d*=0.5mm, a) *r* = 1 μm, b) *r* = 25 μm

A reduction of the cylindrical gap and an increasing in particle size leads to fast rising in boosting of pressure and, consequently, to an earlier removal of the membrane. At the same time, a smaller cylindrical gap delays the time of the pressure drop in the cartridge case after the membrane removal, which leads to an increase in the grain launching speed (figure 6).

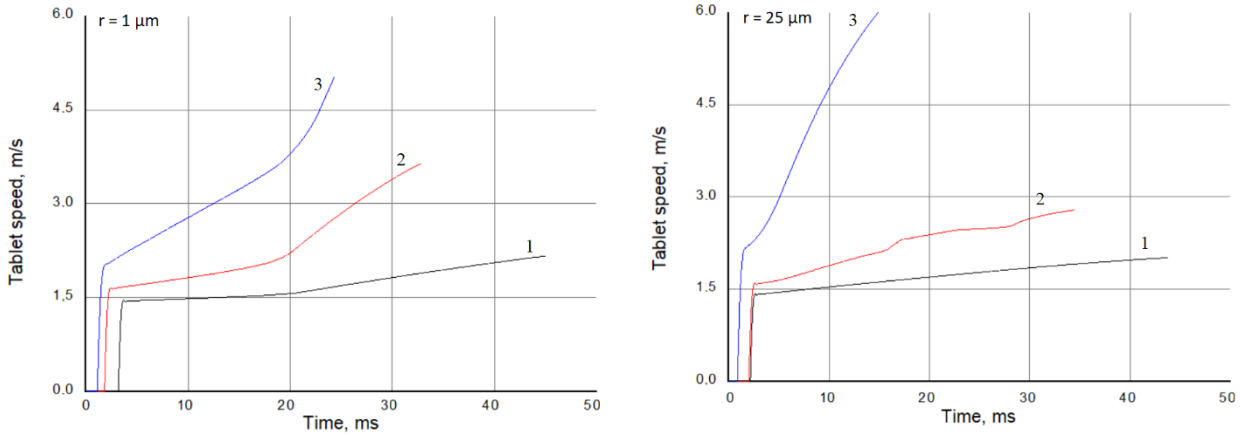

a) b)

Fig.6. Effect of gap size on grain movement speed: 1 - *d*=2mm, 2 - *d*=1mm, *3* - d=0.5mm, a) *r* = 1 μm, b) *r* = 25 μm

An increasing in particle size in the case of a cylindrical gap of 0.5 mm also leads to an increasing in the launching speed of the grain from the cartridge case and does not affect the launching speed for a gap of 2 mm. However, for a 1 mm gap, increasing the particle size reduces the grain ejection rate.

6. Conclusions

Under this study, it was found that the size of the gap between the cylindrical surfaces of the cartridge case and the grain has a significant effect on the ignition process of the end surface of the grain, which is manifested in the fact that increasing the gap size contributes to increasing the temperature grain end surface, and, therefore, leads to decreasing time ignition.

Reducing the particle size leads to increasing ignition time of the grain end part. This dependence is important for designing and creating ignition systems, for example, to achieve certain time characteristics of ignition of different areas of the grain surface.

Reducing the size gap between the cylindrical surfaces of the fuel grain and the cartridge case, and, consequently, the free volume in the cartridge case, leads to increasing in the speed at which the grain leaves the cartridge case.

Obtained results offer the challenge for further research and development in the field of creating more efficient ignition systems. Improved ignition timing and control of the ignition process can lead to increased reliability and efficiency of these systems.

Conflict of interest statement

The authors declare that they have no conflict of interest in relation to this research, whether financial, personal, authorship or otherwise, that could affect the research and its results presented in this paper.

CRediT author statement

Minkov L.L.: Conceptualization, Methodology, Writing - Review & Editing; Gimayeva N.R.: Writing - Original Draft, Visualization, Software. The final manuscript was read and approved by all authors.

Acknowledgments

This work was carried out with financial support from the Ministry of Science and High Education of the Russian Federation (State assignment No. FSMN-2020-0028).

References

1 Vernidub I.I., Puzyrev N.G. *Specialists in explosives, pyrotechnics and ammunition,* 2006. [in Russian]. https://search.rsl.ru/ru/record/01002911196

2 Shidlovskiy A.A., *Fundamentals of Pyrotechnics*, 2021. [in Russian]. https://www.labirint.ru/ books/ 826232/

3 Danilin Yu.G., Nazarov N.A., Novikova N.I. *Explosives, pyrotechnics, means of initiation in the post-war period: People. The science. Production.* 2001. [in Russian]. https://rusneb.ru/catalog/000219_000026_RU_%D0%93%D0%9F%D0%9D%D0%A2%D0%91+%D0%A0%D0%BE%D1%81%D1%81%D0%B8%D0%B8_IBIS_0000277113/

4 Mel'nikov V.E. *Modern pyrotechnics,* 2014. [in Russian]. https://pyrohobby.ru/media/filer/ 86/1a/861aa88a-2ece-4d21-a800-0177eaaacc7e/oglavlenie.pdf

5 Li Q., Liu P., He G. Fluid–solid coupled simulation of the ignition transient of solid rocket motor. *Acta Astronautica*, 2015, Vol. 110, pp.180-190. https://doi.org/10.1016/j.actaastro.2015.01.017

6 Minkov L.L., Shrager E.R., Kiryushkin A.E. Two approaches for simulating the burning surface in gas dynamics. *Key Engineering Materials*, 2016, Vol. 685, pp.114-118. https://doi.org/10.4028, www.scientific.net/ KEM.685.114

7 Nigmatulin R.I. *Dynamics of Multiphase Media*, 1991, 1, Hemisphere, New York, NY.

8 Li Y., Chen X., Xu J., Zhou Ch., Musa O. Three-dimensional multi-physics coupled simulation of ignition transient in a dual pulse solid rocket motor. *Acta Astronautica*, 2018, Vol. 146, pp.46-65. https://doi.org/10.1016/j.actaastro.2018.01.058

9 Arkhipov V.A., Zolotorev E.A., Orlova M.P., Kozlov N.N., Bondarchuk I.S., Bondarchuk S.S. Mathematical modeling of disposal of the payload fairing of a launch vehicle after completion. *Vestnik Tomskogo gosudarstvennogo universiteta. Matematika i mekhanika*, 2023, Vol.84, pp.52-67. https://doi.org/10.17223/19988621/84/5

10 Goodman T.R. Application of integral methods to transient nonlinear heat transfer. Irvine, T. , Hartnett, J. (Eds), *Advances in Heat Transfer*, Academic Press, New-York, 1964, Vol. 1, pp.51-122. https://doi.org/10.1016/S0065-2717(08)70097-2

11 Menter F.R. Two-Equation Eddy-Viscosity Turbulence Models for Engineering Applications. *AIAA Journal*, 1994, Vol. 32, No. 2, pp.1598-1605. https://doi.org/10.2514/3.12149

12 Sorkin R.Ye., *Theory of intra-chamber processes in solid fuel rocket systems*, 1983, Nauka, Moscow. [in Russian]

13 Wang Y., Zhang X. Numerical investigation on muzzle flow characteristics for small combustion chamber with embedded propelled body. *Structures*, 2023, Vol. 50, pp.1783-1793. https://doi.org/10.1016/j.istruc.2023.03.001

14 Wang Y., Ding Sh., Zhang X. A novel structure to inhibit barrel erosion induced by thermal effects in a propulsion system. *International Communications in Heat and Mass Transfer*, 2023, Vol. 147, No. 106991, pp.1-10. https://doi.org/10.1016/j.icheatmasstransfer.2023.106991

15 Vasquez S.A., Ivanov V.A. A phase coupled method for solving multiphase problems on unstructured meshes, in Proceedings of ASME 2000 Fluids Engineering Division Summer Meeting (ASME FEDSM'00), 2000, paper FEDSM2000 - 11281, pp. 1–6, Boston, MA, USA. https://www.researchgate.net/publication/291857375_A_phase_coupled_method_for_solving_multiphase_problems_on_unstructured_meshes

16 Berezovskaya I.E., Tasmukhanova A.A., Ryspaeva M.Zh., Ospanova Sh.S. Investigation of the influence of liquid fuel injection rate on the combustion process using KIVA–II software. *Eurasian Physical Technical Journal*, 2023, Vol.20, No.3 (45), pp.43-51. https://doi.org/10.31489/2023No3/43-51

17 Komarov I.I., Vegera A.N., Bryzgunov P.A., Makhmutov B.A., Smirnov A.O. Development and research of the topology of cooling baffles for blades of the axial carbon dioxide turbines. *Eurasian Physical Technical Journal*, 2022, Vol.19, No.2(40), pp.48-57. https://doi.org/10.31489/2022No2/48-57

AUTHORS' INFORMATION

Minkov, L.L. - Doctor of Phys. - Math. Sciences, Professor, Mathematical Physics Department, Physics Engineering Faculty, Tomsk State University, Tomsk, Russian Federation; ORCID ID: 0000-0001-6776-6375; lminkov@ftf.tsu.ru

Gimayeva, N.R. - Post graduate student, Physics Engineering Faculty, National Research Tomsk State University, Tomsk, Russian Federation; ORCID ID: 0009-0006-9662-6818; natalia.gimaeva@inbox.ru

EURASIAN PHYSICAL TECHNICAL JOURNAL

2024, Volume 21, No. 1 (47)

https://doi.org/10.31489/2024No1/93-103

Received: 18/10/2023 Revised: 21/02/2024 Accepted: 18/03/2024 Published online: 29/03/2024

Original Research Article

UDC 537.322

SIMULATION OF MULTIPOINT CONTACT UNDER THERMOELECTRIC TESTING

Kostina M.A.[1], Soldatov A.I.[1], Soldatov A.A.[1], Abouellail A.A.[2]

[1] National Research Tomsk Polytechnical University, Tomsk, Russia

[2] Sphinx University, New Asyut, Egypt

*Corresponding author: mariyakostina91@mail.ru

Abstract. *The article presents the results of modeling a multipoint contact in the thermoelectric method of testing. Sources of thermoelectromotive force (thermoEMF) have shown different influences, according to their type, on the load characteristics of the equivalent source obtained by parallel connection of several thermocouples as shown in the explanatory figures. The presented model is implemented in the NI LabVIEW package, which is freely available. The model was verified on three types of thermocouples (copper-constantan, copper-nichrome, and chromel-alumel), which have been connected in parallel in different quantities. The calculated load characteristics of the equivalent sources differ from the experimental ones by no more than 6%. The results of modeling the load characteristics of the equivalent thermoEMF sources obtained by parallel connection of different quantities of two types of thermocouples are presented. It is shown that in order to obtain reliable data, it is necessary to provide an equivalent source load of at least 1 kOhm.*

Keywords: thermos EMF, equivalent source, parallel connection, multipoint contact, load characteristics, superposition method.

1. Introduction

Thermoelectric testing is used in many areas of industrial production. One of the undoubted advantages of the thermoelectric method is the possibility of rapid testing. Another advantage is the simplicity of the technical implementation of this method, the compactness and autonomy of thermoelectric testing devices, ease of sample preparation, and intuitive testing procedure, which does not require special training of personnel. The main application area of the thermoelectric method is testing of metal products: sorting by steel grade, quality control of heat treatment, decarbonized layer, plastic deformation [1-20]. In scientific research, the thermoelectric method is used to measure the Seebeck coefficient [21].

A whole lineup of various thermoelectric devices is being produced for thermoelectric testing purposes. The Taiwanese company ACTTR produces Seebeck coefficient analyzer SETARAM SeebeckPro, the French company DIRECTINDUSTRY produces Seebeck coefficient and electrical resistance analyzer SR-3 Linseis, the German company NETZSCH produces NETZSCH SBA 458 Nemesis for thermoelectric testing, the Japanese company ADVENCE-RICO produces ULVAC ZEM-3 for measurement of the Seebeck coefficient and electrical conductivity, the English company QM-PLUS produces MMR Seebeck System for measuring the Seebeck coefficient of metals, the Russian company VELMAS produces a thermoelectric analyzer of metals and alloys TAMIS, and Tomsk Polytechnic University manufactures «THERMO FITNESS TESTING» for differential thermoelectric testing.

Despite the wide range of manufactured devices, all of them have disadvantages associated with low repeatability of test results [21 –22]. This can be attributed to the inhomogeneity of the surface of the tested sample in terms of chemical and phase composition. It should be noted that the influence of the heterogeneity of the chemical composition on thermoEMF is noted in the works of Karzhavin and Sungtaek [23, 24].

2. Formulation of the problem

To reduce the influence of such factors as inhomogeneity in chemical and phase composition, it was proposed to use electrodes with a linear or planar contact [25]. In this case, as the authors indicate, a multipoint contact is obtained. Each contact will be characterized by its own thermoEMF, as a result of alloyed iron, where carbides appear in the structure. Each point of contact will have different thermoelectric characteristics in relation to iron. The value of the carbide phase can vary from 5 to 30 % of the surface area of the sample, depending on the degree of alloying (Fig. 1) [26]. The equivalent thermoEMF will be determined by the parallel connection of these sources. Their number will depend on the size of the electrodes and the surface roughness (Fig. 2).

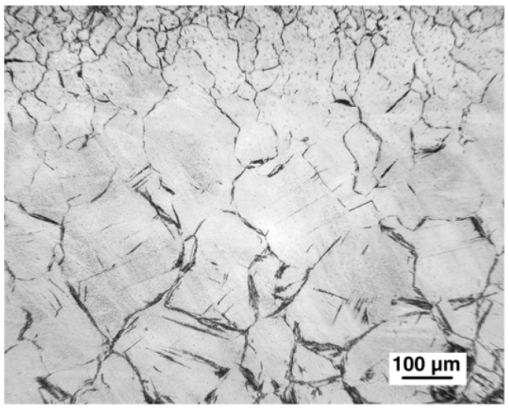

Fig.1. Carbides in alloy steel.

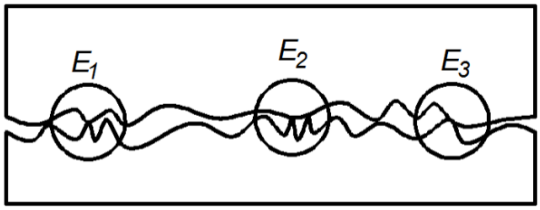

Fig.2. Projection of multi-point contact between the surfaces of the electrodes and the alloy steel

In this case, the equivalent thermoEMF is measured, which is composed of a parallel connection of thermoEMF sources with different thermoelectric characteristics: EMF value, internal resistance, power, and also different contact resistance. One approach to studying this mechanism is to use various types of thermocouples connected in parallel to simulate the circuit of multipoint contact (Fig. 3) [27-28].

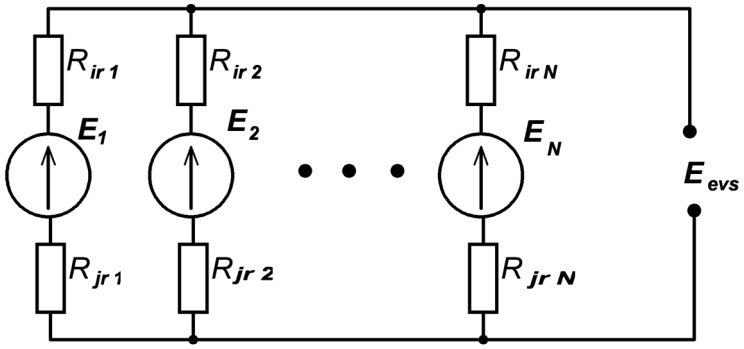

Fig.3. Equivalent electrical circuit for thermoelectric testing with a multipoint contact, $R_{ir\,1}\ldots R_{ir\,N}$ – internal resistances, $E_1 \ldots E_N$ – EMF sources, $R_{jr\,1}\ldots R_{jr\,N}$ – contact resistances, E_{evs} – equivalent EMF source

2. Model Development

The model development began with the circuit as a foundation, containing several thermoEMF sources connected in parallel to a common load (Fig. 4). Such a scheme reflects a multi-point contact, in which a thermoEMF source appears at each point of contact. In this case, taking into account the inhomogeneity in the chemical and phase composition of the surface of the tested sample, the characteristics of thermoEMF sources can be either the same or different.

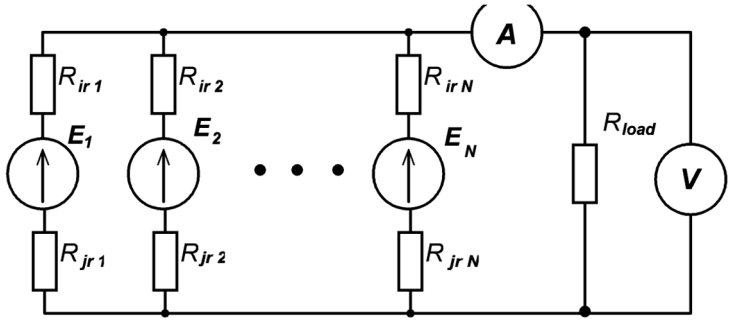

Fig.4. Equivalent circuit multipoint contact of the test sample with the electrode, $R_{\text{ir }1}\ldots R_{\text{ir N}}$ – internal resistances, $E_1\ldots E_{\text{N}}$ – EMF sources, $R_{\text{jr }1}\ldots R_{\text{jr N}}$ – contact resistances, A – ammeter, V – voltmeter

The model algorithm implements the calculation of currents from each thermoEMF source based on the superposition method. The current flowing through the load from the first EMF source is determined by the formula:

$$I_1 = \frac{E_1}{(R_{ir1} + R_{jr1}) + \dfrac{R_{load}\prod_{i=2}^{n}(R_{iri} + R_{jri})}{R_{load} + \sum_{i=2}^{n}(R_{iri} + R_{jri})}}, \tag{1}$$

where I_1 is the current of the first thermoEMF source, E_1 is the EMF of the first source, R_{iri} is the internal resistance of the EMF source under the number i, R_{jri} is the contact resistance of the EMF source under the number i, and R_{load} is the load resistance.

The current flowing through the load from the second EMF source is determined by the formula:

$$I_2 = \frac{E_2}{(R_{ir2} + R_{jr2}) + \dfrac{R_{load}\cdot(R_{ir2} + R_{jr2})\prod_{i=3}^{n}(R_{iri} + R_{jri})}{R_{load} + (R_{ir2} + R_{jr2}) + \sum_{i=3}^{n}(R_{iri} + R_{jri})}}, \tag{2}$$

where I_2 is the current of the second thermoEMF source and E_2 is the EMF of the second source.

In general terms, it can be written that the current flowing through the load from the k-th EMF source will be determined by the formula:

$$I_k = \frac{E_k}{(R_{irk} + R_{jrk}) + \dfrac{R_{load}\cdot\prod_{i=1}^{k-1}(R_{iri} + R_{jri})\cdot\prod_{i=k+1}^{n}(R_{iri} + R_{jri})}{R_{load} + \sum_{i=1}^{k-1}(R_{iri} + R_{jri}) + \sum_{i=k+1}^{n}(R_{iri} + R_{jri})}}, \tag{3}$$

where I_{k} is the current of k-th thermoEMF source and E_{k} is the EMF of the k-th source.

The total current in the load (I_{load}) is the sum of the currents from all thermoEMF sources, it is also the current of the equivalent source:

$$I_{evs} = I_{load} = \sum_{i=1}^{n} I_i . \tag{4}$$

Through the current and internal resistance of an equivalent source, its EMF can be determined:

$$E_{evs} = I_{evs} \cdot R_{ir} \quad , \tag{5}$$

where R_{ir} is the internal resistance of the equivalent thermoEMF source; I_{evs} is the current of the equivalent thermoEMF source.

The load voltage can be found by Ohm's law:

$$U_{load} = I_{load} \cdot R_{load} . \tag{6}$$

Using this technique, it is possible to calculate the load voltage, current and EMF of an equivalent source when any number of thermoEMF sources are connected in parallel.

3. Software Interface

The software was developed by NI LabVIEW software package. It calculates the load characteristics of the equivalent thermoEMF source when an unlimited number of parallel thermoelectric sources, that can have both the same and different characteristics. The obtained characteristics of the equivalent thermoEMF source can be used for further analysis. The user interface includes five different functional tabs (Figures 5-6). The "Read" tab is designed to launch a file from the database (Fig. 5). The database contains experimental data of thermoEMF sources (currents and internal resistances for 11 different values of load resistance under three different temperature conditions: 100 °C, 200 °C, 300 °C). The "Temp Database" field specifies a database file for temporary storage of current data that are used in the process of calculating the load characteristic of an equivalent thermoEMF source. The “Adding New Type” tab is responsible for adding characteristic data of new thermoEMF sources to be simulated. The “Edit” tab is intended for editing the initial values in the database in case of an error. The “Delete” tab is intended for deleting the recently added 6 columns of experimental data of thermoEMF sources. The Simulate tab is responsible for calculating and presenting the results. It contains function buttons such as "Temperature" to set the temperature, and "Number of type X" to select the desired number of thermopower sources to be investigated.

After adjusting the input data in accordance with the test condition, the program displays the calculated output data, such as the dependence of the load voltage "VL", load current, internal resistance and equivalent thermopower on the load resistance "RL" (Fig. 6).

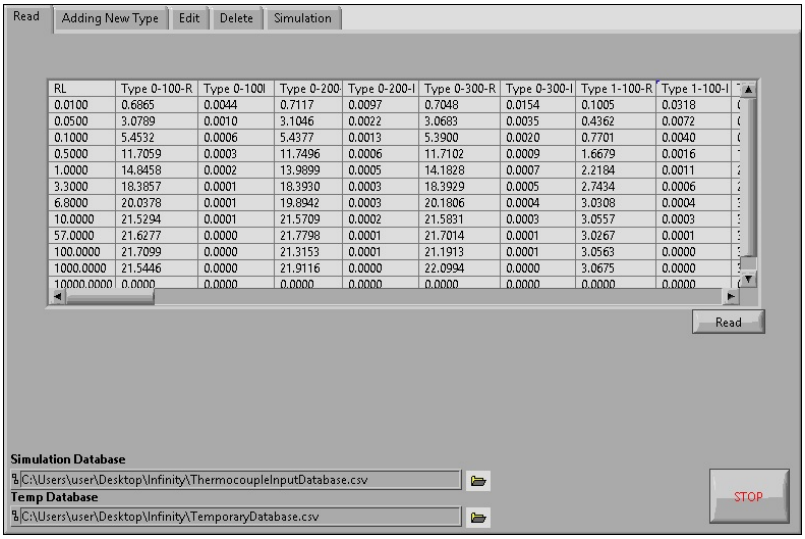

Fig.5. The “Read” tab in the program interface

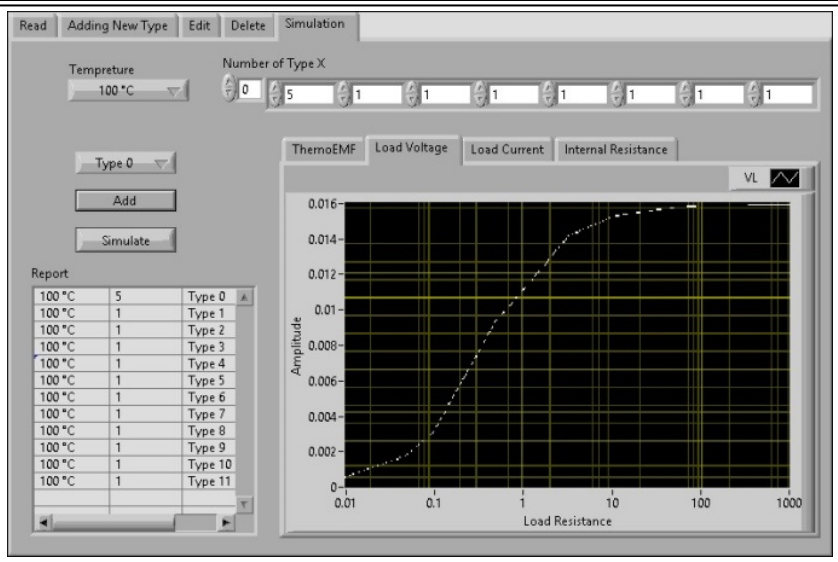

Fig.6. The “Adding New Type” tab in the program interface

The Add button is used to add new data to previous calculations. The "Simulate" button is used to start the simulation process. The simulation result is saved in a temporary file, which is indicated on the "Read" tab. The "Report" field displays the number of thermocouples that were used in the calculations.

4. Model verification

In order to verify the model, a set of experimental data is needed that reflects the electrical characteristics of typical thermoEMF sources and their combinations. Experimental studies were carried out on a specially made installation, which comprises a thermal chamber, in which investigated thermocouples are put, a voltmeter, a variable load, a microcontroller and a personal computer to control all the components of this installation [12, 29]. The thermocouples that are chosen to emulate experimental sources of thermoEMF are of types: copper-constantan, copper-nichrome and chromel-alumel. Fig. 7 shows the experimental characteristics of thermoEMF sources, each experimented individually: copper-nichrome, chromel-alumel, and copper-constantan.

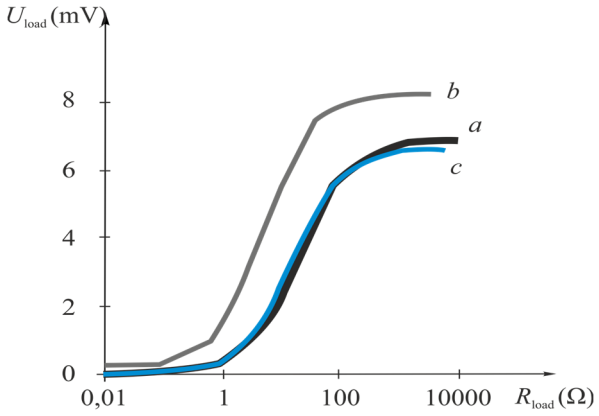

Fig.7. Experimental load characteristics of three thermocouples:
(a) copper-constantan, (b) copper-nichrome, (c) chromel-alumel

The obtained characteristics of the three types of thermocouples were loaded into the developed simulation program and used to calculate the load characteristics of the equivalent thermoEMF source, which is composed of various combinations of the experimented thermocouple types. The influence of the copper-constantan thermocouple on the load characteristic of the equivalent thermoEMF source is presented in Fig.8.

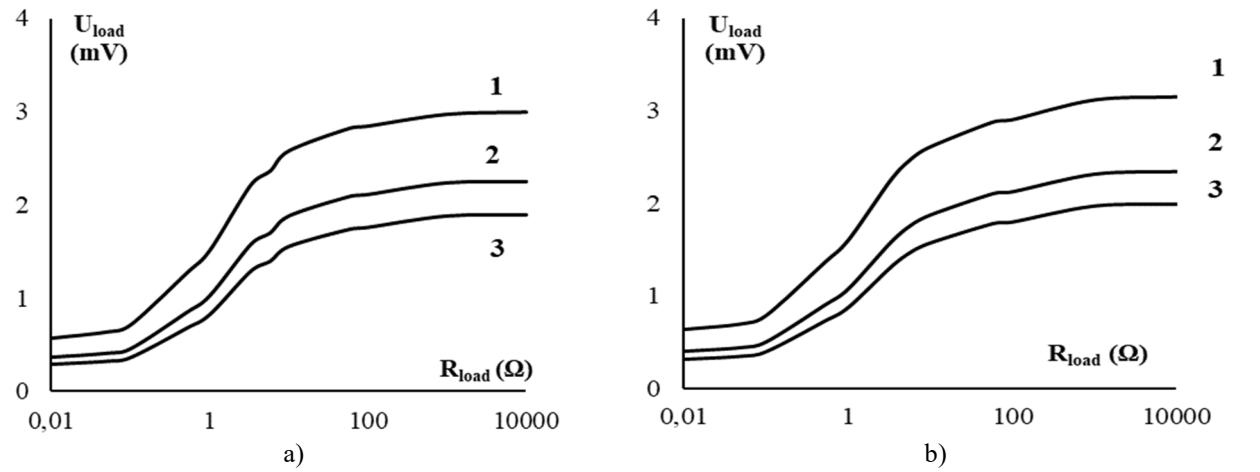

Fig.8. Load characteristics of equivalent thermopower sources for various combinations of thermocouples, (a) experimental results, (b) simulation results. Line No. 1, line No. 2, and line No. 3 indicate combinations of 4:4:4, 1:4:4, and 0:4:4, respectively. (the first digit in the thermocouple combination corresponds to the copper-constantan thermocouple, the second to copper-nichrome and the third to chromel-alumel)

Here Fig. 8.a shows the results of experimental studies, and Fig.8. b shows the results of program simulation. Line No. 1 in the figure indicates a combination of 4:4:4, line No. 2 indicates a combination of 1:4:4, and line No. 3 indicates a combination of 0:4:4.

The combinations indicate the number of thermocouples connected in parallel and their type. The first digit in the thermocouple combination corresponds to copper-constantan thermocouple, the second to copper-nichrome and the third to chromel-alumel, so the combination 4:4:4, for instance, means that four copper-constantan thermocouples, four copper-nichrome thermocouples and four chromel-alumel thermocouples were connected in parallel. The Fig.8 graphs shows a significant effect of copper-constantan thermocouple on the load characteristic of the equivalent thermoEMF source. The maximum value of thermoEMF is 3 mV for four thermocouples, 2.5 mV for one thermocouple and 1.9 mV for no thermocouple. The calculated values were 3.13 mV, 2.35 mV and 1.98 mV. The maximum deviation of the calculated data from the experimental ones did not exceed 6 %.

The influence of a chromel-alumel thermocouple on the load characteristic of the equivalent thermoEMF source is presented in Fig. 9, where Fig. 9.a shows the results of experimental studies, and fig. 9.b shows the results of simulation.

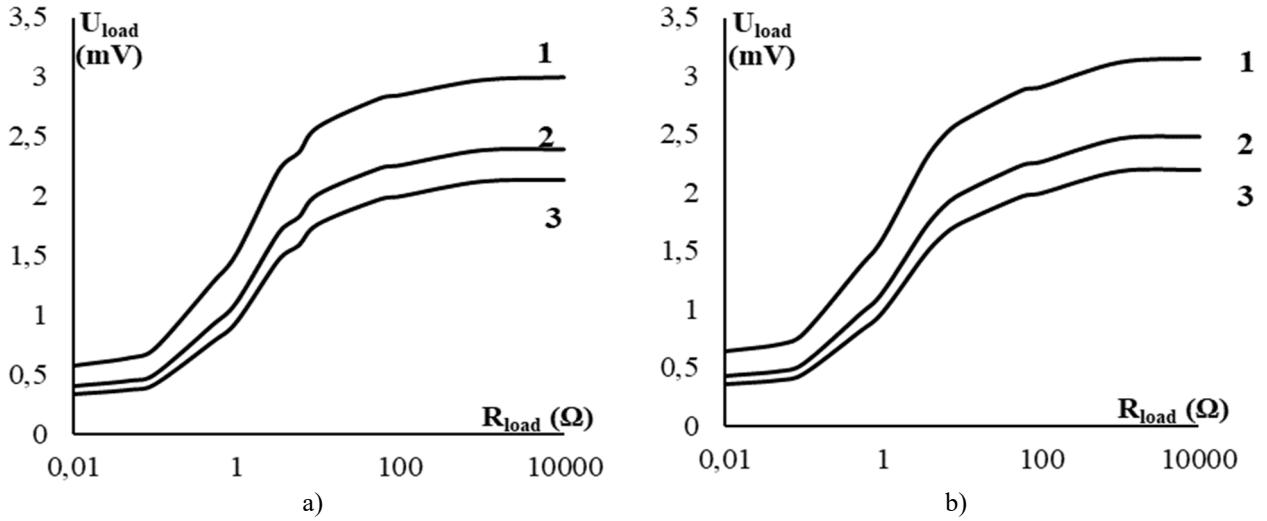

Fig.9. Load characteristic of an equivalent thermoEMF source for various combinations of thermocouples, (a) experimental results, (b) simulation results, line No. 1 - combination 4:4:4, line No. 2 - combination 4:4:1, line No. 3 - combination 4:4:0, (the first digit in the thermocouple combination corresponds to the copper-constantan thermocouple, the second to copper-nichrome and the third to chromel-alumel)

By studying the graphs of Fig. 9, we can conclude that chromel-alumel thermocouple has a noticeable effect on the load characteristic of the equivalent thermoEMF source. The maximum value of thermoEMF is 3 mV for four thermocouples, 2.39 mV for one thermocouple and 2.14 mV for no thermocouple. The calculated values were 3.13 mV, 2.49 mV and 2.19 mV. The maximum deviation of the calculated data from the experimental ones did not exceed 4.3 %.

The influence of copper-nichrome thermocouple on the load characteristic of the equivalent thermoEMF source is presented in Fig. 10, where Fig. 10.a shows the results of experimental studies, and figure 10.b shows the results of simulation.

By analyzing the graphs of Fig.10, we can conclude that chromel-alumel thermocouple has a noticeable effect on the load characteristic of the equivalent thermoEMF source. The maximum value of thermoEMF is 6.47 mV for four thermocouples, 4.89 mV for one thermocouple and 3 mV for no thermocouple. The calculated values were 6.46 mV, 5.1 mV and 3.15 mV. The maximum deviation of the calculated data from the experimental ones did not exceed 5 %. As can be seen from Figures 8-10, the model calculates the characteristics of equivalent thermoEMF sources with an error that does not exceed 6 %, and it can be used for further theoretical analysis.

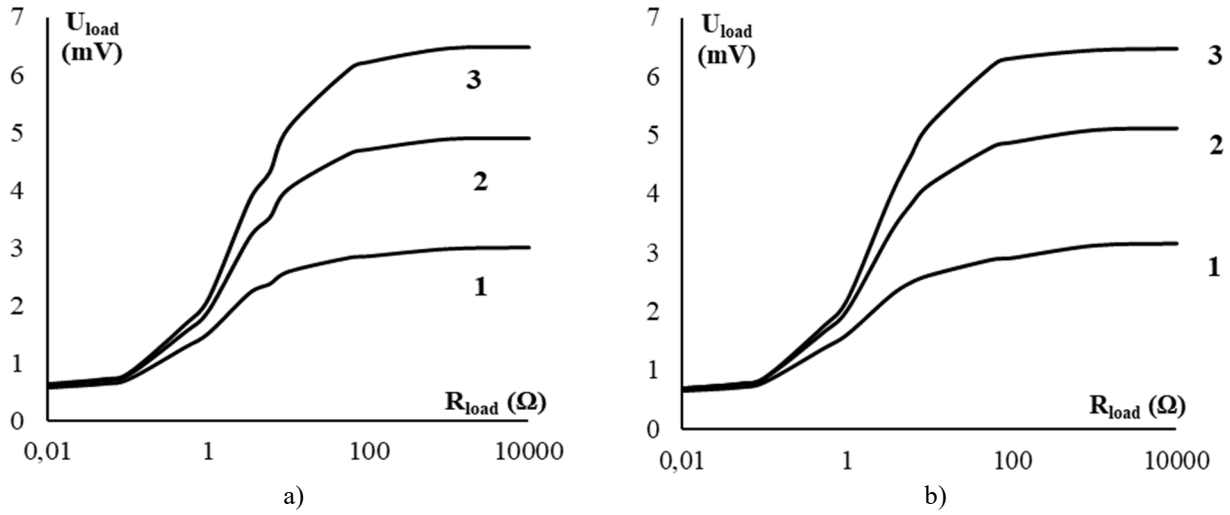

Fig.10. Load characteristic of an equivalent thermopower source for various combinations of thermocouples, (a) experimental results, (b) simulation results, line No. 1 - combination 4:4:4, line No. 2 - combination 4:1:4, line No. 3 - combination 4:0:4, (the first digit in the thermocouple combination corresponds to the copper-constantan thermocouple, the second to copper-nichrome and the third to chromel-alumel)

5. Theoretical Studies of Equivalent Thermoelectric Source Characteristics Caused by Multipoint-Contact Probing

Simulation of theoretical cases is important for studying possible properties that may arise due to the different characteristics of each thermoelectric source on the surface of the tested object in case of multipoint contact between the electrodes and the tested object. In other words, the value of thermoEMF of individual thermoelectric sources can vary over a wide range, which will lead to a change in the characteristics of the equivalent source.

Two types of thermoEMF sources (thermocouples) were used in the simulation. Their number in parallel connection is designated X:Y, where X is the number of thermocouples of the first type, and Y is the number of thermocouples of the second type. For example, the designation 1:1 corresponds to a parallel connection of one thermocouple of the first type and one thermocouple of the second type, and the designation 2:6 corresponds to a parallel connection of two thermocouples of the first type and six thermocouples of the second type. Fig. 11 shows the load characteristics of equivalent sources obtained from the simulation. In this case, two types of sources were used, differing in the thermoEMF value by 25 %.

Fig. 11 shows that at a load of more than 100 Ω, the deviation of the equivalent thermoEMF is no more than 12 % for any ratio of two types of thermoEMF sources connected in parallel. For a load of 1 kΩ, the deviation will be no more than 8 %.

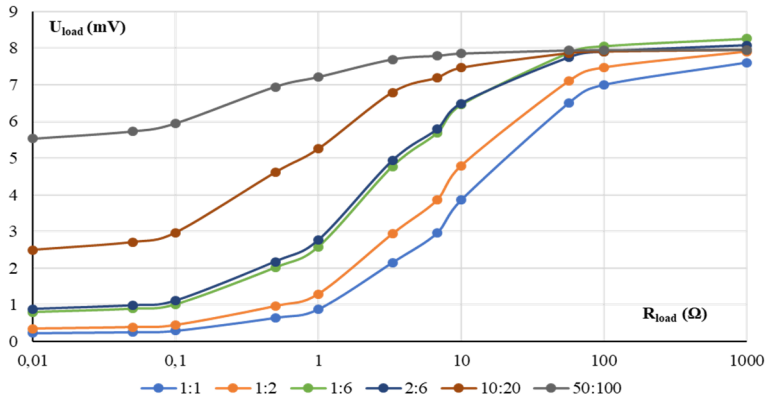

Fig.11. Load characteristics of an equivalent thermoEMF source obtained by parallel connection of two types of thermoEMF sources that differ by 25% (number of connected thermoEMF sources for the colored lines correspond to combination scales 1:1, 1:2, 1:6, 2:6, 10:20, 50:100)

Fig. 12 shows the characteristics of the equivalent source, obtained as a result of simulation, for two types of thermoEMF sources that differ in thermoEMF by 50 and 100 %.

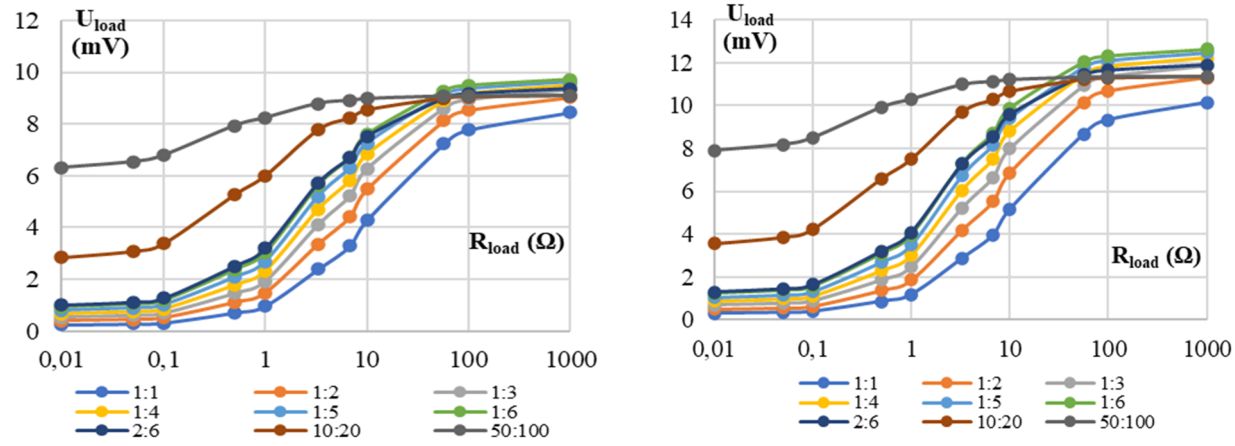

a) b)

Fig.12. Dependence of the load voltage on the load resistance for an equivalent source obtained by parallel connection of two types of thermoEMF sources, differing by 50 % (a) and 100 % (b), (number of connected thermoEMF sources for the colored lines correspond to combination scales 1:1, 1:2, 1:6, 2:6, 10:20, 50:100)

As the number of parallel-connected thermoEMF sources increases, the absolute value of the equivalent thermoEMF increases. It can also be noted that the load resistance has a strong influence in the range from 0.01 to 50 Ohms on the value of the equivalent thermoEMF. In the range above 50 Ohms the influence decreases and at loads above 1 kOhm the differences are insignificant. Fig. 12 shows that at a load of more than 100 Ω, the deviation of the equivalent thermoEMF is no more than 6 % (Figure 12.a) and no more than 20 % (Figure 12.b) for any ratio of two types of thermoEMF sources connected in parallel. For a load of 1 kΩ, the deviation will be no more than 7 % (Fig. 12.a) and no more than 18 % (Fig. 12.b).

6. Experimental application

Experimental studies were carried out on the «THERMO FITNESS TESTING» device (Fig. 13.a). For the study, two grades of steel ShKh15 (Standard: GOST 801) and U8 (Standard: GOST 1435) were taken, from

which two samples were made for the study. One of the two samples served as a reference, and the other as a tested steel product. To obtain contact close to a point, the sensor was placed at an angle to both samples, so that there was only one point of contact (Fig. 13.b). To obtain a planar contact (in our case, a linear contact was obtained), the contact line of the sensor was placed parallel to one of the surfaces of each sample. The size of the contact line of the sensor with the samples was 10 mm, which, with the surface roughness of the sensor and the manufactured samples Rz 100, provided about 50 to 100 contact points.

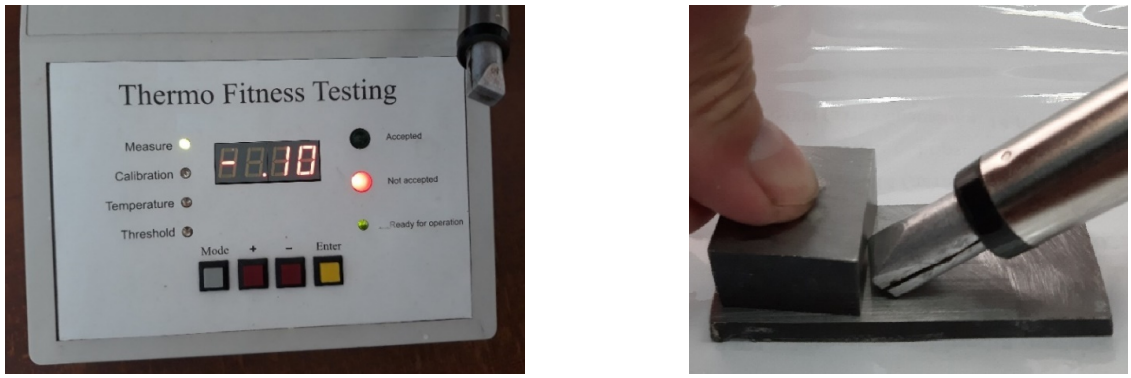

a) b)

Fig.13. «THERMO FITNESS TESTING» thermoelectric testing device, a – electronics unit with sensor, b – location of the sensor and samples during testing

The main technical characteristics of the thermoelectric testing device for metals and alloys «THERMO FITNESS TESTING» are given in Table 1. It should be noted that thermoelectric testing devices are indicator-type devices.

Table 1. Technical characteristics of the device «THERMO FITNESS TESTING».

No.	Parameter name	Unit measurements	Value
1	Supply voltage	Volt	220
2	Sensor temperature setting range	Degree Celsius	50 … 170
3	Accuracy of maintaining the set sensor temperature	Degree Celsius	± 5
4	Threshold voltage setting limits during sorting	μV	0,01…0,4
5	ThermoEMF measurement range	μV	0…±9,99
6	Device readiness time	minutes	15
7	Turning on the “Accepted” signal		EMF is less than threshold voltage
8	Turning on the “Not accepted” signal		EMF is greater than threshold voltage

The results of experimental studies using the «THERMO FITNESS TESTING» showed that the differential thermoEMF fluctuations were ±0.42 μV for ShKh15 when implementing a contact close to a point contact and ±0.14 μV for a planar contact. For U8 steel, respectively, ±0.31 μV for a point contact and ±0.12 μV for a planar contact. Thus, the conducted studies confirmed the prospects of using electrodes with planar contact to reduce the influence of inhomogeneity of the chemical composition on the result of measuring thermoEMF.

7. Conclusion

The conducted studies have shown the importance of taking into account the thermoelectric characteristics of various chemical compounds that are on the surface of the test object. To obtain high repeatability of test results, it is necessary to increase the load resistance of an equivalent thermoEMF source. Under the circumstances of thermoEMF sources with load characteristics differing up to 50 %, the load resistance should be more than 1 kΩ. In this case, the deviation of the maximum thermoEMF value of

the equivalent source will be no more than 10 % for any number of thermoEMF sources connected in parallel. With large differences in the load characteristics of different thermoEMF sources (up to 100 %), the deviation of the maximum thermoEMF value for an equivalent source will be about 20 % for any number of thermoEMF sources connected in parallel. In addition, to ensure a fluctuation of less than 5%, it is necessary to have at least 10 points of contact of each electrode of the testing probe with the test sample, and the load resistance must be equal to or greater than 1 kOhm. However, if the value load resistance is 100 Ohms, then the number of contact points should be more than 30.

The conducted studies also showed the same nature of the dependence of the voltage on the load for three different types of thermoEMF sources: copper-constantan, copper-nichrome and chromel-alumel. A similar nature of the dependence is also observed for equivalent thermoEMF sources formed by various combinations of these thermocouples.

Conflict of interest statement
The authors declare that they have no conflict of interest in relation to this research, whether financial, personal, authorship or otherwise, that could affect the research and its results presented in this paper.

CRediT author statement
Kostina M.A.: Formal analysis; Soldatov A.I.: Conceptualization, Methodology, Project administration; Soldatov A.A.: Investigation, Validation; Abouellail A.A.: Software
The final manuscript was read and approved by all authors.

References

1 Paul E.M. *Introduction to Nondestructive Testing: A Training Guide, Second Edition*. John Wiley & Sons. 2005, 712 p. https://books.google.ru/books?id=LtlFcoeIP-UC&printsec=frontcover&redir_esc=y#v=onepage&q&f=false

2 Nagy P.B. Non-destructive methods for materials' state awareness monitoring. *Insight: Non-Destructive Testing and Condition Monitoring,* 2010, Vol. 52, Is.2, pp. 61-71. https://doi.org/10.1784/insi.2010.52.2.61

3 Soldatov A.A., Seleznev A.I., Fiks I.I., Soldatov A.I., Kröning Kh.M. Nondestructive proximate testing of plastic deformations by differential thermal EMF measurements. *Russian Journal of Nondestructive Testing*, 2012, Vol. 48, Is.3, pp. 184-186. https://doi.org/10.1134/S1061830912030060

4 Li J.F., Liu W.S., Zhao L.D., Zhou M. High-performance nanostructured thermoelectric materials. *Npg Asia Mater*, 2010, Vol. 2, Is.4, pp. 152-158. https://doi.org/10.1038/asiamat.2010.138

5 Kikuchi M. Dental alloy sorting by the thermoelectric method. *European Journal of Dentistry,* 2010, Vol. 4, No.1, pp.66-70. https://www.ncbi.nlm.nih.gov/pmc/articles/PMC2798792/

6 Cooper R.F. Sorting mixed metals by the thermoelectric effect. *Physics Education,* 1976, Vol. 11, Is.4, pp. 290-292. https://doi.org/10.1088/0031-9120/11/4/004

7 Stuart C. Thermoelectric Differences Used for Metal Sorting. *Journal of Testing and Evaluation*, 1987, Vol. 15, No. 4, pp. 224-230. https://doi.org/10.1520/JTE11013J

8 Dragunov V.K., Goncharov A.L. New approaches to the rational manufacturing of combined constructions by EBW. *IOP Conference Series: Materials Science and Engineering*, 2019, Vol. 681, pp. 012010. https://doi.org/10.1088/1757-899X/681/1/012010

9 Goncharov A., Sliva A., Kharitonov I., Chulkova A., Terentyev E. Research of thermoelectric effects and their influence on electron beam in the process of welding of dissimilar steels. *IOP Conference Series: Materials Science and Engineering*, 2020, Vol. 759, Is.1, pp. 012008. https://doi.org/10.1088/1757-899X/759/1/012008

10 Kharitonov I.A., Rodyakina R.V., Goncharov A.L. Investigation of magnetic properties of various structural classes steels in weak magnetic fields characteristic for generation of thermoelectric currents in electron beam welding. *Solid State Phenomena*, 2020, Vol. 299, pp. 1201–1207. https://doi.org/10.4028/www.scientific.net/SSP.299.1201

11 Soldatov A.I., Soldatov A.A., Kostina M.A., Kozhemyak O.A. Experimental studies of thermoelectric characteristics of plastically deformed steels ST3, 08KP and 12H18N10T. *Key Engineering Materials*, 2016, Vol. 685, pp. 310-314. https://doi.org/10.4028/www.scientific.net/KEM.685.310

12 Soldatov A.I., Soldatov A.A., Sorokin P.V., Abouellail A.A., Obach I.I., Bortalevich V.Y., Shinyakov Y.A., Sukhorukov M.P. An experimental setup for studying electric characteristics of thermocouples. *SIBCON 2017 - Proceedings*, 2017, pp. 79985342017. https://doi.org/10.1109/SIBCON.2017.7998534

13 Fulton J.P., Wincheski B., Namkung M. Automated weld characterization using the thermoelectric method. *Rewiew of Progress in Quantitative Nondestructive Evaluation*, 1993, pp. 1611-1618. http://wayback.archive-it.org/1792/20100511094916/http://ntrs.nasa.gov/archive/nasa/casi.ntrs.nasa.gov/20040129656_2004126555.pdf.

14 Carreon H., Medina A. Nondestructive characterization of the level of plastic deformation by thermoelectric power measurements in cold-rolled Ti–6Al–4V samples. *Nondestructive Testing and Evaluation*, 2007, Vol. 22, Is. 4, pp. 299-311. https://doi.org/10.1080/10589750701546960

15 Carreon M. Thermoelectric detection of fretting damage in aerospace materials. *Russian Journal of Nondestructive Testing*, 2013, Vol. 50, Is.11, pp. 86940Z. https://doi.org/10.1117/12.2009448

16 Lakshminarayan B., Carreon H., Nagy P. Monitoring of the Level of Residual Stress in Surface Treated Specimens by a Noncontacting Thermoelectric Technique. *AIP Conference Procceding*, 2003, Vol. 657, pp. 1523-1530. https://doi.org/10.1063/1.1570311

17 Carreon H. Evaluation of Thermoelectric Methods for the Detection of Fretting Damage in 7075-T6 and Ti-6A1-4V Alloys. *Characterization of Minerals, Metals, and Materials,* 2015, pp. 435–442. https://doi.org/10.1007/978-3-319-48191-3_53

18 Carreon M., Barriuso S., Barrera G., González-carrasco J. L., Caballero F. Assessment of blasting induced effects on medical 316 LVM stainless steel by contacting and non-contacting thermoelectric power techniques. *Surface and Coatings Technology,* 2012, Vol. 206, pp. 2942-2947. https://doi.org/10.1016/j.surfcoat.2011.12.026

19 Hu J., Nagy P.B. On the Thermoelectric Effect of Interface Imperfections. *Review of Progress in Quantitative Nondestructive Evaluation*, 1999, Vol. 188, pp. 1487-1494. https://doi.org/10.1007/978-1-4615-4791-4_191

20 Ciylan B., Yılmaz S. Design of a thermoelectric module test system using a novel test method. International Journal of Thermal Sciences, 2007, Vol. 46, Is.7, pp. 717-725. https://doi.org/10.1016/j.ijthermalsci.2006.10.008

21 Zhou Y. and et al. Fast Seebeck coefficient measurement based on dynamic method. *Rev. Sci. Instrum*. 2014, Vol. 85, Is. 5, pp. 054904. https://doi.org/10.1063/1.4876595

22 Hu J., Nagy P.B. On the role of interface imperfections in thermoelectric nondestructive materials characterization. *Applied Physics Letters,* 1998, Vol. 73, pp. 467-469. http://dx.doi.org/10.1063/1.121902

23 Karzhavin V.A. *The influence of thermoelectric inhomogeneity on the accuracy of temperature measurement by thermocouples [Vlijanie termojelektricheskoj neodnorodnosti na tochnost' izmerenija temperatury termoparami]*. Candidate Diss. of the Techn. Science degree, Obninsk, 2010, 148 p. [in Russian]

24 Metals determinant thermoelectric OMET. Passport. Technical description Manual. [in Russian] Available at: https://analyzer24.ru/brosh/port-analiz/OMET/OMET.pdf

25 Sungtaek Ju Y. Study of interface effects in thermoelectric microrefrigerators. *Journal of Applied Physics*, 2000, Vol. 88, Is.7, pp. 4135 – 4139. https://doi:10.1063/1.1289776

26 Abouellail A.A., Chang, J., Soldatov, A.I., Soldatov, A.A., Kostina, M.A., Bortalevich, S.I., Soldatov, D.A. Influence of Destabilizing Factors on Results of Thermoelectric Testing. *Russian Journal of Nondestructive Testing*, 2022, Vol. 58, Is. 7, pp. 607–616. https://doi.org/10.1134/S1061830922070026

27 Hetznera D.W., Van Geertruyden W. Crystallography and metallography of carbides in high alloy steels. *Materials Characterization*, 2008, Vol. 59, pp. 825 – 841. https://doi:10.1016/j.matchar.2007.07.005

28 Corcoran J., Raja S., Nagy, P. Improved thermoelectric power measurements using a four-point technique. *NDT & E International*, 2017, Vol. 94, pp. 92-100. https://doi:10.1016/j.ndteint.2017.12.002

29 Abouellail A.A., Obach I.I., Soldatov A.A., Soldatov A.I. Surface inspection problems in thermoelectric testing. *MATEC Web of Conferences,* 2017, Vol. 102, pp. 01001. https://doi:10.1051/matecconf/201710201001

AUTHORS' INFORMATION

Kostina, M.A. – Candidate of techn. sciences, Associate Professor, National Research Tomsk Polytechnical University, Tomsk, Russia; ORCID ID: 0000-0003-2626-6002; mariyakostina91@mail.ru

Soldatov, A.A.– Candidate of techn. sciences, Associate Professor, National Research Tomsk Polytechnical University, Tomsk, Russia; ORCID ID: 0000-0003-0696-716X; soldatov.88@bk.ru

Soldatov, A.I.– Doctor of techn. sciences, Professor, National Research Tomsk Polytechnical University, Tomsk, Russia, Tomsk, Russia; ORCID iD: 0000-0003-1892-1644; asoldatof@mail.ru

Abouellail, A.A. - Candidate of techn. sciences, Lecturer, Sphinx University, New Asyut, Egypt; ORCID iD: 0000-0002-9357-6214; ahmed.abouellail@sphinx.edu.eg

EURASIAN PHYSICAL TECHNICAL JOURNAL

2024, Volume 21, No. 1 (47)

https://doi.org/10.31489/2024No1/104-113

Received: 16/12/2023 Revised: 23/01/2024 Accepted: 14/03/2024 Published online: 29/03/2024

Original Research Article

UDC 53.082.52

HARDWARE AND SOFTWARE COMPLEX FOR STABILITY CONTROL OF QUARRY SIDES USING OPTICAL FIBER

Madi P.Sh.[1]*, Al'kina A.D.[2], Mekhtiyev A.D.[1], Yurchenko A.V.[3,4]

[1] S. Seifullin Kazakh Agro Technical Research University, Astana, Kazakhstan

[2] Abylkas Saginov Karaganda Technical University, Karaganda, Kazakhstan

[3] Research School of Physics of High-Energy Processes, National Research Tomsk Technical University, Tomsk, Russian Federation

[4] Department of Innovative Technologies, Tomsk State University, Tomsk, Russian Federation

Corresponding author: peri@mail.ru

Abstract. *This article explores solutions to address the issue of implementing a shift monitoring system in quarries, which is the primary cause of collapsing sides and edges. For guaranteed safety and continuous monitoring of the quarry's activities, advanced fiber-optic sensors have been integrated. Their design is based on the use of single-mode optical fibers, which provides the most accurate assessment of displacements in mountainous terrain up to a distance of 30 km. Extensive laboratory studies have been carried out to deeply analyze the deformation and shear processes occurring in this geographical area. The results obtained from these analyses bode well for a significant improvement in quarry performance and a reduction in the likelihood of emergency situations.*

Keywords: fiber-optic sensor, monitoring system, open-pit mining, quarry, safety, mining, optical fiber, deformation, shear.

1. Introduction

The hardware and software system for controlling the stability of quarry sides using optical fibers is an innovative system designed to monitor and prevent hazardous situations in quarries and open-pit mines. Here are the main components and operating principles of such a system: optical sensors, where optical fibers are placed along the sides of the quarry, as well as inside certain points for direct measurement of displacements in the rock massifs; measuring devices, where special sensors and instruments read data from optical fibers and transmit them for processing; software for data analysis and processing, where the complex includes software algorithms for data processing, their analysis and interpretation; warning system, where the received data are processed and interpreted; and a warning system. When potentially hazardous situations are detected, the system can alert operators to take action to prevent accidents; automated control systems, where in some cases, if serious safety hazards are detected, the system can automatically activate measures to stabilise the pit sides, such as activating drainage systems or changing the mining regime.

The use of a hardware-software complex for monitoring the stability of the quarry sides using optical fiber significantly increases the safety of works, prevents possible accidents and provides continuous control over the condition of the quarry sides. Such systems are becoming increasingly popular in the mining

industry, where safety plays a key role, and remain relevant and in demand today. Mining in quarries and open pit mines carries the risk of rockfalls and landslides, which can lead to extremely dangerous situations for workers and have serious environmental consequences. Optical fiber-based technologies offer effective solutions for monitoring the stability of quarry slopes. The advantages of using optical fibers in this context include high accuracy and reliability of signals, resilience and the possibility of remote monitoring. By installing optical fibers on quarry sides and using appropriate hardware and software, displacements in rock masses can be continuously monitored, allowing for the timely identification of potentially hazardous areas and the prevention of accidents. Thus, remains relevant and has great potential for application in the mining and construction industry, as well as for safety and environmental protection.

The purpose of this research is to develop and implement an integrated system for monitoring and controlling the stability of quarry sides using optical fiber.

The main objective is to create a hardware and software system capable of continuously and accurately measuring displacements in rock massifs, as well as warning of possible threats of rockfalls and landslides. Through the integration of optical fibers, sensors and specialised software, we aim to develop an effective system capable of ensuring personnel safety, reducing the risk of accidents and minimising environmental impact in open pit and surface mining environments.

2. Problem statement and literature review

The relevance of the research on the creation of hardware and software complex for controlling the stability of quarry sides using optical fiber is confirmed by several factors:

1. Safety at work, where mining in quarries is associated with the risk of cave-ins and landslides, which can lead to serious accidents and loss of human life. The development of technology to continuously monitor the stability of quarry faces helps to reduce the risk of such accidents.

2. Environmental safety, where rockfalls and landslides in quarries can also cause environmental pollution, which has a negative impact on the environmental conditions in the region. Effective control of the stability of quarry sides helps to prevent such environmental disasters.

3. Production efficiency, where controlling the stability of quarry faces is also important in terms of production efficiency. Preventing rockfalls and landslides avoids temporary production stoppages and equipment damage.

4. Innovation technologies in the mining industry, where the development of new methods for monitoring and controlling the extraction of natural resources is an important area for the modern mining industry. The application of optical fiber to control the stability of quarry sides represents an innovative approach to this problem. Thus, the research in the field of creating a hardware and software system for controlling the stability of pit sides using optical fiber remains relevant and in demand in the modern mining industry, where safety, efficiency and environmental responsibility play a key role.

The novelty of the research in the creation of hardware and software complex for controlling the stability of quarry sides using optical fiber is manifested in several issues.

1. Integration of optical fiber into a monitoring system, where the ability to use optical fiber to monitor the stability of quarry sidings represents an innovative approach. Previous methods may have involved the use of different sensors or transducers, but the use of optical fiber opens up new possibilities for more accurate and continuous monitoring.

2. High accuracy and reliability, where the use of optical fiber achieves high accuracy and reliability in measuring strains and stresses in rock masses. This allows operators to obtain more accurate information on the condition of the quarry faces and take appropriate precautions.

3. Development of specialised software, where specialised software is required to analyse and interpret data obtained from optical fiber. The development of such software includes consideration of the peculiarities of optical monitoring systems operation, signal processing algorithms and visualisation of results. 4. Integration with automated control systems, where the possibility of integrating the data obtained from the monitoring system with automated control systems of the open pit mine allows to promptly respond to detected threats and take measures to prevent emergencies. Thus, the novelty of this study lies in the application of modern optical technologies to create a comprehensive system for monitoring the stability of quarry sides, which leads to increased efficiency and safety in mining.

Open pit mining, compared to underground mining, typically requires less upfront capital investment, provides better access to minerals and has a simpler infrastructure that facilitates more efficient production

management. The main issue is always to improve the efficiency of mineral extraction and ensure the safety of personnel during mining operations. It is necessary to strive for full recovery of mineral reserves with minimum stripping works. However, achieving this goal is only possible if the stability of the instrumental rock mass is ensured. This emphasises the importance of developing methods and technologies aimed at ensuring the safety and efficiency of stripping operations at open pits. To solve this issue there are various methods of control, ranging from manual labour up to the use of geotechnical radar and satellite systems of laser scanning, which quite effectively perform the functions of control of the instrument massif of the quarry, but have a number of disadvantages, such as high manufacturability and cost, as well as some dependence on weather conditions, in addition have limitations on use. The rate of development of open pit mining in Kazakhstan and worldwide is quite high, but there are a number of problems that need to be solved. One of the problems is the development of effective methods for controlling the stability of rocks in open pit mines. The analysis of works [1-4] has uncovered a predicament that defies a definitive resolution, necessitating the implementation of diverse methodologies. To address these prevailing challenges, the indispensable incorporation of a technology focusing on the advancement of sensors utilizing single-mode optical fibers becomes imperative. And the main objective of this research is to create sensors that possess a substantial degree of instability at their sides and edges. This objective has been corroborated by the findings of various simulation experiments conducted by the authors in [5, 6], who extensively discussed the advantages and disadvantages of fiber-optic sensors. Currently, there are many approaches available, each of which has been shown to be effective. However, the main challenge is to develop and implement an innovative technique using fiber-optic technology that combines all the benefits described in the research [7].

Scientists from various countries are actively working on the problem described above, and are exploring different approaches to solve it. Some of the proposed methods include the development of geotechnical radar, the application of geo-scanning methods, as well as the use of fluorometric approach and other innovative techniques. A comprehensive analysis of existing control methods and tools with a detailed description of their advantages and disadvantages is quite well researched and described in [8], which supports the concept proposed in this study. However, the problem of ensuring the stability and safety of open pit sides is still relevant and requires further improvements and search for new solutions, taking into account the variety and complexity of mining operations performed at the open pit or open pit mine, as well as mining and geological conditions [9]. Some innovative methods have limited application due to the high cost of capital and operating costs, which significantly exceed the cost of traditional instrumental measurements. Among the existing methods [8] for measuring and controlling the condition of quarry faces, the most favored are the following: geometric and hydraulic levelling, planning and spatial three-layer measurement, profile line distance measurement using light meters, profile line slope measurement, special ground light stone measurement and automated remote information transmission system for determining the relative displacement of the control point. However, the last method listed above, the automated remote information transfer system, is the most promising and acceptable to the modern mining industry, which tends to utilize digital technology. The scientific substantiation of geological support for controlling the stability of quarry sides allows the development and implementation of observation methods using modern geodetic equipment and technologies, such as high-precision observations using electronic total stations, instrumental observations using global navigation satellite systems, automated system «GEOMOS», ground-based laser scanning and radar interferometry to observe the movement of rocks and the earth's surface. However, the main drawbacks of existing methods are their dependence on obstacles, susceptibility to radio interference and the requirement for expensive equipment.

The control of pit wall stability relies mainly on an accurate assessment of the conditions and causes of deformation. Prediction and monitoring of pit wall stability are key tasks in open pit mining. When considering the factors affecting pit wall stability, the following should be kept in mind: the type of disturbance, the activity of the fracture process, its nature and configuration, as well as the type of deformation and its duration, the parameters of the tool array and the characteristics of the sides. Without systematic monitoring of these parameters, it is difficult to obtain such information.

One of the promising solutions is the use of fiber-optic technologies in the systems for controlling the stability of quarry sides. Creation of a digital control system based on a light wave instead of an electrical signal can partially solve this problem. It will allow not only to save a lot of money when creating a complex of control of the stability of the pit walls, but also to digitalize separate processes of mining production. Optical fiber has a number of advantages over traditional instrumental and electrical measurement systems

such as total stations. It does not require the use of electric current for its operation, has a low signal attenuation coefficient, is insensitive to electromagnetic interference and is fire safe [9].

The paper [10] describes the research of the physical and mathematical model of the system of controlling the stability of quarry sides using optical fiber, its physical basis of construction. In addition, it describes the issues that are related to the development of a system for controlling the stability of quarry sides using optical fiber. A fiber-optic point sensor is used in a quarry wall stability monitoring system using optical fiber. This sensor is based on a laboratory specimen that uses a dual Mach-Zehnder interferometer, which ensures zero drift. It also uses a single-mode optical fiber to control the drift with a change in sensitivity and has low temperature resistance. In addition, similar works by foreign researchers who also work with optical fiber and build fiber-optic sensors were analysed.

The research paper [11] discusses a new water pressure sensor, confirming the effectiveness of using Bragg grating for pressure monitoring. In paper [12] published in 2011, researchers presented a system for continuous pressure monitoring at roof and slab, where the main loads on the measured masses gradually shift. The effectiveness of this system was demonstrated in the same work [12] through the evaluation of the sheathing characteristics to ensure its reliable performance in different geological conditions. [13] provides information on strain measurements in the underground mining field, wherein measuring strain over an infinite length aids in correcting the strain field generated by underground operations outside the fault zone. Field inspection has the advantage of being able to continuously monitor strains under a variety of actions, including tension, compression and shear, as well as respond to tensile strains due to the ability to detect localised shear or expansion in volumetric heterogeneities.

In their paper [14], the authors describe the development and testing of a novel quarry safety monitoring system using Bragg networks. This system offers a number of advantages over traditional monitoring devices, including accurate and reliable remote monitoring of quarry operations. The researchers, who are also authors of another paper [15], present test results demonstrating the high deformation characteristics of a high-strength stainless steel optical fibre. This optical fibeк can be connected to a concrete anchor with uniform deformation, indicating its potential for theoretical and experimental monitoring of quarry movement. In addition, another research paper [16] addresses the problem of work safety by investigating the stability conditions of large-sized mining tools. This work presents an innovative analysis method that combines digital photogrammetry with distributed fibeк-optic sensors, unmanned aerial vehicles and topographic and geotechnical control systems to verify and monitor stability conditions.

The literature review has shown that the existing methods do not fully provide a solution to the problem of board stability control in terms of their efficiency, ease of operation and energy consumption. It should also be noted that the cost of some technical means is quite high for mining companies, which leads to the use of manual labor, which hinders the practical implementation of digital technologies. The human factor also brings some problems with the accuracy and timeliness of detection of potential rock collapse centers. The proposed method takes into account all modern peculiarities of science and technology development as well as the necessity of transition from electronic to optical technologies. Fiber-optic sensors will provide automatic control of rock displacement with minimum cost of one measurement point and minimum energy consumption.

3. Experimental part

The circuit diagram of the pit wall stability sensor based on optical fiber can be explained on the basis of fundamental physical laws, such as the laws of optics and Hooke's law. The laws of optics and Hooke's law play a key role in the circuit diagram of the optical fiber-based pit wall stability sensor. The law of refraction of light (Snellius' law) describes the change in the direction of a light beam when moving from one medium to another. This law is taken into account when calculating the change in the optical path of light in an optical fiber when its length changes due to displacements. Law of conservation of energy in optics, according to this law, the energy of a light beam is conserved during its passage through optical systems. This is taken into account in determining light intensity and phase in the interference phenomena used to measure the displacement of an optical fiber. Hooke's law describes the relationship between stress and displacement in elastic materials. According to this law, stress (tension or compression stress) is proportional to displacement with a constant coefficient of proportionality called the modulus of elasticity or Young's modulus. In the context of a pit wall stability sensor, Hooke's law is used to interpret optical fiber displacement data, which is converted into stresses in rock masses. The measured displacements are used to

determine the stresses in the rock masses, which allows the level of pit wall stability to be assessed. Consequently, the laws of optics and Hooke's law provide the fundamental principles for the operation of a pit wall stability sensor based on optical fibers, allowing to measure displacements and stresses in rock masses with high accuracy and reliability. The main steps of such a sensor are summarised in Table 1.

Table 1. Basic stages of sensor operation.

Change of optical fiber length under stress	Measurement of change using interference	Signal conversion	Data visualisation and analysis
- a fiber impregnated with a certain material is installed along the pit wall - under the action of stresses or deformations occurring in the rock masses - the length of the optical fiber changes, this change in length leads to a change in the optical characteristics of the fiber	- interferometry is used to measure changes in the length of an optical fiber - interference occurs between reflected light waves from different parts of the fiber - a change in the length of the fiber causes a change in the phase of the interfering waves, which can be measured by	- the measured phase change of the interfering waves is converted into a strain or stress value - signal processing algorithms are used for this purpose, which can be implemented in the software of the complex	- the obtained data on deformations and stresses in rock masses are displayed on the monitor for operators - this allows operators to monitor the stability of the pit walls in real time and take appropriate precautions

Thus, the operating principle of the sensor is based on the use of optical fiber to measure deformations in rock massifs, as well as on signal processing methods to analyse the obtained data. This allows operators to effectively monitor the stability of pit sides and prevent dangerous situations.

In this paper, fiber-optic sensors based on a two-way fiber-optic interferometer are considered, which are simple to fabricate and simple to process signals. All types of fiber-optic sensors have certain disadvantages, for example, in sensors based on interferometers, a change in sensitivity is observed, as well as in long measuring channels, the influence of temperature interference and a change in the refractive index is observed, which leads to a «signal freeze» due to a change in the initial value of the phase of light wave propagation through the core of optical fibers. The problems described above are more typical of single-mode optical fibres as they are used to observe objects at distances up to 30 km. Multimode fibres, although less susceptible to temperature interference, can operate effectively over shorter distances of 500-1000 metres. One of the solutions to completely eliminate the disadvantages of two-way fiber-optic interferometers is signal processing software using artificial intelligence algorithms. In this paper, it will be proposed to develop fiber-optic sensors based on the double Mach-Zehnder interferometer principle and using single-mode optical fiber for strain (shear) monitoring. They will have variable sensitivity and low sensitivity to temperature changes to minimise drift.

A Mach-Cender dual beam interferometer fiber sensor based on Single Mode optical fiber is proposed to control the bias change in sensitivity and the effect of zero drift caused by temperature interference. In order to change the sensitivity of the strain meter, the design was modified. The optical fiber is wound on two half-discs and can be made of plastic (Figure 1), where 1 is beam source with wavelength 1310-1625 nm, 2 is optical connector, 3 is optical fiber, 4 is movable half-disc, 5 is fixed half-disc, 6 is resilient element (damper), 7 is movable stand, 8 is fixed half-disc mounting point, 9 is sensor housing, 10 is optical wattmeter. The obtained results are explained by the inverse relationship between the values of the elasticity coefficient: the greater the number of turns of the optical fiber, the lower the elasticity coefficient. To really test the scheme, a laboratory sample of the optical fiber sensor based on the Mach-Cender interferometer was created (Figure 2). Displacement is performed by tightening the tension sleeves. When moving the ends of the ferrule in which the optical fibre is inserted, a distance of up to 3 mm can be formed between them; if necessary, the measuring range can be increased to 100 mm by extending the ferrule. However, there are limitations associated with the parameters of the ferrule surrounding the ends of the optical fiber and the tube through which the ferrule moves. To increase the distance between the ends of the fiber, multiple sensors may be connected in series or a transfer mechanism may be used. As the distance between the ends of the optical fiber increases, the characteristics of the light, such as its intensity and propagation phase, change, which is reflected in a change in the shape of the light spot. The greater the separation between the ends of

the optical fiber, the greater the degree of additional loss and optical power loss. These changes are carefully recorded by the control hardware and software system and visualised on the screen.

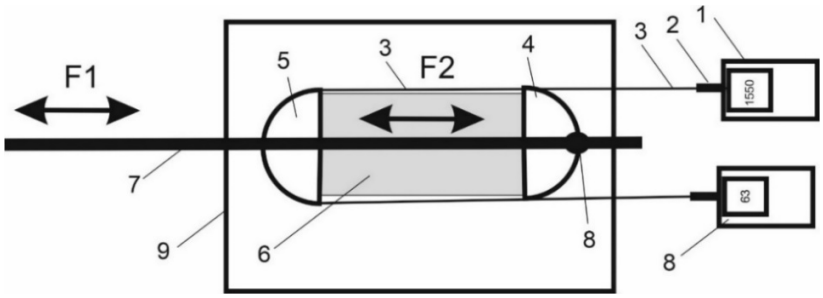

Fig.1. Strain measurement method using fiber optic sensors

Fig. 2. Laboratory sample of a fiber optic sensor based on a Mach-Zehnder interferometer

In the experiment, the initial conditions were: tension force on optical fiber in 0.5 mm increments for optical fiber with wavelength 650, 1310, 1550 nm in chamber conditions at air temperature from 22^0C to 23^0C with relative humidity within 60%. Corning SMF 9/125 μm quartz Single Mode fiber (ITU-T G.652.Standard D) is used as an optical fiber sensor. The optical fiber has a 245 micron thick primary coating. The interferometer arm contains spools with 2.03km and 2.01km optical fibers respectively, connected using a standard 20m jumper, with SC connectors on both sides. The power losses passing through the arms of the fiber-optic sensors were determined using experiments with different boundary values. Measurements of displacement values of the instrument array were repeatedly carried out, experimental data were processed by methods of mathematical statistics with the help of computer programmes. To ensure the accuracy of the obtained results, Student's criterion with a confidence interval of 0.95 will be used. The measures taken will make it possible to achieve high indicators of adequacy, neutrality, validity in relation to the processes and phenomena under study in order to identify various errors, according to the recommendations.

The obtained experimental data were processed using the computer programme Wolfram Alpha (computational knowledge engine), and a graph (Figure 3) of the dependence of the change in the additional light wave losses as a function of the applied tension force was plotted. Using the computer programme Wolfram Alpha, mathematical expressions of various approximations were obtained. Experimental processing of the results was carried out taking into account the minimum value of the Akaike information criterion, and a second-degree approximation with the coefficient of determination R^2=0.982 was chosen as the best option. The laboratory sample of the fiber-optic sensor based on the Mach-Zehnder interferometer demonstrated sufficiently high linearity and accuracy of measurements. After appropriate modification of its design, it can be successfully applied for control of array deformation. Automated approximations of data for optical fibers with wavelengths of 650, 1310, 1550 nm using Wolframalpha software were carried out, data and graphs of dependence of optical fiber loss values were obtained. For example, for a wavelength of 650 nm the dependence graph (Figure 3) of the value of optical fiber losses at step-by-step increase of tension and data diagnostics is presented.

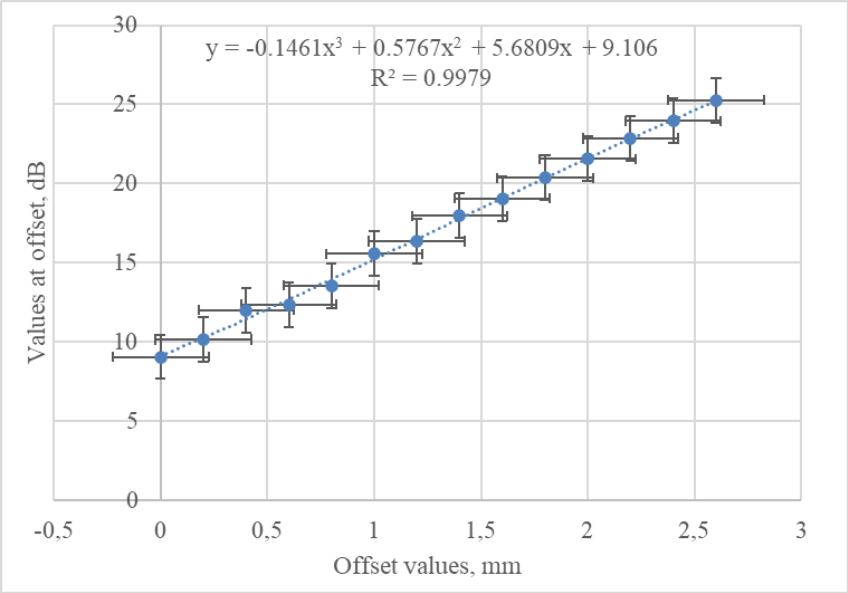

Fig. 3. Graph of the dependence of optical losses on the value of the reference point shift

The results of research in the field of creating a hardware and software complex for controlling the stability of quarry sides using optical fiber are presented as follows.

1. Creation of the prototype of the complex, where the research included the design and construction of the hardware part of the complex, including optical sensors, measuring devices and data transmission systems, as well as software for processing and analysing the obtained data.

2- Testing in laboratory conditions, where the prototype of the complex was subjected to testing in order to assess its efficiency and reliability in real conditions. During the experiments the parameters of measurement accuracy, stability of the system operation and the ability to react promptly to changes in the environment were evaluated.

3. Data acquisition and analysis, where the collected data on changes in the stability of the quarry sides were subjected to analysis using signal processing and statistical analytical methods. This allowed the identification of the main trends and characteristics of changes in rock masses and the assessment of the hazard level of certain areas.

4. Conclusions, where the performance of the complex, its advantages and limitations were determined on the basis of the research results, and recommendations for further improvement of the system were developed. These conclusions can be used to optimise the processes of controlling the stability of quarry sides and improve safety at work.

Such research results are important for the mining and construction industry, as they can contribute to the improvement of technologies for controlling and managing mining processes, as well as reducing the risks of accidents.

4. Results and discussion

As already mentioned, the fiber-optic system that ensures the safety of open-pit mining consists of three main parts: a radiation source, a fiber-optic sensor, a device for data processing and information output. The first two elements are described in detail and studied in the scientific literature. The most important element is the latter, since the effectiveness of measurements and the reliability of results depend on its operation. It is necessary to develop a data processing device and use high technologies associated with artificial intelligence algorithms necessary to output information that meets all modern requirements.

It is noted in the literature that little information about this device has been published, and the developed software package is not freely available. The more complex the devices for data processing and information output, as well as its algorithms related to decision-making, the more accurately it provides measurements and eliminates all errors associated with various interference. For example, in a distributed fiber-optic system, there may be a significant influence of temperature resistance, which leads to a drop or

freezing of the signal. Complicating the algorithm of data processing and decision-making is one of the ways to create efficient devices for processing and extracting data in all respects, but this requires certain equipment and software, which significantly increases the cost of the monitoring system. In addition to the costs of creating a monitoring system, the buyer will need to spend money on expensive and long-term research work. Given the lack of widespread demand and limited use, this creates a fairly high cost of fiber-optic tracking systems based on fiber-optic technologies, which limits the scope of their application.

Also, a number of technical problems have not been fully solved, which do not allow for their widespread implementation at mining enterprises. Taking into account the above, work has begun on the creation of its own hardware and software complex for four measuring channels. So far, the physical number of channels is limited to four, depending on the limited computing capabilities of the computer and the performance of the graphics card, as well as the developed algorithms of the program, but in the future their number will increase to the real needs of the enterprise. An increase in the number of channels leads, first of all, to an increase in cost due to an increase in the length of fiber-optic control cables, but security issues are a priority. If there is a production need, the monitoring system can manage several thousand reference stations at the same time. The appearance of the window of the hardware and software complex is shown in Figure 4.

Intellectual software based on machine learning algorithms was specially developed for the operation of fiber-optic sensors. The hardware-software complex can be multi-channel and can simultaneously work with several fiber-optic sensors, which can be remote from the data processing unit at a distance of up to ten km. The basis of the hardware-software complex is the use of OpenCV (Open Source Computer Vision Library) elements. The OpenCV version for Python programming language is used in this complex. The generation and display of graphs are carried out with the help of Matplotlib library in Python programming language. Matplotlib allows visualizing data using two-dimensional (2D) graphics, and also supports three-dimensional (3D) graphics. The interface of the software and hardware complex is implemented using the Tkinter library. The main window of the programmed, shown in Figure 4, contains the following functional elements: 1 is background start control block and stop button; 2 is camera settings block; 3 is activity monitoring block; 4 is status and signal indicators block, including motion registration function with time logging capability; 5 is button to save settings with «Apply» inscription [7,8].

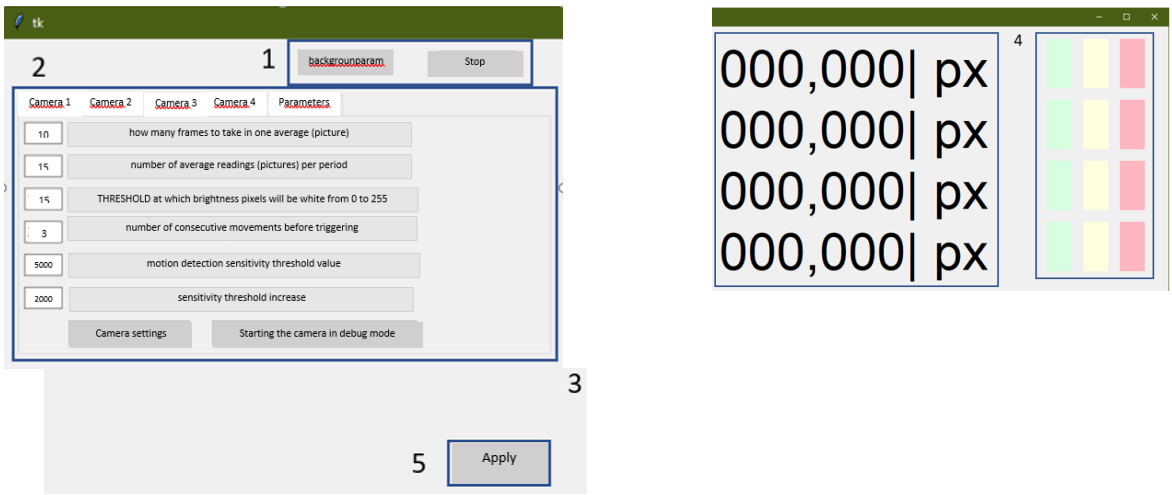

Fig. 4. The appearance of the hardware and software complex

The hardware-software complex has the ability to analyze various disturbances formed by external influences on the fiber-optic sensor. For this purpose, special algorithms have been developed that distinguish changes in the optical wave propagation parameters when the ambient temperature changes, as well as external vibration effects associated with the technological process [7]. The hardware-software complex is capable of evaluating the rate of change of the measured parameters and detecting false signals formed by various disturbances, as well as automatically perform calibration at startup. The rate of amplitude growth and frequency of influences at occurrence of interferences differs significantly from the parameters formed at real displacement of rocks that allows to perform machine learning for recognizing interferences

and real signals. Also, to combat interference hardware-software complex has a number of settings that allow you to deal with external interference, which ensures the reliability of its work and suitability for practical use.

5. Conclusions

Based on the principles of physical kinetics, statistical theory and continuum electrodynamics, an inhouse method was developed. In this work, in accordance with the developed experimental measurement scheme, the sensitivity of the photodetector is determined by the dynamic range of measurements, which includes such parameters as the power of the radiation source (laser), the number of measurement channels, optical power losses of the light pulse propagating along the optical fiber core, losses caused by each connector (connectors, optical fiber welding points), the optical length of the channel, the level of reflected power, micro bends of the optical fiber, and the micro bends of the optical fiber. The aim of this approach is to compare the calculated results with experiment to determine the effect of small deformations of the optical fiber fabricated sample on the strain sensor readings.

In-house tests have shown that the control complex using a fiber-optic sensor has a sufficiently high accuracy and linearity of displacement measurement. The control complex equipped with a fiber-optic sensor has a number of advantages over the existing observation reference stations, which do not have the ability to automate the process of controlling the displacement of rock faces and timely warn the working personnel of the danger. An important point is that the proposed control complex with the use of fiber-optic sensors is fully explosion-proof, as it uses optical fiber through which the light wave propagates. In addition, it can be noted that the design of the sensor itself is simple enough to ensure low cost of its manufacture and does not create problems with operation in the cold climate of Kazakhstan. The created control complex using a fiber-optic sensor can work simultaneously with four such sensors, but in the future their number will be increased up to 32 for one measuring module, which is quite enough for monitoring the mining zone at open-pit mines.

The main objective of the project is to address production concerns linked to enhancing mining operations' safety. Utilizing fiber-optic monitoring systems enables real-time remote monitoring of quarry stability. Findings from laboratory experiments showcase that the developed fiber-optic sensor exhibits highly satisfactory linear characteristics and boasts low power consumption when compared to electrical measuring systems, even at distances ranging from to 30 km. The proposed technical solution is a new stage in the development of systems for monitoring the geotechnical condition of rocks in open pit mines.

Conflict of interest statement

The authors declare that they have no conflict of interest in relation to this research, whether financial, personal, authorship or otherwise, that could affect the research and its results presented in this paper.

CRediT author statement

Madi P.Sh.: Investigation, Data curation, Writing- Original draft preparation; Al'kina A.D.: Software, Visualization; Mekhtiyev A.D.: Conceptualization, Writing - Review & Editing, Project administration; Yurchenko A.V.- Methodology, Validation, Resources. The final manuscript was read and approved by all authors.

Acknowledgments

This research has is funded by the Ministry of Trade and Integration of the Republic of Kazakhstan (Grant No. BR19980899 «Development of a system for monitoring the geotechnical state of mine workings and quarries based on intelligent fiber-optic sensors»).

References

1 Ozhigin S.G., Ozhigina S.B., Ozhigin D. Method of Computing Open Pit Slopes Stability of Complicated-Structure Deposits. *Journal of the Polish Mineral Engineering Society* (*Inzynieria Mineralna),* 2018, 41(1), pp. 203 - 207. https://doi.org/10.29227/IM-2018-01-32

2 Dorokhov D.V., Nizametdinov F.K., Ozhigin S.G. et al. A Technique for Surveying of Ground Surface Deformations in Mine Fiel. *Journal of Mining Science*. 2018, Vol.54 (5), pp. 874–882. https://doi.org/10.1134/S1062739118055011

3 Sannikova A.P., Bazykina L.R., Ozhigin S. Methodology for effective determination of rock jointing in calculation of open pit edges. *Journal of Industrial Pollution Control*, 2017, Vol.33. pp. 852 – 855. https://www.researchgate.net/publication/318272335_Methodology_for_effective_determination_of_rock_jointing_in_calculation_of_open_pit_edges/references

4 Ozhygin D., Šafář V., Dorokhov D., Ozhygina S., Ozhygin S., Staňková H. Terrestrial photogrammetry at the quarry and validating the accuracy of slope models for monitoring their stability. *Proceeding of the IOP Conference Series: Earth and Environmental Science*, 2021, Vol. 906(1), pp. 012062. https://doi.org/10.1088/1755-1315/906/1/012062

5 Yugay V.V., Madi P.Sh., Ozhigina S.B., Gorokhov D.A., Alkina A.D. Questions of application of fiber-optic sensors for monitoring crack growth during rock deformations. *Actual Problems of Radiophysics International Conference (APR 2021) Conference Series. Journal of Physics,* 2021, 2140 pp. 012037. https://doi.org/10.1088/1742-6596/2140/1/0120373

6 Mekhtiyev A.D., Yurchenko A.V., Kalytka V.A., Neshina Y.G., Alkina A.D., Madi, P.Sh. A Fiber-Optic Long-Base Deformometer for a System for Monitoring Rocks on the Sides of Quarries. *Tech. Phys. Lett*., 2022, Vol. 48, Is. 4, pp. 207 – 209. https://doi.org/10.1134/S1063785022070057

7 Yugay V., Mekhtiyev A., Madi P., Neshina Y., Alkina A., Gazizov F., Afanaseva O., Ilyashenko S. Fiber-Optic System for Monitoring Pressure Changes on Mine Support Elements. *Sensors,* 2022, Vol. 22(5), pp.1735. https://doi.org/10.3390/s22051735

8 Madi P.Sh., Alkina A.D., Yurchenko A.V., Mekhtiyev A.D., Aimagambetova R.Zh. Automated system hardware and software control complex. *Kazan State Power Engineering University Bulletin*, 2022, Vol. 14. No. 3(55), pp. 126-143. https://cyberleninka.ru/article/n/apparatno-programmnyy-kompleks-dlya-kontrolya-smescheniya-bortov-karierov/viewer

9 Ozhigin S., Ozhigina S., Ozhigin D. Method of Computing Open Pit Slopes Stability of Complicated-Structure *Deposits Journal of the Polish Mineral Engineering* Society. Inzynieria Mineralna, 2018, Vol. 41(1), pp. 203-207. https://doi.org/10.29227/IM-2018-01-32

10 Mehtiyev A.D., Yurchenko A.V., Neshina E.G., Alkina A.D., Madi P. Physical bases of pressure sensors creation on the basis of light refractive index change at optical fibre microbending. *News of higher educational institutions: Physics,* 2020, Vol.63, No.2, pp. 129 – 136. https://doi.org/10.17223/00213411/63/2/129 [in Russian]

11 Liu, X.-H & Wang, C. & Liu, Tongyu & Wei, Y.-B & Lu, J.-S. Fiber grating water pressure sensor and system for mine. *Acta Photonica Sinica*, 2009, Vol. 38, No.1, pp.112-114. https://m.researching.cn/articles/OJc862bfb9be78ec56

12 Kumar Atul, Kumar Dheeraj, Singh U., Gupta P S., Shankar Gauri. Optimizing fibre optics for coal mine automation *International Journal of Control and Automation*, 2011, Vol. 4, No.3, pp. 63 – 70. https://article.nadiapub.com /IJCA/vol4_no3/2.pdf

13 Madjdabadi B., Valley B., Dusseault M.B., Kaiser P.K. Numerical study of grout–rock mass interaction effect on distributed optical fibre sensor measurements. *Proceedings of the 7th Intern. Conf. on Deep and High Stress Mining, Australian Centre for Geomechanics, Perth.,* 2014, pp. 457-468. https://doi.org/10.36487/ACG

14 Yiming Zhao, Nong Zhang and Guangyao Si. A Fiber Bragg Grating-Based Monitoring System for Roof Safety Control in Underground Coal Mining. *Journal List Sensors (Basel)*, 2016, Vol.16(10), pp. 1759. https://doi.org/10.3390/s16101759

15 Hu T., Hou G., Li Z. The Field Monitoring Experiment of the Roof Strata Movement in Coal Mining Based on DFOS *Sensors*, 2020, Vol. 20(5), pp. 1318. https://doi.org/10.3390/s20051318

16 Lanciano Ch., Salvini R. Monitoring of deformation and temperature in a career with the help of distributed fiber-optic Brillouin sensors. *Sensors*, 2020, Vol. *20*(7), pp.1924. https://doi.org/10.3390/s20071924

AUTHORS' INFORMATION

Madi P.Sh. – Candidate of Techn. Sciences, Department of Electrical Equipment Operation, S. Seifullin Kazakh Agrotechnical University, Astana, Kazakhstan; ORCID iD: 0000-0001-5930-8112; peri@mail.ru

Al'kina A.D. – Master, Department of Energy Systems, Karaganda Technical University named after Abylkas Saginov, Karaganda, Kazakhstan; ORCID iD: 0000-0003-4879-0593; alika_1308@mail.ru

Mekhtiyev, A.D. – Candidate of Techn. Sciences, Professor, Department of Electrical Equipment Operation, S. Seifullin Kazakh Agrotechnical University, Astana, Kazakhstan; ORCID iD: 0000-0002-2633-3976; barton.kz@mail.ru

Yurchenko A.V. – Doctor of Techn. sciences, Professor, Research School of Physics of High-Energy Processes, National Research Tomsk Technical University, Tomsk, Russian Federation; Department of Innovative Technologies, Tomsk State University, Tomsk, Russia; ORCID iD: 0000-0002-7854-549; niipp@inbox.ru

EURASIAN PHYSICAL TECHNICAL JOURNAL

2024, Volume 21, No. 1 (47)

https://doi.org/10.31489/2024No1/114-123

Received: 22/12/2023 Revised: 31/01/2024 Accepted: 07/03/2024 Published online: 29/03/2024

Original Research Article

UDC 532.522.2

NUMERICAL MODELING OF THE PROCESS OF EXTRUSION OF HIGH-VISCOSITY PASTES

Gadirov R.*, Borisov A., Trufanova N., Ragimov E., Artischev S.

Tomsk State University of Control Systems and Radioelectronics, Tomsk, Russia

*Corresponding author: grm882@yandex.ru

Abstract. *This paper provides a theoretical consideration of the process of paste extrusion using a piston dispenser. The paste is considered as a highly viscous suspension of terpineol and silver particle powder. As a result of numerical modeling, the distribution of silver particles in a steady paste flow was obtained. The excess pressure in the piston depending on its speed and the effective width of the track depending on the piston speed were obtained. Modeling showed that the viscosity of the paste has the greatest influence on the extrusion process. Application of the obtained dependencies will allow you to control the paste extrusion process.*

Keywords: extrusion, piston dispenser, silver paste, viscosity, terpineol.

1. Introduction

The application of additive printing technology allowing manufacturing hybrid integrated circuits and devices is gaining popularity due to the reduction in the time expenditures on prototyping and obtaining finished products [1-3]. Studies are being con-ducted in the field of inkjet printing; however, using this technology allows forming only thin-film elements up to 1 μm thick. The inkjet printing technology demonstrates the examples of studying the production of RFID tags [4-7], antennas [8-12] of different types: meander, dual-band, monopole, dipole, ultra-wideband, etc.

Printers that are based on piston, screw and pneumatic extrusion of pastes are used to obtain thick-film elements [1]. The composition and characteristics of the pastes in-tended for piston and screw extrusion differ significantly from the inks used for inkjet printing, as well as from the pastes used for screen printing. The main difference consists in the concentration of solid particles and the material viscosity [2].

The works [13-15] describe the application of piston extrusion of the material used to print microwave antenna systems. The considered antenna systems operate in the range from 2.5 GHz up to 4.7 GHz. The frequency losses of the printed antennas are 5.3 dB at a frequency of 2.5 GHz. The geometric dimensions of the printed antennas are no more than 20×20 mm. A technique used for extracting the frequency electrical parameters of conductive pastes, on the basis of which microstrip lines were formed by piston extrusion, is de-scribed in [16]. A thickness increases in the microstrip line led to a decrease in the frequency losses from 12 dB to 6 dB at a frequency of 1 GHz. A printed multilayer conformal X-band antenna array is considered in [17]. The antenna represents a 32-element X-band superimposed matrix and is manufactured on a surface having several curvilinear lines. The peak antenna gain exceeds 15 dB at a frequency of 10.4 GHz.

Printing the planar components such as inductor, resistor, capacitor is presented in [18,19]. The printed inductor consists of 25 turns. The geometric dimensions of the printed inductor are 14×14 m while the line width is 100 μm and the distance between the lines is about 75 μm. The measured electrical parameters of the inductor have an inductance of 5.42 μH, a resistance of 12.7 kOhm and a capacitance of 50 pF.

Depending on the number of the printed resistor layers, the resistance of the active region varies from 25 Ohms to 650 Ohms. The printed capacitor has a capacity of 322 pF at 1 kHz and a breakdown voltage of 1000 V.

During piston extrusion [3,20], a piston is used to extrude the material being inside the syringe. The extruded volume and the flowrate of the pastes depend on the piston dis-placement inside the syringe. The volume of the extruded pastes and the extrusion rating are related to the piston movement speed [21]. The application of the pastes having different viscosities depends on the power of the drive motor and the mechanical system.

The formation of the printed films structure requires understanding the process of forming a uniform, continuous flow of the paste, its exit from the nozzle and distribution over the substrate. The pressure created in the syringe, the dispenser movement speed and the distance between the nozzle and the substrate influence the printed films quality. The paste extrusion rating depends on such rheological characteristics as viscosity, density, wetting, etc. [22]. Ambient temperature or high pulses of pressure, which can change the outflow rate during the extrusion process, can influence the paste viscosity change.

The dispenser movement rate must be consistent with the linear velocity of the out-flow of the pastes from the nozzle [23]. An extremely high flow rate, as compared to the movement rate of the dispenser, will lead to excessive deformations of the formed films and even to film disruptions [21]. Therefore, the relationship between the movement rate of the dispenser and the linear velocity of the extruded flow, which is a function of a com-plex extrusion process, is crucial for successful deposition and creation of the desired films.

Obtaining high-quality prototypes of printed circuit boards by means of the paste extrusion requires investigating different modes of the printing system operation. This work is devoted to the theoretical study of the capabilities of the dispenser operation during piston extrusion of the paste, consisting of an organic binder (terpineol) and a powder (silver particles).

2. Materials and methods

Let us consider the problem of numerical simulation of squeezing a paste consisting of silver and terpineol particles through a nozzle into the air. Extrusion is carried out in a gravity field using a piston dispenser. (Fig. 1a). This dispenser has axial symmetry, so numerical modeling was carried out in a cylindrical coordinate system. Figure 1b shows the calculated area of the inner part of the dispenser and the air (z_s area).

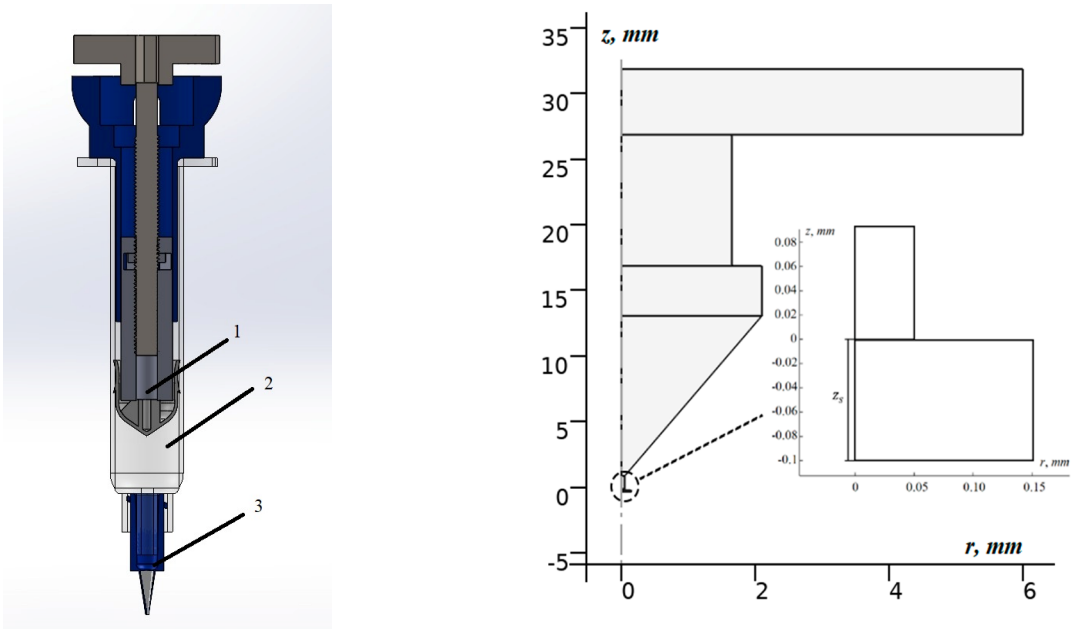

a b

Fig 1. The computational region corresponding to this dispenser (a) 1 is piston, 2 is syringe, 3 is nozzle. Computational region of the model corresponding to the area filled with the paste and air (b).

The left boundary of the calculation area is the axis of symmetry. All other boundaries, with the exception of the top and bottom ones, are considered as impenetrable walls. At the initial moment of time, the dispenser is filled with paste, which is squeezed out under the action of a piston moving at a constant speed along the *z* axis, i.e. a constant paste speed is set perpendicular to the upper boundary. The lower part of the z_s area is an open boundary that air and paste can leave. The pressure at the lower boundary is equal to atmospheric pressure. In this case, for a correct description of the extrusion of paste with silver particles, three-phase medium air/terpineol/silver particles can be considered. Obviously, the case of contact of silver particles with air is not relevant for our task, therefore we will limit ourselves to a description in which only contacts between silver particles with terpineol and terpineol with air are assumed. There are also impermeable walls (syringe surface) where the air/paste/syringe surface area is present.

Let's consider a standard approach to describe our problem based on solving a system of the following equations:

$$\rho\frac{\partial\vec{v}}{\partial t}+\rho(\vec{v}\cdot\nabla)\vec{v}=\nabla\cdot(-p\mathbf{I}+\mathbf{K})+\rho\vec{g}+\vec{F}_\sigma+\vec{F}_\theta \quad (1)$$

$$\frac{\partial\rho}{\partial t}+\nabla\rho\vec{v}=0 \quad (2)$$

$$\frac{\partial\varphi}{\partial t}+\vec{v}\nabla\varphi=\zeta\nabla\cdot\left(\varepsilon\nabla\varphi-\varphi(1-\varphi)\frac{\nabla\varphi}{|\nabla\varphi|}\right)=0 \quad (3)$$

$$\frac{3}{4}\frac{C_d}{d_d}\rho_c|\vec{v}_{slip}|\vec{v}_{slip}=\frac{\rho_2-\rho_d}{\rho_2}\left(\rho_2\frac{\partial\vec{v}}{\partial t}+\rho_2(\vec{v}\cdot\nabla)\vec{v}-\rho_2\vec{g}\right) \quad (4)$$

where Eq. (1) is the Navier-Stokes equation, where Δ is the Laplace operator, ρ is the density, p is the pressure, $\vec{v}=(v^1,v^2)$ is the velocity vector field, $\vec{F}_\sigma$ is the volume force corresponding to surface tension, which characterizes the behavior of the paste at the paste-air interface. This force can be represented in the following form:

$$\vec{F}_\sigma=\sigma\delta\kappa\vec{n},$$

where σ is the terpineol-air surface tension coefficient, $\delta=6|\nabla\varphi|\cdot|\varphi(1-\varphi)|$ is a smooth approximation of the Dirac delta function, κ is the curvature, $\vec{n}$ is the unit vector of the normal to the interface of the terpineol-air phases, $\mathbf{I}$ is the identity matrix, $\mathbf{K}$ is the viscous stress tensor, $\vec{g}$ is the acceleration of gravity. A force arises at the air/paste/syringe surface boundary $\vec{F}_\theta$, directed normal to the paste-air surface:

$$\vec{F}_\theta=\sigma\delta(\vec{n}_{wall}\cdot\vec{n}-\cos(\theta))\vec{n},$$

where $\vec{n}_{wall}$ is the unit vector of the normal to the surface of the syringe.

The viscous stress tensor in the case of a compressible fluid has the form:

$$\mathbf{K}=\mu(\nabla\vec{v}+(\nabla\vec{v})^{\mathrm{T}})-\frac{2}{3}\mu(\nabla\cdot\vec{v})\mathbf{I},$$

where $\nabla\vec{v}$ is the velocity gradient (second-order tensor), $(\ )^{\mathrm{T}}$ indicates the transposition, μ is the dynamic viscosity coefficient.

The air from the paste differs significantly in density and viscosity, therefore, in expressions (1) and (5), the viscosity and density are written as:

$$\rho=\rho_1+(\rho_2-\rho_1)\varphi,$$

$$\mu=\mu_1+(\mu_2-\mu_1)\varphi,$$

where ρ_1, μ_1 are the density and viscosity of the air, ρ_2, μ_2 are the density and viscosity of the paste, φ is a level function obeying equation (3), which is zero in the paste area and one in the air [24], where the ζ parameter characterizes the maximum speed and the ε parameter defines the phase boundary thickness.

The paste velocity $\vec{v}$ depends on the organic binder velocity $\vec{v}_c$ and the relative velocity of the dispersed phase particles $\vec{v}_{slip}$ as follows:

$$\vec{v} = \frac{s_c \rho_c \vec{v}_c + s_d \rho_d (\vec{v}_c + \vec{v}_{slip})}{\rho_2} \quad (5)$$

where $\rho_2 = s_c \rho_c + s_d \rho_d$, s_d takes values from 0 to 1 and characterizes the volume fraction of the dispersed phase particles and $s_c = 1 - s_d$.

Note that at the initial moment of time, silver particles are surrounded by terpineol, and contact between silver is undesirable, therefore, numerical modeling considered only those solutions in which there was no contact between silver particles and air. In this case, the velocity $\vec{v}$ is the velocity of the paste where it is present and the velocity of the air where the paste is absent. The velocity field obeys the corresponding continuity equation Eq. (2). The Eq. (4) describes the behavior of solid particles in a liquid, where C_d is the coefficient characterizing the balance between viscous resistance and buoyancy forces influencing the dispersed phase, d_d is the effective diameter of the dispersed phase particles (solid particles), ρ_d is the dispersed phase density, $\vec{v}_{slip}$ is the velocity of the dispersed phase particles relatively the organic binder, ρ_c is the organic binder density.

A number of approximations of the Rayleigh curve are proposed to describe the transition region for the Reynolds numbers $\mathrm{Re} = \frac{d_d \rho_c}{\mu_2} \left| \vec{v}_{slip} \right|$ that are less than 1000 [25]. The smallest relative error of up to 3 % in the transition region is shown by the Schiller-Neumann approximation [26], according to which the coefficient C_d in the Eq. (4) has the following form:

$$C_d = \frac{24}{\mathrm{Re}} (1 + 0.15 \mathrm{Re}^{0.687})$$

Numerical simulation of the system (1)-(4) was carried out under the following initial and boundary conditions:

1. At the initial moment of time (Figure 2a), the dispenser is completely filled with paste ($\varphi = 1$), and the extrusion area is air ($\varphi = 0$), while the velocity field is zero.

2. As noted above, at the lower boundary of the free space corresponding to the air, the pressure is equal to atmospheric, at the upper boundary a constant value of the paste feed rate $v_{in} = const$ (normal) is set, which corresponds to a constant piston speed. All other boundaries (except for the axis of symmetry) the boundary conditions of an impermeable wall correspond, which is written as follows:

$$\vec{v} \cdot \vec{n} = 0,$$

$$\vec{n} \cdot \left(\varepsilon \nabla \varphi - \varphi (1 - \varphi) \frac{\nabla \varphi}{|\nabla \varphi|} \right) = 0.$$

Let us note that the main geometric characteristics of the internal area of the dispenser are a nozzle diameter of 0.1 mm and a piston diameter of 12 mm.

The paste extrusion was modeled using the COMSOL Multiphysics 6.1 package. In this study, the physical modules Laminar Flow, Level Set and Phase Transport, as well as the calculation modules Phase Initialization and Time-Dependent, were used. An approach that is similar to the one applied in the work was used [26]. The problem was solved using the finite element method, while an appropriate partition was selected for each of the regions, and a finite element grid was selected for each region taking into account the proportion of silver particles in the paste s_d (Fig. 2b).

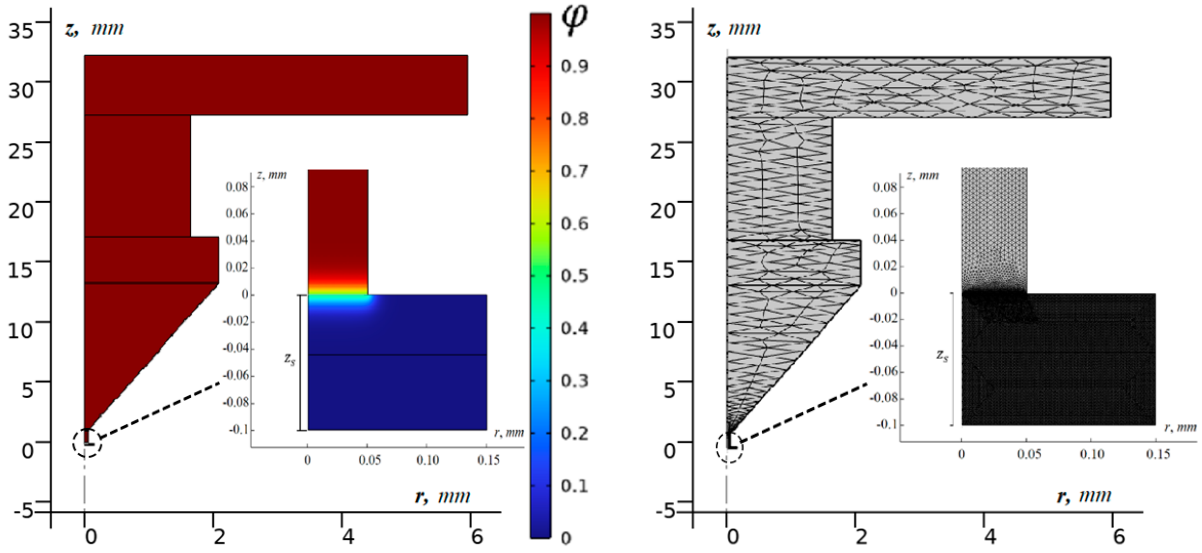

a b

Fig. 2 Initial paste distribution in the calculation area (a) and the grid used for calculation (b)

The (1)-(4) system was numerically modeled using the parameters given in Table 1, considering the influence of surface tension and gravity forces. Table 1 provides the initial physical parameters.

Table 1. Initial parameters for modeling

Parameter	Value	Reference
Terpineol density ρ_c	930 kg/m^3	[27]
Silver density ρ_d	10500 kg/m^3	[28]
Air density ρ_1	1.28 kg/m^3	[29]
Sliver particle size d_d	$2 \cdot 10^{-6}$ m	[30]
Terpineol dynamic viscosity μ_c	0.097 Pa·s	[27]
Air dynamic viscosity μ_1	$1.81 \cdot 10^{-5}$ Pa·s	[29]
Terpineol surface tension	0.033 N/m	[27]
Wetting angle at the interface of terpineol/air/syringe surface	$\pi/2$	[31]

The dynamic viscosity coefficient μ of the paste is of particular interest since it significantly depends on the shear rate $\dot{\gamma}$ in the local region of the space (Fig. 2). This dependence is well described by the Carreau's model [26]:

$$\mu_2 = \mu_{inf} + (\mu_0 - \mu_{inf})(1 + (\lambda\dot{\gamma})^2)^{(n-1)/2} \quad (6)$$

In this case μ_{inf}, μ_0, λ, n are the Carreau's model parameters determined by the experimental data approximation.

A rotary viscometer ViscoQC 300 (Anton Paar, Austria, Graz) in the Heli-Plus configuration was used to determine the dynamic viscosity of the paste; this viscometer allowed obtaining the dependence of the paste dynamic viscosity on the shear rate. The approximation of this dependence in accordance with the Carreau's model Eq. (11) is shown in Fig. 3.

Note that the experimentally obtained dependence (Fig. 3), approximated using the model (6), allows in the process of modeling the extrusion of paste to calculate the viscosity depending on the shear rate $\dot{\gamma}$, which is affected by the redistribution of particles during the movement of the paste.

The following parameters correspond to the dependence presented in Fig. 3: $\mu_{inf} = 0.053$ MPa, $\mu_0 = 0.241$ MPa, $\lambda = 1.151$ s, $n = 0.324$.

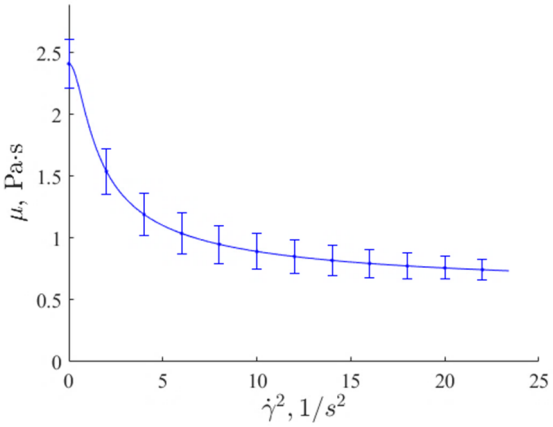

Fig. 3. Approximation of the experimentally obtained dependence of the viscosity on the squared shear velocity with the Carreau's model Eq. (6)

In the Eq. (5), the concept of the volume fraction of the dispersed phase (silver powder) is used, but in experiments, the paste is usually prepared by the mass fraction of the silver powder:

$$\omega = \frac{m_d}{m_d + m_c} \tag{7}$$

where m_d, m_c are the masses of the silver powder and terpineol, respectively.

Knowing the mass fraction of the silver powder allows calculating its volume fraction as follows:

$$s_d = \frac{\rho_c \omega}{\rho_c \omega + \rho_d (1-\omega)} \tag{8}$$

where ρ_d, ρ_c are the density of the silver powder and terpineol, respectively.

3. Results and discussion

The Eq. (1)-(4) system was numerically modeled for different values of the mass fraction of the silver powder Eq. (7) and the piston velocity. Fig. 4a shows the dependences of the volume fraction of the silver powder and the dependence of the function φ on the distance r up to the vertical axis of the dispenser in the steady-state extrusion mode at a distance of $z_s = 0.1$ mm (Fig. 4b) from the outlet section of the nozzle, obtained by means of the numerical modeling. Fig. 4b demonstrates the distribution of the function φ in the computational region of the nozzle and below the nozzle when the mass fraction is ω = 0.7.

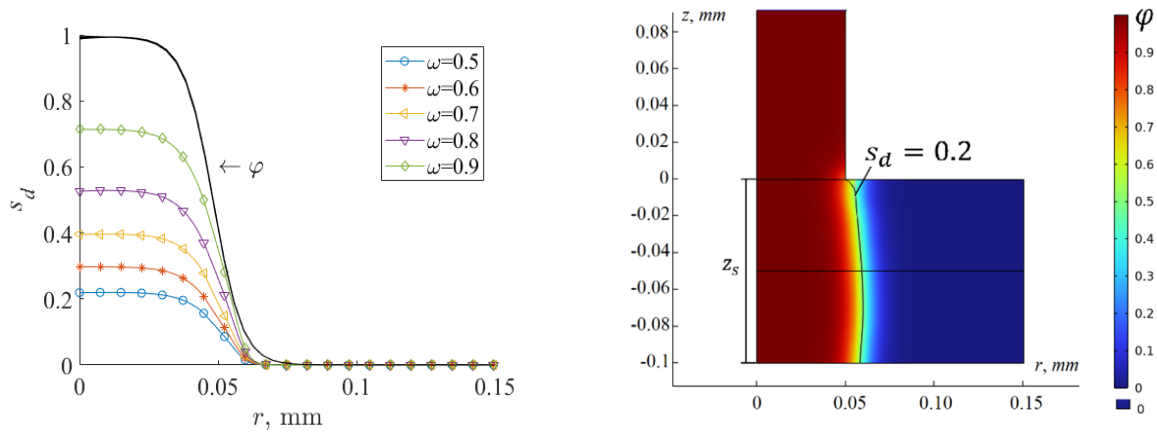

a b

Fig. 4. Dependences of the volume fraction of the silver powder and the dependence of the function φ on the distance r up to the vertical axis of the dispenser in the steady-state extrusion mode at a distance of z_s=0.1 mm from the outlet section of the nozzle (a), distribution of the function φ in the computational region of the nozzle and below the nozzle when the mass fraction is ω=0.7; an additional line of the volume fraction level has been drawn (s_d=0.02) (b).

The function φ type practically does not depend on the mass fraction of the silver powder present in the paste; however, the volume fraction distribution of the silver powder varies significantly. At a sufficiently large interval, when the distance r is increasing, the volume fraction of the dispersed phase remains constant, but it decreases nonlinearly closer to the edge. An increase in the mass fraction of the silver powder obviously leads to a significant increase in the cross-sectional area of the printed tracks, which is proportional to the area under the curves s_d shown in Fig. 3b (the effective width of the track at ω=0.7 is r_e =0.122 mm). The calculations have shown that this dependence is nonlinear, but it is linear in the case of using the volume fraction instead of the mass fraction, which is related to the mass fraction according to the Eq. (8). Let us note that in practice the proposed statements are valid for a stable (debugged) technical process.

Let us consider the dependence of the overpressure (pressure above atmospheric) present on the vertical axis of the dispenser on the distance up to the nozzle section at the outlet as a characteristic of a stable process (Fig. 5a). The maximum pressure inside the dispenser was 0.288 MPa. Changing the piston speed allows obtaining a maximum overpressure that depends on the speed (Fig. 5b).

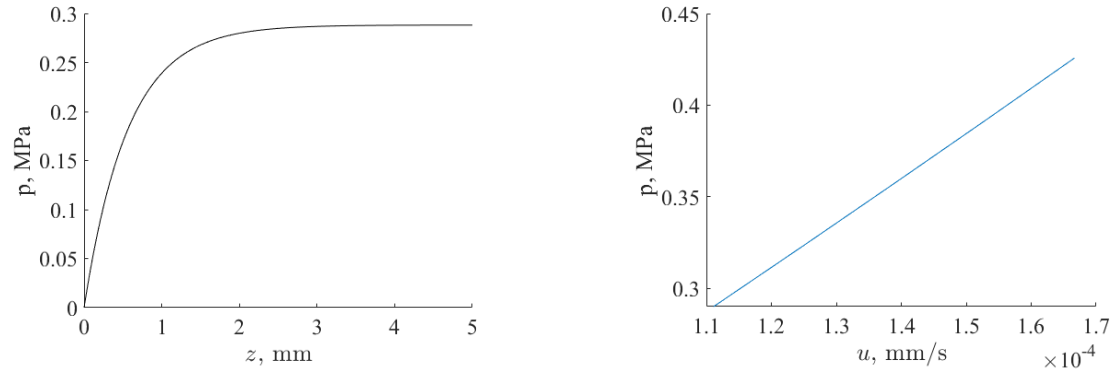

Fig. 5. Dependence of the overpressure present on the vertical axis of the dispenser (the mass fraction is ω=0.7) on the distance to the nozzle section at the outlet (a) and the dependence of the maximum overpressure present in the piston on its velocity (b).

A linear increase in the overpressure accompanied by a piston speed increase leads to a critical value at which the piston will not start to deform; but before reaching this value, the stable operation of the technological process is disrupted because the piston speed increase entails a non-linear increase in the effective width of the track r_e (Fig. 6).

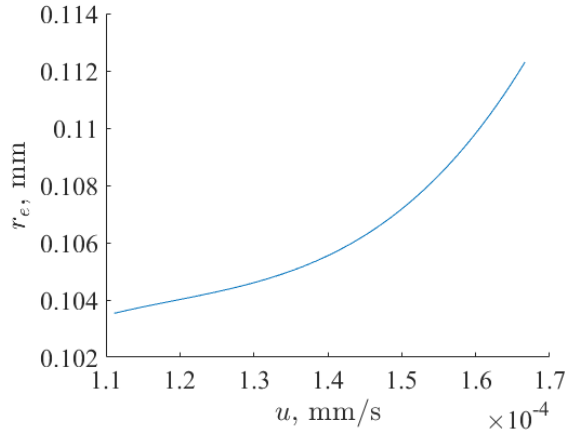

Fig. 6. Dependence of the effective width of the track r_e on the piston speed when ω=0.7.

Fig. 6 shows that the nonlinear growth of the effective width of the track begins at a speed exceeding the value of $1.3 \cdot 10^{-4}$ mm/s. The calculations were additionally carried out in the case of different surface tensions and wetting angles, which proved that the wetting angle did not influence significantly the extrusion process, and the surface tension increase, when other parameters were fixed, led to a strong nonlinearity depending on $r_e(u)$. That is, it is necessary to monitor the terpineol quality when preparing the paste.

According to the numerical modeling results, the effective parameters of the printing system operation are the following. The distance of the dispenser from the substrate is z_s =0.1 mm, the mass fraction of the silver powder in the paste is ω=0.7, the piston speed is $1.1 \cdot 10^{-4}$ mm/s, the maximum pressure in the dispenser is 0.288 MPa, the effective width of the track is r_e =0.122 mm.

4. Conclusions

In this work, a numerical simulation of the piston extrusion process was carried out using the example of terpineol paste and silver particle powder. The main emphasis is placed on obtaining the dependencies for the basic physical quantities on the control parameters and properties of the paste that characterize the dispenser operation in the track printing system.

A mathematical model that allows describing the pastes extrusion has been selected. The numerical modeling has allowed obtaining a set of the parameters of the printing system making the system operation stable. The dependences of the volume fraction of the silver powder on the distance up to the dispenser vertical axis in the steady-state extrusion mode have been obtained. The dependence of the overpressure present on the vertical dispenser axis on the nozzle section distance at the outlet has been studied. The dependences of the maximum over-pressure present in the piston on its speed and the effective width of the track on the piston speed have been determined. The numerical modeling has shown that the paste viscosity influences significantly the extrusion process. An increase in the extrusion speed is shown to increase non-linearly the printed track width. Based on the mathematical model used in the work, a process for manufacturing prototypes of printed circuit boards with subsequent sintering will be developed.

Conflict of interest statement

The authors declare that they have no conflict of interest in relation to this research, whether financial, personal, authorship or otherwise, that could affect the research and its results presented in this paper.

CRediT author statement

Gadirov R.: Writing - Review & Editing, Conceptualization; Borisov A.: Methodology, Formal analysis; Trufanova N.: Writing - Original Draft; Ragimov E.: Visualization; Artischev S: Supervision, Funding acquisition

The final manuscript was read and approved by all authors.

Funding

This research was funded by Ministry of Science and Higher Education of the Russian Federation. State assignment (Goszadanie) – FEWM-2022-0005.

References

1 Divakaran N., Das J.P., PV A.K., Mohanty S., Ramadoss A., Nayak S.K. Comprehensive review on various additive manufacturing techniques and its implementation in electronic devices. *Journal of Manufacturing Systems*, 2022, Vol. 62, pp. 477 – 502. https://doi.org/10.1016/j.jmsy.2022.01.002

2 Hassan K., Nine M.J., Tung T.T., Stanley N., Yap P.L., Rastin H., et al. Functional inks and extrusion-based 3D printing of 2D materials: a review of current research and applications. *Nanoscale*, 2020, Vol. 12, No. 37, pp.19007 – 19042. https://doi.org/10.1039/D0NR04933F

3 Tan H.W., Choong Y.Y.C., Kuo C.N., Low H.Y., Chua C.K. 3D printed electronics: Processes, materials and future trends. *Progress in Materials Science*, 2022, Vol. 127, p. 100945. https://doi.org/10.1016/j.pmatsci.2022.100945

4 Rida A., Yang L., Tentzeris M.M. Design and characterization of novel paper-based inkjet-printed UHF antennas for RFID and sensing applications. *In IEEE Antennas and Propagation Society International Symposium.* HI, USA, 2007, pp. 2749 – 2752. https://doi.org/10.1109/APS.2007.4396104

5 Cook B.S., Mariotti C., Cooper J.R., Revier D., Tehrani B.K., Aluigi L., Roselli L., Tentzeris, M.M. Inkjet-printed, vertically-integrated, high-performance inductors and transformers on flexible LCP substrate. *In 2014 IEEE*

MTT-S International Microwave Symposium (IMS2014), 2014, pp. 1 – 4. https://doi.org/10.1109/MWSYM.2014.6848575

6 Kim S. Inkjet-Printed Electronics on Paper for RF Identification (RFID) and Sensing. *Electronics*, 2020, Vol. 9, No. 10, pp. 1636. https://doi.org/10.3390/electronics9101636

7 Tentzeris M.M., Rida A., Traille A., Lee H., Lakafosis V., Vyas R. Inkjet-printed paper/polymer-based RFID and Wireless Sensor Nodes: The final step to bridge cognitive intelligence, nanotechnology and RF? *XXXth URSI General Assembly and Scientific Symposium.* Istanbul, Turkey, 2011, pp. 1 – 4. https://doi.org/10.1109/URSIGASS.2011.6050690

8 Cook B.S., Fang Y., Kim S., Le T., Goodwin W.B., Sandhage K.H. Inkjet catalyst printing and electroless copper deposition for low-cost patterned microwave passive devices on paper. *Electronic Materials Letters*, 2013, Vol. 9, pp. 669 – 676. https://doi.org/10.1007/s13391-013-3027-0

9 Abutarboush H.F., Shamim A. Wide frequency independently controlled dual-band inkjet-printed antenna. *IET Microwaves, Antennas & Propagation*, 2014, Vol. 8, No. 1, pp. 52 – 56. https://doi.org/10.1049/iet-map.2013.0229

10 Kim S., Cook B.S., Le T., Cooper J., Lee H., Lakafosis V. Inkjet-printed antennas, sensors and circuits on paper substrate. *IET Microwaves, Antennas and Propagation*, 2013, Vol. 7 No. 10, pp. 858 – 668. https://doi.org/10.1049/iet-map.2012.0685

11 Pongpaibool P., Wallada W., Siwamogsatham S. A Thickened-and-Widened Feed Dipole Antenna with an Inductive Matching Loop for a Printed UHF RFID Tag. *In National Electronics and Computer Technology Center*. Sapporo, Japan, 2014, pp. 2092 – 2096. https://doi.org/10.1109/InfoSEEE.2014.6946293

12 Shaker G., Safavi-Naeini S., Sangary N., Tentzeris M.M. Inkjet Printing of Ultrawideband (UWB) Antennas on Paper-Based Substrates. *IEEE Antennas and wireless propagation letters,* 2011, Vol. 10, pp. 111 –114. https://doi.org/10.1109/LAWP.2011.2106754

13 Haerinia M., Noghanian S. Design of Hybrid Wireless Power Transfer and Dual Ultrahigh-Frequency Antenna System. *Proceeding of the URSI International Symposium on Electromagnetic Theory (EMTS)*. California, USA, 2019, 4 p. https://doi.org/10.23919/URSI-EMTS.2019.8931514

14 Haerinia M., Noghanian S. A Printed Wearable Dual-Band Antenna for Wireless Power Transfer. *Sensors*, 2019, Vol. 19, No. 7, p. 1732. https://doi.org/10.3390/s19071732

15 Shadid R., Haerinia M., Noghanian S. Study of Rotation and Bending Effects on a Flexible Hybrid Implanted Power Transfer and Wire-less Antenna System. *Sensors*, 2020, Vol. 20, No. 5, p. 1368. https://doi.org/10.3390/s20051368

16 Trufanova, N.S., Artishchev S.A., Ragimov E.R., Loschilov A.G., Malyshenko A.M.. Technique for extraction of electric frequency parameters of conductive ink. *Journal of Physics: Conference Series*, 2022, Vol. 2291, No. 1, p. 012015. https://doi.org/10.1088/1742-6596/2291/1/012015

17 Kreit E., Steffen T., Aga R., Bartsch C., Wu B.I., Heckman E. Printed multilayer conformal x-band antenna array. *Flexible and Printed Electronics*, 2017, Vol. 2, No. 4, p. 045009. https://doi.org/10.1088/2058-8585/aa940b

18 Correia V., Mitra K.Y., Castro H., Rocha J.G., Sowade E., Baumann R.R., Lanceros-Mendez S. Design and fabrication of multilayer inkjet-printed passive components for printed electronics circuit development. *Journal of Manufacturing Processes*, 2018, Vol. 31, pp. 364 – 371. https://doi.org/10.1016/j.jmapro.2017.11.016

19 Hardin J.O., Grabowski C.A., Lucas M., Durstock M.F., Berrigan J.D. All-printed multilayer high voltage capacitors with integrated processing feedback. *Additive Manufacturing*, 2019, Vol. 27, pp. 327 – 333. https://doi.org/10.1016/j.addma.2019.02.011

20 Kwon K.S., Rahman M.K., Phung T.H., Hoath S.D., Jeong S., Kim J.S. Review of digital printing technologies for electronic materials. *Flexible and Printed Electronics,* 2020, Vol. 5, No. 4, p. 043003. https://doi.org/10.1088/2058-8585/abc8ca

21 Li W., Ghazanfari A., Leu M.C., Landers R.G. Extrusion-on-demand methods for high solids loading ceramic paste in freeform extrusion fabrication. *Virtual and Physical Prototyping*, 2017, Vol. 12, No. 3, pp. 193 – 205. https://doi.org/10.1080/17452759.2017.1312735

22 Chen X.B., Kai J. Modeling of positive-displacement fluid dispensing processes. *IEEE Transactions on Electronics Packaging Manufacturing*, 2004, Vol. 27, No. 3, pp. 157 – 163. https://doi.org/10.1109/TEPM.2004.843083

23 Bruneaux J., Therriault D., Heuzey M.C. Micro-extrusion of organic inks for direct-write assembly. *Journal of Micromechanics and Microengineering*, 2008, Vol. 18, No. 11, p. 115020. https://doi.org/10.1088/0960-1317/18/11/115020

24 COMSOL. The Level Set Method. https://www.comsol.com/forum/thread/attachment/37361/The-level-set-methodfrom-MEMS-Module-5198.pdf.

25 Besagni G., Varallo N., Mereu R. Computational Fluid Dynamics Modelling of Two-Phase Bubble Columns: A Comprehensive Review. *Fluids*, 2023, Vol. 8, No. 3, p. 91. https://doi.org/10.3390/fluids8030091

26 Schmidt G.A., Lin Y.J., Xu Y., Wang D., Yilmaz G., Turng L.S. Viscosity characterization and flow simulation and visualization of polytetrafluoroethylene paste extrusion using a green and biofriendly lubricant. *Polymer Engineering & Science*, 2021, Vol. 61, No. 4, pp. 1050 – 1065. https://doi.org/10.1002/pen.25632

27 Shen F., Dixit M.B., Zaman W., Hortance N., Rogers B., Hatzell, K.B. Composite electrode ink formulation for all solid-state batteries. *Journal of The Electrochemical Society*, 2019, Vol. 166, No. 14, p. A3182. https://doi.org/10.1149/2.0141914jes

28 Slistan-Grijalva A., Herrera-Urbina R., Rivas-Silva J.F., Ávalos-Borja M., Castillón-Barraza F.F., Posada-Amarillas A. Classical theoretical characterization of the surface plasmon absorption band for silver spherical nanoparticles suspended in water and ethylene glycol. *Physica E: Low-dimensional Systems and Nanostructures*, 2005 Vol. 27, No. 1 – 2, pp. 104 – 112. https://doi.org/10.1016/j.physe.2004.10.014

29 El-Said M., Bhuse V., Arendsen A. An empirical study to investigate the effect of air density changes on the DSRC performance. *Procedia computer science*, 2017, Vol. 114, pp. 523 – 530. https://doi.org/10.1016/j.procs.2017.09.025

30 Won H.I., Nersisyan H., Won C.W., Lee J.M., Hwang J.S. Preparation of porous silver particles using ammonium formate and its formation mechanism. *Chemical Engineering Journal*, 2010, Vol. 156, No. 2, pp. 459 – 464. https://doi.org/10.1016/j.cej.2009.10.053

31 Fujasova-Zednikova M., Vobecka L., Vejrazka J. Effect of solid material and surfactant presence on interactions of bubbles with horizontal solid surface. *The Canadian Journal of Chemical Engineering*, 2010, Vol. 88, No. 4, pp. 473 – 481. https://doi.org/10.1002/cjce.20326

AUTHORS' INFORMATION

Gadirov, R. – PhD, Head of laboratory, Tomsk State University of Control Systems and Radioelectronics, Tomsk, Russia; ORCID iD: 0000-0003-3953-3384; grm882@yandex.ru

Borisov, A. – PhD, Senior Researcher, Tomsk State University of Control Systems and Radioelectronics, Tomsk, Russia; ORCID iD: 0000-0003-1752-1649; borisov@phys.tsu.ru

Trufanova, N. – Graduate student, Junior researcher, Tomsk State University of Control Systems and Radioelectronics, Tomsk, Russia; ORCID iD: 0000-0002-2055-5316; natalia.s.trufanova@tusur.ru

Ragimov, E. – Master student, Engineer, Tomsk State University of Control Systems and Radioelectronics, Tomsk, Russia; ORCID iD: 0009-0007-9946-2377; ragimov_30@mail.ru

Artischev, S. – PhD, head of laboratory, Tomsk State University of Control Systems and Radioelectronics, Tomsk, Russia; ORCID iD: 0000-0002-9905-621X; sergei.a.artishchev@tusur.ru

EURASIAN PHYSICAL TECHNICAL JOURNAL

2024, Volume 21, No. 1 (47)

https://doi.org/10.31489/2024No1/124-137

Received: 26/01/2024 Revised: 22/02/2024 Accepted: 18/03/2024 Published online: 29/03/2024

Original Research Article

UDC: 530.145.61; 539.192; 539.194

ENERGY SPECTRA, EXPECTATION VALUES, AND THERMODYNAMIC PROPERTIES OF HCl AND LiH DIATOMIC MOLECULES

Inyang E.P.[1,2], Ali N.R.[2,3], Endut R.[2,3], Aljunid S.A.[2,3]

[1] Department of Physics, National Open University of Nigeria, Jabi-Abuja, Nigeria
[2] Faculty of Electronic Engineering & Technology, Universiti Malaysia Perlis, Perlis, Malaysia
[3] Centre of Excellence Advanced Communication Engineering, Universiti Malaysia Perlis, Perlis, Malaysia
*Corresponding authors: etidophysics@gmail.com

Abstract. *The Schrödinger equation is solved by applying the Nikiforov-Uvarov-Functional Analysis method to the Hulthén plus screened Kratzer Potential. The Greene-Aldrich approximation is employed to determine the closed form expressions for the energy equation and the wave function. The Hellmann-Feynman theorem was employed to calculate the energy spectra and expectation values of various quantum states for diatomic molecules of HCl and LiH. Subsequently, we employed the energy equation that we had previously derived to compute the partition function, which in turn enabled us to determine the thermodynamic properties associated with the diatomic molecules. The partition function for the diatomic molecules of* H_2 *and LiH was calculated at different temperatures. The results indicate that the partition function of the two diatomic molecules rose as the temperature increased. The findings we obtained align with the results documented in the literature.*

Keywords: Greene-Aldrich approximation, Bound State; Hellmann-Feynman theorem; Thermodynamic properties.

1. Introduction

The partition function (PF) which is dependent on temperature, enables the investigation of the thermodynamic properties (TPs) of a system. The partition function, widely employed in molecular physics and statistical physics, facilitates the computation of various thermodynamic properties such as entropy, specific heat capacity, mean free energy, and others [1]. To analyze the behavior of non-relativistic particles in quantum mechanics, including the properties of the system's elementary particles and the mass distribution of mesons, the Schrodinger equation (SE) needs to be solved [2,3]. Several scholars [4–10] have examined these solutions, exploring a range of potential functionalities. The utilization of computational methods to solve the SE is of great significance in understanding the behavior of non-relativistic particles in the realm of quantum science. Consequently, numerous researchers have recognized the high importance of solving this equation. Utilizing these techniques is crucial for evaluating the thermodynamic properties of the entire structure, as well as the mass distribution of mesons and other related phenomena. To analyze the SE with different potentials, several methods have been employed, such as the asymptotic iteration method (AIM) [11], the Nikiforov-Uvarov Functional Analysis (NUFA) technique [12], and others [13, 14]. Lately, theorists have shown increasing interest in examining the energy of bound states in various diatomic molecules (DMs) using both a lone potential and collective potential functions [15–20]. For example, Inyang

et al. [21] investigated a small number of DMs by employing the Eckart and Hellmann potential model. In addition, Obogo et al. [22] examined several dynamical models with a q-deformed Hulthén potential combined with a quadratic exponential-type potential. Edet and Ikot [23] also analyzed a selected few DMs with the Deng-Fan (DF) potential. In addition, Edet et al. [24] calculated several diatomic molecules using the DF plus Eckart potential. We have utilized the Hulthén plus screened Kratzer potential (HSKP) to investigate the HCl and LiH diatomic molecules through the SE using the newly suggested NUFA method, taking into consideration the previous research conducted by certain scholars. To analyze the interaction between two particles, the Hulthén potential (HP) [25] is employed. The application of this concept extends to diverse fields including condensed matter, nuclear, particle, chemical, atomic, and molecular physics [26, 27]. Conversely, Ikot et al. [28] introduced the screened Kratzer potential (SKP), a model widely employed in molecular physics and used by several authors in the literature [29, 30]. The goal of this study is to solve the SE using the HSKP and applying the NUFA method. The purpose is to analyze the energy spectra, expectation values, and thermodynamic properties of diatomic molecules of HCl and LiH.

Utilizing two potential functions enhances the potential strength (PS) for improved outcomes [31]. The combined potential is as follows:

$$V(r_1) = -\frac{Z_I e^{-\vartheta_1 r_1}}{1-e^{-\vartheta_1 r_1}} - \frac{Z_{II} e^{-\vartheta_1 r_1}}{r_1} + \frac{Z_{III} e^{-\vartheta_1 r_1}}{r_1^2} \tag{1}$$

where Z_I is the PS the HP, ϑ_1 is the screening parameter. The letter $Z_{II} \equiv 2D_e r_e$ and $Z_{III} \equiv D_e r_e^2$. In this case, the equilibrium bond length is r_e , and the dissociation energy is D_e.

2. Review of the NUFA Technique

The NUFA technique is a work conducted by Ikot et al. [12] that presents a modern methodology for resolving a second-order differential equation. It is straightforward and refined. This technique combines the factorization, parametric NU, and NU approaches.

$$\psi_I''(y) + \frac{\tilde{\tau}_I(y)}{\sigma_I(y)}\psi_I'(y) + \frac{\tilde{\sigma}_I(y)}{\sigma_I^2(y)}\psi_I(y) = 0 \tag{2}$$

where $\tilde{\sigma}_I(y)$ and $\sigma_I(y)$ are quadratic polynomials, while $\tilde{\tau}_I(y)$ is a linear polynomial. Tezcan and Sever [32] subsequently presented the parametric formulation of the NU technique as follows:

$$\psi_I'' + \frac{\beta_I - \beta_{II} y}{y(1-\beta_{III} y)}\psi_I' + \frac{1}{y^2(1-\beta_{III} y)^2}\left[-\xi_I y^2 + \xi_{II} y - \xi_{III}\right]\psi_I(y) = 0, \tag{3}$$

where β_i and $\xi_i (i = I, II, III)$ are all parameters. We consider the wave function in the specified form (Eq. 4) due to the presence of two singularities at points $y \to 0$ and $y \to 1$ in the differential equation mentioned in Eq. (3). $y \to 0$ and $y \to 1$.

$$\psi_I(y) = y^{\lambda}(1-y)^{v} f(y) \tag{4}$$

Equation that results from substituting Eq. (4) into Eq. (3) is as follows:

.

$$y(1-\beta_{III}y)f''(y)+\left[\beta_I+2\lambda-\left(2\lambda\beta_{III}+2v\beta_{III}+\beta_{II}\right)y\right]f'(y)$$
$$-\beta_{III}\left(\lambda+v+\frac{\beta_{II}}{\beta_{III}}-1+\sqrt{\left(\frac{\beta_{II}}{\beta_{III}}-1\right)^2+\frac{\xi_I}{\beta_{III}}}\right)$$
$$\left(\lambda+v+\frac{\beta_{II}}{\beta_{III}^2}-1+\sqrt{\left(\frac{\beta_{II}}{\beta_{III}}-1\right)^2+\frac{\xi_I}{\beta_{III}^2}}\right)f(y) \tag{5}$$
$$+\left[\frac{\lambda(\lambda-1)+\beta_I\lambda-\xi_{III}}{y}+\frac{\beta_{II}v-\beta_I\beta_{III}v+v(v-1)\beta_{III}-\frac{\xi_I}{\beta_{III}}+\xi_{II}-\xi_{III}\beta_{III}}{(1-\beta_{III}y)}\right]f(y)=0.$$

Equation (5) can be simplified to a Gauss hypergeometric equation if and only if the subsequent functions are removed:

$$\lambda(\lambda-1)+\beta_I\lambda-\xi_{III}=0, \tag{6}$$

and

$$\beta_{II}v-\beta_I\beta_{III}v+v(v-1)\beta_{III}-\frac{\xi_I}{\beta_{III}}+\xi_{II}-\xi_{III}\beta_{III}=0. \tag{7}$$

Thus, it becomes

$$y(1-\beta_I y)f''(y)+\left[\beta_I+2\lambda-\left(2\lambda\beta_{III}+2v\beta_{III}+\beta_{II}\right)y\right]f'(y)$$
$$-\beta_{III}\left(\lambda+v+\frac{\beta_{II}}{\beta_{III}}-1+\sqrt{\left(\frac{\beta_{II}}{\beta_{III}}-1\right)^2+\frac{\xi_I}{\beta_{III}}}\right)\left(\lambda+v+\frac{\beta_{II}}{\beta_{III}^2}-1+\sqrt{\left(\frac{\beta_{II}}{\beta_{III}}-1\right)^2+\frac{\xi_I}{\beta_{III}^2}}\right)f(y)=0. \tag{8}$$

Upon resolving equations (6) and (7), equations (9) and (10) are transformed into the following expressions:

$$\lambda=\frac{(1-\beta_I)}{2}\pm\frac{1}{2}\sqrt{(1-\beta_I)^2+4\xi_{III}} \tag{9}$$

$$v=\frac{(\beta_{III}+\beta_I\beta_{III}-\beta_{II})\pm\sqrt{(\beta_{III}+\beta_I\beta_{III}-\beta_{II})^2+\left(\frac{\xi_I}{\beta_{III}}+\beta_{III}\xi_{III}-\xi_{II}\right)}}{2} \tag{10}$$

Equation (8) features a hypergeometric equation in the form of a type

$$y\left(1-y\right)f''(y)+\left[c_I+\left(a_I+b_I+1\right)y\right]f^1(y)-a_Ib_If(y)=0 \tag{11}$$

Equations (4), (8), and (11), respectively, are used to obtain the energy equation and the associated wave equation for the NUFA technique:

$$\lambda^2+2\lambda\left(v+\frac{\beta_{II}}{\beta_{III}}-1+\frac{n}{\sqrt{\beta_{III}}}\right)+\left(v+\frac{\beta_{II}}{\beta_{III}}-1+\frac{n}{\sqrt{\beta_{III}}}\right)^2-\left(\frac{\beta_{II}}{\beta_{III}}-1\right)^2-\frac{\xi_I}{\beta_{III}^2}=0, \tag{12}$$

$$\psi(y)=Ny\frac{(1-\beta_I)+\sqrt{(1-\beta_I)^2+4\xi_{III}}}{2}$$
$$(1-\beta_{III}y)\frac{(\beta_{III}+\beta_I\beta_{III}-\beta_{II})+\sqrt{(\beta_{III}+\beta_I\beta_{III}-\beta_{II})^2+\left(\frac{\xi_I}{\beta_{III}^2}+\beta_{III}\xi_{III}-\xi_{II}\right)}}{2}{}_2F_1\left(p_1,p_2,p_3;y\right), \tag{13}$$

where $p_1, p_2, \text{and } p_3$ are given as follows;

$$p_1 = \sqrt{\beta_{III}}\left(\lambda + v + \frac{\beta_{II}}{\beta_{III}} - 1 + \sqrt{\left(\frac{\beta_{II}}{\beta_{III}} - 1\right)^2 + \frac{\xi_I}{\beta_{III}}}\right) \tag{14}$$

$$p_2 = \sqrt{\beta_{III}}\left(\lambda + v + \frac{\beta_{II}}{\beta_{III}} - 1 - \sqrt{\left(\frac{\beta_{II}}{\beta_{III}} - 1\right)^2 + \frac{\xi_I}{\beta_{III}}}\right) \tag{15}$$

$$p_3 = \beta_I + 2\lambda \tag{16}$$

3.The Schrodinger equation solutions using the HSKP

The SE reads [1]

$$\frac{d^2\psi_I(r_1)}{dr_1^2} + \left[\frac{2\mu}{\hbar^2}\left(E_{nl} - V(r_1)\right) - \frac{l(l+1)}{r_1^2}\right]\psi_I(r_1) = 0\,, \tag{17}$$

where $\psi_n(r)$ is the Eigen functions, $E_{\hbar}$ is the energy eigenvalues, The system's reduced mass is denoted by μ, the reduced Planck's constant by $\hbar$, and the radial distance by r_1.

Equation (17) is solved using the Greene-Aldrich approximation (GAA) [33] in order to get past the centrifugal barrier. This GAA, which is expressed as follows, is a better approximation to the centrifugal barrier and is valid for $\vartheta_I << 1$,

$$\frac{1}{r_1^2} \approx \frac{\vartheta_I^2}{\left(1 - e^{-\vartheta_I r_1}\right)^2}. \tag{18}$$

Equations. (1) and (18) are substituted into Eq. (17) to obtain Eq. (19).

$$\frac{d^2\psi_I(r_1)}{dr_1^2} + \left[\frac{2\mu E_{nl}}{\hbar^2} + \frac{2\mu Z_I e^{-\vartheta_I r_1}}{\hbar^2\left(1 - e^{-\vartheta_I r_1}\right)} + \frac{2\mu Z_{II}\vartheta_I e^{-\vartheta_I r_1}}{\hbar^2\left(1 - e^{-\vartheta_I r_1}\right)} - \frac{2\mu Z_{III}\vartheta_I^2 e^{-\vartheta_I r_1}}{\hbar^2\left(1 - e^{-\vartheta_I r_1}\right)^2} - \frac{\vartheta_I^2 l(l+1)}{\left(1 - e^{-\vartheta_I r_1}\right)^2}\right]\psi_I(r_1) = 0 \tag{19}$$

Let, $y = e^{-\vartheta_I r_1}$ (20)

Equation (20) yields Eq. (21) as

$$\frac{d^2\psi_I(r)}{dr^2} = \vartheta_I^2 y^2 \frac{d^2\psi_I(y)}{dy^2} + \vartheta_I^2 y \frac{d\psi_I(y)}{dy} \tag{21}$$

Following a number of simplifications and the integration of Eqs. (20) and (21) into Eq. (19), we obtain:

$$\frac{d^2\psi_I(y)}{dy^2} + \frac{1-y}{y(1-y)}\frac{d\psi_I(y)}{dy} + \frac{1}{y^2(1-y)^2}\left[-(\varepsilon + \eta_I)y^2 + (2\varepsilon + \eta_I - \eta_{II})y - (\varepsilon + \gamma)\right]\psi_I(y) = 0, \tag{22}$$

where

$$-\varepsilon = \frac{2\mu E_{nl}}{\vartheta_I^2\hbar^2},\quad \eta_I = \frac{2\mu Z_I}{\vartheta_I^2\hbar^2} + \frac{2\mu Z_{II}}{\vartheta_I\hbar^2},\quad \eta_{II} = \frac{2\mu Z_{III}}{\hbar^2},\quad \gamma = l(l+1)\Big\}. \tag{23}$$

Combining Eqs. (22) and (3) yields the following:

$$\beta_I = \beta_{II} = \beta_{III} = 1, \xi_I = \varepsilon + \eta_I, \xi_{II} = 2\varepsilon + \eta_I - \eta_{II}, \xi_{III} = \varepsilon + \gamma\} \tag{24}$$

Equation (24) is inserted into equations (9) and (10) to produce

$$\lambda = \frac{1}{2}\sqrt{4(\varepsilon + \gamma)} \tag{25}$$

.

$$v = \frac{1+\sqrt{1+4(\eta_{II}+\gamma)}}{2} \tag{26}$$

Furthermore, the HSKP energy equation is obtained as follows when Eq. (12) is substituted with Eqs. (23), (24), (25), and (26).

$$E_{nl} = \frac{\vartheta_I^{\,2}\hbar^2 l(l+1)}{2\mu} - \frac{\vartheta_I^{\,2}\hbar^2}{8\mu}\left[\frac{\left(n+\frac{1}{2}+\sqrt{\left(l+\frac{1}{2}\right)^2+\frac{2\mu D_e r_e^2}{\hbar^2}}\right)^2 - \frac{2\mu Z_I}{\vartheta^2\hbar^2} + \frac{4\mu D_e r_e}{\hbar^2\vartheta} + l(l+1)}{n+\frac{1}{2}+\sqrt{\left(l+\frac{1}{2}\right)^2+\frac{2\mu D_e r_e^2}{\hbar^2}}}\right]^2. \tag{27}$$

To obtain the appropriate unnormalized wave function, Eq. (13) is substituted with Eq. (24) and the result is given as

$$\psi_I(y) = N\frac{\sqrt{4(\varepsilon+\gamma)}}{2}\times(1-y)\frac{1+\sqrt{1+\eta_{II}+\gamma}}{2}\,{}_2F_1(p_1,p_2,p_3;y), \tag{28}$$

where,

$$p_1 = \sqrt{\varepsilon+\gamma}+\frac{1+\sqrt{1+\eta_{II}+\gamma}}{2}+\sqrt{\varepsilon+\eta_I} \tag{29}$$

$$p_2 = \sqrt{\varepsilon+\gamma}+\frac{1+\sqrt{1+\eta_{II}+\gamma}}{2}-\sqrt{\varepsilon+\eta_I} \tag{30}$$

$$p_3 = 1+2\sqrt{\varepsilon+\gamma} \tag{31}$$

3.1 Special cases of the HSKP

1. We possess the HP described in Equation (32) and its corresponding energy equation as stated in Equation (33) for the case $Z_{II} = Z_{III} = 0$.

$$V(r_1) = -\frac{Z_I e^{-\vartheta_I r_1}}{1-e^{-\vartheta_I r_1}} \tag{32}$$

$$E_{nl} = \frac{\vartheta_I^{\,2}\hbar^2 l(l+1)}{2\mu} - \frac{\vartheta_I^{\,2}\hbar^2}{8\mu}\left[\frac{(n+l+1)^2 - \frac{2\mu Z_I}{\vartheta_I^{\,2}\hbar^2} + l(l+1)}{n+l+1}\right]^2. \tag{33}$$

Equation (33) and Equation (32) of [4] agree.

2. We possess the SKP described in Equation (34) and its corresponding energy equation as stated in Equation (35) for the case $Z_I = 0$.

$$V(r_1) = -\frac{Z_{II} e^{-\vartheta_I r_1}}{r_1} + \frac{Z_{III} e^{-\vartheta_I r_1}}{r_1^2} \tag{34}$$

$$E_{nl}=\frac{\vartheta_I^{\,2}\hbar^2 l(l+1)}{2\mu}-\frac{\vartheta_I^{\,2}\hbar^2}{8\mu}\left[\frac{\left(n+\frac{1}{2}+\sqrt{\left(l+\frac{1}{2}\right)^2+\frac{2\mu D_e r_e^2}{\hbar^2}}\right)^2+\frac{4\mu D_e r_e}{\hbar^2\vartheta}+l(l+1)}{n+\frac{1}{2}+\sqrt{\left(l+\frac{1}{2}\right)^2+\frac{2\mu D_e r_e^2}{\hbar^2}}}\right]^2. \quad (35)$$

The results of Equation (35) and Eq. (29) of [28] agree.

3. When setting $Z_I=\vartheta_I=0$ is used, the Kratzer potential (KP) is represented by Equation (36), and the energy equation for the KP is given by Equation (37).

$$V(r_1)=-\frac{Z_{II}}{r_1}+\frac{Z_{III}}{r_1^2} \quad (36)$$

$$E_{nl}=-\frac{2\mu D_e^2 r_e^2}{\hbar^2\left(n+\frac{1}{2}+\sqrt{\left(l+\frac{1}{2}\right)^2+\frac{2\mu D_e r_e^2}{\hbar^2}}\right)^2} \quad (37)$$

Equation (37) and Eq. (46) of [28] are identical;

4.The expectation values of HSKP via the Hellmann-Feynman theorem

The expectation values of different quantum systems are derived by utilizing the Hellmann-Feynman Theorem (HFT) [5,17,21]. Suppose that the Hamiltonian of a specific quantum system is dependent on a parameter. Let the eigenvalues and eigenfunctions of the Hamiltonian $\hat{H}(q_I)$ be $E(q_I)$ and $\Psi(q_I)$, respectively. The HFT states that

$$\frac{\partial E_{nl}(q_I)}{\partial q_I}=\langle\psi_{nl}(q_I)\left|\frac{\partial\hat{H}(q_I)}{\partial q_I}\right|\psi_{nl}(q_I)\rangle \quad (38)$$

The effective Hamiltonian has the following form:

$$\hat{H}=-\frac{\hbar^2}{2\mu}\frac{d^2}{dr_1^2}-\frac{\hbar^2}{\mu r_1}\frac{d}{dr_1}+\frac{\hbar^2}{2\mu r_1^2}l(l+1)-\frac{Z_I e^{-\vartheta_I r_1}}{1-e^{-\vartheta_I r_1}}-\frac{Z_{II}e^{-\vartheta_I r_1}}{r_1}+\frac{Z_{III}e^{-\vartheta_I r_1}}{r_1^2} \quad (39)$$

4.1 Expectation value of $\langle r_1^{-2}\rangle$

The expectation value (EV) of $\langle r_1^{-2}\rangle$ is obtain when replacing $q_I=l$ in Eq. (38) and by taking the partial derivative (PD) of Eq. (27) with respect to l, then equating the resulting equations yields the EV of $\langle r_1^{-2}\rangle$ as:

$$\langle r_1^{-2}\rangle=\vartheta_I$$
$$-\frac{4\mu BV}{\hbar^2(2l+1)}\left[\frac{1}{2\sqrt{F}}-\frac{\left\{\left(n+\frac{1}{2}+\sqrt{F}\right)(2l+1)+\left(+\frac{2Z_1\mu}{\hbar^2\vartheta_I^{\,2}}+\frac{4\mu D_e r_e}{\hbar^2\vartheta_I}+l(l+1)\right)\frac{1}{2\sqrt{F}}(2l+1)\right\}}{\left(n+\frac{1}{2}+\sqrt{F}\right)^2}\right] \quad (40)$$

.

4.2 Expectation values for $\langle T\rangle$ and $\langle \hat{P}^2\rangle$

The EV of $\langle T\rangle$ and $\langle \hat{P}^2\rangle$ are obtain when replacing $q=\mu$ in Eq. (38) and by taking the PD of Eq. (39) with respect to μ, which implies $-\frac{1}{\mu}\langle T\rangle=-\frac{1}{\mu}\left(H-V\right)$. From the relation $T=\frac{p^2}{2\mu}$, we substitute for T in $-\frac{1}{\mu}\langle T\rangle=-\frac{1}{\mu}\left(H-V\right)$ which yields

.

$$\langle\psi_{nl}(\mu)\left|\frac{\partial\hat{H}(\mu)}{\partial\mu}\right|\psi_{nl}(\mu)\rangle=-\frac{1}{\mu}\langle T\rangle \tag{41}$$

Putting $-\frac{1}{\mu}\langle T\rangle=-\frac{1}{2\mu^2}\langle\hat{P}^2\rangle$ into Eq. (41) yields

$$\langle\psi_{nl}(\mu)\left|\frac{\partial\hat{H}(\mu)}{\partial\mu}\right|\psi_{nl}(\mu)\rangle=-\frac{1}{2\mu^2}\langle\hat{P}^2\rangle \tag{42}$$

The PD of Eq. (27) with respect to μ gives

$$\frac{\partial E_{nl}(\mu)}{\partial\mu}=-\frac{\vartheta_1\hbar^2 l(l+1)}{2\mu^2}$$

$$+2BV\left[\frac{D_e r_e^2}{\hbar^2\sqrt{F}}-\frac{\left\{\left(n+\frac{1}{2}+\sqrt{F}\left(\frac{2Z_1}{\vartheta_1{}^2\hbar^2}+\frac{4D_e r_e}{\hbar^2\vartheta_1}\right)\right)-\left(\frac{2Z_1}{\vartheta_1{}^2\hbar^2}+\frac{4D_e r_e}{\hbar^2\vartheta_1}+l(l+1)\right)\frac{D_e r_e^2}{\hbar^2\sqrt{F}}\right\}}{\left(n+\frac{1}{2}+\sqrt{F}\right)^2}\right] \tag{43}$$

Eqs. (41) and (43) must be solved to obtain the EV of $\langle T\rangle$.

Hence,

$$\langle T\rangle=\frac{\vartheta_1\hbar^2 l(l+1)}{2\mu}$$

$$-\frac{\hbar^2\vartheta_1{}^2\mu}{4\mu^2}V\left[\frac{D_e r_e^2}{\hbar^2\sqrt{F}}-\frac{\left\{\left(n+\frac{1}{2}+\sqrt{F}\left(\frac{2Z_1}{\vartheta_1{}^2\hbar^2}+\frac{4D_e r_e}{\hbar^2\vartheta_1}\right)\right)-\left(\frac{2Z_1}{\vartheta_1{}^2\hbar^2}+\frac{4D_e r_e}{\hbar^2\vartheta_1}+l(l+1)\right)\frac{D_e r_e^2}{\hbar^2\sqrt{F}}\right\}}{\left(n+\frac{1}{2}+\sqrt{F}\right)^2}\right] \tag{44}$$

Also, Eqs. (42) and (43) must be solved to obtain the EV of $\langle\hat{P}^2\rangle$.

Hence,

$$\langle\hat{P}^2\rangle=\vartheta_1\hbar^2 l(l+1)$$

$$-\frac{\hbar^2\vartheta_1{}^2}{2}V\left[\frac{D_e r_e^2}{\hbar^2\sqrt{F}}-\frac{\left\{\left(n+\frac{1}{2}+\sqrt{F}\left(\frac{2Z_1}{\vartheta_1{}^2\hbar^2}+\frac{4D_e r_e}{\hbar^2\vartheta_1}\right)\right)-\left(\frac{2Z_1}{\vartheta_1{}^2\hbar^2}+\frac{4D_e r_e}{\hbar^2\vartheta_1}+l(l+1)\right)\frac{D_e r_e^2}{\hbar^2\sqrt{F}}\right\}}{\left(n+\frac{1}{2}+\sqrt{F}\right)^2}\right] \tag{45}$$

5.Thermodynamic properties

An essential thermodynamic variable that enables the calculation of additional thermal properties for the system is the partition function (PF). The Boltzmann-Gibbs partition function reads [1]

$$Z(\beta)=\sum_{n=0}^{\lambda}e^{-\beta E_n} \qquad \beta=\frac{1}{k_B T} \tag{46}$$

where k_B, λ and T are the respective Boltzmann constant, maximum vibrational and the absolute temperature.

In the classical limit, the PF may be expressed as an integral at high temperatures.

$$Z(\beta)=\int_{0}^{\lambda}e^{-\beta E_n}dn \tag{47}$$

Further simplification of the energy equation in Eq.(27) is as follows:

$$E_n=Q_0-Q_1\left(n+\Delta+\frac{Q_2}{n+\Delta}\right)^2=\Lambda-\left(Q_1\rho^2+\frac{Q_1Q_2^2}{\rho^2}\right) \tag{48}$$

where

$$\Lambda=Q_0+2Q_1Q_2$$

$$\rho=n+\Delta$$

$$Q_0=\frac{\vartheta_l^{\,2}\hbar^2 l(l+1)}{2\mu}$$

$$Q_1=\frac{\vartheta_l^{\,2}\hbar^2}{8\mu}$$

$$Q_2=\frac{2\mu Z_I}{\vartheta_l^{\,2}\hbar^2}-\frac{4\mu D_e r_e}{\vartheta_l\hbar^2}-l(l+1)$$

$$\Delta=\frac{1}{2}+\sqrt{\left(l+\frac{1}{2}\right)^2+\frac{2\mu D_e r_e^2}{\hbar^2}}$$

The maximum vibration principal quantum number is obtained as $\lambda=-\Delta+\sqrt{Q_2}$

Inserting Eq. (48) into (47) and performing the integration with MAPLE software yields the PF

$$Z(\beta)=\frac{e^{-\beta Q_0}\sqrt{\pi}}{\Upsilon_3\sqrt{\beta}}\left(e^{\Upsilon_0\beta}\left(erf\left(\Upsilon_1\sqrt{\beta}\right)-1\right)+erf\left(\Upsilon_2\sqrt{\beta}\right)+1\right) \tag{49}$$

where

$$\Upsilon_0=4Q_0Q_1$$

$$\Upsilon_1=\sqrt{-Q_1}\left(\rho+\frac{Q_2}{\rho}\right), \Delta\prec\rho\prec\sqrt{Q_2}$$

$$\Upsilon_2=\sqrt{-Q_1}\left(\rho-\frac{Q_2}{\rho}\right), \Delta\prec\rho\prec\sqrt{Q_2}$$

$$\Upsilon_3=\sqrt{-Q_1}$$

Using Eq. (49) other thermodynamic relations are found as follows:

.

(a)vibrational mean energy

$$U(\beta) = -\frac{\partial InZ(\beta)}{\partial \beta} \tag{50}$$

(b) Vibrational specific heat capacity

$$C(\beta) = k_B \beta^2 \left(\frac{\partial^2 InZ(\beta)}{\partial^2 \beta} \right) \tag{51}$$

(c) Vibrational free energy

$$F(\beta) = -k_B T InZ(\beta) \tag{52}$$

(d)Vibrational entropy

$$S(\beta) = k_B InZ(\beta) - k_B \beta \frac{\partial InZ(\beta)}{\partial \beta} \tag{53}$$

6.Results and Discussion

The experimental results from Ref. [1,5], which are shown in Table 1, were applied using Eq. (27), together with the conversion $\hbar c = 1973.29$ eV Å [5]. As shown in Tables 2 and 3, we calculated the energy spectra of the HSKP for HCl and LiH diatomic molecules. For each vibrational quantum number, it has been found that, for each of the diatomic molecules, the vibrational energies rise in proportion to the increase in the rotational quantum number. In addition, the HFT technique was employed to analyze the expectation value (EV) of $\langle r_1^{-2} \rangle$, $\langle T \rangle$ and $\langle \hat{P}^2 \rangle$. The resulting numerical calculations for the selected diatomic molecules are presented in Tables 2 and 3. The results indicate that the expectation value of $\langle r_1^{-2} \rangle$ decreases as the vibrational quantum number increases. Additionally, for the chosen diatomic molecules, the expectation value of $\langle T \rangle$ and $\langle \hat{P}^2 \rangle$ rise as the rotational quantum number rises for each vibrational quantum number. Table 4 shows how temperature affects partition function for H_2 and LiH diatomic molecules. The partition function of the two diatomic molecules increases with temperature. Engineers can use this prediction because hydrogen (H_2) is a vital gas with many industrial and technological uses.

Table 1. Parameters of selected diatomic molecules [1,5]

Molecules	$D_e(eV)$	$\alpha = \vartheta\left(\text{Å}^{-1}\right)$	$r_e(\dot{A})$	$\mu(MeV)$
HCl	4.6190309050	1.86770	1.2746	0.09129614886
LiH	2.5152672118	1.12800	1.5956	0.08198284801
H_2	4.7446000000	1.94260	0.7416	0.503910

The plots of thermodynamic properties for HCl and LiH molecules are shown in Figure 1 (a–e) as a function of the thermodynamic parameter (β). As β is raised, it can be seen in (a) that the PF of the diatomic molecules decreases. The internal energy of the molecules with β is displayed in (b), as can be observed. In this instance, when β is raised, the molecules' internal energy drops. The molecules' specific heat capacity is seen in (c). Each molecule of specific heat capacity rises as β is raised. The plot of the free energy's behavior as a function of β are shown in (d). For each diatomic molecule, we observed that the free energy rises with a rise in β and converges at a particular point. We display a graph of the diatomic molecules ' entropy as a function of β as is seen in (e). It has been shown that as β is raised, each diatomic molecules entropy reduces.

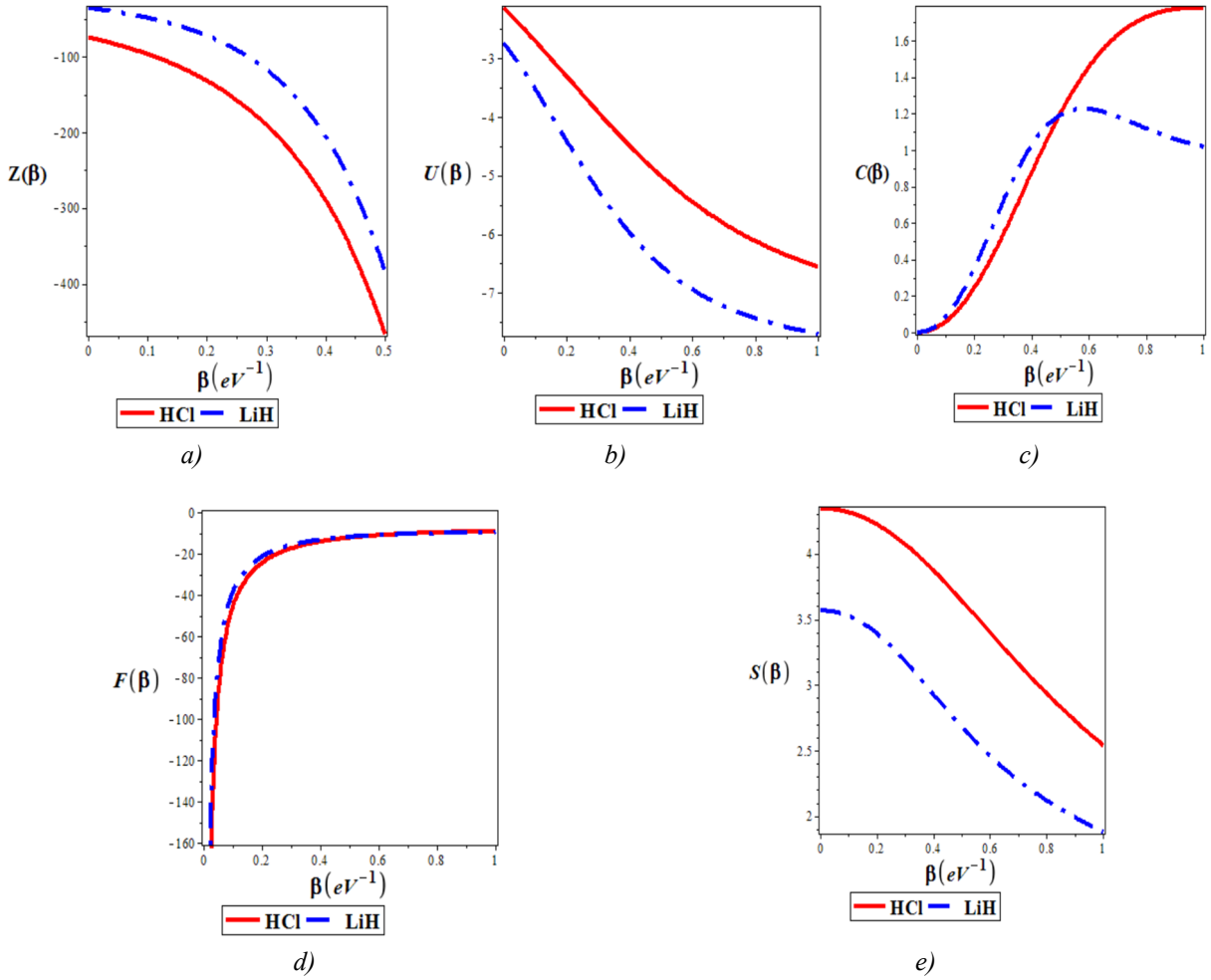

Fig.1 (a-e). Thermodynamic properties as a function of thermodynamic beta parameter for HCl and LiH molecules. Red line (-) represent HCl and blue line (-) represent LiH.

7. Conclusion

The HSKP was used to study the energy eigenvalues and expectation value of LiH and HCl diatomic molecules. The NUFA methodology and HFT were employed, along with the Greene-Aldrich approximation. The findings demonstrated a positive correlation between the quantum numbers and the elevation of energy eigenvalues and expectation value. This suggests that quantum numbers exert a substantial influence on the energy levels of these molecules. In addition, the PF of the system was calculated, followed by the determination of other thermodynamic properties. Our findings align with the results of previous studies. Additional investigation in this field can yield valuable knowledge about diverse physical systems, encompassing atoms, molecules, and condensed matter systems. We calculated the partition function for two diatomic molecules (H_2 and LiH) at different temperatures. With increasing temperature, the partition function of the two diatomic molecules increases. Because hydrogen (H_2) is a vital gas with many industrial and technological uses, this prediction can help engineers.

Conflict of interest statement

The authors declare that they have **no conflict of interest** in relation to this research, whether financial, personal, authorship or otherwise, that could affect the research and its results presented in this paper.

CRediT author statement

Inyang E. P.: Conceptualization, Methodology, Writing- Original draft preparation, Funding acquisition; Ali N.: Software, Data curation, Funding acquisition; Endut R.: Visualization, Investigation; Aljunid S.A.: Validation, Supervision, Writing- Reviewing and Editing. The final manuscript was read and approved by all authors.

.

Funding

This research was carried out under the 2017-2022 merged TETFUND INSTITUTION BASED RESEARCH (IBR) with grant number NOUN/DRA/TETFUNDAW/VOL I.

This research was also carried out under LRGS Grant LRGS/1/2020/UM/01/5/2 (9012-00009) Fault-tolerant Photonic Quantum States for Quantum Key Distribution provided by Ministry of Higher Education of Malaysia (MOHE).

Acknowledgements.

Inyang, E.P. acknowledges the Tertiary Education Trust Fund (TETFUND) of Nigeria for funding this research through the National Open University of Nigeria (Nigeria)-Tertiary Education Trust Fund-Institutional Based Research Grant (TETFUND-IBR) scheme with grant number NOUN/DRA/TETFUNDAW/VOL I. N. Ali and Inyang, E.P. acknowledges the support from the UniMAP Special Research Grant-International Postdoctoral with grant number: 9004-00100.

References

1 Inyang E.P., Ayedun F., Ibanga E.A., Lawal K.M., Okon I. B., William E.S., Ekwevugbe O., Onate C.A., Antia A. D., Obisung E. O. Analytical Solutions of the N-Dimensional Schrödinger equation with modified screened Kratzer plus Inversely Quadratic Yukawa potential and Thermodynamic Properties of selected Diatomic Molecules**.** *Results in Physics,* 2022, Vol.43, 106075. https://doi.org/10.1016/j.rinp.2022.106075

2 Edet C.O., Mahmoud S., Inyang E.P., Ali N., Aljunid A., Endut R., IkotA.N., Asjad M. Non-Relativistic Treatment of the 2D Electron System Interacting via Varshni-Shukla Potential Using the Asymptoptic Iteration Method. *Mathematics.*2022, Vol.10, pp. 2812-2824. https://doi.org/10.3390/math10152824

3 Inyang E.P., Obisung E.O., Iwuji P.C., Ntibi J.E., Amajama J., William E.S. Masses and thermal properties of a charmonium and Bottomonium mesons*. Recent Advances in Applications of Potential Models*, 2022, Vol.4, pp.875-884. https://doi.org/10.46481/jnsps.2022.884

4 Bayrak O., Kocak G., Boztosun I. Any l-state solutions of the Hulth´en potential by the asymptotic iteration method. *Journal of Physics A*, 2006, Vol.39, pp.11510-11521. https://doi.org/10.1088/0305-4470/39/37/012

5 Oluwadere O. J., Oyewumi K. J. Energy spectra and the expectation values of diatomic molecules confined by the shifted Deng-Fan potential. *European Physical Journal plus*, 2018, Vol.133, pp.410-422. https://doi.org/10.1140/epjp/i2018-12210-0

6 Ibekwe E.E., Okorie U.S., Emah J.B., Inyang E.P., Ekong S.A. Mass spectrum of heavy quarkonium for screened Kratzer potential (SKP) using series expansion method. *European Physical Journal Plus*, 2021, Vol.87, pp.1-11. https://doi.org/10.1140/epjp/s13360-021-01090-y

7 Inyang E.P., Inyang E.P., Ntibi J. E., Ibekwe E. E., William E. S. Approximate solutions of D-dimensional Klein-Gordon equation with Yukawa potential via Nikiforov-Uvarov method**.** *Indian Journal of Physics,* 2021, Vol.95, pp.2733-2739. https://doi.org/10.1007/s12648-020-01933-x

8 Omugbe E., Osafile O.E., Inyang E.P., Jahanshir A. Bound state solutions of the hyper-radial Klein-Gordon equation under the Deng-Fan potential by WKB and SWKB methods. *Physica Scripta*, 2021, Vol. 96, pp. 125408. https://doi.org/10.1088/1402-4896/ac38d4

9 Omugbe E., Osafile O.E., Okon I.B., Inyang E.P., William E.S., Jahanshir A. Any L-state energy of the spinless Salpeter equation under the Cornell potential by the WKB Approximation method: An Application to mass spectra of mesons. *Few-Body Systems,* 2022,Vol. 63, pp 1-7. https://doi.org/10.1007/s00601-021-01705-1

10 Inyang E.P., William E.S., Omugbe E., Inyang E.P., Ibanga E.A., Ayedun F., Akpan I.O., Ntibi J.E. Application of Eckart-Hellmann potential to study selected diatomic molecules using Nikiforov-Uvarov-Functional analysis method. *Revista Mexicana de Fisica. 2022,* Vol. 68, pp.1-14. https://doi.org/10.31349/revmexfis.68.020401

11 Ciftci H., Kisoglu H.F. Nonrelativistic-Arbitrary l-states of quarkonium through Asymptotic Iteration method. *Advances in High Energy Physics,* 2018, 4549705. https://doi.org/10.1155/2018/4549705

12 Ikot A.N., Okorie U.S., Amadi P.O., Edet C.O., Rampho G.J., Sever R. The Nikiforov-Uvarov –Functional Analysis (NUFA) Method: A new approach for solving exponential – Type potentials. *Few-Body System*, 2021, Vol.62**,** pp.1-9. https://doi.org/10.1007/s00601-021-021-01593-5

13 Ibekwe E.E., Emah J.B., Inyang E.P. Akpan A. O. MASS Spectrum of Heavy Quarkonium for Combined Potentials (Modified Kratzer Plus Screened Coulomb Potential). *Iranian Journal of Science and Technology,* 2022, Vol.46, pp.1741-1748. https://doi.org/10.1007/s40995-022-01377-4

14 Inyang E.P., Inyang E.P., Ntibi J.E., William E.S. Analytical solutions of Schrodinger equation with Kratzer-screened Coulomb potential for a Quarkonium system. *Bulletin of Pure and Applied Sciences*, 2021, Vol.40, pp.1-12. https://doi.org/10.5958/2320-3218.2021.0002.6

15 Inyang E.P., Inyang E.P., William E.S., Ntibi J.E., Ibanga E.A. Bound State Solutions of the Schrödinger equation with Frost-Musulin potential using the Nikiforov-Uvarov-Functional Analysis (NUFA) method. *Bulgarian Journal of Physics*, 2022, Vol.20, pp. 1-11. https://doi.org/10.55318/bgjp.2022.49.4.329

16 William E. S., Inyang E. P., Thompson E. A. Arbitrary ℓ-solutions of the Schrödinger equation interacting with Hulthén-Hellmann potential model. *Revista Mexicana Fisica,* 2020, Vol. 66, pp.730-741. https://doi.org/10.31349/RevMexFis.66.730.

17 Okoi P.O., Edet C.O., Magu T.O. Inyang E.P. Eigensolution and Expectation values of the Hulthén and Generalized Inverse Quadratic Yukawa potential. *Jordan Journal of Physics,* 2022, 15, pp.137-148. https://doi.org/10.47011/15.2.4

18 Inyang E.P., Obisung E.O., Amajama J., Bassey D.E., William E.S., Okon I.B. The Effect of Topological Defect on The Mass Spectra of Heavy and Heavy-Light Quarkonia. *Eurasian Physical Technical Journal*, 2022, Vol. 9, 4(42), pp. 78 – 87. https://doi.org/10.31489/2022No4/78-87

19 Ikot A.N., Obagboye L.F., Okorie U.S., Inyang E.P., Amadi P.O., Abdel-Aty A. Solutions of Schrodinger equation with generalized Cornell potential (GCP) and its applications to diatomic molecular systems in D-dimensions using Extended Nikiforov–Uvarov (ENU) formalism. *The European Physical Journal Plus*, 2022, Vol.137, pp.1370 https://doi.org/10.1140/epjp/s13360-022-03590-x

20 William E.S., Inyang E.P., Akpan I.O., Obu J.A., Nwachukwu A.N., Inyang E.P. Ro-vibrational energies and expectation values of selected diatomic molecules via Varshni plus modified Kratzer potential model. *Indian Journal of Physics*, 2022, Vol.96,pp.3461-3476. https://doi.org/10.1007/s12648-0222-02308-0

21 Inyang E.P., William E.S., Obu J.O., Ita B. I., Inyang E.P., Akpan I.O. Energy spectra and expectation values of selected diatomic molecules through the solutions of Klein-Gordon equation with Eckart-Hellmann potential model. *Molecular Physics*, 2021, Vol.119, pp. e1956615 https://doi.org/10.1080/00268976.2021.1956615

22 Obogo U.P., Ubi O.E., Edet C.O., Ikot, A.N. Effect of the deformation parameter on the nonrelativistic energy spectra of the q-deformed Hulthen-quadratic exponential-type potential. *Ecletica Quimica Journal,* 2021, Vol. 46, pp.63-73. https://doi.org/10.26850/1678-4618eqj.v46.4.2021.p60-73

23 Edet C.O., Ikot A.N., Superstatistics of Diatomic molecules with the shifted Deng-Fan potential model. *Biointerface Research in Applied Chemistry*. 2022, Vol.**12**, pp.4128-4139. https://doi.org/10.33263/BRIAC123.41264139

24 Edet C.O., Okorie U.S., Osobonye G., Ikot A.N., Rampho G.J., Sever R. Thermal properties of Deng-Fan-Eckart potential model using Poisson summation approach. *Journal Mathematical Chemistry*, 2020, Vol.10, pp.12-25. https://doi.org/10.1007/s10910-020-01107-4

25 Inyang E.P., William E.S., Obu J.O Eigensolutions of the N-dimensional Schro¨dinger equation interacting with Varshni-Hulthen potential model. *Revista Mexicana Fisica,* 2021, Vol**.** 67, pp. 193-205. https://doi.org/10.31349/RevMexFis.67.193.

26 Hassanabadi H., Ghominejad M., Zarrinkamar S., The Yukawa potential in semi relativistic formulation via supersymmetry quantum mechanics. *Chinese Physics B*, 2013, Vol.22, pp.060303. https://doi.org/10.1088/1674-1056/22/6/060303

27 Okon I.B, Omugbe E., Antia A.D., Onate C.A., Akpabio L.E., Osafile O.E. Spin and pseudospin solutions to Dirac equation and its thermodynamic properties using hyperbolic Hulthen plus hyperbolic exponential inversely quadratic potential. *Scientific Reports*, 2021, Vol. 11, pp.9- 21. https://doi.org/10.1038/s41598-020-77756-x

28 Ikot A.N., Okorie U.S., Sever R., Rampho G.J. Eigensolution, expectation values and thermodynamic properties of the screened Kratzer potential. *European Physical Journal Plus*, 2019, Vol. 134, pp 386. https://doi.org/10.1140/epjp/i2019-12783-x

29 Inyang E.P., Obisung E.O. The study of electronic states of NI and ScI molecules with screened Kratzer Potential. *East European Journal of Physics,* 2022, Vol. 3, pp.32-38. https://doi.org/10.26565/2312-4334-2022-3-04

30 Ikot A.N., Edet C.O., Amadi P.O., Okorie U.S., Rampho G.J., Abdullah H.Y. Thermodynamic properties of Aharanov-Bohm (AB) and magnetic fields with screened Kratzer potential. *European Physical Journal D*, 2020, Vol.74, pp.1-13. https://doi.org/10.1140/epjd/e2020-10084-9

31 Inyang E.P., Inyang E.P., Akpan I.O., Ntibi J.E., William E.S. Masses and thermodynamic properties of a Quarkonium system. *Canadian Journal Physics*, 2021, Vol. 99, pp.982-990. https://doi.org/10.1139/cjp-2020-0578

32 Tezcan C., Sever R. A general approach for the exact solution of the Schrodinger equation. *International Journal of Theoretical Physics,* 2009, Vol. 48, pp.328-337. https://doi.org/10.1007/s10773-008-9806-y

33 Greene R.L., Aldrich C. Variational wave functions for a screened Coulomb potential. *Physical Review A., 1976, Vol.* 14, pp. 2363-2374. https://doi.org/10.1103/PhysRevA.14.2363

34 Servatkhah M., Khordad R., Ghanbari A. Accurate prediction of thermodynamic functions of H2 and LiH using theoretical Calculations. *International Journal of Thermophysics,* 2020, Vol. 41, pp.30-37. https://doi.org/10.1009/s10775-020-2616-0

AUTHORS' INFORMATION

Inyang, Etido P. – Dr. (Sci.), Professor, Department of Physics, National Open University of Nigeria, Victoria Island, Lagos, Nigeria; Nigeria Institute of Physics, Nigeria; ORCID iD: 0000-0002-5031-3297; etidophysics@gmail.com

.

Ali, **Norshamsuri R.** – Dr. (Sci.), Professor, Faculty of Electronic Engineering & Technology, University Malaysia Perlis, Perlis, Malaysia; Centre of Excellence Advanced Communication Engineering (ACE), University Malaysia Perlis, Perlis, Malaysia; ORCID iD: 0000-0002-9348-0714; norshamsuri@unimap.edu.my
Endut, R. – Dr. (Sci.), Professor, Faculty of Electronic Engineering & Technology, University Malaysia Perlis, Perlis, Malaysia; Centre of Excellence Advanced Communication Engineering (ACE), University Malaysia Perlis, Perlis, Malaysia; ORCID iD: 0000-0003-3659-9740; rosdisham@unimap.edu.my

Aljunid, S.A. – Dr. (Sci.), Professor, Faculty of Electronic Engineering & Technology, University Malaysia Perlis, Perlis, Malaysia; Centre of Excellence Advanced Communication Engineering (ACE), University Malaysia Perlis, Perlis, Malaysia; ORCID iD: 0000-0003-2739-6220; syedalwee@unimap.edu.my

Appendix A

Table 2. Energy spectra and expectation values of the HSKP for HCl molecule

n	l	$E_{nl}(\mathrm{eV})$	$\left\langle r_1^{-2}\right\rangle\left(\mathring{\mathrm{A}}\right)^{-2}$	$\langle T\rangle(\mathrm{eV})$	$\left\langle P^2\right\rangle(\mathrm{eV}/c)^2$
0	0	−22.17032494	1.4461305900	-1.527357607	-0.2430954250
0	1	−22.17022128	0.4934942126	-1.527879485	-0.2365343415
0	2	−22.17001432	0.3089006158	-1.528850921	-0.2230060212
0	3	−22.16970474	0.2328634781	-1.530131019	-0.2018428796
0	4	−22.16929354	0.1919356503	-1.531517495	-0.1723326932
0	5	−22.16878209	0.1661204903	-1.532756774	-0.1339118832
1	0	−22.24690799	1.5187697310	-1.512273934	-0.2397598466
1	1	−22.24679078	0.5157465898	-1.512585935	-0.2328013301
1	2	−22.24655670	0.3200992442	-1.513146168	-0.2185951989
1	3	−22.24620649	0.2388704404	-1.513830364	-0.1966640774
1	4	−22.24574126	0.1949209917	-1.514459993	-0.1664947819
1	5	−22.24516244	0.1672300249	-1.514811074	-0.1276768573
2	0	−22.33432382	1.5676664310	-1.499019961	-0.2380244021
2	1	−22.33419477	0.5306022009	-1.499146722	-0.2307718818
2	2	−22.33393705	0.3274233022	-1.499343883	-0.2160599846
2	3	−22.33355145	0.2426244599	-1.499501576	-0.1935463559
2	4	−22.33303911	0.1965821729	-1.499461878	-0.1628618456
2	5	−22.33240157	0.1675873809	-1.499026507	-0.1237106879
3	0	−22.43212310	1.6000110030	-1.487438213	-0.2375700761
3	1	−22.43198398	0.5402950041	-1.487400766	-0.2300928725
3	2	−22.43198398	0.3320371224	-1.487275955	-0.2149910763
3	3	−22.43129039	0.2447983109	-1.486966448	-0.1920208669

Table 3. Energy spectra and expectation values of the HSKP for LiH molecule

n	l	$E_{nl}(\mathrm{eV})$	$\left\langle r_1^{-2}\right\rangle_{\left(\mathring{\mathrm{A}}\right)^{-2}}$	$\langle T\rangle(\mathrm{eV})$	$\left\langle P^2\right\rangle(\mathrm{eV}/c)^2$
0	0	−9.044861721	0.48384419100	-1.529859845	-2.733360767
0	1	−9.044847651	0.16604146380	-1.531954979	-2.742387859
0	2	−9.044819582	0.10527772010	-1.536098894	-2.751403066
0	3	−9.044777634	0.08115099160	-1.542199980	-2.764720459
0	4	−9.044722014	0.06914333150	-1.550123565	-2.782099026
0	5	−9.044652964	0.06254753050	-1.559695049	-2.803226301
1	0	−9.033844252	0.60792631400	-1.518791268	-2.718030441
1	1	−9.033836790	0.20701468020	-1.520693254	-2.722233863
1	2	−9.033821914	0.12940273500	-1.524454369	-2.730564012
1	3	−9.033799708	0.09790208600	-1.529989917	-2.742869320
1	4	−9.033770284	0.08168807260	-1.537175349	-2.758926885
1	5	−9.033733821	0.07233546910	-1.545849125	-2.778447621
2	0	−9.029306244	0.71587103800	-1.508675050	-2.699926444
2	1	−9.029304880	0.24265837200	-1.510399495	-2.703812140
2	2	−9.029302176	0.15038870280	-1.513808697	-2.711512506
2	3	−9.029298171	0.11247235160	-1.518824211	-2.722887159
2	4	−9.029292928	0.09259811150	-1.525330645	-2.737729591
2	5	−9.029286529	0.08084615000	-1.525330645	-2.755771878
3	0	−9.030892408	0.81001512100	-1.499451470	-2.683419916
3	1	−9.030896786	0.27374373700	-1.501012381	-2.687012953
3	2	−9.030905540	0.16868922100	-1.504097390	-2.694133144
3	3	−9.030918685	0.12517627150	-1.508633721	-2.704650248

Table 4: The partition function of the H_2 and LiH Diatomic Molecules

T(K)	LiH (Our work)	LiH [34]
2000	47.3888750	47.38997454
2100	48.3713842	48.37247223
2300	49.3314884	49.33159274
2400	50.2688135	50.26893405
2500	51.1858283	51.18591962
2600	52.9638837	52.96379383
2700	53.8269754	53.82686513
2800	54.6748887	54.67397768

T(K)	H_2 (Our work)	H_2 [34]
300	20.9471874	20.94709840
400	23.3731582	23.37304905
500	25.4964598	25.49634848
600	27.4086363	27.40872531
700	29.1632280	29.16311708
800	30.7934865	30.79338849
900	32.3228778	32.32276890
1000	33.7681845	33.76801939

.

SUMMARIES	ТҮСІНІКТЕМЕЛЕР	АННОТАЦИИ

Рыбина Н.В., Рыбин Н.Б., Литвинов В.Г.

Аморфты гидрогенизацияланған кремний мысалында күрделі беттердің рельефіндегі корреляцияларды зерттеу

Scale-space әдістемесінің көмегімен құрылымдық құраушыларын оқшаулау жолымен жою трендімен орташа өзара ақпарат әдісімен және екі өлшемді флуктуациялық талдау әдісімен аморфты гидрогенизацияланған кремнийдің беттік рельефіндегі корреляцияны зерттеу нәтижелері ұсынылған. Эксперименттік үлгілер аморфты гидрогенизацияланған кремнийдің модельдік және нақты беттері болып табылды. Модель беті «Стохастикалық фрактал», «Бөлшектер» және «Гаусс шуы» беттерін қабаттастыру арқылы құрылды. Флуктуациялық функцияның масштабқа тәуелділігінен есептелген скейлинг көрсеткішінің мәндері, сондай-ақ орташа өзара ақпарат пен максималды өзара ақпараттың мәндері анықталды. Аморфты гидрогенизацияланған кремнийдің модельдік және нақты беттерінің корреляциялық тәуелділіктерінің салыстырмалы талдауы эксперименттік үлгінің беттік құрылымына «Бөлшек» модельдік бетінің сипаттамалары бойынша ең жақын екенін көрсетті. Эксперименттік үлгінің беткі құрылымында өлшемдері 65±10 нм болатын бөлшектер бар екендігі анықталды.

Кілт сөздері:аморфты гидрогенизацияланған кремний, бет, рельефі, ақпараттық-корреляциялық сипаттамалар, өзара ақпарат, флуктуациялық талдау, scale-space.

Рыбина Н.В., Рыбин Н.Б., Литвинов В.Г.

Исследование корреляций в рельефе сложных поверхностей на примере аморфного гидрогенизированного кремния

Представлены результаты исследования корреляций в рельефе поверхности аморфного гидрогенизированного кремния методами средней взаимной информации и двумерного флуктуационного анализа с исключенным трендом путем выделения его структурных составляющих с помощью методики scale-space. Экспериментальными образцами являлись модельная и реальная поверхности аморфного гидрогенизированного кремния. Модельная поверхность формировалась путем наложения поверхностей «Стохастический фрактал», «Частицы» и «Гауссов шум». Определены значения скейлингового показателя, рассчитанные из зависимостей флуктуационной функции от масштаба, а также значения средней взаимной информации и максимальной взаимной информации. Проведенный сравнительный анализ корреляционных зависимостей модельной и реальной поверхности аморфного гидрогенизированного кремния показал, что наиболее близка к структуре поверхности экспериментального образца по своим характеристикам модельная поверхность «Частицы». Было выявлено, что в структуре поверхности экспериментального образца присутствуют частицы с размерами 65±10 нм.

Ключевые слова: аморфный гидрогенизированный кремний, поверхность, рельеф, информационно-корреляционные характеристики, взаимная информация, флуктуационный анализ, scale-space.

Козловский А.Л.

Жоғары температуралы күйдіру кезінде коррозиялық процестермен байланысты сыртқы әсерлерге төзімділікке беткі қабаттағы зақымданудың жинақталған дозасының әсерін зерттеу

Электролиз әдістерін қолдана отырып, сутекті өндіру үшін үлкен әлеуетке ие керамикалық отын элементтерінің құрылымдық және беріктік деградациясының мәселелерін зерттеудің өзекті бағыттарының бірі болып табылады, себебі деградация процестерін және олардың жүру жылдамдығын түсіну энергияны алудың балама әдістері (сутегі энергетикасы) саласында берілген керамиканы қолдану әлеуетін анықтау үшін өте маңызды. Бұл зерттеудің негізгі мақсаты 50 атомға ығысу дозасына ие протондармен сәулеленген $NiAl_2O_4$ керамикасының алюминий нитридімен коспалаудың жоғары температуралық деградацияның төзімділігіне және онымен байланысты тотығу және ісіну коррозиялық процестеріне, сондай-ақ имплантацияланған сутектің миграциялық процестеріне әсерін анықтау болып табылады. Зерттеу нысандары ретінде керамиканың үш түрі таңдалды: $NiAl_2O_4$ керамикасы, 0,05 М AlN тұрақтандырылған $NiAl_2O_4$ керамикасы, 0,15 М AlN тұрақтандырылған $NiAl_2O_4$ керамикасы, олар үшін $Al_7O_3N_8$-де орторомбты кристалдық торлы қоспа фазаларының түзілуімен сипатталады. Жоғары температуралық сынақтардың нәтижесінде тұрақтандырылған $NiAl_2O_4$ керамикасы беріктік сипаттамаларының деструктивті өзгеруіне аз ұшырайтыны анықталды, олардағы өзгерістер ең алдымен, оның ісінуі нәтижесінде кристалдық құрылымның деформациялық бұрмалануына байланысты. Бұл жағдайда сәулеленген үлгілер жағдайында жоғары температуралық коррозияға ең аз төзімді үлгі -тұрақтандырылмаған $NiAl_2O_4$ керамикалары болып табылады, олар үшін беріктік қасиеттерінің деградациясы 15 – 18 % - дан асады. Әсер ету температурасының өзгеруі кезінде жоғары температуралық коррозияға төзімділікке жүргізілген сынақтар барысында температураның 500-ден 700°С-қа дейін жоғарылауы деструкция процестерінің тез жүруіне әкелетіні анықталды. Бұлкристалдық тор көлемінің деформациялық ісінуімен байқалатын кристалдық құрылымның жылулық ұлғаюының артуымен байланысты.

Кілт сөздері: керамикалық отын элементтері, радиациялық сынғыштық, жоғары температуралы ескіру, деградация, ісіну, беріктік параметрлерінің төмендеуі.

Козловский А.Л.

Исследование влияния накопленной дозы повреждений в приповерхностном слое на устойчивость к внешним воздействиям, связанным с коррозионными процессами при высокотемпературном отжиге.

Изучение проблем структурной и прочностной деградации керамических топливных элементов, обладающих большим потенциалом для производства водорода с применением электролизных методов является одним из актуальных направлений исследований, так как понимание процессов деградации и скорости их протекания имеют весьма важное значение для определения потенциала применения данных керамик в области альтернативных способов получения энергии (водородной энергетике). Основной целью данного исследования является определение влияния допирования нитридом алюминия $NiAl_2O_4$ керамик, облученных протонами с дозой порядка 50 сна, на устойчивость к высокотемпературной деградации, и связанными с ней коррозионными процессами окисления и распухания, а также миграционными процессами имплантированного водорода. В качестве объектов исследования были выбраны три типа керамик: $NiAl_2O_4$ керамики, $NiAl_2O_4$ керамики, стабилизированные 0.05 M AlN, $NiAl_2O_4$ керамики, стабилизированные 0.15 MAlN, для которых характерно формирование примесных фаз в $Al_7O_3N_8$, с ромбическим типом кристаллической решетки. В результате высокотемпературных испытаний было установлено, что стабилизированные $NiAl_2O_4$ керамики менее подвержены деструктивному изменению прочностных характеристик, изменение которых обусловлено в первую очередь деформационным искажением кристаллической структуры в результате ее распухания. При этом в случае облученных образцов, наименее устойчивыми к высокотемпературной коррозии являются нестабилизированные $NiAl_2O_4$ керамики, для которых деградация прочностных свойств составляет более 15 – 18 %. В ходе проведенных испытаний на устойчивость к высокотемпературной коррозии при вариации температуры воздействия было установлено, что увеличение температуры с 500 до 700°C приводит к ускорению процессов деструкции, которые связаны с увеличением теплового расширения кристаллической структуры, выражающейся в деформационном распухании объема кристаллической решетки.

Ключевые слова: керамические топливные элементы, радиационное охрупчивание, высокотемпературное старение, деградация, распухание, снижение прочностных параметров.

Курбанов У.Т., Жумабаева Г.К., Джуманов С.

Жаңа металл / асқын өткізгіш-диэлектрлік ауысулары және олардың легирленбеген және оңтайлы легирленген купраттардағы жоғары температуралы асқын өткізгіштікке әсері

Металл/асқын өткізгіш-диэлектрик поляröндардың түзілуін және олардағы легирленген заряд тасымалдаушылардың (тесіктердің) локализациясын және металл немесе асқын өткізгіш жүйені диэлектрикке айналдыру мүмкіндігін зерттеу арқылы легирленген купраттарда ауысуының жаңа әдіс-тәсіл әзірленді. Мұндай фазалық ауысудың неғұрлым қолайлы критерийі үлкен поляröндардың жолақ енін (немесе Ферми энергиясын) олардың купраттардағы байланыс энергияларымен салыстыру арқылы алынды. Легирленген купраттардағы металл/асқын өткізгіш - диэлектрлік ауысу және фазалық ыдырау мүмкіндігі болжанған, нәтижесінде легирленбеген, оңтайлы легирленген және тіпті аса легирленген жоғары температуралы купраттарда бәсекелес металл/асқын өткізгіш және диэлектрлік фазалар пайда болады. Содан кейін әртүрлі бұзылулардың (мысалы, поляröндардың түзілуі және заряд тығыздығының толқындық ауысуы) және қатар болатын диэлектрлік және асқын өткізгіш фазалардың легирленбеген және оңтайлы легирленген купраттардың асқын өткізгіштік ауысуының T_C критикалық температурасына ықтимал зиянды және пайдалы әсері зерттелді. Бұл материалдардағы асқын өткізгіштік ауысуының T_C нақты температурасы жоғары температуралы купраттардағы сәйкес T_C мәнін болжай алмайтын Бардин-Купер-Шриффер типті Ферми-сұйықтық асқын өткізгіштік теориясын емес, Бозе-сұйықтықтың асқын өткізгіштік теориясын қолдана отырып анықталды. Оңтайлы легирленген купраттардағы поляröндық және заряд тығыздығы толқынының әсерлерін кемуі T_c –ның жоғарылауына әкелетінін және купраттардағы кейбір тор ақаулары (мысалы, аниондық бос орындар) T_c-ға қатты әсер етіп, олардағы жоғары температуралық асқын өткізгіштікті күшейтетінін анықталды.

Кілт сөздері: поляröндардың және заряд тығыздығы толқындарының түзілуі, металл / асқын өткізгіш-диэлектрлік ауысу, купраттар, Бозе-сұйықтық асқын өткізгіштік, әртүрлі бұзылулар, жоғары температуралы асқын өткізгіштікті әлсірету және күшейту.

Курбанов У.Т., Жумабаева Г.К., Джуманов С.

Новые металл/сверхпроводник-диэлектрик переходы и их влияние на высокотемпературную сверхпроводимость в недолегированных и оптимально легированных купратах

Разработан новый подход к металл/сверхпроводник-диэлектрик переходу в легированных купратах путем изучения образования поляронов и локализации в них легированных носителей заряда (дырок) и возможности превращения металлической или сверхпроводящей системы в диэлектрик. Более подходящий критерий такого фазового перехода был получен путем сравнения ширины полосы (или энергии Ферми) больших поляронов с

их энергиями связи в купратах. Предсказана возможность металл/сверхпроводник- диэлектрик перехода и фазового расслоения в легированных купратах, приводящего к образованию конкурирующих металлических/сверхпроводящих и диэлектрических фаз в недолегированных, оптимально легированных и даже в сверхлегированных высокотемпературных купратах. Затем было исследовано возможное вредное и благотворное влияние различных нарушений (например, образования поляронов и перехода волны зарядовой плотности) и сосуществующих диэлектрических и сверхпроводящих фаз на критическую температуру T_c сверхпроводящего перехода недолегированных и оптимально легированных купратов. Определена реальная температура сверхпроводящего перехода T_c в этих материалах с использованием теории сверхпроводимости Бозе-жидкости, а не теории сверхпроводимости Ферми-жидкости типа Бардина-Купера-Шриффера, которая не способна предсказать соответствующее значение T_c в высокотемпературных купратах. Обнаружено, что подавление поляронных эффектов и эффектов волны зарядовой плотности в оптимально легированных купратах приводит к увеличению T_c, а некоторые дефекты решетки (например, анионные вакансии) в купратах могут сильно влиять на T_c и усиливать высокотемпературную сверхпроводимость в них.
Ключевые слова: образование поляронов и волны зарядовой плотности, металл/сверхпроводник-диэлектрик переход, купраты, Бозе-жидкостная сверхпроводимость, различные нарушения, подавление и усиление ВТСП.

Ибраев И.Қ., Ибраева О.Т., Жакупов Т.М.

Құю кезінде ішкі және беттік ақаулардың пайда болу механизмі және олардың қаңылтыр бетінің ақауларына айналуы

Зерттеудің мақсаты құймалардың қыртысты аймағында микро- және макроқұрылымдық біртексіздіктердің пайда болу механизмдерін және олардың қыздыру, пластикалық деформация және илемдеу процестерінде беттік ақауларға айналуын түсіндіру болып табылады. Құймалар мен дайын прокаттың макро, микроқұрылымдық және химиялық біртексіздіктерін зерттеу әдістемесі мен нәтижелері көрсетілген. Құйма – плита – прокат металлургиялық өңдеу сатысында металды құрылымдық-концентрациялық талдаудың салыстырмалы әдісі әзірленді. Әдістеме металл емес қосындылардың құрылымын және сапалық талдауын зерттеуге арналған металлографиялық әдістерге негізделген. Зерттеу нәтижелері көрсеткендей, прокат бетініңсапасы негізінен құйманың қыртысы аймағының физикалық біртексіздігімен, ал жұқапрокаттың ішкі ақаулары көбінесе металдың металл емесқосындылармен ластануымен анықталады. Құйма қыртыс аймақтағы ақауларды прокат парақтарындағы беттік және ішкі ақауларға айналдырудың жаңа механизмі ұсынылды. Бұл зерттеу металды өңдеу кезінде ақаулардың пайда болу және түрлену процестерін тереңірек түсінуге ықпал етеді және прокаттың сапасын жақсарту стратегияларын жасауға мүмкіндік береді. Сонымен қатар, зерттеу жоғары сапалы прокат алу үшін құйманың қыртыс аймағының физикалық біртексіздігін бақылаудың және металл емес ластануды азайтудың маңыздылығын көрсетеді.
Кілт сөздері: құйма, макро- және микробіртексіздік, пластина, қаңылтыр, ақау, құрылым.

Ибраев И.К., Ибраева О.Т., Жакупов Т.М.

Механизм формирования внутренних и поверхностных дефектов при литье и их трансформация в дефекты поверхности листа

Целью исследования было выяснение механизмов образования микро- и макроструктурных неоднородностей в корковой зоне слитков и их трансформации в поверхностные дефекты в процессах нагрева, пластической деформации и прокатки. Представлены методика и результаты исследования макро-, микроструктурных и химических неоднородностей слитков и готового листового проката. Разработан сравнительный метод структурно-концентрационного анализа металла на сквозном металлургическом переделе слиток – сляб – листовой прокат. Методика основана на проведении металлографических методов изучения структуры и качественного анализа неметаллических включений. Результаты исследований свидетельствуют о том, что качество поверхности листового проката преимущественно определяется физической неоднородностью корковой зоны слитка, а на внутренние дефекты тонколистового проката в значительной степени определятся загрязненность металла неметаллическими включениями. Предложен новый механизм трансформации дефектов корковой зоны отливки в поверхностные и внутренние дефекты листового проката. Данное исследование способствует более глубокому пониманию процессов образования и трансформации дефектов при обработке металлов и позволяет разработать стратегии повышения качества листового проката. Кроме того, в исследовании подчеркивается важность контроля физической неоднородности зоны корки слитка и минимизации загрязнения неметаллическими включениями для получения высококачественного проката.
Ключевые слова: слиток, макро- и микронеоднородность, сляб, листовой прокат, дефект, структура.

Байкенов М.И., Сельдюгаев О.Б., Гученко С.А., Афанасьев Д.А.

Теңіз суындағы мартенситті болаттың нүктелік коррозиясының себебі

Ұсынылған жұмыста мартенситті тот баспайтын болаттан жасалған Х17 бұйымдарының теңіз суындағы коррозиясы өнімдер бетіндегі ұяшықтарындағы хром атомдарының толық тотылмағандығынан болады деп болжанады. Х17 болатының ұяшықтарындағы хром атомдарының толық тотығуы 350°С-қа дейінгі

температуралардағы оттегі молекулаларының мартенситті тот баспайтын болаттың текше көлемдік-орталықтандырылған ұяшықтарының құрамына кіретін үш валентті хром атомдарымен химиялық әрекеттесу үшін энергияның жеткіліксіздігінен туындайды. Х17 тот баспайтын болаттан жасалған бұйымдарды этанолдағы йодтың 5% ерітіндісіне салғанда бұйымның бетін оттегінің белсенді түрлерімен алдын ала өңдегеннен кейін коррозия жылдамдығының айтарлықтай төмендеуі көрсетілген. Өңдеу оттегінің химиялық белсенді түрлерімен (озон және синглет оттегі) 350°C температурада 12 сағат бойы жүргізілген. Оттегінің жоғары белсенді түрлерімен 12 сағаттық әсер ету нәтижесінде Х17 болаттан жасалған бұйымдар үлгілерінің бетіндегі хром атомдарының көпшілігі толығымен тотыққандығы көрсетілді. Жаңа ХРОМ – ОТТЕГІ – ХРОМ байланыстарының түзілуі нәтижесінде өнімдердің бетіндегі оксид пассивті қабатының тығыздығы айтарлықтай өсті. Бұл коррозияға төзімділіктің жоғарылауына әкеледі. Реактивті оттегі түрлерімен өңделген Х17 тот баспайтын болаттан жасалған бұйымдардың бетінде галоген иондары бар спирт ерітіндісімен әрекеттесу жылдамдығы өңделмеген Х17 болат үлгілерімен салыстырғанда 71% төмендеген қабат пайда болады.

Кілт сөздері: көміртекті болат, теңіз суы, локализацияланған коррозия, тотығу, галогендер, көлемдік-орталықтандырылған текше құрылым.

Байкенов М.И., Сельдюгаев О.Б., Гученко С.А., Афанасьев Д.А.

Причина точечной коррозии мартенситной стали в морской воде

В представленной работе сделано предположение, что коррозия изделий из мартенситной нержавеющей стали Х17 в морской воде возникает из-за неполного окисления атомов хрома в ячейках на поверхности изделий. Неполное окисление атомов хрома в ячейках стали Х17 происходит по причине того, что у молекул кислорода при температурах до 350°C не хватает энергии для химического взаимодействия с трехвалентными атомами хрома входящими в кубические объемно-центрированные ячейки мартенситной нержавеющей стали. Показано, что происходит значительное уменьшение скорости коррозии при размещении изделий из нержавеющей стали Х17 в 5% растворе йода в этаноле после предварительной обработки поверхности изделий активными формами кислорода. Обработка производилась в течении 12 часов химически-активными формами кислорода (озон и синглетный кислород) при температуре 350 °C. Показано, что в результате 12 часового воздействия высокоактивными формами кислорода большая часть атомов хрома на поверхности образцов изделий из стали Х17 была полностью окислена. В результате образования новых связей ХРОМ – КИСЛОРОД – ХРОМ плотность оксидного пассивирующего слоя на поверхности изделий значительно увеличилась. Это привело к повышению коррозийной стойкости. На поверхности изделий из обработанной активными формами кислорода нержавеющей стали Х17 образовался слой, у которого скорость взаимодействия со спиртовым раствором содержащем ионы галогенов снижена на 71% по сравнению с образцами необработанной стали Х17.

Ключевые слова: углеродистая сталь, морская вода, локализованная коррозия, окисление, галогены, объемно-центрированная кубическая структура.

Омарова Г.С., Сериков Т.М., Селиверстова Е.В., Аужанова А.А., Ибраев Н.Х.

Титан диоксидінің бояғыш молекулаларымен сенсибилизациясына плазмондық эффектінің әсері

Эозин мен родамин Б бояғыштарынан TiO_2-ге электронның тасымалдануына металл нанобөлшектерінің плазмондық эффектісінің әсері зерттелген. Спектрлік-кинетикалық өлшеулер SiO_2-мен салыстырғанда TiO_2 бетінде екі бояғыштың қарқындылығы ғана емес, сонымен қатар флуоресценция ұзақтығы да төмендейтінін көрсетті, бұл зарядтың бояғыштан жартылай өткізгішке өтуін көрсетеді. Плазмондық наноқұрылымдары болған жағдайда ядро@қабықшада ($Ag@TiO_2$) жылдам флуоресценцияның қарқындылығы, сондай-ақ бояғыштардың жарқырау ұзақтығының қысқаруы байқалады. $Ag@TiO_2$ НҚ үшін максималды плазмондық әсер тіркелген оңтайлы концентрация 3 мас.% болып табылады. Плазмондық эффект сонымен қатар зерттелетін бояғыштардың молекулалары арқылы өткізгіштің сенсибилизациясының тиімділігінің артуына әкеледі, бұл зерттелетін жартылай өткізгіш қабыршақтардың фотовольтаикалық және зарядтау-тасымалдау сипаттамаларының өсуінен көрінеді. Алынған нәтижелерді фотовольтаика, фотокаталитикалық және оптоэлектрондық элементтерге арналған құрылғыларды әзірлеу кезінде пайдалануға болады.

Кілт сөздері: жартылай өткізгіш, бояғыш, ядро-қабықша наноқұрылымдары, плазмондық эффект, зарядты тасымалдау, сенсибилизация.

Омарова Г.С., Сериков Т.М., Селиверстова Е.В., Аужанова А.А., Ибраев Н.Х.

Влияние плазмонного эффекта на сенсибилизацию диоксида титана молекулами красителей

Изучено влияние плазмонногоэффекта металлических наночастиц на перенос электрона от красителей эозин и родамин Б к TiO_2. Спектрально-кинетические измерения показали, что по сравнению с SiO_2 на поверхности TiO_2 уменьшается не только интенсивность, но и длительность флуоресценции обоих красителей, что свидетельствует о передаче заряда от красителя к полупроводнику. В присутствии плазмонных наноструктур ядро@оболочка ($Ag@TiO_2$) наблюдается интенсификация быстрой флуоресценции, а также сокращение длительности свечения красителей. Оптимальной концентрацией, для которой был зарегистрирован максимальный плазмонный эффект является 3 мас% $Ag@TiO_2$. Плазмонный эффект также приводит к

увеличению эффективности сенсибилизации полупроводника молекулами исследуемых красителей, что выражается в росте фотовольтаических и зарядо-транспортных характеристик исследуемых полупроводниковых пленок. Полученные результаты могут быть использованы при разработке устройств для фотовольтаики, фотокаталитических и оптоэлектронных элементов.
Ключевые слова: полупроводник, краситель, наноструктура ядро-оболочка, плазмонный эффект, перенос заряда, сенсибилизация

Скаков М.К., Бакланов В.В.,Нурпаисова Г.С.,Акаев А.С., Бекмулдин М.К., Толеубеков К.О.

Атом электр станциясындағы ауыр апаттар кезінде кориумда қалдық энергия бөлуді имитациялау әдістерін салыстырмалы талдау

Атом электр станциясындағы ауыр апаттың даму процесінде белсенді аймақ материалдарының еруі және кориумның пайда болатыны белгілі. Кориумның ерекшелігі-оның реактор қондырғысының құрылымдық материалдарымен өзара әрекеттесу сипатына елеулі үлес қосатын қалдық энергия бөлудің болуы. Осы себепті кориум прототипіндегі қалдық энергия бөлінуін модельдеу әдістеріне көлемдік таралудың біркелкілігіне де, оның қарқындылығына да қатысты айтарлықтай талаптар қойылады. Берілген жұмыста кориумдағы қалдық энергия бөлінудің имитациялаудың қолданыстағы әдістеріне салыстырмалы талдау келтірілген. Бұл әдістер атом электр станциясындағы реактордың балқуымен ауыр апаттар кезінде пассивті қорғаныс жүйелерінің жұмысын зерттейтін әртүрлі эксперименттік қондырғыларда қолданылады. Әдістердің артықшылықтар мен кемшіліктерін салыстыру арқылы қалдық энергияны имитациялаудың неғұрлым практикалық әдісі анықталады және нақты кориумның жылулық өрісін толығымен имитациялау үшін таңдалған әдісті одан әрі жетілдіру жолдары ұсынылады.
Кілт сөздері: атом электр станциясы, ауыр апат, кориум, қалдық энергияның бөлінуі,модельдеу.

Скаков М.К., Бакланов В.В.,Нурпаисова Г.С.,Акаев А.С., Бекмулдин М.К., Толеубеков К.О.

Сравнительный анализ методов имитации остаточного энерговыделения в кориуме во время тяжелых аварий на атомных электростанциях

Известно, что в процессе развития тяжелой аварии на атомных электростанциях происходит расплавление материалов активной зоны и образование кориума. Особенностью кориума является наличие остаточного энерговыделения, которое вносит ощутимый вклад в характер его взаимодействия с конструкционными материалами реакторной установки. По этой причине к методам имитации остаточного энерговыделения в прототипе кориума предъявляются достаточно серьезные требования, которые касаются, как равномерности объемного распределения, так и его интенсивности. В данной работе приведен сравнительный анализ существующих методов имитации остаточного энерговыделения в кориуме, которые применяются на различных экспериментальных установках, исследующих работу пассивных систем защиты при тяжелых авариях с расплавлением реактора на атомных электростанциях. Путем сравнения преимуществ и недостатков определяется более практичный метод имитации остаточного энерговыделения и предлагаются пути дальнейшего совершенствования выбранного способа для полной имитации теплового поля реального кориума.
Ключевые слова: Атомная электростанция, тяжелая авария, кориум, остаточное энерговыделение, моделирование

Шаймерденова К.М., Сакипов К.Е., Абдирова Н.Т., Сулейменова С.Е.

Құрғақ байыту әдісімен Екібастұз көмірінің сапасын арттыру

Берілген жұмыста «құрғақ байыту» технологиясын пайдалану есебінен Екібастұз көмірінің сапасын арттыру мүмкіндіктері талқыланады. Жүргізілген эксперименттер мен есептеулер «Ангренсор-Энерго» ЖШС «Екібастұз»қабаттарындағы энергетикалық көмірүлгілерін байытудың оңтайлы сұлбасын анықтауға мүмкіндік берді. Ылғалдылық, күл, ұшпа заттардың шығуы сияқты техникалық сипаттамаларды сынау және энергетикалық көмірдің байытылған үлгілерінің энергетикалық сипаттамаларын есептеу көмірхимия зертханасында 3 кезеңде жүргізілді. Нәтижесінде байытылған отын үлгілерінің энергия мөлшері бастапқы отындікінен 28,5% - на дейін артқаны анықталды. Бұл жоғары сапалы көмір концентратының максималды өнімділігін алу арқылы тұтынушылық қасиеттерін айтарлықтай жақсартты. Демек, әзірленген байыту сұлбасы электр энергиясын тұтынуды едәуір азайтуға, атмосфераға шығарындыларды төмендетуге, қоршаған ортағазиянды әсерді азайтуға, көмір нарықтарын кеңейтуге мүмкіндік береді.
Кілт сөздері: Екібастұз көмірі, энергетикалық көмір, зиянды шығарындылар, ылғалдылық, күлділік, ұшпа заттар, «құрғақ байыту» технологиясы.

Шаймерденова К.М., Сакипов К.Е., Абдирова Н.Т., Сулейменова С.Е.

Улучшение качества экибастузского угля с использованием метода сухого обогащения

В данной работе обсуждаются возможности повышения качества экибастузского угля за счет использования технологии «сухого обогащения». Проведенные эксперименты и расчеты позволили определить оптимальную схему обогащения образцов энергетических углей из разреза «Экибастузский» ТОО «Ангренсор-Энерго».

Тестирование технических характеристик, таких как влажность, зольность, выход летучих веществ и расчет энергетических характеристик обогащенных образцов энергетического угля проведено в 3 этапа в углехимической лаборатории. В результате установлено, что энергосодержание образцов обогащенного топлива увеличилось до 28,5% от исходного. Это значительно улучшило потребительские свойства за счет получения максимального выхода высококачественного угольного концентрата. Следовательно, разработанная схема обогащения позволяет значительно сократить потребление электроэнергии, сократить выбросы в атмосферу, уменьшить вредное воздействие на окружающую среду, расширить рынки сбыта угля.
Ключевые слова: экибастузский уголь, энергетические угли, вредные выбросы, влажность, зольность, летучие вещества, технология «сухого обогащения».

Маликов В.Н., Ишков А.В., Войнаш С.А., Загидуллин Р.Р., Сабитов Л.С., Ворначева И.В., Иванов А.А.
Құйынды ток әдісін қолдануымен жұқа қабықшалардың өткізгіштігін автоматтандырылған бақылау
Мақалада жұқа металл қабықшалардың электр өткізгіштігін өлшеу есептері үшін бұзбайтын бақылаудың құйынды ток әдісін қолдану мүмкіндігі қарастырылған. Өлшеу объектісі ретінде вакуумдағы газ фазасынан тұндыру әдісімен алынған әртүрлі қалыңдықтағы мыс қабықшалары қолданылды. Қазіргі заманғы өнеркәсіп пен ғылымда мыс қабықшаларын қолданудың өзекті бағыттарына шолу жасалып, жұқа мыс қабықшаларын зерттеуге жарамды бұзбайтын бақылаудың өзекті әдістеріне талдау жасалды. Қабықшаның электр өткізгіштігін өлшеуге арналған бүрку әдісі мен бағдарламалық-аппараттық кешеннің қысқаша сипаттамасы берілген. Қабықшаның электр өткізгіштік мәндерін құйынды ток түрлендіргішінің дабылы мәні бойынша қалпына келтіруге мүмкіндік беретін калибрлеу қисығы келтірілген. Калибрлеу қисығын құру үшін GaAs галлий арсенидінің үлгілері алынды. Бұл шешім берілген химиялық қосылыстың электр өткізгіштік мәндерінің алынған жұқа қабықшалардың есептелген көрсеткіштеріне жақындығымен түсіндіріледі, әртүрлі сипаттамалары бар қабықшаларды сынау нәтижелері ұсынылған және партияға байланысты қабықшалардың электр өткізгіштігінің таралуы көрсетілген. Жұқа қабықшаларды практикалық өлшеу сериясы бүркуге ұшыраған бастапқы заттың массасы мен алынған қабықшалардың сипаттамалары арасындағы байланыстың бар екендігін көрсетті. Электр өткізгіштігінің әртүрлі мәндері бойынша бір партия шеңберінде әртүрлі қабықшаларды бүрку сапасының айырмашылығы туралы қорытынды жасалды.
Кілт сөздері: құйынды ток түрлендіргіші, электр өткізгіштік, жұқа қабықшалар, мыс, бұзбайтын бақылау.

Маликов В.Н., Ишков А.В., Войнаш С.А., Загидуллин Р.Р., Сабитов Л.С., Ворначева И.В., Иванов А.А.
Автоматизированный контроль проводимости тонких пленок с использованием вихретокового метода
В статье рассмотрена возможность применения вихретокового метода неразрушающего контроля для задач измерения электропроводности тонких металлических пленок. В качестве объекта измерения использовались медные пленки различной толщины, полученные методом осаждения из газовой фазы в вакууме. Представлен обзор актуальных направлений использования медных пленок в современной промышленности и науки и проведен анализ актуальных методов неразрушающего контроля, пригодного для исследования тонких медных пленок. Представлено краткое описание метода напыления и программно-аппаратного комплекса по измерению электропроводности пленки. Приведена калибровочная кривая, позволяющая восстанавливать значения электрической проводимости пленки по значению сигнала вихретокового преобразователя. Для построения калибровочной кривой были отобраны образцы арсенида галлия GaAs. Решение объясняется близостью значений электропроводности данного химического соединения к рассчитанным показателям полученных тонких пленок Представлены результаты тестирования пленок, имеющих различные характеристики и показано распределение электропроводности пленок в зависимости от партии. Проведенная серия практических измерений тонких пленок продемонстрировала существование взаимосвязи между массой исходного вещества, которое было подвергнуто напылению и характеристиками полученных пленок. По различным значениям электропроводности в рамках одной партии был сделан вывод о разнице в качестве напыления различных пленок.
Ключевые слова: вихретоковый преобразователь, электропроводность, тонкие пленки, медь, неразрушающий контроль.

Миньков Л.Л., Гимаева Н.Р.
Екі фазалы ағынның отын таблеткасының тұтануына және оның гильзадан шығуына әсері
Жалған жылулық мақсаттар ұшақтар мен тікұшақтар үшін қауіпсіз жағдай жасауда маңызды рөл атқарады. Бұл ретте негізгі міндет таблетканың гильзадан ұшар алдында оның тұрақты тұтануын қамтамасыз ету болып табылады. Бұл процесті оңтайландыру үшін әр түрлі параметрлердің әсерін, мысалы, гильза мен отын таблеткасының цилиндрлік беті арасындағы алшақтықтың өлшемін, сондай-ақ инициатор мен отын таблеткасынан келетін бөлшектердің өлшемдерін зерттеу маңызды. Берілген мақалада таблетканың тұтану және ұшу процесінің физика-математикалық моделі ұсынылған, сонымен қатар аталған параметрлердің тұтану уақытына әсері зерттелген. r = 1 мкм және r = 25 мкм-ге тең бөлшектердің әртүрлі өлшемдері үшін дәннің кесіктік бетінің тұтану уақыты бағаланды. Патрон гильзасы мен дәннің цилиндрлік беті арасындағы алшақтық

0,5 мм-ден 2 мм-ге дейін құрады. Гильзадан таблетканың ұшып шығу жылдамдығы 1 мкм және 25 мкм бөлшектер үшін және гильза мен жанармай таблеткасының цилиндрлік беті арасындағы әртүрлі саңылаулар үшін алынды.

Кілт сөздері: жалған жылулық мақсаттар, жану, жану өнімдері, математикалық модельдеу, бастапқы жылдамдық, ішкі баллистика.

Миньков Л.Л., Гимаева Н.Р.

Влияние двухфазного потока на зажигание таблетки топлива и ее вылет из гильзы

Ложные тепловые цели играют важную роль в создании безопасных условий для самолетов и вертолетов. При этом основной задачей является обеспечение стабильного зажигания таблетки топлива перед ее вылетом из гильзы. Для оптимизации этого процесса важно изучить влияние различных параметров, таких как размер зазора между гильзой и цилиндрической поверхностью таблетки топлива, а также размер частиц, поступающих из инициатора и таблетки топлива. В данной статье предложена физико-математическая модель процесса воспламенения и вылета таблетки, а также исследовано влияние указанных параметров на время зажигания. Оценены времена зажигания торцевой поверхности зерна для различных размеров частиц, равные r = 1 мкм и r = 25 мкм. Зазор между гильзой патрона и цилиндрической поверхностью зерна составлял от 0.5 мм до 2 мм. Скорости вылета таблетки из гильзы получены для частиц размером 1 мкм и 25 мкм и разных зазоров между гильзой и цилиндрической поверхностью таблетки топлива.

Ключевые слова: ложные тепловые цели, горение, продукты сгорания, математическое моделирование, начальная скорость, внутренняя баллистика.

Костина М.А., Солдатов А.И., Солдатов А.А., Абуэллаиль А.А.

Термоэлектрлік бақылау кезінде көп нүктелік контактіні модельдеу

Мақалада термоэлектрлік әдіс кезіндегі көп нүктелі контактіні модельдеу нәтижелері келтірілген. ТермоЭҚК көздерінің әртүрлі түрлерінің бірнеше терможұптарды параллель қосу арқылы алынған эквивалентті термоЭҚК көзінің жүктеме сипаттамасына әсері көрсетілген. Ұсынылған модель еркін қол жетімді NI LabVIEW пакетінде жүзеге асырылған. Модельді тексеру терможұптардың үш түрінде жүзеге асырылды: мыс\константан, мыс\нихром және хромель\алюмель, олардың параллель қосылғанжәне саны әртүрлі. Алынған эквивалентті көздің есептік жүктеме сипаттамалары эксперименттік сипаттамалардан 6% - дан аспайды. Терможұптардың екі түрінің әр түрлі санын параллель қосу арқылы алынған эквивалентті термоЭҚК көзінің жүктеме сипаттамаларын модельдеу нәтижелері келтірілген. Сенімді мәліметтерді алу үшін кем дегенде 1 кОм-ның баламалы көзінің жүктемесін қамтамасыз ету қажет екендігі көрсетілген.

Кілт сөздері: термоЭҚК, эквивалентті көз, параллель жалғау, көп нүктелікконтакт, жүктеме сипаттамасы, суперпозиция әдісі.

Костина М.А., Солдатов А.И., Солдатов А.А., Абуэллаиль А.А.

Моделирование многоточечного контакта при термоэлектрическом контроле

В статье приведены результаты моделирования многоточечного контакта при термоэлектрическом методе. Показано влияние разных типов источников термоЭДС на нагрузочную характеристику эквивалентного источника термоЭДС, получаемого за счет параллельного соединения нескольких термопар. Представленная модель реализована в пакете NI LabVIEW, находящаяся в свободном доступе. Верификация модели проведена на трех типах термопар: медь\константан, медь\нихром и хромель\алюмель, с разным их количеством, соединенных параллельно. Полученные расчетные нагрузочные характеристики эквивалентного источника отличаются от экспериментальных не более 6%. Представлены результаты моделирования нагрузочных характеристик эквивалентного источника термоЭДС, получаемого за счет параллельного соединения разного количества двух типов термопар. Показано, что для получения достоверных данных необходимо обеспечить нагрузку эквивалентного источника не менее 1 кОма.

Ключевые слова: термоЭДС, эквивалентный источник, параллельное соединение, многоточечный контакт, нагрузочная характеристика, метод суперпозиции.

Мади П.Ш., Алькина А.Д., Мехтиев А.Д., Юрченко А.В.

Оптикалық талшықты қолдануымен карьер бортының тұрақтылығын бақылауға арналған бағдарламалық-аппараттық кешен

Берілген мақалада борттар мен жиектердің құлауының негізгі себебі болып табылатын карьерлердегі ауысымдық мониторинг жүйесін енгізу туралы шешімдер қарастырылған. Карьердің қауіпсіздігі мен үздіксіз бақылауын қамтамасыз ету үшін талшықты-оптикалық датчиктер қолданылды. Бұл датчиктер бір режимді оптикалық талшықтарды қолдануымен жасалған, бұл тау массивінің 30-50 км радиуста жылжуын дәл бағалауға мүмкіндік береді. Тау массивінде болып жатқан деформациялар мен ығысу процестерін жан-жақты талдау үшін жете зертханалық зерттеулер жүргізілген. Нәтижесінде бұл зерттеулердің нәтижелері карьерлердің тиімділігін едәуір арттыруға және төтенше жағдайлардың ықтималдығын азайтуға мүмкіндік береді.

Кілт сөздері:талшықты-оптикалық датчик, бақылау жүйесі, ашық тау-кен жұмыстары, карьер, қауіпсіздік, тау-кен өндірісі, оптикалық талшық, деформация, ығысу.

Мади П.Ш., Алькина А.Д., Мехтиев А.Д., Юрченко А.В.

Программно-аппаратный комплекс для контроля устойчивости бортов карьера с использованием оптического волокна

В данной статье рассматриваются решения по внедрению системы мониторинга сменности в карьерах, которая является основной причиной обрушения бортов и кромки. Для обеспечения безопасности и бесперебойного наблюдения за работой карьера были применены волоконно-оптические датчики. Эти датчики изготовлены с использованием одномодовых оптических волокон, что позволяет точно оценить смещение горного массива в радиусе 30-50 км. Для всестороннего анализа деформаций и сдвиговых процессов, происходящих в горном массиве, были проведены тщательные лабораторные исследования. В конечном итоге результаты этих исследований позволят значительно повысить эффективность работы карьеров и снизить вероятность возникновения аварийных ситуаций.

Ключевые слова: волоконно-оптический датчик, система мониторинга, открытые горные работы, карьер, безопасность, добыча, оптическое волокно, деформация, сдвиг.

Гадиров Р., Борисов А., Труфанова Н., Рагимов Э., Артищев С.

Тұтқырлығы жоғары пасталарды экструзиялау процесін сандық модельдеу

Мақалада поршеньді дозатор көмегімен пастаны экструзиялау процесіне теориялық шолу ұсынылған. Паста-терпинеол мен күміс бөлшектерінің ұнтағының жоғары тұтқыр суспензиясы болып табылады. Сандық модельдеу нәтижесінде пастаның тұрақты ағынында күміс бөлшектерінің таралуы алынған. Поршеньдегі артық қысым және поршень жылдамдығына байланысты жолдың тиімді ені алынады. Модельдеу экструзия процесіне ең үлкен әсер пастаның тұтқырлығы екенін көрсетті. Алынған тәуелділіктерді пайдалану пастаны экструзиялау процесін басқаруға мүмкіндік береді.

Кілт сөздері: экструзия, поршеньді дозатор, күміс паста, тұтқырлық, терпинеол.

ГадировР., Борисов А., Труфанова Н., Рагимов Э., Артищев С.

Численное моделирование процесса экструзии высоковязких паст

В статье представлено теоретическое рассмотрение процесса экструзии пасты с помощью поршневого дозатора. Паста представляет собой высоковязкую суспензию терпинеола и порошка частиц серебра. В результате численного моделирования получено распределение частиц серебра в установившемся потоке пасты. Получены избыточное давление в поршне и эффективная ширина дорожки в зависимости от скорости поршня. Моделирование показало, что наибольшее влияние на процесс экструзии оказывает вязкость пасты. Использование полученных зависимостей позволит управлять процессом экструзии пасты.

Ключевые слова: экструзия, поршневой дозатор, серебряная паста, вязкость, терпинеол.

Inyang, E.P., Ali N., Endut R., Aljunid S.A.

HCL және LiH қосатомды молекулаларының энергетикалық спектрлері, күтілетін мәндері және термодинамикалық қасиеттері

Шредингер теңдеуі Кратцерэкрандалған потенциалды ескере отырыпХультенус бойынша Никифоров-Уваровтың функционалды талдау әдісін қолдану арқылы шешіледі. Грин-Олдричтің жуықтауы энергия теңдеуі мен толқындық функция үшін тұйық түрдегі өрнектерді анықтау үшін қолданылады. Хеллман-Фейнман теоремасы HCL және LiH қосатомдық молекулаларының (DM) әртүрлі кванттық күйлерінің энергетикалық спектрлері мен математикалық күтімдерін есептеу үшін пайдаланылған. Кейіннен статистикалық қосындыны есептеу үшін бұрын алынған энергия теңдеуі қолданылды, бұл өз кезегінде қосатомдық молекулалармен байланысты термодинамикалық қасиеттерді анықтауға мүмкіндік берді. ҚосатомдықмолекулаларменLiHүшінстатистикалыққосындыәртүрлітемпературадаесептелген. Нәтижелер екі қосатомды молекуланың статистикалық қосындысы температураның жоғарылауымен артанын көрсетеді. Алынған нәтижелер әдебиетте сипатталған нәтижелермен сәйкес келеді.

Кілт сөздері: Грин-Олдричтің жуықтауы, байланысқан, күй, Хеллман-Фейнман теоремасы, термодинамикалық қасиеттер.

Inyang, E.P., Ali N., Endut R., Aljunid S.A.

Энергетические спектры, ожидаемые значения и термодинамические свойства двуатомных молекулHCli LiH

Уравнение Шредингера решается путем применения метода функционального анализа Никифорова-Уварова по Хюльтенус учетом экранированного потенциалаКратцера. Приближение Грина-Олдрича используется для определения выражений в замкнутой форме для уравнения энергии и волновой функции. Теорема Хеллмана-

Фейнмана была использована для расчета энергетических спектров и математических ожиданий различных квантовых состояний двухатомных молекул (DM) HCl и LiH. Впоследствии использовано уравнение энергии, которое ранее было выведено для расчета статистической суммы, что, в свою очередь, позволило нам определить термодинамические свойства, связанные с двухатомными молекулами. Статистическая сумма для двухатомных молекул и LiH рассчитана при различных температурах. Результаты показывают, что статистическая сумма двух двухатомных молекул растет с повышением температуры. Полученные результаты согласуются с результатами, описанными в литературе.

Ключевые слова: приближение Грина-Олдрича, связанное состояние; теорема Хеллмана-Фейнмана; термодинамические свойства.